BREAST IMPLANT SURFACE DEVELOPMENT

A Thesis submitted to The University of Manchester for the degree of Doctor of Philosophy in the Faculty of Engineering and Physical Sciences

2015

ANAI ALICIA VALENCIA LAZCANO

SCHOOL OF MECHANICAL, AEROSPACE AND CIVIL ENGINEERING

Contents

Contents **2**

List of Tables **5**

List of Figures **6**

List of abbreviations **9**

Nomenclature **10**

Abstract **11**

Declaration **12**

Copyright **13**

Acknowledgements **14**

The Author **15**

Chapter I Introduction **16**

1.1 Overview 16
1.2 Research background 17
1.3 Objectives and methodology 18
1.4 Thesis structure 19

Chapter II Breast implants **21**

2.1 Introduction 21
2.2 Breast anatomy 21
2.2.1 Mammary gland 22
2.2.2 Function of the nipples and the surrounding pigmented tissue 22
2.2.3 Internal features of the breast 23
2.2.4 Pectoral fascia 23
2.2.5 Breast shape 23
2.3 Breast implants 24
2.3.1 Evolution of breast implants 24

2.3.2 Material 28
2.3.3 Shapes 28
2.3.4 Sizes 29
2.3.5 Implant shell 30
2.3.6 Manufacturing process of silicone breast implants 31
2.4 Breast augmentation surgery 33

Chapter III Capsular contracture and cell adhesion 35

3.1 Introduction 35
3.2 Complications related to breast implants 36
3.2.1 Capsular contracture 42
3.3 Tissue response to breast implants 44
3.3.1 Inflammation 45
3.3.2 Granulation tissue formation 47
3.3.3 Re-epithelialisation 48
3.3.4 Matrix formation and remodelling 49
3.4 Cell-surface adhesion process 49
3.4.1 Forces at the interface between cells and their environment 51
3.5 Formation of the scar encapsulation around the textured surface of a silicone breast implant 53

Chapter IV Surface characterisation: parameters and equipment, microscopy principles and surface coatings 55

4.1 Introduction 55
4.2 Parameters and equipment 56
4.2.1 Roughness 56
4.2.2 Wettability 62
4.3 Principles of microscopy 64
4.3.1 Fluorescence microscopy 64
4.3.2 Confocal microscopy 68
4.3.3 Deconvolution 70
4.4 Surface coatings 72
4.4.1 Surface coatings requirements 72
4.4.2 Surface coating selection procedure 73
4.4.3 Surface coating selection tables 74
4.4.4 The selected surface coatings 81

Chapter V Characterisation of breast implant shells and correlation with fibroblast adhesion 83

5.1 Introduction 83
5.2 Materials and Methods 84
5.2.1 Characterisation of the silicone surfaces 85
5.2.2 Kinetics of fibroblast–surface detachment mediated by trypsin 90
5.3 Results 91
5.3.1 Surface characterisation 91

5.3.2 Kinetics of fibroblast–silicone implant surfaces detachment mediated by trypsin 101
5.4 Discussion 106

Chapter VI Physico-chemical characteristics of coated silicone textured versus smooth breast implants differentially influence breast-derived fibroblast morphology and behaviour 109

6.1 Introduction 109
6.2 Materials and Methods 110
6.2.1 Sample preparation 110
6.2.2 Characterisation 111
6.2.3 Cell culture 111
6.2.4 Cytotoxicity 113
6.2.5 Fibroblast adhesion to surfaces 113
6.2.6 Fibroblast proliferation 114
6.2.7 Immunofluorescence 114
6.2.8 Quantification of gene adhesion expression 115
6.2.9 Statistical analysis 117
6.3. Results 117
6.3.1 Physico-chemical characterisation of smooth versus textured implants 117
6.3.2 Cytotoxic effect of specific coatings on breast fibroblasts 121
6.3.3 Effect of specific coatings on breast fibroblast attachment 122
6.3.4 Effect of specific coatings on cell proliferation 123
6.3.5 Effect of coatings on cytoskeleton organization 124
6.3.6 Effect of aggrecan, collagen I, fibronectin and hyaluronic acid coatings on adhesion expression in breast fibroblasts 127
6.4 Discussion 130

Chapter VII Conclusions 136

7.1 Conclusions 136
7.2 Limitations of the work 137
7.3 Recommendations for future work 137

References 139

Appendix 154

Final words count 33,294

List of Tables

Chapter III

Table 3.1 Macrophage activities in wound repair ……. 47

Table 3.2 Late inflammatory and early granulation tissue phases components. 48

Table 3.3 Fibroblast activities in wound repair…….. 49

Chapter IV

Table 4.1 Selection of the down-regulated genes from a microarray data……. 75

Table 4.2 Genes related to the extracellular matrix……...……..….. 76

Table 4.3 Genes selected from the microarray according to the lowest *p*-value 77

Table 4.4 Genes that correspond to the three categories…… 78

Table 4.5 Molecules involved in fibrosis and breast capsule...……. 80

Table 4.6 Biomolecules related to fibrosis, wound healing in the body ……... 81

Chapter V

Table 5.1 3D Surface height parameters: skewness and kurtosis…….. 95

Table 5.2 Summary of results……. 105

Chapter VI

Table 6.1 Sequences of primers used to amplified adhesion related genes……117

List of Figures

Chapter II

Figure 2.1 Breast anatomy……..... 22

Figure 2.2 Breast implants generations…….....……... 25

Figure 2.3 Schematic representation of Silicone…….....…….. 28

Figure 2.4 Breast implants shapes. ……...… 29

Figure 2.5 Breast implants projections……..…… 30

Figure 2.6 Breast implants textures…….....…….. 31

Figure 2.7 Types of incisions …….....…… 33

Figure 2.8 Types of implant placement..……..……. 34

Chapter III

Figure 3.1 Adverse effects associated with breast implants ……. 38

Figure 3.2 Phases of wound repair …….....…… 45

Chapter IV

Figure 4.1 Arithmetical mean deviation ……. 57

Figure 4.2 Maximum peak height …….……. 57

Figure 4.3 Maximum valley depth …….…… 58

Figure 4.4 Skewness ……...…… 58

Figure 4.5 Kurtosis……..…… 59

Figure 4.6 Material ratio curve…… 60

Figure 4.7 Volume parameters ……. …… 61

Figure 4.8 Cut-off length ……. …… 61

Figure 4.9 Contact angles of drops on a smooth homogeneous solid surface 63

Figure 4.10 Forces of liquid molecules at the surface ……. …….. 63
Figure 4.11 Simplified Jablonski-diagram of states...……. 65
Figure 4.12 Visible light region of electromagnetic radiation …… 65
Figure 4.13 Principle of excitation and emission …… 66
Figure 4.14 4´-6 diamidino -2- phenylindole (DAPI)……. …… 67
Figure 4.15 Absorption and emission spectra with overlap profile ……. 67
Figure 4.16 Laser scanning confocal microscope optical configuration…..…. 69
Figure 4.17 Widefield versus confocal point scanning of specimens ……. 69
Figure 4.18 Acquisition of optical sections for deconvolution……. 71
Figure 4.19 Flowchart of protein selection from microarray data……... 74

Chapter V

Figure 5.1 TS1 surface topography……...……...…….…..... 85
Figure 5.2 TS2 surface topography……...……...……. 86
Figure 5.3 SS1 surface topography……...……...…… 86
Figure 5.4 SS2 surface topography……...….……..…. 87
Figure 5.5 Contact angle values of the silicone sample surfaces. ….……. 88
Figure 5.6 Microtest 5kN tensile module and TS1 tensile test……..… 89
Figure 5.7 3D functional parameters ……..…… 96
Figure 5.8 Core and valley fluid retention indexes…….…… 97
Figure 5.9 Mean force-displacement curves …….……. 100
Figure 5.10 Mean dynamic stretching stiffness for all samples…….. 100
Figure 5.11 Fibroblast attachment to surfaces after 24 hours of incubation… 102
Figure 5.12 Fibroblast attachment to surfaces after 48 hours of incubation… 103
Figure 5.13 Fibroblast attachment to surfaces after 72 hours of incubation… 103
Figure 5.14 Ln of number of cells attached at a time point over all surfaces.. 104

Chapter VI

Figure 6.1 Study design for physico-chemical and *in-vitro* characterisation. 110

Figure 6.2 Confocal laser 3-D topography of silicone breast implants…….. 112

Figure 6.3 Raman spectra of silicone breast implants…… 119

Figure 6.4 Confocal laser 3-D topography of silicone breast implants…….. 120

Figure 6.5 Changes in Sa of the modified coated surfaces……. 121

Figure 6.6 Cytotoxicity of fibroblasts seeded on surfaces…….. 122

Figure 6.7 Effect of coatings and roughness on fibroblast attachment…….. 123

Figure 6.8 Effect of coatings and roughness on fibroblast proliferation…… 124

Figure 6.9 Effect of coatings and roughness on fibroblast morphology……. 126

Figure 6.10 Effect of coatings and roughness on fibroblast adhesion gene expression…….. 129

List of abbreviations

3-D	Three-dimensional
ANOVA	Analysis of Variance
Calcein AM	Calcein acetoxymethyl ester
cDNA	Complementary DNA
D.F.D	Depth from defocus
DAPI	4',6-diamidino-2-phenylindole
DMEM	Dulbecco's Culture Medium
DNA	Deoxyribonucleic Acid
ECM	Extra cellular matrix
FAK	Focal adhesion kinase
FBS	Fetal bovine serum
FITC	Fluorescein Isothiocyanate dye
LDH	Lactate dehydrogenase
mRNA	Messenger RNA
PBS	Phosphate-Buffered Saline
PCR	Polymerase chain reaction
PDMS	Poly (dimethylsiloxane)
Pen/strep	Penicillin/streptomycin
qRT-PCR	Quantitative reverse-transcriptase polymerase chain reaction
RNA	Ribonucleic acid
RPE	RNA precipitating elution buffer
RPL32	60S ribosomal protein L32
rpm	Revolutions per minute
TRITC	Tetramethylrhodamine Isothiocyanate
WST-1	Water-soluble tetrazolium salt-1

Nomenclature

μL	Microlitre
°C	Degrees Celsius
D	Bending stiffness
E	Young's modulus
h	Hour
k	Stretching stiffness
kN	Kilonewton
min	Minute
mL	Microlitre
mm	Millimetre
ms	Millisecond
ng	Nanograms
nm	Nanometre
PV	Maximum peak to valley height roughness
Sk	Core roughness
Sku	Kurtosis of roughness surface
SMr1	Load area ratio of reduced peak part to core part
SMr2	Load area ratio of reduced valley part to core part
Spk	Reduced Peak Height
Ssk	Skewness of roughness surface
Svk	Reduced Valley Depth
t	Thickness
Vmc	Actual volume at a core part
Vmp	Actual volume at a peak region
Vvc	Void volume at a core part
Vvv	Void volume at valley region
θ	Water contact angle

Abstract

Bilateral breast augmentation is one of the most common cosmetic surgical procedures carried out on women in the western world. Breast augmentation involves increasing the volume of a woman's breasts through surgery by placing a silicone implant in the subglandular or subpectoral cavity. Although a capsule forms inevitably around breast implants as a natural part of healing, it can cause significant morbidity if the capsule becomes firm and contracted, a condition known as breast capsular contracture (BCC). The aetiology of BCC remains unknown however it is characterised by dense fibrocollagenous connective tissue with a local inflammatory response. Host response is influenced by several factors including implant surface texture, chemistry and interactions between cells and the extracellular matrix. Texturing holds the implant in place, thus preventing micromotion at the host prosthesis interface. While in smooth surfaces, the implant moves inside the breast, making the fibroblasts repeatedly produce collagen in response to this host-prosthesis shearing motion. In this thesis, the effect of surface characteristics and specific coatings on the cell-surface interaction has been examined on smooth compared to textured surfaces using commercially available breast implants.

The properties of breast implants shells have been characterised using confocal laser microscopy, contact angle measurements, confocal Raman spectroscopy and tensile testing. Confocal laser microscopy was used to evaluate the topographical features and surface roughness of the implant surfaces. Contact angle measurements were carried out to determine the hydrophobicity of the implant surfaces. Chemical characterisation was carried out recording Raman images and spectra of the implants using confocal Raman spectrometer. The mechanical properties of the breast implant shells were measured via tensile testing. Adhesive interactions of breast-derived fibroblasts with breast implant surfaces were examined *in-vitro*. For this purpose, the effect of four molecule coatings (aggrecan, collagen I, fibronectin, and hyaluronic acid) was evaluated on fibroblast attachment, proliferation, fibroblast morphology, spreading, cytotoxicity and gene expression.

Results from *in-vitro* assays demonstrated cell susceptibility to topography and protein coatings and further showed cytoskeletal re-organisation and modification with specific cell adhesion patterns. Combination of diverse topographies and specific coatings induced differential regulation of the expression of adhesion related genes, such as focal adhesion kinase, paxillin, vinculin, and α-actinin on breast fibroblasts.

In conclusion, this thesis has demonstrated the extent and strength of cell adhesion and subsequent cell proliferation and differentiation. This is based on the physical interactions between cells and the extracellular environment in the form of topography and on the chemical interactions mediated by specific coatings. Precise characterisation of the silicone breast implant surfaces was achieved. This may play an important role in the development of improved breast implant surfaces with improved qualities leading the development of surfaces that may be less prone to capsular contracture.

Declaration

No portion of the work referred to in the thesis has been submitted in support of an application for another degree or qualification of this or any other university or other institute of learning.

Copyright

Acknowledgements

I would like to convey my gratitude to my supervisors, Prof. Teresa Alonso-Rasgado, and Dr. Ardeshir Bayat for support, enthusiastic guidance, valuable suggestions, and constructive criticisms. I also wish to express my sincere gratitude to Dr. Alison Patrick, Dr. Alan Walmsley and Dr. Farhatullah Syed for their guidance, patience and constant encouragement indispensable for improving this work.

I wish to gratefully acknowledge the PhD scholarship and associated financial support provided by The National Council on Science and Technology of Mexico (CONACYT).

To my family and friends.

The Author

Ms Anai Valencia is currently a member of both, the Bio-engineering Group at the School of Materials and the Plastic and Reconstruction Surgery Research Group at the University of Manchester, UK. She graduated with a bachelor's degree in Robotics Engineering from the National Polytechnic Institute, Mexico, before obtaining a Master's degree in Mechanical Engineering from the National Polytechnic Institute, Mexico.

Publications resulting from this research work:

Characterisation of breast implant surfaces and correlation with fibroblast adhesion. **Valencia-Lazcano, A. A.**, Alonso-Rasgado, T. and Bayat, A., Journal of the Mechanical Behavior of Biomedical Materials, 21**:**133-148, 2013. DOI:10.1016/j.jmbbm.2013.02.005.

Physico-chemical characteristics of coated silicone textured versus smooth breast implants differentially influence breast-derived fibroblast morphology and behaviour. **Valencia-Lazcano A. A.**, Alonso-Rasgado T. and Bayat A., Journal of the Mechanical Behavior of Biomedical Materials, 40**,** 140-155, 2014. DOI: 10.1016/j.jmbbm.2014.08.018

Poster presentations

Understanding the effect of protein coatings on cell-surface interaction and physicochemical properties of breast implants: evaluated using tensile stress testing, confocal laser microscopy and Raman spectroscopy, Wound Healing Society Annual Meeting, Denver, Colorado, 2013.

Surface coatings & substrata topographies induce differential regulation of the expression of adhesion related genes in breast tissue fibroblasts,
European Tissue Repair Society, Reims, France, 2013.

Chapter I Introduction

1.1 Overview

Bilateral breast augmentation is one of the most common cosmetic surgical procedures carried out on women in Great Britain (Kim et al., 2014) and the rest of the of the western world. Breast augmentation involves increasing the volume of a woman's breasts through surgery by placing a silicone implant in the subglandular or submuscular cavity (Tebbetts, 2006).

A breast implant is a prosthesis used to alter the size and shape of a woman's breast. Breast implants may be required for one of a number of reasons including: aesthetic purposes, to correct congenital chest wall abnormalities, for male-to-female gender-reassignment, or for breast reconstruction after mastectomy. Round and anatomical silicone breast implants are constructed of a smooth or textured silicone outer shell and filled with silicone gel. Implants size can range from 80 to 800 cm^3 volume, 7.5 to 16.8 cm diameter and 1.5 to 7.5 cm projection (Hester et al., 1988).

Despite the minimal cytotoxicity associated with the silicone implant shells; there are significant post-operative risks involved following breast augmentation. When any foreign material is placed in the body, a capsule develops around the implant and in some patients undergoing breast augmentation this takes the form of a relatively thin membrane that remains undetectable externally. However the reaction to the implant can be greater and the membrane becomes thicker. The incidence of capsular contracture will increase over time and can reach 10% after 10 years of implantation (Gurunluoglu et al., 2013). The capsule around the implant can become thickened and contracted. This can lead to pain in the breast, and / or an abnormally hard feel of the implant in the breast. This problem usually starts at about a year after surgery although it may take many years to become noticeable when looking at the chest.

Capsular contracture is more common following infection, hematoma, and seroma, and the chances of this happening to the implanted breast may increase over time. The exact aetiology of capular contracture remains unknown; however, a variety of associations including the implant surface topography have been proposed to date (Burkhardt et al., 1986, Adams et al., 1998, Handel et al., 1995) that may increase the predisposition to capsular contracture formation (Ersek and Navarro, 1991, Hakelius and Ohlsen, 1997).

1.2 Research background

In view of the role of implant surface topography, in order to reduce breast capsular contracture formation, one option would therefore be to attempt to improve the performance of breast implants by enhancing their surface topography. Publications on implanting synthetic materials in living tissue have shown that surface texturing affects healing favourably, with regards to capsule pliability, and seems to inhibit tumour formation in laboratory rats (Oppenheimer et al., 1955).

By texturing the silicone surface, it is thought that the host response will be altered to one of wound healing (Ersek et al., 1990). Tissue ingrowth may produce a host-prosthesis interface that would be more stable, pliable, bio-compatible, thinner and with a reduced propensity to contract (Ersek et al., 1990).

Additonally, a number of studies have proposed the use of extracellular matrix (ECM) coatings to elicit specific cellular responses, such as cell adhesion, proliferation and migration (Bloom et al., 1999, Arthur and Burridge, 2001).

Physico-chemical properties of biomaterials that have been shown to influence cell behaviour include: wettability and surface topography (Clark et al., 1990). However, characterisation of the physico-chemical properties of several well established and commercially available implant surfaces, to evaluate the reaction of breast derived fibroblast to these surfaces, has not been previously investigated thoroughly.

1.3 Objectives and methodology

The aim of this research was to evaluate in detail the biomechanical characteristics of commercially available smooth versus textuted silicone implant surfaces and to investigate the effect of the physical, chemical and mechanical features of breast implant surfaces on breast-derived fibroblast morphology and behaviour. The research findings provide valuable information about the characteristic expression of adhesion related genes, cell morphology and proliferation in breast fibroblasts following the application of specific coatings on smooth, compared to textured, breast implant surfaces.

In order to investigate the effect of the physico-chemical characteristics of breast implants that may potentially influence the cell adhesion to surfaces, three different breast implants, with different characteristics, were evaluated in this research.

The properties of these commercially available smooth and textured silicone breast implants were explored to find physical, mechanical and chemical characteristics that could trigger cell-surface adhesion. Confocal laser microscopy was performed to measure surface roughness parameters and to image the topography of the breast implant surface. Contact angle measurement was performed to determine the surface wettability. Raman spectroscopy was employed to study the chemical composition of the breast implant surface. Tensile testing was employed to measure the stiffness of the breast implant shells.

Finally, having determined the breast implants' characteristics that could trigger cell-surface adhesion it was possible to study the effect of four unique protein and glycosaminoglycan (GAG) coatings (aggrecan, collagen I, fibronectin and hyaluronic acid) on breast-derived fibroblast initial cell attachment, cytotoxicity, proliferation, and cell morphology; the gene expression of α-actinin, vinculin, paxillin, and focal adhesion kinase (FAK) on these surfaces.

Precise characterisation of the silicone implant surfaces is likely to play a pivotal role in the development of improved implant surfaces with enhanced cell-surface interaction. Knowledge of how cell adhesion-related gene expression is regulated in response to specific coatings and surface features will enable a better understanding of silicone surface-fibroblast interaction, allowing the development of surfaces that may be less prone to capsular contracture formation.

1.4 Thesis structure

In this thesis, Chapter I provides a brief overview of breast augmentation and capsular contracture. This chapter also provides the research background and describes the objectives and methodology employed in this thesis. Finally, the structure of the thesis is presented.

Chapter II provides a brief background of breast implants. Firstly, a review of breast anatomy, characteristics of the silicone gel breast implants such as shape, size, material, texture and manufacture and the breast augmentation surgical procedure will be provided. In addition, the evolution of breast implants through the years is described with the aim of showing the measures taken to reduce the rate of complications related to breast augmentation.

Chapter III reviews the relevant literature on the body-surface interaction when breast implants are placed in the breast cavity. Firstly, the risks and complications associated with breast implants are given. Secondly, the characteristics of capsular contracture are presented. Thirdly, the tissue response once the breast implants are inserted into the body is described. Finally, the cell-surface adhesion process is given with the aim of describing the molecular interactions which determine and regulate cell behaviour on surfaces.

Chapter IV reviews the relevant literature on surface parameters that could induce cell adhesion onto breast implant surfaces. This chapter also describes the process used for selecting the relevant surface coatings for improving the performance of silicone breast implants. Finally, the principles of microscopy to identify fibroblasts adhered to the surfaces and sharp image acquisition are explained.

Chapter V describes the findngs regarding the characteristics of breast implant surfaces that can influence cell-surface adhesion such as surface roughness, stiffness and surface wettability.

In Chapter VI, the effect of four unique protein and glycosaminoglycan coatings (aggrecan, collagen I, fibronectin and hyaluronic acid) on breast-derived fibroblast cytotoxicity, attachment, proliferation, morphology, and gene expression is examined.

Chapter VI presents the conclusions of the thesis.

Chapter II Breast implants

2.1 Introduction

A breast implant is a prosthesis used to alter the size and shape of a woman's breast for aesthetic reasons, congenital chest wall abnormalities correction, male-to-female gender-reassignment, or breast reconstruction after mastectomy. Attempts to augment the size and shape of breasts can be traced back to the late 1880s. Among the materials inserted in breasts were ivory, glass balls, ground rubber, ox cartilage, sponges and tapes made from various synthetic substances (Grigg et al., 2000). In 1963, the Dow Corning Corporation introduced the first silicone-gel-filled implant. Since then, the characteristics of breast implants have been modified in order to create a positive biological response with the host tissue (Berry and Davies, 2010).

Biointegration of breast implants implies an understanding of the anatomy of the breast; breast implant characteristics and the breast augmentation procedure. This chapter provides a review of breast anatomy, the evolution of breast implants through the years and the actual characteristics of silicone gel breast implants such as shape, size, material, texture and manufacture. In addition, the breast augmentation surgical procedure is described. The risks and complications associated with breast implants will be covered in the next chapter.

2.2 Breast anatomy

The breast is the tissue overlying the pectoralis muscles and is composed of glandular and fatty tissues. The normal breast shape is given by the connective tissue and ligaments that provide support to the breast parenchyma (Bethesda, 2014).

2.2.1 Mammary gland

The mammary gland is a milk-producing gland that is composed mainly of fat. The endocrine system regulates mammary glands and under the influence of hormonal changes become functional (Muschler and Streuli, 2010). There is a complex network of branching ducts within the mammary gland (Shackleton et al., 2006). These ducts come from the lobules which are sac-like structures. When the lobules receive the appropriate hormonal stimulation can produce milk in females (Figure 2.1). Milk is transported by the breast ducts from the lobules out to the nipple.

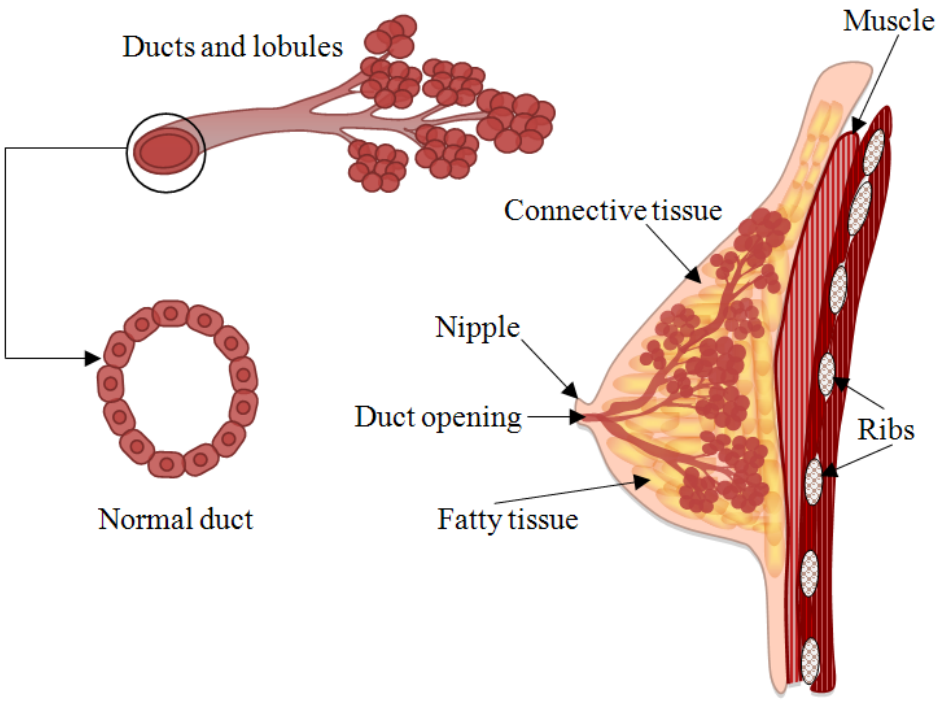

Figure 2.1 Breast anatomy (modified from (Bethesda, 2014)).

2.2.2 Function of the nipples and the surrounding pigmented tissue

The nipple is innervated by the fourth intercostal nerve and becomes erect when stimulated by a cold environment, sexual activity or breastfeeding. During lactation, the female mammary glands produce milk which the nipple delivers to the infant.

The areola is the small dark pigmented circular area around the nipple. The areola spreads in size and darkens in pregnancy. Glands in the areola secrete moisture that serves as a lubricant during lactation (Ellis and Mahadevan, 2013).

2.2.3 Internal features of the breast

The suspensory ligaments and the surrounding fatty tissue support the lobules and ducts in the breast. The elasticity of the matrix of connective tissue fibres in the breast provides the characteristic bounce of the breast (Drew et al., 2007).

Inside the breast, there are blood vessels and lymphatics whose function is to carry blood (blood vessels) and collect and carry tissue fluid (lymphatics). The lymphatic system drains the waste products from the body; the tissue fluid flows through this system and drains into veins. The lymphatic system runs from the centre of the chest, by the sternum to the axilla (Pandya and Moore, 2011).

2.2.4 Pectoral fascia

The pectoral fascia is a thin layer of tissue that encloses the pectoralis major and minor muscles. Pectoral fascia wraps the two muscles allowing them to glide smoothly when contracting. It is adhered to the clavicle, while laterally and below extends, to the scapular region forming the axillary fascia (Dempsey and Latham, 1968).

2.2.5 Breast shape

Skin, fat, and breast tissue (lactiferous ducts along with breast stroma) comprise the breast structure. Breast begins to develop a functional organ in puberty on the anterior chest along the embryonic milk line. During puberty the breasts have the

shape of a cone, but gravity elongate and make bigger the lower half of the breasts to form a teardrop shape. The universally accepted concept of well-shaped breast says that breast will almost not face downwards; the inferior pole of the breast will have the shape of a half cone; the lateral breast will not go beyond a few centimeters posterior to the anterior axillary fold; the nipple will be located at the anteriormost point of the breast mound and a straight line will be formed from the clavicle to the nipple (Westreich, 2009).

2.3 Breast implants

2.3.1 Evolution of breast implants

In 1895, autogenous fat was used to reconstruct a volume defect after benign tumour extirpation (Goldwyn, 1978). In 1899 Gersuny performed percutaneous injections of paraffin (Lewis, 1965). In the 1940s paraffin and petroleum jellies, among other liquid substances, were injected into the breast.

In 1951 the Ivalon sponge, a synthetic implant made of a polyvinyl alcohol and formaldehyde polymer, was created by Pangman (Middleton and McNamara, 2000). The Ivalon sponge elicited ingrowth of scar tissue into the sponge creating seroma and severe firmness.

Industrial medical-grade silicones were subsequently injected into the breast by unlicensed practitioners, sometimes in astonishing amounts. Pain, infection, skin discoloration, disfigurement, ulceration, breast loss, respiratory distress, pulmonary embolism, liver problems, and even coma and death were caused by silicone breast injections**.** Breast injections caused capsular contracture reaching 100% of occurrence. In 1976, Nevada state law declared the procedure to be a felony after 12,000 - 40,000 women had received breast injections in Las Vegas (Bondurant et al., 1999).

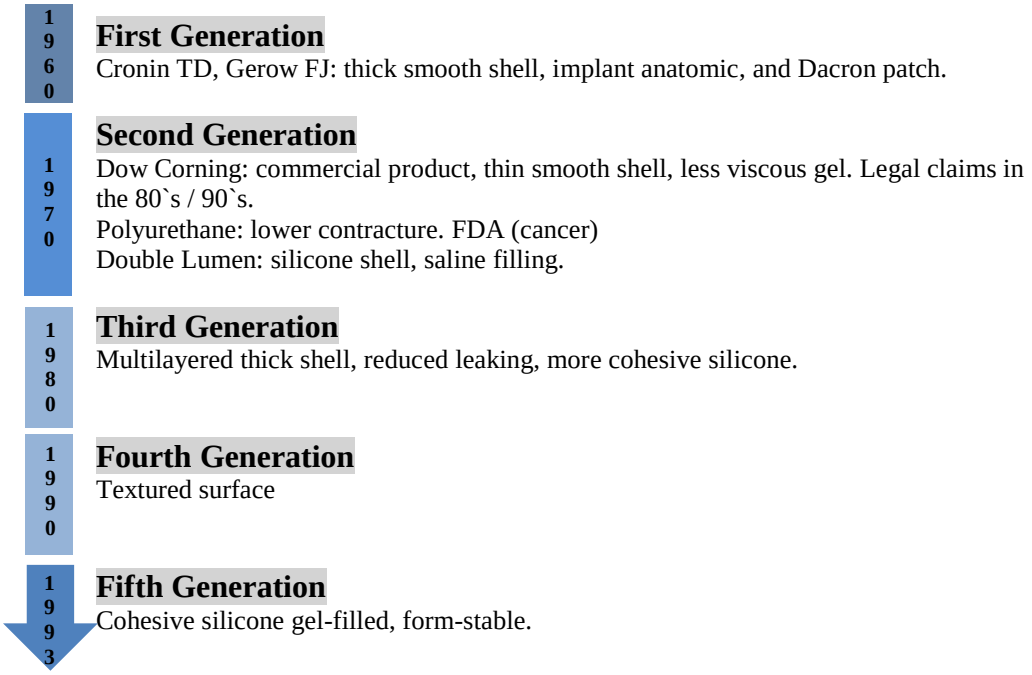

Figure 2.2 Breast implant generations (modified from (Berry and Davies, 2010))

In 1963, the first silicone-gel-filled implant was introduced by Dow Corning Corporation (Braley, 1973). A high-molecular-weight "gum" filled with amorphous silica constituted the first Dow implants, in which the gel in the implant was platinum cured.

88% of all Dow Corning Dacron-patched implants were sold at the beginning of the 1970s (Figure 2.2).Thick shells, with seams and a smooth surface, constituted these early implants which in the inside contained a firm silicone gel and fluids. The tough shell reduced the rupture rates, but gel-fluid leakage and capsular contracture were common. Dow's shells became less thick and were seamless by the late 1960s (Thomsen et al., 1990).

Saline-filled implants were firstly manufactured by Heyer Schulte Corporation in 1968. The strengthening process of the first saline implants caused there to be a high

deflation rate of up to 76% due to the process involving high-temperature for vulcanizing. They also were heavy and fragile producing audible sloshing (Crosby, 2013).

In the 1970s and early 1980s the thick-shell models were replaced by implants with thin shells, increasing the tendency to rupture and deflate. These "second-generation" implants were characterised by a smooth surface, high contracture and gel-fluid leakage rates. From 1972 to 1975 more companies introduced flexible gels and thinner elastomer shells (Grigg et al., 2000).

With the aim of reducing contracture a polyurethane foam coating on the implant shell was developed in the 1970s. This popular implant was placed in approximately 110,000 women before it was discontinued in 1991. The polyurethane coating caused an inflammatory reaction that repels the formation of fibrous tissue around the capsule. This implant caused pain, infection and fluid accumulation. Disintegration of the polyurethane coating ended in a capsule containing foam fragments which made the implant difficult to remove (Barr et al., 2009).

In order to prevent collagen and other fibrous tissue forming excessive growth around the implant capsule, a textured shell surface was produced at the beginning of the mid-1980s. The textured surface allowed the growth of tissue into the irregular spaces of the shell. Friction from the movement, common in all breast implants, results in synovium. Textured implants also developed a thin membrane that secreted synovial fluid, a sticky substance (Grigg et al., 2000).

Another attempt to control contracture, gel and fluid leakage and rupture was the creation of a double lumen implant. These implants consisted of two cavities and two shells containing gel in the inside cavity and saline in the outside lumen. By using

the saline lumen as an expander or for injections of antibiotics or steroids cosmetic benefits were expected, but the expectations were not accomplished (Nichter and Hamas, 2012).

The third generation of implants dating from the mid-1980s, decreased the deflation, bleeding, contractures and rupture rates by manufacturing stronger shells with barrier layers and texturing surfaces (Bondurant et al., 1999).

Nowadays, most implants have one cavity filled with silicone gel. The shell is manufactured with silicone rubber and, to prevent the escape of silicone fluid, has an inside barrier coated with fluorosilicone or a modified layer of elastomer (Bondurant et al., 1999).

The 1992 Food and Drug Administration (FDA) moratorium on the use of silicone gel and saline-filled implants caused the single-lumen implants to almost entirely replace the gel-filled models. Implant reconstruction after mastectomy increased from 3% of implants in 1983 to more than 25% in 1992 (Cohen, 1994).

Current saline implants are improved by eliminating visible wrinkles through the skin and audible fluid waves within the implant by slightly overfilling the implant and placing it behind the chest muscles. Some saline implants used in reconstruction have valves that allow new tissue forms around the pockets to be created by gradually inflating the valve after surgery (Maxwell and Gabriel, 2009).

The period from 1992 to 1994 was marked by complaints to the FDA by numerous law suits resulting in much negative publicity, despite the fact that majority of women were satisfied with their implants (Brody, 1997).

2.3.2 Material

Silicone has been used in medical devices because of its low toxicity and biological stability and has the capacity to be easily shaped and moulded (Prasad et al., 2010). Silicone belongs to the organic silicon polymer family mainly composed of a chain of alternating oxygen and silicon atoms. Each silicon in the chain has two methyl groups (CH_3-) and the material is named poly (dimethylsiloxane) (PDMS) as shown on Figure 2.3.

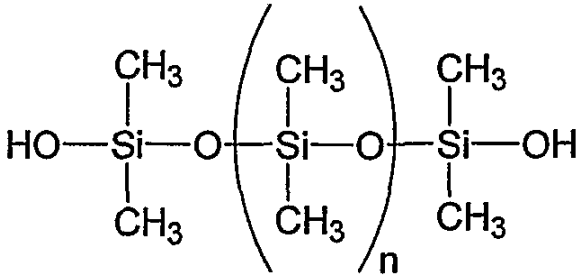

Figure 2.3 Schematic representation of Silicone showing one end and two central subunits

Silicone gel is composed of a matrix of cross-linked long silicone chains soaked in a bath of non-cross-linked long silicone chains. The matrix is generally formed by vinyl groups placed as cross-links, between silicon atoms, on neighbouring silicone molecules. Vinyl cross-links are often created by catalysis of platinum in an exothermic reaction (Middleton, 1998). Silicone gel has the capacity of providing the feel of human adipose tissue, but has enough strength to maintain its shape (Bondurant et al., 1999).

2.3.3 Shapes

Breast implants come in round and anatomical shapes (Figure 2.4). The anatomical shape has a tear drop shape that mimics the slope of a natural breast. The implant stays upside down due to its textured surface that avoids the implant flipping inside the breast. When the patient is lying down, the implants will maintain the same shape. In the supine position round implants settle back evenly like normal breasts.

In the standing-up position, gravity makes the filler substance go to the bottom of the implants and the implants assume a natural tear drop shape. Round implants have a more natural appearance when placed under the muscle than anatomical implants which can look elongated in some women (Berry et al., 2010).

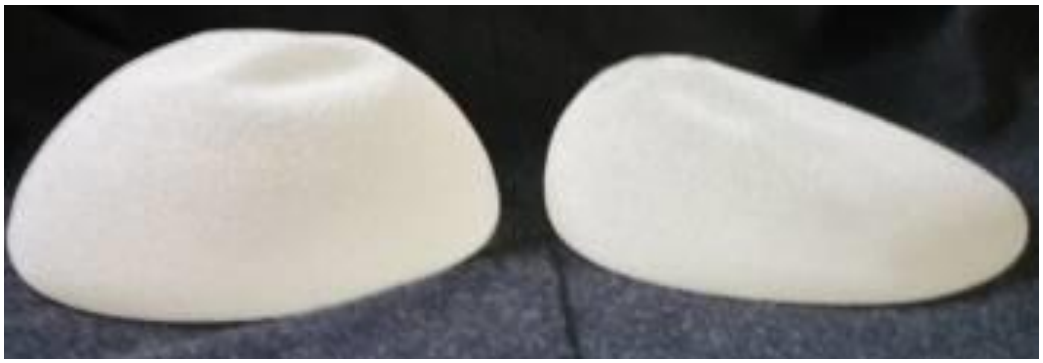

Figure 2.4 Lateral view of breast implants: on the left, round shape; on the right, anatomical shape

2.3.4 Sizes

Implant sizes vary from 80 to 800 cubic centimetres in volume, but there are also 1,000 cc implants (Hester et al., 1988). The diameter ranges from 7.5 to 16.8 cm and the profile is from 1.5 to 7.5 cm as seen on Figure 2.5 (Hester et al., 1988). The diameter of the implant should adequately cover the natural diameter of the breast size without taking the implant too far towards the cleavage and underarm.

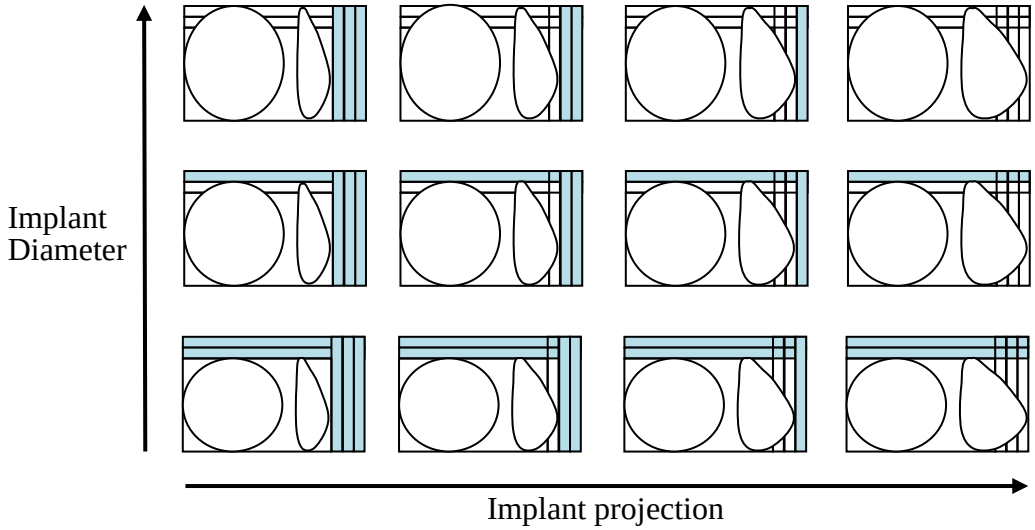

Figure 2.5 Projections of breast implants (modified from (Allergan, 2006))

2.3.5 Implant shell

Breast implant shells are made of silicone rubber, whose composition of amorphous silica is approximately 21-27% in the elastomer for the shell and in shell patches, and 16.5% in barrier coats according to Dow Corning corporation, but the chemical composition of other manufacturers could vary (Bondurant et al., 1999). Shell thickness varies from 0.13 to 0.75 mm. Depending on the manufacturer; shells have either smooth elastomer rubber or are textured with a different surface topography of varying coarseness:

Textured surface

Textured surface was created in the 1980s with the aim of reducing capsular contracture. The texture was designed for fibroblasts to grow into the interstices of the pores, disorienting collagen fibrils, and weakening their contractile forces forming a thinner capsule and minimizing the contracture (Barone et al., 1992, Whalen, 1988, Ulrich et al., 2009). Formation of peri-implant synovial tissue, which is a joint lining-like tissue reaction, can appear in textured silicone implants (Raso and Greene, 1997), which along with a more cellular capsule can cause excessive contracture.

Depending on the manufacturer, the size and shapes of the texture of the silicone implant surfaces vary (Figure 2.6). For instance, the SILASTIC® MSI breast implant (Micro Structured Implant) had regular pillars of 750 μm high, diameter of 250 μm, and distance between pillars of 500 μm. McGhan Biocell has the topography of an open pore network at 3.1 pores per μm^2, and side size of 289 μm, the height varies from 500 to 800 μm. Mentor Siltex has bumps of 65-150 μm high and 60-275 μm wide. Bioplasty Misti is composed of pores 20-800 μm wide (Jenkins et al., 1996).

Figure 2.6 Textured (left) and smooth (right) breast implants

2.3.6 Manufacturing process of silicone breast implants

The usual multiple dipping method to manufacture commercially conventional silicone breast implants consists of using mandrels with the shape of the implant to form the scaffolds that support the implant. The mandrel is immersed in liquid silicone until a homogeneous layer is formed, then it is polymerized into a laminar flow cabinet or oven. The thickness of the implant is increased by repeating this procedure (Barr and Bayat, 2011).

The smooth surface is created by immersing the implant in solvent to flatten this outer surface. To prevent silicone gel leakage through the shell silicone prepared

with a phenyl group, instead of the methyl group, is used to make a second layer on the shell (Barr and Bayat, 2011).

The textured surface is created, after the mandrel is coated with silicone, to be then pushed into specific molecules whose shape and size produce three-dimensional projections of 20 - 500 microns in size. This is polymerized into a laminar flow oven. The molecules are removed by washing after it is cured (Biocell® surface) or by brushing before curing (Cereform surface) (Ersek et al., 1990).

Dow Corning's Medical Grade Silastic® was produced by making mould surfaces with photolithography in a class-100 clean room. Impression casting of silicone monomer on the wafers is used to create textured and smooth silicone surfaces. Silicone was applied on the wafers under vacuum conditions and then cured at room temperature for 3 days and subsequently at 55 °C for 2 h. The silicone sheets are then detached from the wafer and inspected with phase contrast microscopy for regularity of the pattern, dimensions (deviations up to 10% for depth, groove and ridge width), transparency and contamination of air bubbles or dust. Ultraviolet (UV) light exposure is used to sterilize the samples, and extraction in sterile phosphate-buffered saline (PBS) was performed to remove any hazardous substances that might have been released during UV irradiation.

Patterning PDMS using etching is another way to create varied surface roughness by controlled etching with potassium hydroxide (KOH) in mixed organic/aqueous solvents. The silicone elastomer is placed in the basic etchant solution and shaken for 6 h at room temperature. At the end of the etching process, the elastomer disks were washed extensively to remove any adhering materials, and finally flushed with nitrogen and then let to dry overnight in a vacuum chamber at room temperature (Prasad et al., 2010).

2.4 Breast augmentation surgery

The overall method of augmenting the breast will depend on factors such as preferences made by the patient and the surgeon as well as the patient's anatomy. The routine surgical procedure often involves first making an incision (inframammary, periareolar and axillary incision) (Figure 2.7). Then the implant can be placed subgladular or subpectoral (Figure 2.8), depending on the volume and shape of the breast tissue. (Tebbetts, 2006).

An incision should be of an appropriate length to accommodate the style, size, and profile of the implant in order to reduce the stress to the implant during insertion. The most common type of incision is the inframammary. The periareolar incision usually causes minimal scarring and is thought to be more concealed (Spear et al., 1995). In the axillary incision bleeding may be difficult to control and the abundance of lymphatics in the axilla can produce an untoward lymphangitis of the upper arm, clearly a dangerous and unacceptable complication for an elective cosmetic procedure.

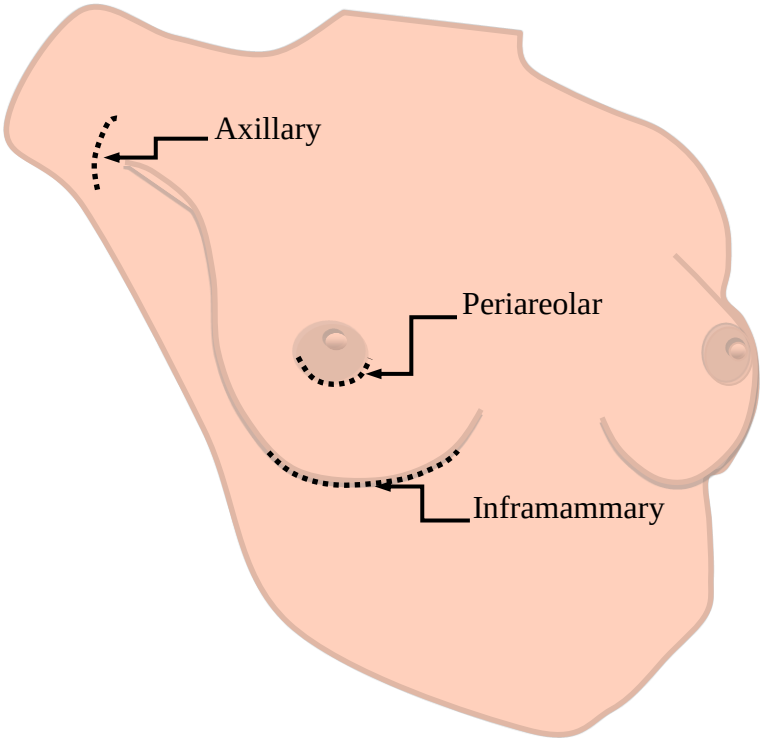

Figure 2.7 Types of incisions (modified from (Berry et al., 2010))

Placement of an implant in any pocket location initiates a complex series of events (anatomic, mechanical, and biological) that vary significantly from patient to patient over time (Tebbetts, 2006). Subglandular placement may result in more palpable implants with greater likelihood of capsular contracture, (Henriksen et al., 2005, Kulmala et al., 2004) and increased difficulty in imaging the breast with mammography (Spear et al., 2004). Subpectoral placement may result in less palpable implants, less likelihood of capsular contracture (Hidalgo, 2000), and easier imaging of the breast for mammography.

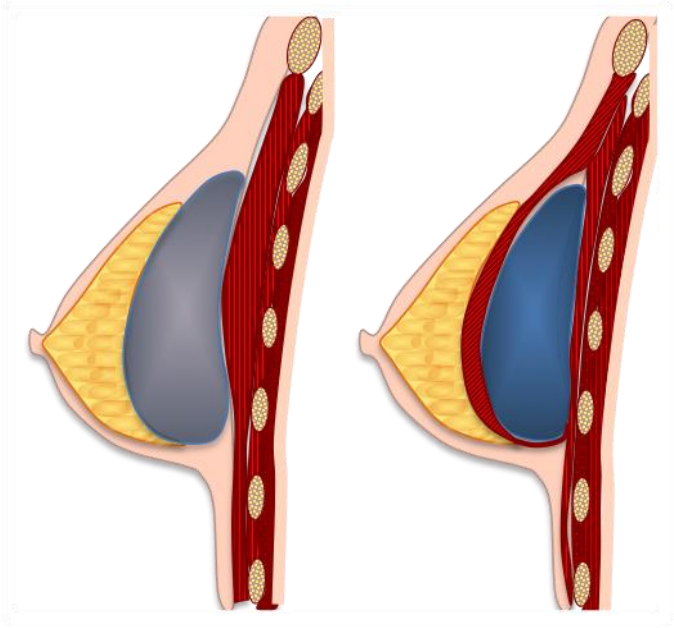

Figure 2.8 Subglandular (left) and subpectoral (right) placement (modified from (Berry et al., 2010))

Chapter III Capsular contracture and cell adhesion

3.1 Introduction

Capsular contracture is the most common complication of breast augmentation occurring in approximately 10% of the patient population (Zahavi et al., 2006). The causes of capsular contraction remain unknown, but it is characterised by dense fibrocollagenous connective tissue with local inflammatory response.

This tissue response may be affected by factors related to the implant or tissue. These include implant design, implant localization, physico-chemical surface properties, the host bed conditions, surgical technique and mechanical load (Hilborn and Bjursten, 2007).

Tissue response can be affected by the shear stress and strain elicited at the tissue implant interface by the natural movements of the tissue. Any movement of the host creates a shearing effect and stresses will be concentrated at the interface between the implant and tissue. Cells respond to shear stress with the production of proinflammatory signals that recruit immune cells (Bao et al., 1999) and foreign body reaction. Thus, the effect of stress on cellular response is inherently coupled to the rearrangement of the cells in the cytoskeleton, to the adhesion to the ECM and to other cells, and in the remodelling of the ECM itself.

In this thesis, cell-surface adhesion will be studied as well as the characteristics of breast implant surfaces as it is known that surface topography influences cell morphology and adhesion, which in turn influence the incidence of capsular contracture. The rationale behind the efficacy of reducing capsular contracture with textured breast implants is based on the fact that, on these types of surfaces, cells are able to grow in and around the interstices of the surfaces creating a connection with the host prosthetic interface to prevent micro-motion. This results in thinner capsule formation, whereas smooth implant surfaces elicit a fibrous reaction where collagen fibrils align cumulatively in a connective-tissue capsule adjacent to the implant. Therefore, any movement of the host creates a shearing effect of any microscopic surface irregularity, resulting in a chronic inflammatory, thickly scarred pseudo-bursa around the smooth implant (Emery *et al*., 1994).

In order to understand capsular contracture, this chapter first addresses the risks and complications associated with breast implants. Therefore, it is essential to understand how tissue responds to the breast implants once inserted into the body. This involves the study of the foreign body reaction, the phases of wound repair, the process of prosthesis encapsulation, and the contraction of the capsule. Finally, when investigating cell-surface adhesion, the role of molecular interactions in the determination and regulation of cell behaviour on surfaces is discussed in this chapter. The tissue response may be influenced by the physico-chemical properties of the implant surface. A detailed description of these properties will be given in the following chapter.

3.2 Complications related to breast implants

Risks and complications associated with breast implants can be categorized in immediate, short-term, and long-term adverse effects (Pereira and Sterodimas, 2009) as shown in Figure 3.1. In the paragraphs below, the most common complications are briefly explained.

- **Rupture**

Pain, hard lumps in the armpit or around the implant, swelling, change in size or shape of the breast or implant, burning, tingling, hardening, or numbness of the breast can be symptoms of gel implant rupture (Brown et al., 1997). Breast implant rupture refers to a tear or hole in the implants' shell. Rupture can be caused by damage by surgical instruments; trauma; wrinkling or folding of the implant which may weaken the shell; severe capsular contracture; and compression during mammographic imaging (Berry and Davies, 2010). Mechanical testing of explanted ruptured silicone breast implants revealed that elasticity, toughness, and shell strength declines with time, probably because of lipid infiltration (Adams et al., 1998). The consequences of rupture can make silicone gel remain between the scar tissue capsule and the implant (intracapsular rupture), flow outside the capsule (extracapsular rupture), or move beyond the breast (migrated gel).

- **Reoperations**

Reasons for reoperation includes rupture, capsular contracture, hypertrophic scarring (irregular, raised scar), asymmetry, infection, and implant shifting (Adams and Mallucci, 2012).

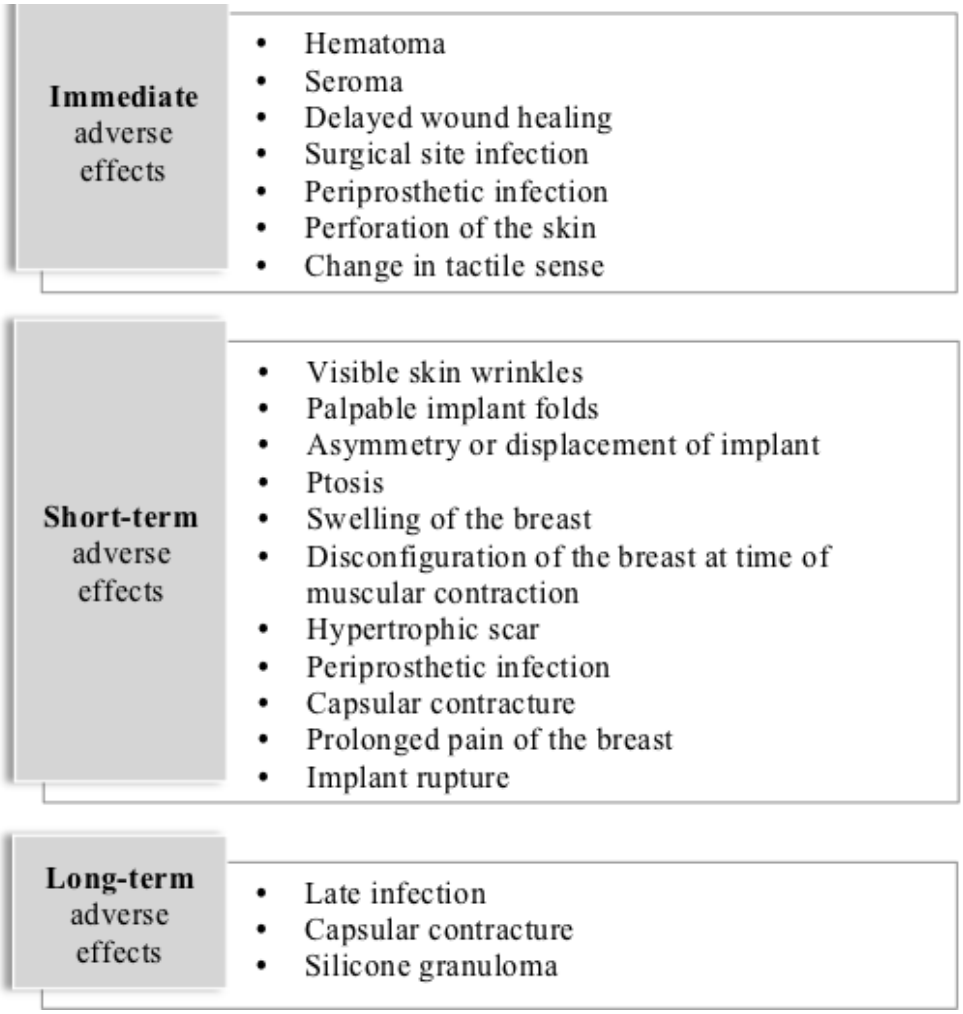

Figure 3.1 Adverse effects associated with breast implants

- **Implant removal**

Reasons for implant removal include dissatisfaction, an unacceptable cosmetic result, or a complication such as symptomatic capsular contracture. There is a chance of future complications resulting from having the implants removed and replaced.

Women who have their implants removed have them replaced with the same implants; the implants may be cosmetically unacceptable due to dimpling, wrinkling, puckering, and other cosmetic changes of the breast. Moreover, implant removal may result in loss of breast tissue, so implant replacement increases the risks of future

complications. Implant replacement increases the risks of capsular contracture and reoperation in comparison to first time placement of the implant (Gabriel et al., 1997).

- **Unsatisfactory results**

Breast augmentation can have unsatisfactory results such as asymmetry, wrinkling, implant displacement, implant palpability, incorrect size, scar deformity, and/or hypertrophic scarring (Steiert et al., 2013).

- **Pain**

Following breast implant surgery, pain of varying intensity and length of time may occur and persist. Furthermore, pain can result from improper size, surgical technique, placement, or capsular contracture (Zhibo and Miaobo, 2009, Young et al., 2004).

- **Changes in nipple sensation**

During a periareolar incision, the nerve or the nerve endings can be damaged, so sensation in the nipple-areolar complex decreases or disappears and the suckling reflex will be lost (Hurst, 1996). Studies show that 3 years after surgery, nipple sensation was lost in 8–10% of women and after 5 years in 10% of women (Kostas, 2007).

- **Infection**

Infections following breast augmentation surgery appear within a few days to a few weeks after the operation (Pittet et al., 2005). Reasons for infection can be due to any

of the following: skin atrophy, corticosteroids in subglandular augmentation, additional simultaneous surgery, massage and trauma postsurgically, vigorous exercising, pregnancy, preceding lactation. Pain, inflammation, sudden fever, sunburn-like rash on the operated area, discharge and swelling are symptoms and signs indicating possibility of implant related infection. The bacteria that can cause infection include: mycobacteria, *Staphylococcus aureus* and *Staphylococcus epidermidis*, *Pseudomonas*, *Klebsiella*, *Streptococci* A and B and enterobacteria (Brand, 1993). Removal of the implant and new implant replacement will be necessary if an infection does not respond to antibiotics.

- **Hematoma / Seroma**

Swelling, pain, and bruising soon after surgery can be symptoms of hematoma or seroma. Seroma is an accumulation of fluid around the implant and hematoma is a collection of blood within the space around the implant. Seroma and/or hematoma could develop infection and / or capsular contracture. Surgery on hematomas and seromas involves draining and temporarily placing a surgical drain in the wound for proper healing. Surgical draining can damage the implant causing its rupture (Grigg et al., 2000).

- **Breastfeeding**

Breastfeeding difficulties have been reported proceeding a periareolar incision and there is a chance of lactation insufficiency (Marianne et al., 1990, Tran et al., 2014).

- **Calcium deposits**

Pain and firmness can be symptoms of calcium deposits, the occurrence of which increases significantly with age post-implantation. Calcium deposits can form in the tissue capsule surrounding the implant. The appearance of calcium on mammograms

can be similar to the appearance of cancer, resulting in additional surgery to examine or remove calcifications. Additional surgery may also damage the implants (Lee et al., 2011).

- **Extrusion**

Extrusion can occur when breast tissue covering the implants weakens, or when the wound has not closed. Extrusion is when the breast implant comes through the skin. It has been reported that radiation therapy could increase the likelihood of extrusion. Extrusion requires additional surgery and possible removal of the implant, resulting in loss of breast tissue and/or additional scarring (Allergan, 2006).

- **Necrosis**

Infection, use of steroids, smoking, chemotherapy/radiation, and excessive heat or cold therapy can lead to necrosis. Necrosis is the death of cells, or even tissues; that delay or prevent wound healing. Necrosis will require surgical correction, resulting in loss of breast tissue or additional scarring (Gabriel et al., 1997).

- **Delayed wound healing**

After augmentation mammaplasty, a prolonged wound healing time can be experienced. This increases the risk of extrusion, infection, and necrosis. Wound healing times may vary depending on the type of surgery or the incision (Prantl et al., 2007).

- **Breast tissue atrophy / chest wall deformity**

Thinning of breast tissue and chest wall deformity are caused by the pressure of the breast implant following implant removal without replacement or while implants are still in place. Implant visibility and palpability may result in additional surgeries and/or puckering or dimpling of the breast (Tebbetts and Teitelbaum, 2010).

- **Lymphadenopathy**

A chronic enlargement of the lymph nodes is called lymphadenopathy. Lymph nodes are located in the lower axilla near the breast (Rivero et al., 1994). Removal of the lymph node(s) will be necessary if they become too large or painful (Katzin et al., 2005).

- **Capsular contracture**

Following augmentation mammaplasty, a capsule forms around a breast implant, but the abnormal hardening and tightening of the capsule forms what is called capsular contracture (Yang and Muradali, 2011). Characteristics of capsular contracture will be studied in detail below.

3.2.1 Capsular contracture

The most common complication of breast augmentation is capsular contracture that encircles the implant. This occurs in approximately 10% of the patient population after 10 years of implantation (Kjoller et al., 2001, Zahavi et al., 2006, Gurunluoglu et al., 2013). A fibrous capsule usually forms around silicone breast implants. This is a relatively hypocellular membrane of rather uniform thickness which is rich in collagen. There may be a thin discontinuous layer of activated epithelioid myofibroblasts next to where the implant was situated and a thin acellular protein film between the implant and capsule. Both within and directly below this

membrane, there are usually foam cells and lymphocytes, often in large numbers (Van Diest et al., 1998). The scar tissue (capsule) that normally forms around the implant may tighten and squeeze the implant, making the breast feel firmer and sometimes painful. This is called capsular contracture (Yang and Muradali, 2011).

Capsular contracture may be more common following infection, hematoma, and seroma, and the chance of it happening may increase over time. Capsular contracture is a risk factor for implant rupture and it is one of the most common reasons for reoperation. However, whilst aeiology remains unknown, a variety of causal associations have been proposed (Burkhardt et al., 1986, Adams et al., 1998, Handel et al., 1995) that may predispose implants to capsular contracture formation including the implant surface topography (Ersek and Navarro, 1991, Hakelius and Ohlsen, 1997).

Capsular contracture is currently evaluated according to the Baker grading score. Capsular contracture is graded into 4 levels according to its symptoms (Spear et al., 1995). According to Baker's system, class I represents a soft and natural breast appearance without any detectable capsular contracture (Young and Watson, 2000). Class II represents an implant easily detected by the surgeon, where the surrounding scar capsule suggests some degree of contraction. In class III there is discomfort and the breast is firm and the implant is palpable. Class IV is characterised by severe pain, a distorted shape of the implant, and an easily palpable implant. Severe capsular contracture requires capsule tissue and/or implant removal. This procedure implicates loss of breast tissue and there is a possibility that capsular contracture occurs again (Spear et al., 2004, Marshall et al., 1989).

Closed and open capsulotomies are two ways to reduce the firmness of a contracture. In the closed capsulotomy, the hardened implant is manually squeezed tightly from the outside, in an attempt to tear the scar envelope. When successful the result is

instantaneous and the implant immediately feels soft. Due to some scars being very hard it makes it impossible for them to be torn. A closed capsulotomy can result in bruising, bleeding, or even rupture of the implant itself. If rupture occurs then surgery will be needed to remove and replace it. Due to this, closed capsulotomy is the less favorable method and not in current use in modern practice. (Kjoller et al., 2001).

Open capsulectomy is the most successful and commonly used method for capsular contracture, whereby the surgeon makes an incision to enter into the pocket and makes cuts into the scar tissue. These cuts are made to release tension around the implant caused by capsular contracture. The implant is then reinserted into the breast pocket. Unfortunately, even after a successful capsulectomy, there is always the possibility of recurrent hardening and capsular contracture development (Kjoller et al., 2001).

3.3 Tissue response to breast implants

Once the breast implant is inserted into the body, the immediate tissue response is to flood the injured area with fibrinogen and blood which will cleave to fibrin and form a blood clot that will promote platelet adhesion and aggregation. White blood cells are recruited by cytokines and growth factors that the blood clot released. This will make monocytes appear and differentiate into macrophages that will clean the wound site of dead cells, bacteria, and foreign material. Fibroblasts and endothelial cells, recruited by macrophages, convert the fibrin clot into a highly vascularised tissue. The extracellular matrix (ECM), deposited mainly by fibroblasts, replaces the vascularised tissue (Hilborn and Bjursten, 2007). Following resolution of the acute and chronic inflammatory responses, granulation tissue identified by the presence of macrophages, infiltration of fibroblasts and neovascularization in the new healing tissue, is identified. The cellular components of foreign body reaction: 1-2 cell layers of monocytes, macrophages and foreign body giant cells, separate the implant from the granulation tissue. Granulation tissue is the precursor to fibrous capsule

formation. The inflammatory reaction leads to capsule formation that often forms undesirable growth of fibrotic tissue around the implant (Hilborn and Bjursten, 2007). Tissue response to breast implants follows the wound healing phases (Figure 3.2). These phases overlap, but are biologically different and are characterised by events that promote closure of the injury. The wound healing phases are described below.

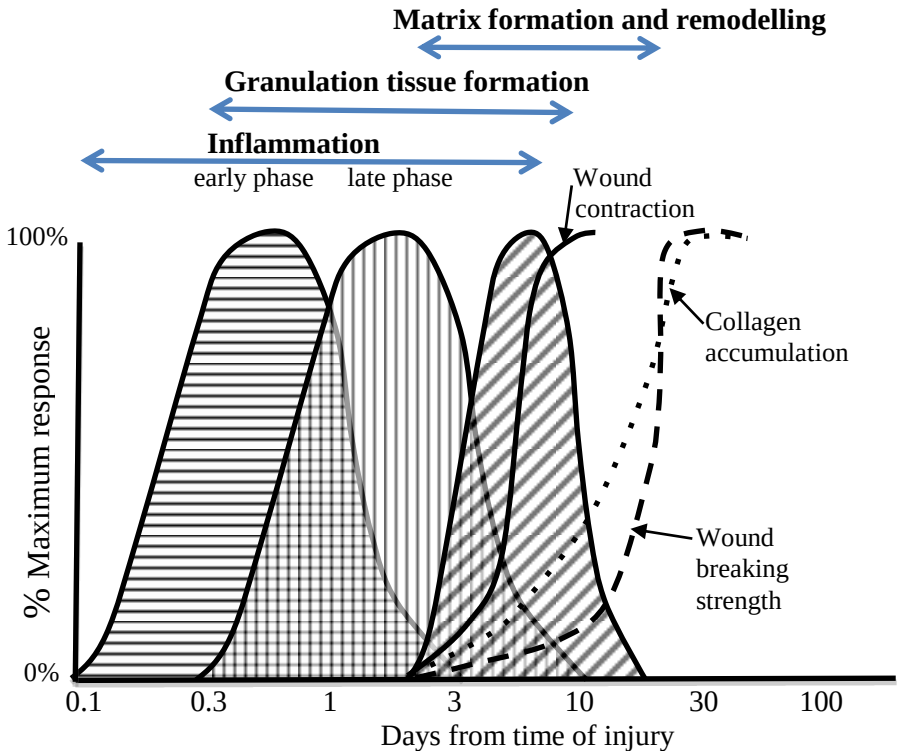

Figure 3.2 Phases of wound repair (adapted from (Mendonca and Coutinho-Netto, 2009))

3.3.1 Inflammation

During the early inflammatory phase, the leaking of blood constituents and concomitant platelet aggregation, blood coagulation, and generation of bradykinin and complement-derived anaphylatoxins occurs after the blood vessel is disrupted (Williams and Jose, 1981). Blood coagulation is triggered when the activated platelets aggregate. This makes hemostasis in the disrupted blood vessels and releases biologically active substances. These substances are an array of molecules

that promote cell migration and growth in the injury (Ginsberg, 1981). The extent of platelet aggregation and blood coagulation to the wounded area are limited by intrinsic activities of the blood vessel endothelium.

Neutrophils and monocytes are attracted by the chemotactic factors to sites of tissue injury and inflammation. Contaminating bacteria is eliminated by neutrophils in the early inflammatory phase of tissue injury. The early inflammatory phase of wound healing ends once the bacteria is eliminated (Hilborn and Bjursten, 2007). The set of events necessary to clear the wounds from bacterial contaminations is listed above (Hilborn and Bjursten, 2007).

1. Opsonisation of bacteria by complement
2. Generation of chemotactic factors
3. Adhesion of polymorphonuclear leukocytes to endothelial cells
4. Emigration of polymorphonuclear leukocytes through blood vessels
5. Attachment of opsonised bacteria to polymorphonuclear leukocytes
6. Phagocytosis of bacteria
7. Killing and digestion of bacteria

The acute inflammatory phase will continue if there is wound contamination, so the next phases of wound healing will be interfered. Therefore, the attempt to eliminate foreign objects and bacteria from the injured area will provoke more inflammation and tissue destruction.

Tissue repair is initiated at the time monocytes convert to macrophages (Leibovich and Ross, 1975). The pathogenic organisms are phagocytosed and digested by macrophages and neutrophils. Macrophages also scavenge tissue debris and effete neutrophils. The release a biologically active substances by the macrophages,

facilitate the recruitment of additional inflammatory cells. This aid the macrophage in tissue decontamination and debridement, and releases growth factors and other substances those are necessary for granulation tissue formation (Table 3.1).

Table 3.1 Macrophage activities in wound repair (modified from (Wynn et al., 2011))

Activity	Elements involved
Scavenging	Pathogenic organisms Tissue debris
Secretion of biologically active substances	Vasoactive mediators Chemotactic factors Growth factors Proteases

3.3.2 Granulation tissue formation

Granulation tissue is composed by a loose matrix of collagen, hyaluronic acid and fibronectin, where macrophages, neovasculature and fibroblasts reside. The growth and chemotactic factors released by macrophages stimulates the granulation tissue formation (Table 3.2). These factors stimulate fibroblast to proliferate, migrate, and deposit matrix. Fibroblasts form the connective tissue matrix which provides a substratum for macrophages, new blood vessels, and fibroblasts themselves to migrate (Table 3.3) (Enoch and Leaper, 2008).

In response to macrophage growth stimuli and fibroblast neomatrix, the endothelial cells form capillary buds toward the centre of the wound. Neovasculature provides macrophage and fibroblast with oxygen and nutrients necessary to grow. Therefore, during granulation tissue generation, the macrophages, fibroblasts, and blood vessels depend on each other (Hunt, 1980).

Table 3.2 Major components of late inflammatory and early granulation tissue formation phases of tissue repair (modified from (Eming et al., 2007))

Composition of granulation tissue	Components
Matrix componets	Fibrin Fibronectin Collagen I/III Hyaluronic acid
Cellular components	Epidermal cells Macrophages Endothelial cells Fibroblasts

3.3.3 Re-epithelialisation

At the time of tissue injury, the epidermal barrier is disrupted and re-epithelialisation occurs as rapidly as possible to re-establish the skins permeability barrier. This process begins when the of epithelial cells migrate from the free edge of the tissue across the injury (Winter, 1962). An additional population of migrating cells is generated by the proliferation of epithelial cells remaining at the original edge of the wound.

Winter (Winter, 1962) suggested that during epidermal regeneration no single epidermal cell moves more than two or three cell lengths from its original position. The successive implantation of cells on the wound surface forms the new epidermis. The first basal cell of the new epidermis is the first cell that moved from the parent epidermis onto the wound surface and became stationary. The new basal cell is stretched by the cells above and behind it, until came to lie on the wound surface ahead of it. The cells surrounding the first basal cell became stationary new basal cells. This process is repeated and the new epidermis becomes four to six cells deep at the outset

3.3.4 Matrix formation and remodelling

Matrix and granulation tissue formation begins simultaneously. While granulation tissue dissolves, the matrix is modified because most fibronectin is eliminated from the matrix and large fibrous bundles of collagen I are accumulated to provide the residual scar with increasing tensile strength (Hilborn and Bjursten, 2007).

The granulation tissue extracellular matrix continuously changes its composition and structure from the time of its first deposition. The characteristics of the more mature ECM at the wound margin will be different to those of the ECM initially deposited centrally. Therefore, the composition and structure of the granulation tissue ECM will depend on the distance from the wound margin and on the time elapsed since tissue injury (Hilborn and Bjursten, 2007).

Table 3.3 Fibroblast activities in wound repair (modified from (Enoch and Leaper, 2008))

Process	Activities and elements involved
Wound contraction	Phenotypic alteration a) Retraction of Golgi and endoplasmic reticulum b) Formation of large actin bundles Migration into wound defect Deposition of fibronectin and collagen I/III Formation of fibronexus Contraction
Formation and remodeling of matrix	Fibronectin Hyaluronic acid Collagen I/III Proteoglycans Proteases and other enzymes

3.4 Cell-surface adhesion process

Foreign body reaction is elicited by the implant placement in the body; this initiates an initial inflammatory phase where the prosthesis is encapsulated or eliminated by

the host. The adhesion of animal cells to polymer surfaces occurs generally in two steps. Firstly, the cell examines the surface for suitable protein ligands by approaching to a surface and expanding out a temporary pseudopodial extension to later form an initial temporary focal attachment. Secondly, the cell spreads over the surface and creates more permanent local attachments. Thus, a combination of non-specific and specific interactions creates the adhesion process. There are many forces considered the sources of cell sticking (Khorasani and Mirzadeh, 2004): specific charge-charge interactions at contact, electrostatic repulsion, hydration repulsion, and van der Waals attraction. Specific adhesion involves receptor-ligand bonding, that is the case of integrins that binds to ECM molecules such as fibronectin, collagen and laminin.

Anchorage-dependent cells adhere and grow upon the provision of a suitable substratum, which allows the establishment of a complex set of molecular interactions. These determine and regulate morphology, motility, growth and metabolism (Lydon et al., 1985). Therefore, the anchorage-dependant cell behaviour will be regulated by the definition of the substratum properties.

The ECM in the breast tissue is comprised of specific proteins and proteoglycans (Muschler and Streuli, 2010). Fibroblasts use surface receptors to interact physically with their immediate environment (Bershadsky et al., 2003). ECM receptors, mainly integrins, provide attachment to the surrounding stroma. The associations of the heterodimeric receptors formed by integrins define the influence to different ECM components.

A protrusion is sent in the direction of the movement in cell migration, integrin clustering and formation of adhesion complexes are induced by the extracellular substrate bound by integrin receptors (Biname et al., 2010). This leads to eliciting the adaptor proteins to connect the adhesion points to the actin cytoskeleton. This starts

focalized intracellular signalling which depend on the proteins created and the type of integrin engaged in the interaction with its specific extracellular substrate. At the leading edge of the protrusions, small temporary adhesion complexes mature into larger structures named focal contacts when they are under tension. Focal adhesions, the more stable structures, are connected to actin stress fibres (Berrier and Yamada, 2007).

3.4.1 Forces at the interface between cells and their environment

The cell's own contractile machinery and a variety of environmental factors act at the interface between cells and the extracellular matrix or between cells and their neighbours, Cells sense these forces and their application triggers physiological responses that affect the cell behaviour and structure. Local structural changes in adhesion sites and the attached cytoskeleton, alterations in cell proliferation, motility, and survival are responses to these mechanical perturbations. However, it is uncertain the mechanism underlying the conversion of physical signals in adhesion sites into chemical signals (Gillespie and Walker, 2001, Hamill and Martinac, 2001).

The forces that the cell produces are primarily generated by the different cytoskeletal networks that span the cytoplasm. Actin polymerization generates forces that can be applied to organelles, membranes, and other cytoskeletal systems, thus leading to their deformation (e.g., protrusion of the lamellipodium) or translocation (e.g., organelle transport) (Carlier et al., 2003).

3.4.1.1 Cell adhesions

In focal adhesions, the integrin receptors are heterodimers whose alpha and beta subunits link the ECM to the cytoskeleton. Networks of adapter or anchor proteins that form a submembrane plaque mediate this transmembrane interaction. These connections are stablished by the cytoplasmic domains of β-integrin subunits. Talin,

α-actinin, filamin and tensin can directly link integrins with the actin filaments (Geiger et al., 2001, Liu et al., 2000, Zamir and Geiger, 2001). Appart from these direct linkers, there are several potential connections composed of two or more links (Zamir and Geiger, 2001, Geiger et al., 2001), and new discovered components is increasing (Tu et al., 2003).

Focal adhesions and focal complexes are apparently associated with different sub-domains of actin cytoskeleton (Geiger and Bershadsky, 2001, Rottner et al., 1999). A dense, rapidly polymerizing branching network of actin filaments are contained in a protruding lamellipodia

The actin-related protein-2/3 (ARP2/3) complex is contained in focal complexes, and it is reported a transient molecular interaction between vinculin and Arp2/3 (DeMali et al., 2002). Transition of the associated actin mesh into densely packed straight bundles of filaments (stress fibres) accompain the transition of the focal complexes into focal adhesions (Heath and Dunn, 1978).

Among the actin-associated proteins contained in the stress fibres, myosin II in an active form apparently apply tension to the membrane-bound adhesion plaque (Matsumura et al., 1998, Katoh et al., 2001). These tension forces are transmitted via integrins to the extracellular matrix.

3.4.1.2 Forces the cell exerts via focal adhesions

Different cell types generally produce different traction forces and develop matrix adhesions of different sizes. Thus, different cell types exert similar forces per unit of the adhesion area (stress) (Balaban et al., 2001, Beningo et al., 2001). The actin cytoskeleton generates forces that the integrin-mediated matrix adhesions transmit,

and these forces are proportional to the size of the adhesion site. Focal adhesion assembly, growth, and maintenance depend on mechanical forces applied to them. The formation of new focal adhesions and the stability of the existing ones is affected by the inhibitors of myosin II-driven contractility (Balaban et al., 2001, Chrzanowska-Wodnicka and Burridge, 1996, Helfman et al., 1999). When the myosin II-driven tension decreases, the focal adhesion size decreases as well (Balaban et al., 2001); if the contractility is blocked, the focal adhesions will be completely dissolved (Chrzanowska-Wodnicka and Burridge, 1996, Helfman et al., 1999). Whereas, focal complexes do not disassemble if myosin II contractility is inhibited (Riveline et al., 2001).

The forces applied to adhesion sites are also determined by the mechanical nature of the underlying substrate. In a soft flexible substrate which can be easily deformed, the necessary force to sustain the adhesion site and the attached stress fibers is higher than the tension acting on the adhesion plaques. Thus, the typical dimensions of focal adhesions formed with soft substrates are considerably smaller than those formed following attachment to a rigid surface (Pelham and Wang, 1997). Therefore, the cells will sense a gradient in substrate rigidity and move towards the higher rigidity substrate (Lo et al., 2000).

The growth of the focal adhesion brings an increase in number of filaments forming the stress fibre associated with the adhesion plaque, so the applied tension increases and further focal adhesion growth is promoted (Bershadsky et al., 1996).

3.5 Formation of the scar encapsulation around the textured surface of a silicone breast implant

Surface topography plays a role in biological processes such as cell attachment, proliferation, motility, differentiation and regulation of gene expression (Prasad et al., 2010). It is postulated that the contracture rate is disminished by: 1) maintaining

the macrophages in a state of phagocytic readiness to delay fibroblast fibrogenesis, and 2) creating a nonlongitudinal organization of the collagen fibres, formed during the tissue reaction, to the irregular, porous structure of the envelope (Brohim et al., 1992).

It has been found that capsules around smooth surface implants are thicker and more contracted in comparison to the capsules surrounding textured surface implants. In smooth surfaces, the entire portion of the cell that is in contact with the surface prevents contact with other cells (except at their very periphery) and the orientation of the fibroblasts leads to collagen fibres to effectively contract (Prasad et al., 2010).

Whereas in textured surfaces, contact guidance directs the fibroblast into the crevices and indentations of the substrate surface, so the advancing edge of the fibroblast touch each other in several planes (contact inhibition), creating a minimal encapsulation response and a thinner capsule (Ersek et al., 1990).

Texturing has the function of holding the implant in place, thus preventing micromotion at the host prosthesis interface. While in smooth surface implants, the implant moves inside the breast, making the fibroblasts repeatedly produce collagen in response to this host-prosthesis shearing motion (Ersek et al., 1990).

It was found that the fibroblasts' response to oriented grooves was better than to the randomly oriented surfaces: thicker capsules formed on the oriented grooves in comparison to the randomly oriented grooves. However, the thinner capsules on random rough surfaces led to greater inflammatory responses (Parker et al., 2002).

Chapter IV Surface characterisation: parameters and equipment, microscopy principles and surface coatings

4.1 Introduction

In order to understand cell responses to surface properties, it is fundamental to know how the cells interact with their natural surroundings in the ECM. The ECM is three-dimensional, composed of functional groups, specific proteins such as collagen, laminin and proteoglycans, and growth factor reservoirs. The ECM provides, with its three-dimensional surface topography, the biophysical cues and the chemical stimulus for the cells adhered to it. Cells adhere, change their morphology, proliferate, migrate and differentiate by the ECM influence (Mwenifumbo and Stevens, 2007).

Cells interact with the substrate on which they grow by producing ECM proteins. These ECM proteins transduce both the chemical and physical extracellular signals through the cytosol membrane using focal contacts. The types of cell–matrix adhesions organized by integrins *in vitro* and the signals they transduce are strongly affected by their microenvironment (Mwenifumbo and Stevens, 2007). Therefore, a closer approximation to *in vivo* environments should be attained by growing cells on three-dimensional surfaces.

This chapter identifies the parameters that can influence cell adhesion and describes the techniques and equipment used for their quantification. Among the factors that influence cell-surface adhesion, surface coating is studied as a factor that will modify the original properties of wettability and surface roughness in the breast implants analysed. Wettability was considered in this study due to the fact that cell attachment

is known to be more favourable on moderately wettable (hydrophilic) surfaces compared to hydrophobic substrates. Surface roughness allows cells to grow into the interstices and creates a bigger area for cells to spread and proliferate. The successful adhesion of a cell depends on the presence of suitable adhesion cues on the surface. Therefore, implants have been coated with proteins that promote cell-adhesion (fibronectin, collagen, and hyaluronic acid).

The selection of surface coatings that will improve the properties of the actual breast implants is based on a genome microarray study. The microarray study identified genes whose expression would correlate with breast capsular contracture. The study of cell morphology represented a considerable challenge in this research due to the topography and the semitransparency of the textured surfaces. Therefore knowledge of the principles of microscopy was essential to identifying fibroblasts adhered to the surfaces and to obtaining sharp images. The information from this chapter will form the basis of the forthcoming experiments to characterise the breast implants shells and study cell morphology.

4.2 Parameters and equipment

4.2.1 Roughness

Surface roughness is a constituent of surface texture and is defined by the vertical deviations measuring the real surface against its ideal form. The surface is considered rough if these deviations are large, and smooth if the deviations are small (Chi et al., 2005). Surface roughness is essential to determine the interaction of an object with its environment, for instance rough surfaces promote adhesion. In this thesis the roughness value was calculated on a surface and the parameters measured in the breast implant surfaces are described below.

Amplitude parameters

Arithmetic mean surface roughness (*Sa*) is defined as the arithmetic average deviation (Figure 4.1) of the surface peaks and valleys measured in micrometers. The measurement is taken while the stylus of a profilometer traverses the sampling length on the surface (Trelleborg, 2008). The total height of the profile *St* is the height between the highest peak and the deepest valley on the evaluation length (Chi et al., 2005). The maximum profile peak height *Sp*, as seen on Figure 4.2, is measured from the mean line to the highest peak on the sampling length, while the maximum profile valley depth *Sv*, as seen on Figure 4.3, is measured from the mean line to the highest peak on the sampling length (Whitehouse, 2002).

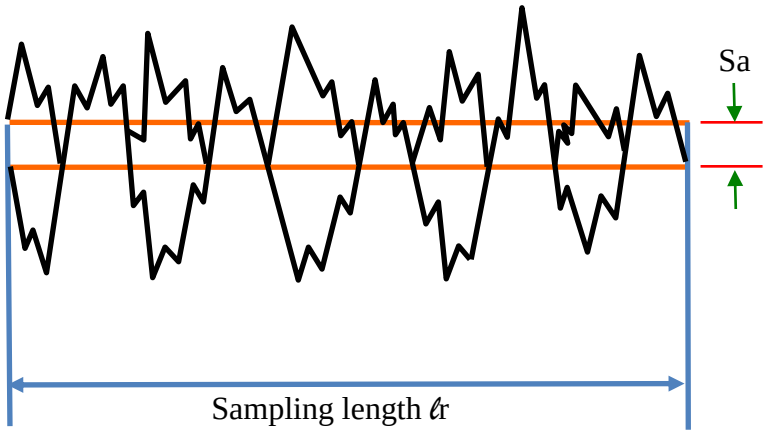

Figure 4.1 Arithmetical mean deviation (modified from (Zygo, 2005))

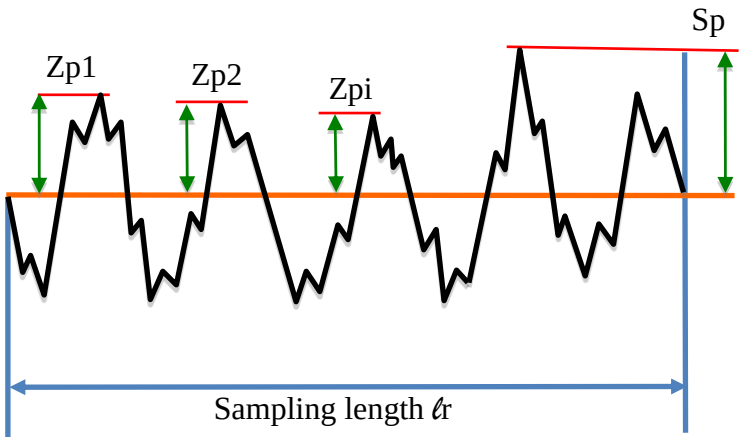

Figure 4.2 Maximum peak height (modified from (Zygo, 2005))

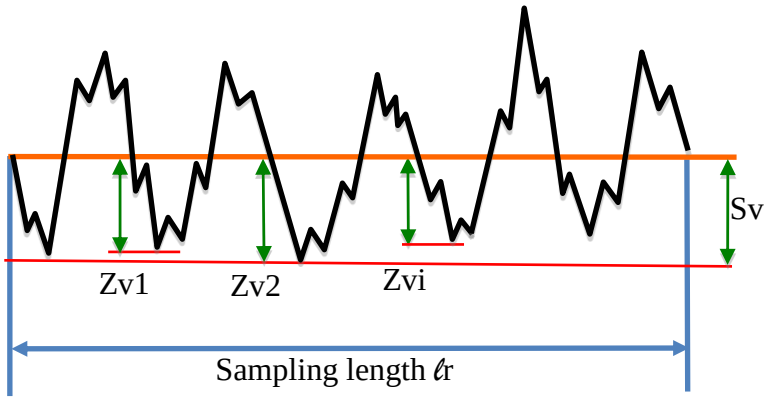

Figure 4.3 Maximum valley depth (modified from (Zygo, 2005))

Hybrid Parameters

Skewness *Ssk* refers to the symmetry of the profile with respect to the mean line (Figure 4.4). This parameter is important as it gives information on the morphology of the surface texture. A negative value of skewness indicates the predominance of valleys; a positive value indicates the predominance of peaks (Stout, 1993).

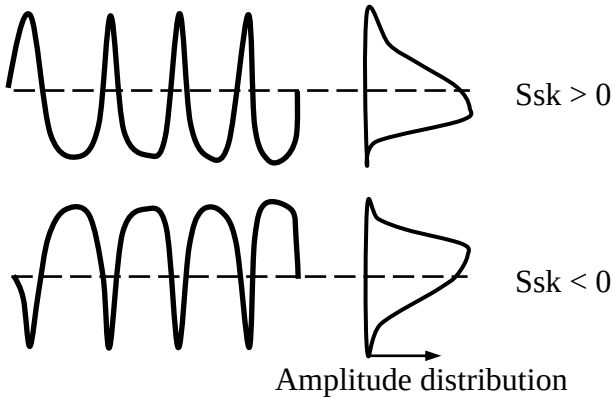

Figure 4.4 Skewness (modified from (Zygo, 2005))

Kurtosis *Sku* indicates the randomness of heights and sharpness of the structures comprising the surface. A perfectly random surface has a kurtosis value of 3; the farther the result is from 3, the less random and more repetitive the surface is (Figure 4.5) (Stout, 1993).

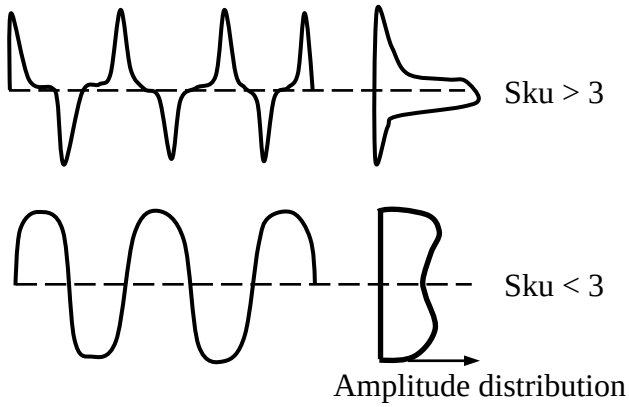

Figure 4.5 Kurtosis (modified from (Zygo, 2005))

Functional parameters

The material ratio curve (Figure 4.6) devises the ratio of material to air from the first contact at the highest peak showing the change with depth (Abbott and Firestone, 1993). From the material ratio curve, the core roughness depth *Sk* refers to the depth of the roughness core profile. The reduced peak height *Spk* refers to the average height of the prominent peaks above the roughness core profile, while reduced valley depth *Svk* refers to the average height of the profile valleys below the roughness core profile.

The material portion % *Mr1* refers to the intersection line which divides the roughness core profile from the prominent peaks, while the % *Mr2* refers to the intersection line which divides the roughness core profile from the valleys (Trelleborg, 2008).

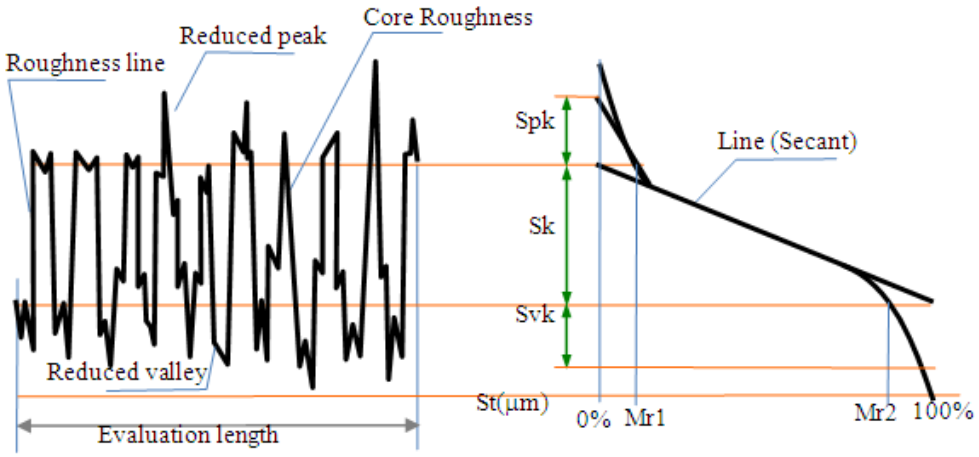

Figure 4.6 Material ratio curve (modified from (Zygo, 2005))

Volume Parameters

These parameters are defined with respect to the material ratio curve (Figure 4.7). The parameters are defined with respect to two bearing ratio thresholds, set by default to 10% and 80%. Two material volume and two void volume parameters are defined: the peak material volume *Vmp* is the volume of material contained in the surface from the height corresponding to the 10% material ratio to the highest peak. The core material volume *Vmc* is the volume of material contained in the texture between heights corresponding to the 10% to the 80% material ratio. The core void volume *Vvc* and the valley void volume *Vvv* provide the void volume for cells to adhere and spread (Stout, 1993).

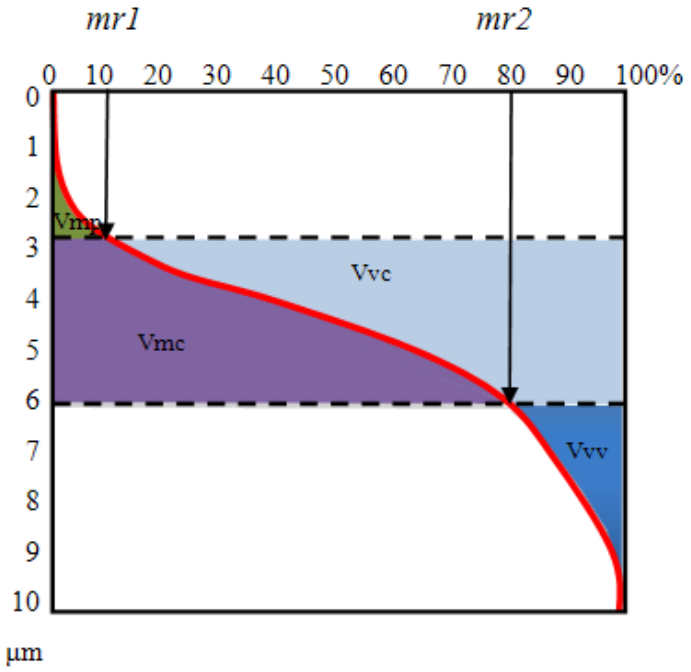

Figure 4.7 Volume parameters (modified from (Zygo, 2005))

Sampling length and Evaluation length

Sampling length is used to cover enough surface to ensure a reliable value of the parameter measured. It is calculated on profile segments (sampling lengths) and then averaged. The sampling length is defined as the cut-off length (λc) of the filter used to separate waviness and roughness. For instance, using a cut-off length of 0.8 mm and 5 sampling lengths, parameters are measured on each segment (Sa1, Sa2, ., Sa5) and the parameter value would be the mean of these estimated values (Figure 4.8) (Srinivasan, 1998).

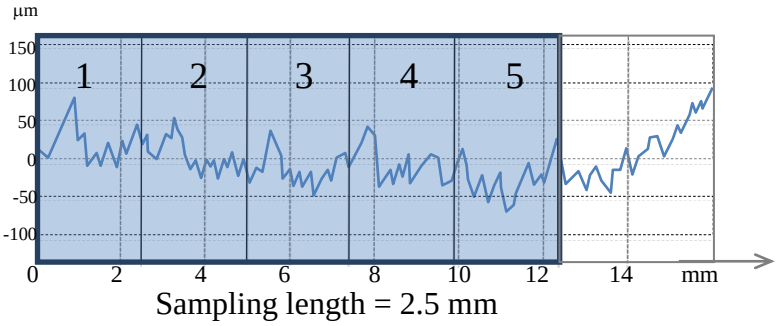

Figure 4.8 Cutt-off length (modified from (Srinivasan, 1998))

4.2.1.1 Surface roughness measurement by confocal laser microscope

In order to prevent damaging the soft surface of the breast implants, as a hard needle-shaped stylus would do, a non-contact laser microscope was used. Measuring surface roughness using a laser scanning microscope (LSM) does not require sample preparation, because the sample is just placed on the stage. In comparison the scanning electron microscope requires the sample to be altered to fit into the observation chamber and an extensive sample preparation. The LSM measured the surface roughness at high resolution due to its 0.2 μm laser spot diameter.

The values of the surface roughness texture parameters were obtained by applying the Olympus LEXT laser microscope software to the scanned images. The cut-off length was chosen to be 80 μm as the dimensions of the scanned area were 644 x 642 μm. The principles of the confocal microscope are given below in 4.2.3.

4.2.2 Wettability

Wettability indicates the degree of wetting when a solid and liquid interact by measuring contact angles. A contact angle can be defined as the angle formed by the liquid-vapour interface and the intersection of the liquid-solid interface (Young, 1805). A contact angle can be acquired by drawing a tangent line from the contact point along the liquid-vapour interface in the droplet profile as seen in Figure 4.9.

Wetting of a surface is considered favourable when the contact angle is fewer than 90° so the liquid will spread over a large area on the surface. An unfavourable surface wetting will have a contact angle higher than 90° and the liquid will form a compact droplet with minimal contact with the surface. Finally, a surface is considered super hydrophobic when the contact angle is greater than 150° (Lafuma and Quere, 2003).

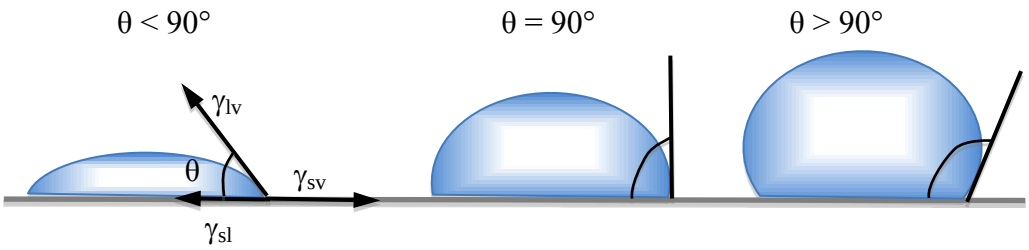

Figure 4.9 Contact angles formed by sessile liquid drops on a smooth homogeneous solid surface (modified from (Lafuma and Quere, 2003))

The shape of a liquid droplet and the contact angle is determined by a combination of surface tension and external forces (usually gravity). Surface tension is defined as the intermolecular force to contract the surface of the liquid. Surface tension can be explained in Figure 4.10 where the liquid molecules pull equally each molecule in the bulk in all directions, but the molecules at the surface are pulled inward by the neighbouring molecules, creating an internal pressure. Consequently, the liquid keeps the lowest surface free energy by contracting its surface area to form a sphere droplet (Snoeijer and Andreotti, 2008).

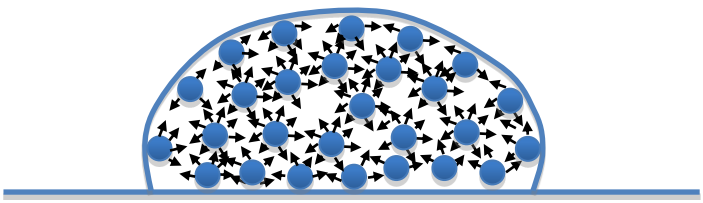

Figure 4.10 Forces of liquid molecules at the surface (modified from (Lafuma and Quere, 2003))

The mechanical equilibrium drops under the action of three interfacial tensions which define the contact angle of a liquid drop on an ideal solid surface (Young, 1805) (Figure 4.10):

$$\gamma_{lv} \cos \theta_Y = \gamma_{sv} - \gamma_{sl} \quad (4.1)$$

γ_{lv} = liquid-vapor interfacial tension
γ_{sv} = solid-vapor interfacial tension
γ_{sl} = solid-liquid interfacial tension
θ_Y = contact angle

4.3 Principles of microscopy

4.3.1 Fluorescence microscopy

Fluorescence microscopy involves three basic concepts: photoluminescence, phosphorescence and fluorescence. Photoluminescence occurs when specimens absorb and subsequently reradiate the light. Phosphorescence happens after the excitation energy is discontinued and the emission of light persists for up to a few seconds. Fluorescence refers to the light emission only during the absorption of the excitation light, so the time interval between absorption and emission of light is usually less than a millionth of a second (Haugland et al., 2002).

When a photon gets absorbed by a molecule, this leads to one electron raises from its ground state (S_0) to a higher vibrational level of an excited singlet state (S_2). In the next step, some energy is lost as heat (S_1), returning the electon to its ground state (S_0) and the absorbed energy is released again by emission of light. This light is called fluorescence which is illustrated in Figure 4.11. Because a part of this energy is dissipated into heat; the energy of the emmited fluorescence light is lower than the energy of the absorbed light, so the emission occurs at a longer wavelength than absorption (Didenko, 2006, Kubitscheck, 2013). The visible light region of electromagnetic radiation covers a wavelength range from approximately 400 to 700 nanometres as seen in Figure 4.12 (Nassau, 2001).

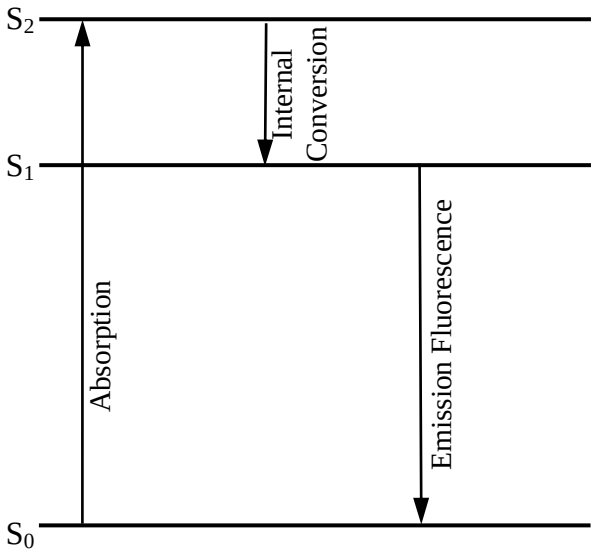

Figure 4.11 Simplified Jablonski-diagram of states (adapted from (Lakowicz, 2007))

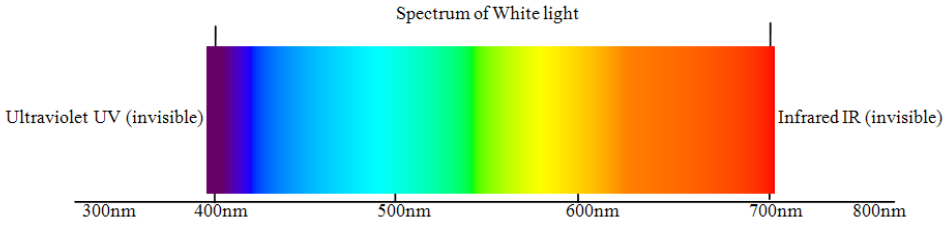

Figure 4.12 Visible light region of electromagnetic radiation (adapted from (Abramowitz, 1993))

4.3.1.1 Electron excitation and emission

The principle of a fluorescence microscope is that only the emission light from the specimen reaches the eye or the detector by allowing only the excitation light to irradiate the specimen and isolating the brighter excitation light from the much weaker emitted fluorescent light as seen on Figure 4.13. Thereafter, only the brighter fluorescing areas will shine against a dark background with sufficient contrast to be detected (Hibbs, 2000).

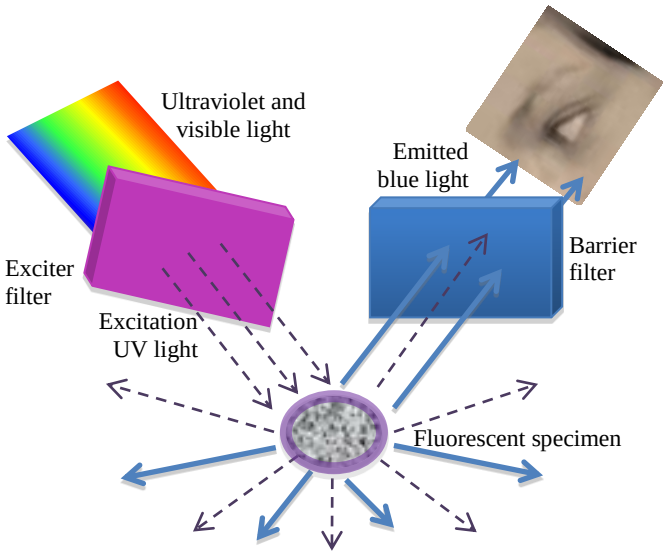

Figure 4.13 Principle of excitation and emission (adapted from (Abramowitz, 1993))

Autofluorescence and secondary fluorescence have been used to study materials that are fluoresced in their natural form or by treating them with chemicals able to fluoresce. Secondary fluorescence uses an appropriate fluorochrome capable of absorbing and then re-radiating light with known intensity curves of excitation (absorption) and emission and which are highly specific in their attachment biological targeting (Goldstein, 1999).

Illustrated in Figure 4.14 is one of the fluorochromes that stained the nucleus of the studied fibroblasts blue, 4',6-diamidino-2-phenylindole (DAPI). DAPI binds preferentially to adenosine and thymidine (A-T) base pair regions in DNA and is excited by ultraviolet light with a maximum absorption wavelength of 355 nanometres (Foster, 1997). The appropriate fluorochrome for any fluorescence application must possess a high likelihood of absorbing the exciting light, a satisfactory yield of emitted fluorescence light, and should remain attached to the target molecules (Eftink, 2000).

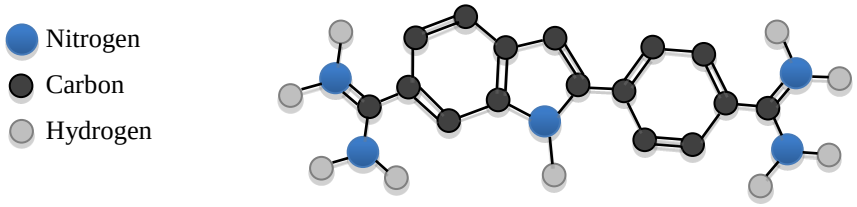

Figure 4.14 4´-6 diamidino -2- phenylindole (DAPI) (adapted from (Foster, 1997))

The absorption spectrum of a typical fluorochrome is illustrated in Figure 4.15 (a). Excitation is induced (usually by means of a monochromator) at various excitation wavelengths and the emitted fluorescence intensity is measured as a function of wavelength to plot the emission spectrum as seen on Figure 4.15 (b) (Herman, 1998). Excitation and emission filters prevent the much brighter excitation light overwhelming the weaker emitted fluorescence light by eliminating the overlap of excitation and emission intensities and wavelengths (Figure 4.15 (c) (Goldstein, 1999).

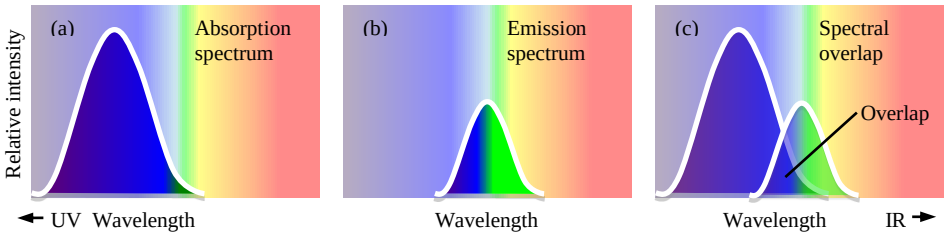

Figure 4.15 Absorption and emission spectra of a typical fluorochrome (adapted from (Abramowitz, 1993))

4.3.1.2 Fading or photobleaching

The intensity of fluorescence is reduced by specific conditions that may affect the re-radiation of light by an excited fluorophore. This reduction of emission intensity is called fading and can be reduced using a neutral density filter in the light path before

the illumination reaches the excitation filter, thus diminishing the excitation light intensity. In our study, fading effects were reduced by using anti-bleaching agents and rapidly changing the field of view while digital imaging the specimens (Slayter, 1970).

4.3.2 Confocal microscopy

The confocal approach eliminates out-of-focus light or glare in specimens whose thickness exceeds the immediate plane of focus using spatial filtering techniques. Confocal microscopy was chosen for this study because the fibroblast seeded into rough surfaces that exhibited a high degree of fluorescence emission and most of the fine detail was lost. Confocal microscopes have the capability to exclude secondary fluorescence in areas, removed from the focal plane, from resulting images. Another property is that it has control over the depth of field making it possible to collect serial optical sections from our thick specimens (Pawley et al., 2006).

The principles of confocal microscopy can be explained using Figure 4.16 where the excitation source beam light first passes through a pinhole aperture located in a conjugate plane (confocal), with a scanning point on the specimen, and then passes through a second pinhole aperture in front of the detector. The dichromatic mirror reflects the laser that is scanned across the specimen in a defined focal plane. Atthe same time, in the same focal plane; the specimen emits secondary fluorescence that passes back through the dichromatic mirror and is focused as a confocal point at the detector pinhole aperture. In the aperture plane, extended airy disks are formed with the fluorescence emission that was not confocal with the pinhole, so a small portion of the out-of-focus fluorescence emission is delivered through the pinhole aperture. Therefore, the photomultiplier does not detect most of this unnecessary light and does not contribute to the resulting image (Pawley and Inoué, 2006).

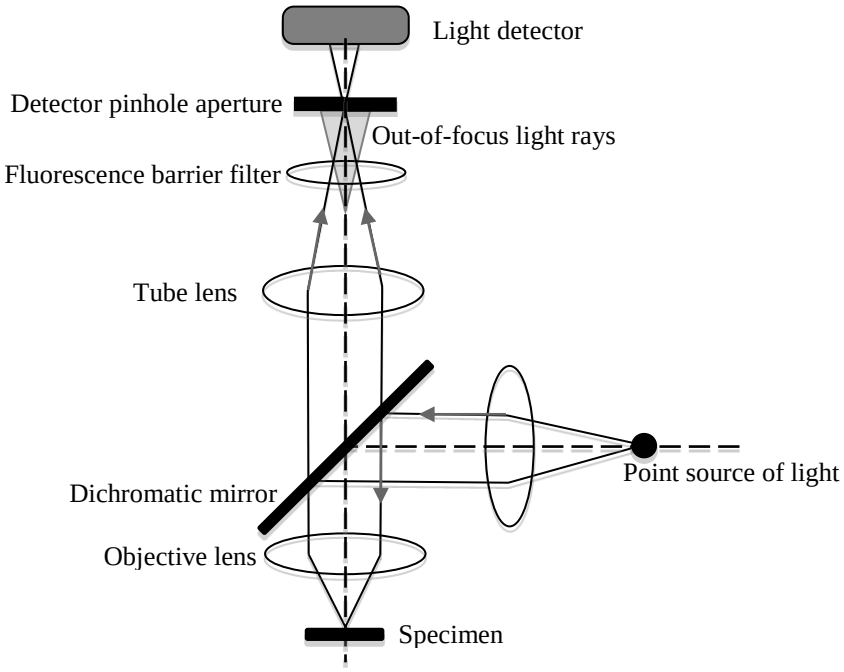

Figure 4.16 Laser scanning confocal microscope optical configuration (adapted from (Claxton et al., 2006))

The above can be illustrated in Figure 4.17 when comparing the typical illumination cones of point scanning confocal microscope and widefield at the same numerical aperture. In the confocal microscope the specimen is scanned with a finely focused spot of illumination that is centred in the focal plane, while in the widefield microscope the entire depth of the specimen over a wide area is illuminated. The result is a diminished resolution and image contrast due to the significant amount of signal as a result of the emitted background light and autofluorescence of areas above and below the focal plane (Claxton et al., 2006).

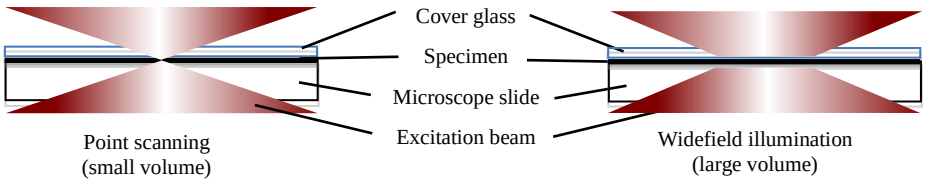

Figure 4.17 Widefield versus confocal point scanning of specimens (modified from (Claxton et al., 2006))

Fluorescence emission passes through the pinhole aperture and is converted by the photomultiplier into an analogue electrical signal. It is later converted into pixels that will compose the confocal image of a specimen (Claxton et al., 2006).

4.3.3 Deconvolution

Deconvolution was used in this study to improve the contrast and resolution of digital images captured in the confocal microscope. Deconvolution is based on methods that can remove or reverse the out-of-focus blur from images generated by the narrow aperture of the objective (McNally et al., 1999, Spector et al., 1988). Blur is described by a non-random spreading of light that occurs by passing through the imaging system's optical train. As blur is a function of any microscope optical system, (generally the objective function), can be modelled to reverse the blurring process mathematically by deconvolution methods (Shaw, 1998).

Principles of acquisition of serial optical sections for deconvolution analysis can be explained using Figure 4.18 where a series of optical sections of a specimen are recorded along the z-axis of an optical microscope. The detector records an image plane for each focal plane of the specimen and then stores them in a data analysis computer. Deconvolution analyses the resulting images to subtract blurred light and the entire sequence of optical sections to create a three-dimensional montage (McNally et al., 1999).

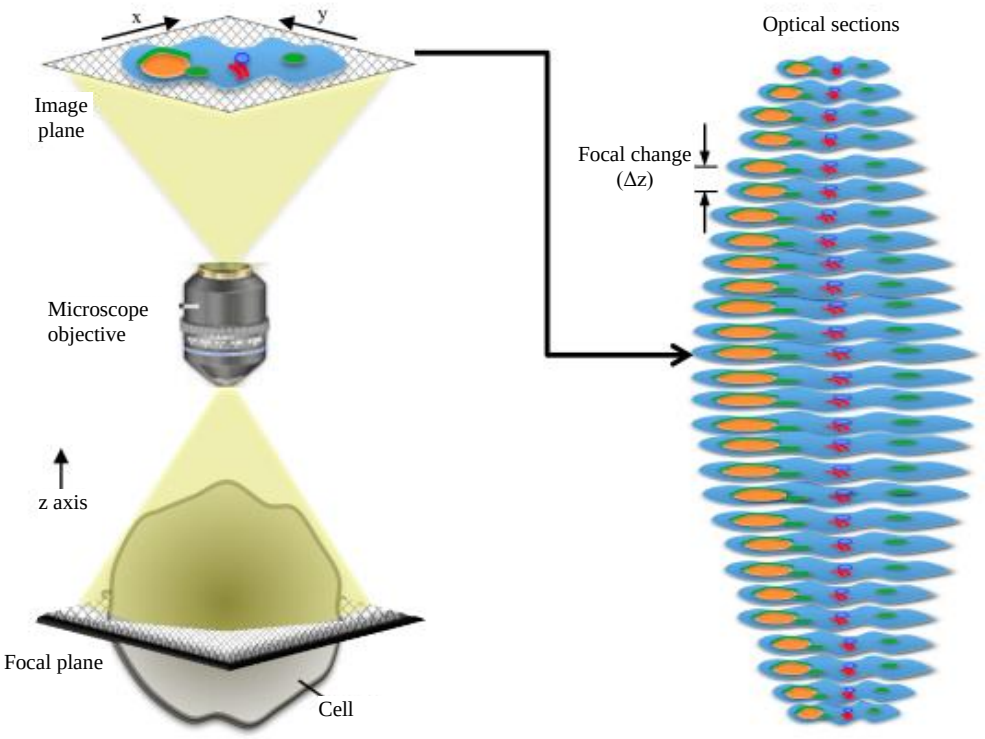

Figure 4.18 Acquisition of optical sections for deconvolution (adapted from (Davidson and Abramowitz, 1998))

4.3.3.1 The point spread function

The point spread function refers to an infinitely small point source of light originating in the specimen. Microscope imaging systems cannot focus the light into a perfect three-dimensional image of the point because it gathers just a fraction of the light emitted by this point. Therefore, the point appears wide and spreads into a three-dimensional diffraction pattern (Claxton et al., 2006).

The basic unit of an image, according to the theoretical model of image formation, is the point spread function. Therefore, the best image is an assembly of point spread functions. Convolution is a mathematical model of the blurring process (Rietdorf and Sibarita, 2005). The final image is produced when light, emitted from each point in the object, is convolved with the point spread function. But this causes points in the

specimen to become blurred zones in the image. This process is reversed with deconvolution in an attempt to reconstruct the specimen from a blurred image (Rietdorf and Sibarita, 2005).

4.4 Surface coatings

To successfully elicit specific cellular responses and direct new tissue formation, biological cues were created by the design of biomimetic scaffolds modifying biomaterials with ECM molecules (Shin et al., 2003). When proteins of the ECM interact with cells via cell surface integrin family receptors, the resulting focal contacts are important for the maintenance of tissue architecture and for supporting a variety of cellular processes. Binding of an ECM molecule and integrin may initiate a network of signal transduction cascades that influence cell spreading, adhesion, proliferation and migration.

4.4.1 Surface coatings requirements

The objective of coating the breast implant surfaces is to direct new tissue formation using biological cues with ECM molecules (Steward et al., 2011, Li et al., 2012b, Hauser et al., 2009). To achieve this, the coatings used in this research were selected based on their properties to:

- Interact with cells via cell surface integrin family receptors
- Promote cell-surface adhesion, cell spreading,
- Provide a scaffold for cells to proliferate and migrate
- Do not relate to capsular contracture and fibrosis
- Do not contribute to fibrosis
- Be commercially available

4.4.2 Surface coating selection procedure

The surface coatings were chosen from a whole genome microarray study (Kyle et al., 2013) performed in cDNA of 23 breast capsules from which 12 capsules correspond to Baker grades I and II and 11 capsules correspond to Baker grades III and IV (Baker grades I and II refer to normal capsules compared to grades III and IV which refer to severely contracted capsules). 122 genes were found to be up-regulated and 22 down-regulated. The candidate genes were selected from the microarray data by grouping genes according to 5 categories (Figure 4.19).

The first category consisted of all the down-regulated genes, the second category was comprised of the genes related to cell adhesion and extracellular matrix and the third category was formed according to the smallest statistical *p*-value. A selection of genes was chosen that matched the 3 criterions and a literature review was conducted in order to further investigate the potential use of the selected genes as coatings. Research into gene and protein expression of fibrosis and breast capsules was undertaken to facilitate a comparison with the selected genes from the microarray. Moreover, a literature review was carried out to identify bio-molecules related to fibrosis and wound healing in the body, and the results were compared with the genes selected from the microarray. Finally, the candidate genes were evaluated according to their commercial availability.

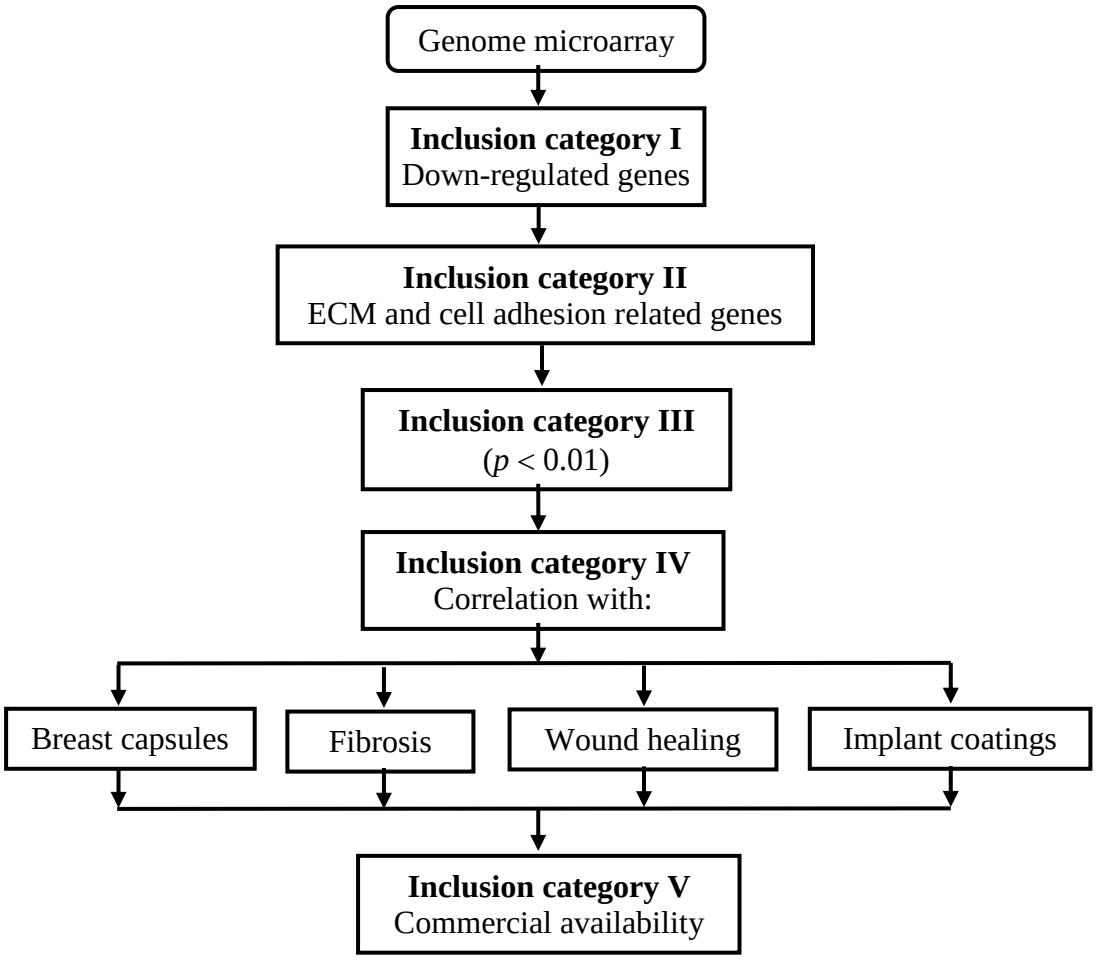

Figure 4.19 Flowchart of the steps taken to find the gene to be a protein candidate for coating from a microarray data

4.4.3 Surface coating selection tables

This study is primarily focused on those whose expression is down-regulated in breast capsules (Table 4.1). Within the set of down-regulated genes, genes from different biological processes were identified, such as cell adhesion, extracellular matrix, basement membrane, nucleus, nervous system development, lipid transport, sensory perception of smell, and visual perception. Since the purpose is to create a list of genes related to cell adhesion and ECM, these were selected as seen on Table 4.2.

Table 4.1 Selection of the most down-regulated genes from a microarray data. Selected genes were highlighted.

Comparison 1 Log ratio	Comparison *P*-value	Gene Symbol	Name
-1.2723	0.0097	HIST1H2BH	Histone cluster 1, H2bh
-1.2955	0.0097	CRYGC	Crystallin, gamma C
-1.3424	0.0085	RGS10	Regulator of G-protein signalling 10
-1.3558	0.002	C10orf132	Chromosome 10 open reading frame 132
-1.383	0.0058	VPS28	Vacuolar protein sorting 28 homolog (S. cerevisiae)
-1.4505	0.002	SEMA3A	Sema domain, immunoglobulin domain (Ig), short basic domain, secreted, (semaphorin) 3A
-1.5191	0.0066	SLC5A5	Solute carrier family 5 (sodium iodide symporter), member 5
-1.5888	0.0014	CRTAC1	Cartilage acidic protein 1
-1.6137	0.0028	SPNS1	Spinster homolog 1 (Drosophila)
-1.6823	0.0078	SCRG1	Scrapie responsive protein 1
-1.7233	0.0036	C1orf173	Chromosome 1 open reading frame 173
-1.8075	0.0076	TIMP4	TIMP metallopeptidase inhibitor 4
-1.8473	0.0024	TNMD	Tenomodulin
-2.0432	0.0001	DLX3	Distal-less homeobox 3
-2.2717	0.0009	SMOC1	SPARC related modular calcium binding 1
-2.4866	0.0007	TNFSF11	Tumor necrosis factor (ligand) superfamily, member 11
-2.9522	0	VWC2	Von Willebrand factor C domain containing 2
-2.9897	0	SMOC1	SPARC related modular calcium binding 1
-3.5333	0	ACAN	Aggrecan

Table 4.2 Genes related to the extracellular matrix. Selected genes were highlighted.

Comparison 1 Log ratio	Comparison *P*-value	Gene Symbol	Name	Biological Process
-1.2955	0.0097	CRYGC	Crystallin, gamma C	Response to stimulus, sensory perception of smell.
-1.2723	0.0097	HIST1H2BH	Histone cluster 1, H2bh	Nucleosome assembly
-1.342	0.0085	RGS10	Regulator of G-protein signaling 10	Negative regulation of signal transduction
-1.682	0.0078	SCRG1	Scrapie responsive protein 1	Nervous system development, ECM
-1.808	0.0076	TIMP4	TIMP metallopeptidase inhibitor 4	ECM
-1.519	0.0066	SLC5A5	Solute carrier family 5 (sodium iodide symporter), member 5	Iodide transport, ion transport, sodium ion transport
-1.383	0.0058	VPS28	Vacuolar protein sorting 28 homolog (S. cerevisiae)	Protein transport
-1.147	0.0049	MEGF10	Multiple EGF-like-domains 10	Cell adhesion, phagocytosis
-1.176	0.0037	NELL1	NEL-like 1 (chicken)	Cell adhesion, nervous system development
-1.247	0.0029	OR7G1	Olfactory receptor, family 7, subfamily G, member 1	Response to stimulus, sensory perception of smell, signal transduction
-1.614	0.0028	SPNS1	Spinster homolog 1 (Drosophila)	Lipid transport
-1.847	0.0024	TNMD	Tenomodulin	Integral to membrane
-1.356	0.002	C10orf132	Chromosome 10 open reading frame 132	Golgi apparatus, Golgi membrane, membrane
-1.451	0.002	SEMA3A	Sema domain, immunoglobulin domain (Ig), short basic domain, secreted, (semaphorin) 3A	Cell differentiation, multicellular organismal development, negative chemotaxis,
-1.589	0.0014	CRTAC1	Cartilage acidic protein 1	ECM
-2.487	0.0007	TNFSF11	Tumor necrosis factor (ligand) superfamily, member 11	Cell differentiation, immune response
-2.043	0.0001	DLX3	Distal-less homeobox 3	Blood vessel development, multicellular organismal development, placenta development
-2.9897	0	SMOC1	SPARC related modular calcium binding 1	Basement membrane, extracellular region
-3.533	0	ACAN	Aggrecan	Cell adhesion, ECM organization, proteolysis, skeletal system development
-2.9522	0	VWC2	Von Willebrand factor C domain containing 2	Basement membrane, extracellular region, extracellular space

Another group was created according to the lowest statistic *p*-value < 0.01. Genes on Table 4.3 demonstrated a statistically significant difference for the gene expression levels between severe and mild capsular contracture. A comparison among the above lists was done, and the genes that matched in the three categories (Table 4.4) were SPARC related modular calcium binding 1 (SMOC1), Von Willebrand factor C domain-containing protein 2 (VWC-2), TIMP metallopeptidase inhibitor 4 (TIMP-4), Tumor necrosis factor (ligand) superfamily, member 11 (TNFSF11) and Aggrecan (ACAN). These genes were analysed as follows:

Table 4.3 Genes selected from the microarray data according to the lowest statistic *p*-value. Selected genes were highlighted.

Comparison 1 Log ratio	**Comparison *P*-value**	**Gene Symbol**	**Name**
-1.2955	0.0097	CRYGC	Crystallin, gamma C
-1.2723	0.0097	HIST1H2BH	Histone cluster 1, H2bh
-1.342	0.0085	RGS10	Regulator of G-protein signalling 10
-1.682	0.0078	SCRG1	Scrapie responsive protein 1
-1.808	0.0076	TIMP4	TIMP metallopeptidase inhibitor 4
-1.519	0.0066	SLC5A5	Solute carrier family 5 (sodium iodide symporter), member 5
-1.383	0.0058	VPS28	Vacuolar protein sorting 28 homolog (S. cerevisiae)
-1.147	0.0049	MEGF10	Multiple EGF-like-domains 10
-1.176	0.0037	NELL1	NEL-like 1 (chicken)
-1.247	0.0029	OR7G1	Olfactory receptor, family 7, subfamily G, member 1
-1.614	0.0028	SPNS1	Spinster homolog 1 (Drosophila)
-1.847	0.0024	TNMD	Tenomodulin
-1.356	0.002	C10orf132	Chromosome 10 open reading frame 132
-1.451	0.002	SEMA3A	Sema domain, immunoglobulin domain (Ig), short basic domain, secreted, (semaphorin) 3A
-1.589	0.0014	CRTAC1	Cartilage acidic protein 1
-2.487	0.0007	TNFSF11	Tumour necrosis factor (ligand) superfamily, member 11
-2.043	0.0001	DLX3	Distal-less homeobox 3
-2.9897	0	SMOC1	SPARC related modular calcium binding 1
-3.533	0	ACAN	Aggrecan
-2.9522	0	VWC2	Von Willebrand factor C domain containing 2

Table 4.4 Genes that correspond to the three categories. Selected genes were highlighted.

Comparison Gene Relative Expression	Gene Symbol	Comparison 1 p-value	Gene Symbol	ECM Relation
-1.8075	TIMP4	0.002	SEMA3A	TIMP-4
-1.8473	TNMD	0.0014	CRTAC1	NELL1
-2.0432	DLX3	0.0007	TNFSF11	SEMA3A
-2.4866	TNFSF11	0.0001	DLX3	SMOC1
-2.9522	VWC2	0	SMOC1	TNFSF11
-2.9897	SMOC1	0	ACAN	ACAN
-3.5333	ACAN	0	VWC2	VWC2

SPARC related modular calcium binding 1 (SMOC1) is a secreted glycoprotein that is a member of the SPARC family of matricellular molecules (Aroca-Aguilar et al., 2011). A signalling role for SMOC1 was shown in rat mesangial cells in which induction of nitric oxide in response to inflammatory cytokines downregulates SMOC1 which, in turn, downregulates expression of TGF-β (Dreieicher et al., 2009). This mechanism was proposed to limit the profibrotic effects of TGF-β in the glomerulus, but in the microarray it was found to be already down-regulated, so using SMOC1 as a coating would increase expression of TGF-β. Also, an elevated expression of SMOC-1 was found in brain tumours (Bradshaw, 2012). Von Willebrand factor C domain-containing protein 2 (VWC-2) is a secreted protein, which is a BMP antagonist and may play a role in neural development promoting cell adhesion. VWC-2 was dismissed from the list due to it being both predominantly expressed in neural tissues in embryos and also in the adult brain, and potentially playing roles in neural development and functions (Koike et al., 2007, Miwa et al., 2009).

TIMP metallopeptidase inhibitor 4 (TIMP-4) belongs to the TIMP gene family. The proteins encoded by this gene family are inhibitors of the matrix metalloproteinases, a group of peptidases involved in degradation of the extracellular matrix. The secreted, netrin domain-containing protein encoded by this gene is involved in regulation of platelet aggregation and recruitment and may play a role in hormonal regulation and endometrial tissue remodelling. TIMP-4 was removed from our list since it was found that the decrease in MMP-to-TIMP expression during capsule formation around smooth and textured silicone implants may contribute to increased synthesis and deposition of collagen, leading to a severe fibrotic reaction after cosmetic breast augmentation with alloplastic material (Ulrich et al., 2009). Also, TIMP-4 resulted in a significant stimulation of primary mammary tumorigenes, since TIMP-4 has a growth-stimulating and anti-apoptotic (by stimulate Bcl-2 and Bcl-XL expression) (Jiang et al., 2001).

The tumour necrosis factor (ligand) superfamily, member 11 (TNFSF11) encodes a member of the tumour necrosis factor (TNF) cytokine family which is a ligand for osteoprotegerin and functions as a key factor for osteoclast differentiation and activation. This protein was shown to be a dentritic cell survival factor and is involved in the regulation of T cell-dependent immune response. T cell activation was reported to induce expression of this gene and lead to an increase of osteoclastogenesis and bone loss. This protein was shown to activate antiapoptotic kinase AKT/PKB, through a signalling complex involving SRC kinase and tumour necrosis factor receptor-associated factor (TRAF) 6, which indicated this protein, may have a role in the regulation of cell apoptosis. TNFSF11 was not considered as a coating candidate since its use as a protein coating did not show any statistically significant reduction in fibrosis in the periprosthetic capsule after treating implants with it (San-Martin et al., 2010).

Aggrecan (ACAN) plays an important role in mediating chondrocyte-chondrocyte and chondrocyte-matrix interactions through its ability to bind hyaluronan (Kiani et al., 2002). The presence of aggrecan seems to increase the amount of link protein on

the cell surface. Expression of hyaluronic acid in periprosthetic breast capsules was found, so there is a positive correlation between the HA and Baker grade of capsular contracture (Tan et al., 2011). Aggrecan was chosen to be a candidate of protein coating due to its ability to bind HA, thus reducing levels of free hyaluronan in contracted capsules. Aggrecan is commercially available.

A literature review of these genes was undertaken with the aim of finding any correlation with capsular contracture (Table 4.5), wound healing and fibrosis (Table 4.6). None of these four genes were found to be related to these processes.

Table 4.5 Research on gene and protein expression in relation to fibrosis and breast capsular contracture formation

Function	**Molecules involved**	**Reference**
Overproduction	High levels of fibrogenic cytokines	(Kuhn et al., 2000)
Transforming Growth	Induce Fibrosis	
Factor Beta TGF-*B*	TGF-*B1* (modulating cell proliferation, survival and apoptosis, enhancing ECM production and adhesion)	
	TGF-*B2*	
Immunologic response is	Interleukin-1 (IL-1)	(Diao et al., 2011)
mediated by cytokines and	Interleukin-6 (IL-6)	
growth factors:	Tumour Necrosis Factor-a (TNF-a)	
	Platelet-derived growth factor (PDGF)	
	TGF-*B* (angiogenic and inflammatory mediator)	

Table 4.6 Literature review of biomolecules related to fibrosis, wound healing in general

Biomolecule	Relation with		Reference
	Fibrosis	Wound healing	
Tenascin-C		Wound healing	(Udalova et al., 2011)
Platelet-derived growth factor (PDGF)	Fibrosis	Wound healing	(Zaccone et al., 2003)
Fibroblast growth factor		Wound healing	(Caldas et al., 2008)
Insulin-like growth factor		Wound healing	(Prakobwong et al., 2009)
ET-1	Fibrosis		(Wangoo et al., 2001)
OPN	Fibrosis		(Ajmal et al., 2003)
IGF-1	Fibrosis		(Demedts et al., 2005)
EGF	Fibrosis		(Wilson et al., 2007)
bfgf	Fibrosis		(Gruber et al., 1996)
CTGF	Fibrosis		(Tulinska et al., 2004)
Epidermal growth factor		Wound healing	(Notas et al., 2009)
Transforming growth factor		Wound healing	(Wynn, 2008)
12-Hydroxyeicosatetranouic acid		Wound healing	(Fallowfield et al., 2007)
Thromboxanes		Wound healing	(Polo et al., 1999)
Leukotrines		Wound healing	(Roberts, 1995)
Prostacyclin		Wound healing	(Tredget et al., 1998)

4.4.4 The selected surface coatings

The coatings used in this research were selected based on their properties to promote fibroblasts activity (collagen I, fibronectin and hyaluronic acid), and from a whole genome microarray study (Kyle et al., 2013) performed in cDNA of 23 breast capsules. The description of properties of the selected coatings is described below.

Aggrecan is a proteoglycan found in the ECM of cartilage, which has a molecular mass of >2,500 kDa (Roughley et al., 2006). Another constituent element of ECM is collagen, which enhances cell attachment and proliferation and can be found in the form of filaments, sheets and fibrils (Li et al., 2012a), which provides tensile strength to the tissue scaffolding. Collagen triggers cell-ECM interactions as well as cell-to-cell interactions and fibroblasts activation (Roberts et al., 2013).

An essential component of ECM related to cell adhesion is fibronectin, a 450kDa dimeric glycoprotein that can bind specifically to two widely expressed cell surface receptors, integrins α5β3, and αvβ3 (Elter et al., 2012). Fibronectin plays an important role in the adhesion of cells to material surfaces. It can even strengthen the cell-surface adhesion (Elter et al., 2012). Hyaluronic acid transports the metabolites and nutrients, provides tissue resistance to compressive forces, and controls cell migration and cell proliferation (Cohen et al., 2003). Hyaluronic acid provides the perfect scaffold for cells to proliferate and migrate (Collins and Birkinshaw, 2013, Korurer et al., 2014).

Chapter V Characterisation of breast implant shells and correlation with fibroblast adhesion

5.1 Introduction

Research into breast implants has increased through the years with the aim of diminishing the number of complications related to breast implant surgery. Notwithstanding this interest, there are relatively few studies concerned with characterisation of breast implant shells and there is a clear lack of qualitative and quantitative data on this subject (Barr et al., 2009, Danino et al., 2001, Abramo et al., 2010, Prasad et al., 2010, Lampin et al., 1997).

In the previous chapter, the principles of the properties that influence cell-adhesion were reviewed. In this chapter, the properties of commercially available smooth and textured silicone breast implants are analysed to find physical and mechanical characteristics that could trigger cell-surface adhesion.

This study is based on the hypothesis that the breast implant surface affects adhesion-related breast tissue fibroblast function to a different degree depending on the scale of micro-topography, stiffness, and wettability properties.

The results acquired from the study described in this chapter give a unique compilation of information to enable characterisation of the smooth and textured surfaces of commercial available breast implants, providing a valuable reference for studying cell-surface interaction on silicone breast implants. The effects of altering the original surface properties by coating the implant and following interaction with fibroblasts are analysed in the subsequent chapter.

5.2 Materials and Methods

Circular samples of 14 mm diameter were removed from each silicone implant shell. These samples were then sterilised by initial sonication in detergent for 10 min, before being rinsed in distilled water. This was followed by sonication in acetone for 10 min. Subsequently the samples were air dried and kept in petri dishes (Barr et al., 2010). The samples were sterilised in order to eliminate any possible contamination from particles on their surfaces.

The silicone breast implants studied were chosen from some of the commonly available implants in clinical practice: (1) Textured Surface-1 (TS1) (Mentor Siltex® (Mentor Worldwide LLC, Skyway Circle North Irving, Texas)); (2) Textured Surface-2 (TS2) (Allergan Biocell® (Allergan, Inc, Santa Barbara, California)). (3) Smooth Surface-1 (SS1) (Mentor® Smooth (Mentor Worldwide LLC, Skyway Circle North Irving, Texas)); and (4) Smooth Surface-2 (SS2) (Allergan (Allergan, Inc, Santa Barbara, California)).

The characterisation of the breast implant surface shells was investigated using three approaches:

1) 3D imaging—surface roughness texture parameter measurement.
2) Optical tensiometry (goniometry) —contact angle measurement.
3) Micro tensile testing—measurement of bending and stretching stiffness.

In addition, the kinetics of fibroblast–silicone implant surface detachment mediated by trypsin was undertaken in order to investigate the adhesive interaction between the fibroblasts and the breast implant surfaces. All experiments were conducted in triplicate. The characterisation and kinetics of detachment tests were performed on the surfaces that come into contact with the tissue of the patient. All tests were performed on these surfaces.

5.2.1 Characterisation of the silicone surfaces

5.2.1.1 3-D images

Silicone surfaces were observed at 20x magnification in three different areas (dimension of each area 644x 642 μm) of each implant after being scanned using a LEXT OLS4000 3D confocal laser scanning microscope. The LEXT OLS4000 uses a 408 nm laser diode and has a resolution on the Z-axis of 10 nm with finely controlled movement of the nosepiece. The microscope creates optical slices from in-focus pixels and combines a stack of slices (z-stack) into one image forming a 2D representation as shown in Figures 5.1—5.4a. These optical slices were then arranged into a highly accurate 3D image (Figures 5.1–5.4b) from which the surface roughness parameter values were obtained. The 20x objective has a depth of field of 6 μm and the number of z slices to construct the 3D image was selected automatically by the software from the objective and magnification settings. The tests were undertaken five times in order to ensure repeatability.

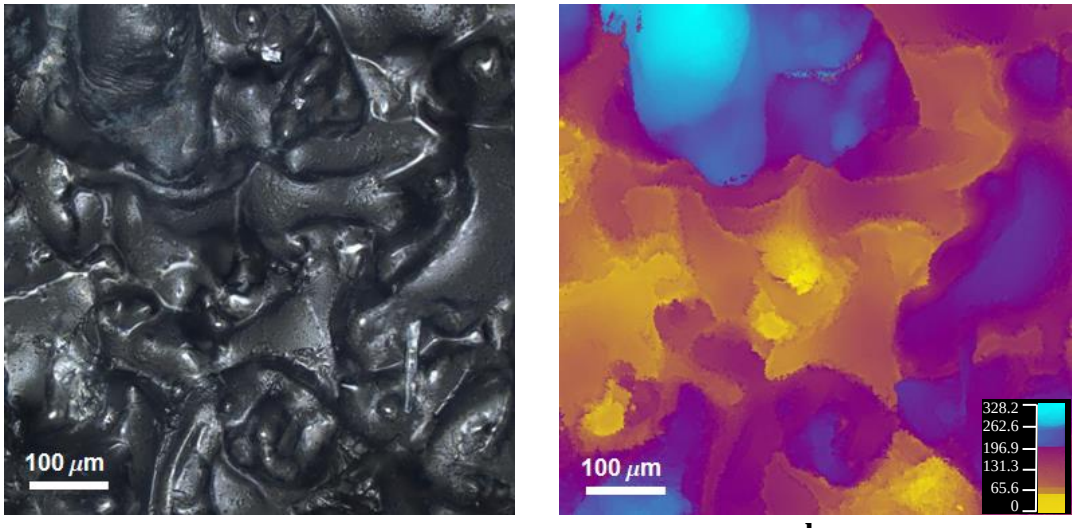

a **b**

Figure 5.1 Confocal laser scanning microscope images (644x642 μm) of uncoated TS1 surface a) surface topography b) using colour height information.

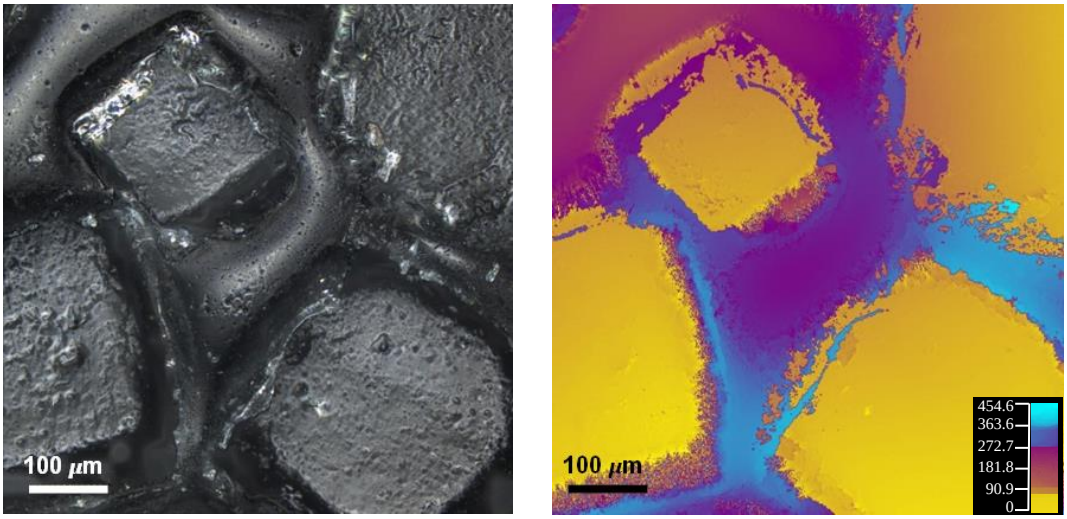

a **b**

Figure 5.2 Confocal laser scanning microscope image (644x642μm) of uncoated TS2 surface a) surface topography b) using colour height information.

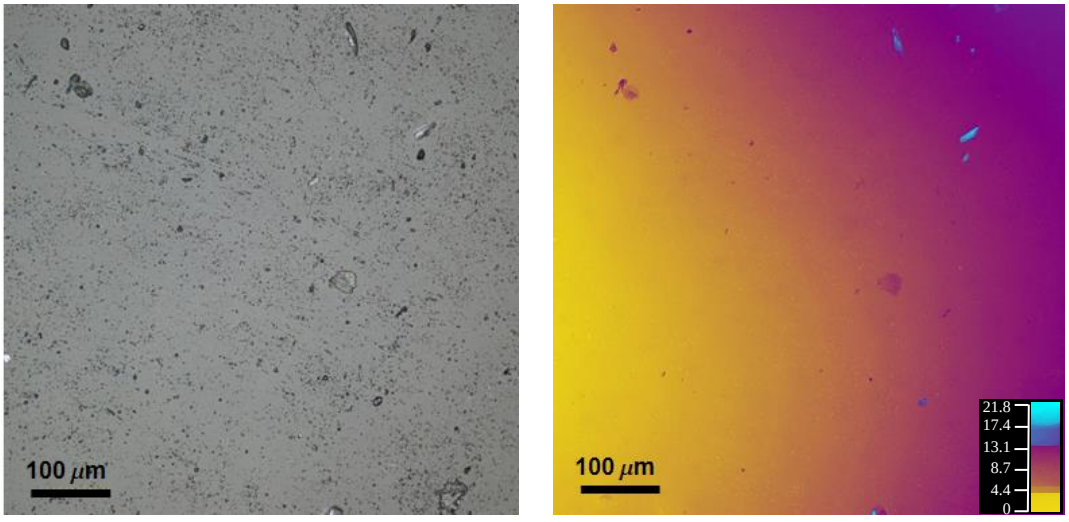

a **b**

Figure 5.3 Confocal laser scanning microscope image (644x642μm) of SS1 surface a) surface topography b) image using colour height information.

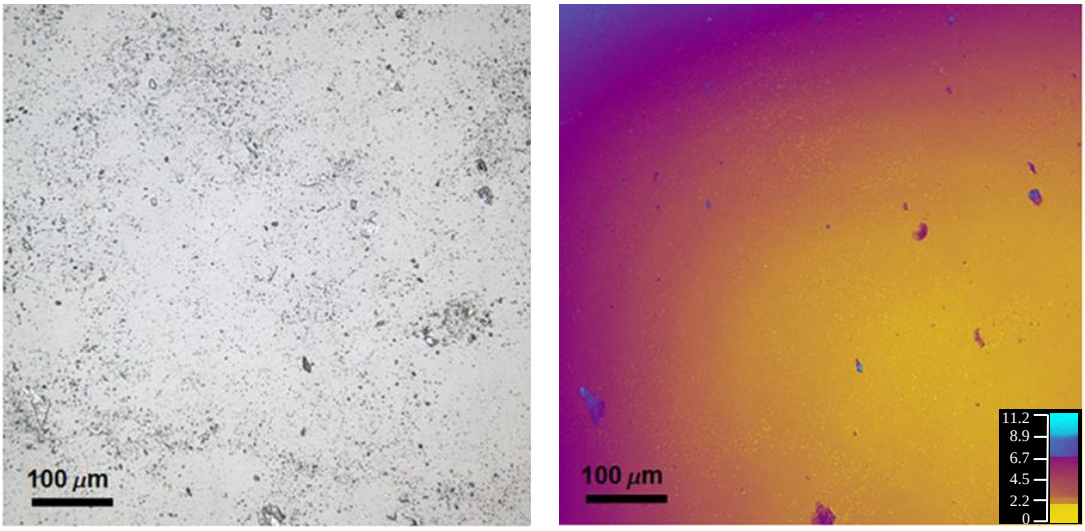

a **b**

Figure 5.4 Confocal laser scanning microscope image (644x642μm) of SS2 surface a) surface topography b) image using colour height information.

5.2.1.2 Surface roughness parameters

Surface texture measurements were carried out using the Olympus LEXT laser microscope (Olympus Corporation, Japan). The tests were carried out on three sample areas using a 100 μm scale. Roughness, skewness and kurtosis were measured in order to characterise the surface of the implants. Maximum values of peak height, valley depth and surface height of the surface were also obtained.

In addition, measurements of the core roughness of the surface, reduced peak height, reduced valley depth, load area ratio of reduced peak part to core part and load area ratio of reduced valley part to core part, were undertaken. Void volume parameters were ascertained for each sample of the implant surfaces, namely, the void volume at a valley region, void volume at a core part, actual volume at a peak region and actual volume at a core part.

The values of the surface roughness texture parameters were obtained by applying the Olympus LEXT laser microscope software to the scanned images. The cut-off length was chosen to be 80 μm as the dimensions of the scanned area were 644 x 642 μm.

5.2.1.3. Optical tensiometry—contact angle measurement

The technique of contact angle measurement used in this study is a direct measurement of the tangent angle at the three-phase contact point on a sessile drop profile. The contact angle of a drop of water on the textured (TS1 and TS2) and smooth (SS1 and SS2) implant surfaces was measured enabling a comparison to be made. Measurements were taken using a contact angle meter CAM 200 system (rame-hart instrument co, USA). The CAM 200 is a video camera based computer with a controlled contact angle meter that provides video capture of images for analysis. The DROPimage image analysis software package (ramé-hart instrument co, USA) was employed to calculate contact angle values from the images obtained from the CAM 200 system (Jopp et al., 2004). Figure 5.5 shows the profile views of a 10 μl drop of nuclease-free water on the implant sample surfaces. The baseline is shown to indicate where the droplet ends and the surface begins. The droplet shape was determined and from this the contact angles were calculated. The contact angle is the average of the right (θ_R) and left (θ_L) contact angles for the drop. Values are the average of 9 measurements.

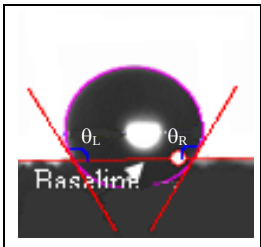	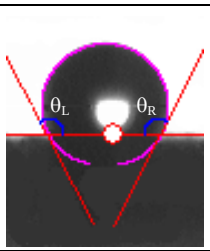	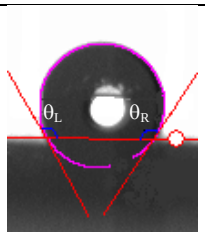	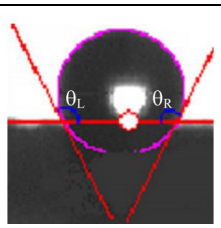
TS1	TS2	SS1	SS2
130 ± 2°	142 ± 2°	110.9°± 1.4°	111.8°± 1.2°

Figure 5.5 Contact angle values of the silicone sample surfaces measured using a Contact Angle Meter.

5.2.1.4. Micro tensile testing—measurement of bending and stretching stiffness.

In order to determine the mechanical properties of the breast implant surfaces a tensile test was carried out using a Microtest 5kN tensile testing device (Deben, UK). Figure 5.6a depicts the tensile-testing instrument used for this test. Three samples from each of TS1, TS2, SS1 and SS2 implants were tested. These samples had dimensions of 30 mm x 10 mm and their thicknesses varied from 0.45 to 0.75 mm. In order to carry out the test, a sample was mounted horizontally onto the machine. The sample was clamped by a pair of jaws leaving 10 mm length in the middle as gauge length. During the tensile test a dual screw pulled the jaws symmetrically in opposite directions (Figure 5.6b). The samples were stretched at a constant speed of 1.5 mm per minute up to 100% strain and force–elongation data was recorded every 200 ms. The tensile testing stage was computer controlled and the resulting force/displacement curves were displayed in real time. The force–displacement data were used to estimate the stiffness of the samples at biologically relevant strains.

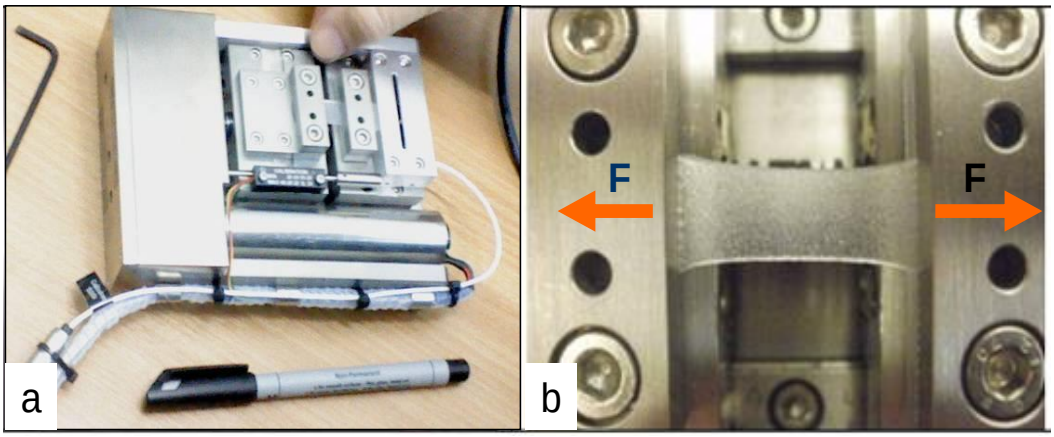

Figure 5.6 Tensile test of TS1 a) sample prior to testing b) sample during tensile testing.

For the purpose of characterisation of the breast implant surfaces, stiffness is a more suitable parameter than the Young's modulus (E), as stiffness includes the effect of implant thickness (t). Hence two stiffness parameters— stretching stiffness (k) and bending stiffness (D) (Fenner, 1989)—were estimated for the samples.

5.2.2 Kinetics of fibroblast–surface detachment mediated by trypsin

Cultured human skin fibroblasts were established from skin biopsies taken from a healthy subject. All cultures were passage three and were grown to confluence in 125 mL culture flasks in Dulbecco's Culture Medium (DMEM) substituted with 10% fetal bovine serum, 1% L-glutamine (PAA), 1% non-essential amino acid solution (Sigma) and 1% penicillin/ streptomycin (PAA) at 37°C in a 5% CO_2 atmosphere.

The cells were arrested to take them to the G0/G1 phase, 16 h later dissociated cell suspensions were seeded in triplicate on silicone surfaces placed in the tissue culture in 24 well-plates to a concentration of 5.1 x 10^4 cells in 1 mL of complete media per well and incubated for 24, 48 and 72 hrs at 37°C. After setting times the incubation media was discarded and the surfaces were washed once with PBS. 400 μl of 0.25% trypsin was added to each well. At 2-min intervals (from 5 to 17 min) a sample of 100 μl of trypsin was then removed from each well and replaced with 100 μl of fresh trypsin. The well plate was moved gently before taking the sample to homogenize it. The sample of trypsin was poured into an eppendorf tube and 200 μl of complete media was added to stop the trypsin reaction. The detached cells were then centrifuged and resuspended in 200 μl complete media and their number counted with a C6 flow cytometer (Accuri Cytometers, Inc., Michigan, U.S.A.). Wells of cells prepared for the zero-time point of trypsinisation were incubated in trypsin until they were completely detached. Cell-substratum detachment at a given time point was expressed as the percentage of detached cells relative to those detached at time zero. Each experiment was conducted in triplicate.

5.3 Results

5.3.1 Surface characterisation

5.3.1.1 3-D images

The 3-D images of the surfaces obtained using the LEXT OLS4000 3D laser measuring microscope are shown in Figures 5.1–5.4. The planar images obtained are depicted in Figures 5.1–5.4a; the corresponding topological models obtained using colour-height information are shown in Figures 5.1–5.4b. The images reveal the textured surfaces to be relatively rough and nodular, consisting of high peaks and deep crevasses, having roughness (Sa) values in the range 8.88–18.83 μm. The smooth implant surfaces are more regular and repetitive and less rough, exhibiting roughness (Sa) values in the range 0.06–0.07 μm.

TS1 implant

The TS1 shows high peaks and deep plunging crevasses (Figure 5.1). The topography reveals a rough surface composed of textured nodules. The texture is an outcome of the manufacturing process in which a negative-contact imprint of polyurethane foam is formed on the surface (Barr and Bayat 2011). The nodular outcrops are separated from one another by apparently smooth-surface crevasses. The surface is almost geographical with peaks that are frequently covered in silicone debris. Figure 5.1b shows the confocal laser scanning microscope image obtained using colour height information (taken on the Olympus LEXT with 20 x magnifications, image scale bar 100 μm). The yellow coloured areas indicate the valleys, which are from 0 to 66 μm deep, while the purple areas correspond to the core of the profile, which is between 132 and 197 μm in height. The peaks of the surface can be discerned by the blue coloured areas, which are 263 to 328 μm high. The image was captured as a 3D data set and the measurement of plane roughness on the entire surface (644x642μm) was taken. The average surface roughness measurement of 3 different areas was evaluated and an arithmetic mean roughness value of 8.88±0.5 μm was obtained.

TS2 implant

The TS2 depicts a granular surface which is pitted with cuboid shaped wells (Figure 5.2). These wells are formed by granular salt during the manufacturing phase, which are subsequently washed away (Barr and Bayat, 2011). The bases of these pits are irregular with ridges. The polyhedra are approximately 235–522 μm in width and the distance between them varies from 37 to 358 μm. Figure 5.2b shows the confocal laser scanning microscope image obtained using colour height information (taken on the Olympus LEXT with 20x magnification, image scale bar 100 μm). The valleys of the surface, shown in yellow, are from 0 to 91 μm deep. The purple coloured regions, which correspond to the core of the profile, are between 182 and 273 μm high. The peaks of the surface can be distinguished in blue, and range from 364 to 455 μm in height. The image was captured as a 3D data set and the measurement of plane roughness on the entire surface (644x642 μm) was taken. The average surface roughness measurement of 3 areas was evaluated and an arithmetic mean roughness value of 18.83±0.91 μm was obtained.

SS1 and SS2 implants

The SS1 and SS2 are characterised by an inherently regular, ridged topography; both surfaces depicted a geographical surface with rocky formations and small pits (Figures 5.3 and 5.4). The topography observed results from silicone creeping down the implant template during the curing process (Barr and Bayat, 2011). The arithmetic mean roughness was 0.07±0.01 μm for the SS2 and 0.06±0.02 μm for the SS1. Figure 5.3b shows the confocal laser scanning microscope image of SS1 surface obtained using colour height information (taken on the Olympus LEXT with 20x magnification, image scale bar 100μm). The deepest areas of the sample are shown in yellow and range from 0 to 4.4μm in depth, while the purple areas correspond to the core of the profile, which are from 8.7 to 13 μm high. The surface peaks are coloured blue and range from 17.4 to 22μm in height. The average surface roughness measurement of 3 areas was evaluated and an arithmetic mean roughness value of 0.06±0.02μm was obtained.

Figure 5.4b shows the confocal laser scanning microscope image of SS2 obtained using colour height information (taken on the Olympus LEXT with 20 x magnifications, image scale bar 100μm). The deepest areas of the sample are shown in yellow and range from 0 to 2.2μm in depth, while the purple areas correspond to the core of the profile, which are from 4.5 to 6.7 μm high. The surface peaks are coloured blue and range from 9 to 11μm in height. The average surface roughness measurement of 3 areas was evaluated and Sa of 0.07±0.01μm was obtained.

5.3.1.2 Surface roughness parameters

The roughness parameters of the textured and smooth samples were obtained using the LEXT OLS4000 3D laser measuring microscope. The maximum Sa was obtained for TS2 textured sample, which had a value of 18.83 μm and the lowest, 0.06 μm, was obtained for the SS1 surface. The values obtained for the additional roughness parameters are given in Figures 5.7 and 5.8.

The negative skewness value measured for the TS1 sample (Ssk=-0.22) indicates the predominance of valleys on this surface; the positive skewness values exhibited by the TS2 (Ssk=0.38), SS2 (Ssk=12.27) and the SS1 (Ssk=14.11) samples reveal that peaks are the prevailing characteristic on the surfaces of these samples.

The SS1 samples exhibited a relatively high kurtosis value (Sku=333.57) indicating a repetitive surface with spikes. The lower kurtosis values obtained for the TS1 (Sku=8.38), and TS2 (Sku=10.23) implants indicate that these surfaces are more random and bumpy.

The relatively large reduced peak height value obtained for the TS2 (Spk=62.75 μm), implies a surface composed of high peaks providing small initial contact area and

thus high areas of contact stress (force/area) when the surface is contacted. Thus reduced peak height may represent the nominal height of the material that may be removed during a 'running-in' operation. Consistent with reduced peak height, the load area ratio of reduced peak part to core part (SMr1) represents the percentage of the surface that may be removed during 'running-in'. The TS2 has the highest SMr1 value indicating that for this sample, a larger percentage of area would be removed once the implant was in place in the body. The core roughness measure indicates the roughness of the surface over which a load may be distributed after the surface has been 'run-in'. The TS1 has the highest core roughness value, Sk=17.52 μm, which is relatively high in comparison with the value obtained for the SS1, Sk=0.11 μm.

The reduced valley depth is a measure of the valley depth below the core roughness and may be related to fluid retention and debris entrapment. The implant surface which would potentially retain the greatest amount of fluid and debris is the TS2 sample, with Svk=58.67 μm and load area ratio of reduced valley part to core part, SMr2=74.19%. The implant that is likely to retain the least fluid is the SS2 surface, with Svk=0.17 μm and SMr2=86.94%.

The void volume parameters ascertained for the samples indicate that the TS2 surface can contain the largest volume of fluid, with Vvc + Vvv = 36.92 $\mu m^3/\mu m^2$ while the SS1 implant can only contain Vvc + Vvv = 0.07 $\mu m^3/\mu m^2$, the lowest value of all the samples considered. Of the four implant surfaces tested, the TS2 sample exhibited the highest value for the volume that may be worn away in the run-in period, having a Vmp value of 3.32 $\mu m^3/\mu m^2$. The TS2 textured sample has the greatest volume of material available to support load, with Vmc=14.04 $\mu m^3/\mu m^2$.

Table 5.1 3D Surface height parameters: skewness and kurtosis of breast implant surfaces.

Breast implant	**Skewness**		**Kurtosis**	
TS1	-0.22±0.27	Predominance of valleys	8.38±1.57	Random and bumpy surfaces
TS2	0.38±0.35	Predominance of peaks	10.23±0.26	
SS1	14.11±3.6		333.57±11	More repetitive surface with spikes
SS2	12.27±1.03		281.53±48	

Breast implant	Profile	Functional Parameters
TS1	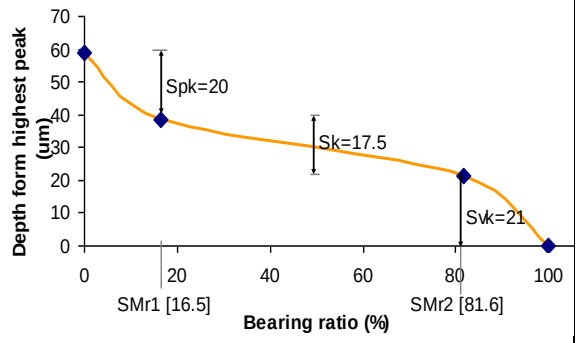	Sk(µm) 17.52±1.4 Spk(µm) 20.05±2.1 Svk(µm) 21.09±1.6 SMr1(%) 16.58±0.3 SMr2(%) 81.68±1.1
TS2	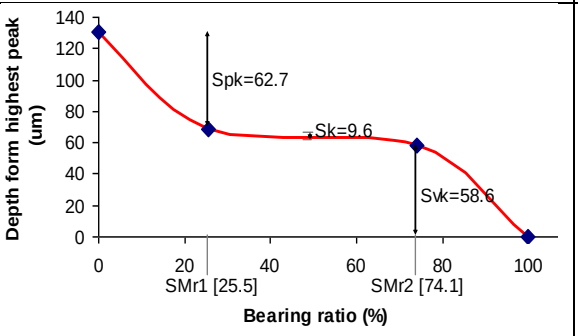	Sk (µm) 9.63±2.8 Spk (µm) 62.75±3.9 Svk (µm) 58.67±2.1 SMr1 (%) 25.50±0.7 SMr2 (%) 74.19±1.3
SS1	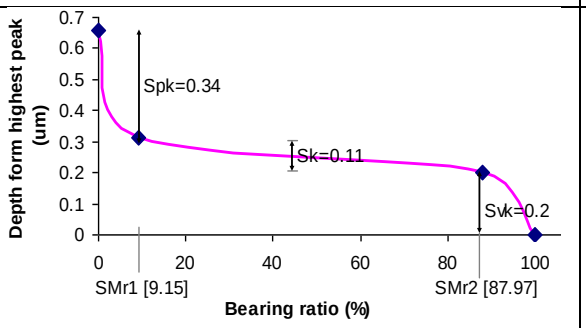	Sk (µm) 0.11±0.01 Spk (µm) 0.34±0.2 Svk (µm) 0.20±0.1 SMr1(%) 9.15±0.1 SMr2(%) 87.97±1
SS2	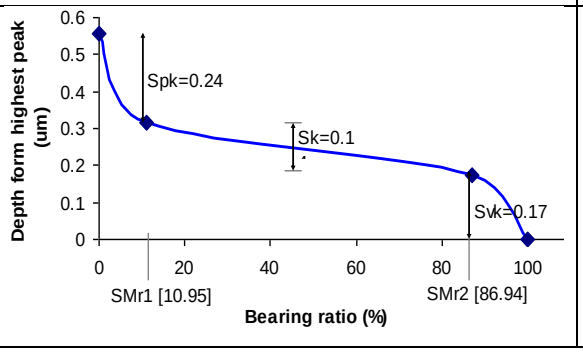	Sk (µm) 0.14±0.006 Spk (µm) 0.24±0.04 Svk (µm) 0.17±0.01 SMr1(%) 10.95±0.6 SMr2(%) 86.94±0.1

Figure 5.7 3D functional parameters: Spk (reduced peak height), Sk (core roughness depth), Svk (reduced valley depth), SMr1 (load area ratio to separate between a reduced peak part and a core part) and SMr2 (load area ratio to separate between a reduced valley part and a core part).

Breast implant	Profile	Material volume parameters ($\mu m^3/\mu m^2$)
TS1	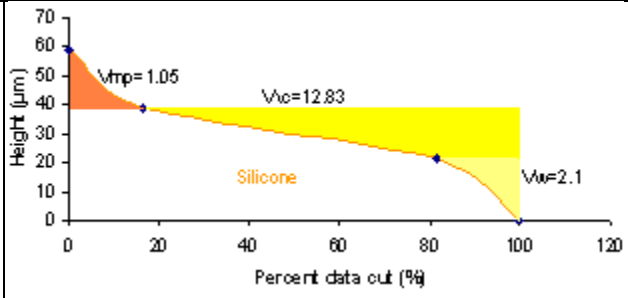	Vvv 2.1±0.16 Vvc 12.83±0.8 Vmp 1.05±0.13 Vmc 8.56±0.31 Vvc+Vvv 14.93 ±0.8
TS2	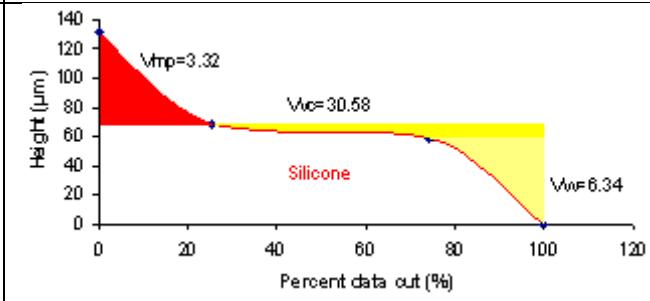	Vvv 6.34±0.39 Vvc 30.58±0.9 Vmp 3.32±0.36 Vmc 14.04±0.4 Vvc+Vvv 36.92±1.07
SS1	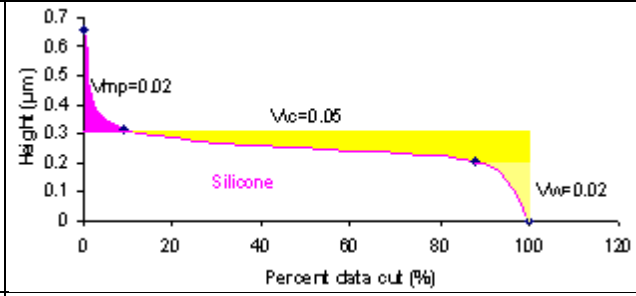	Vvv 0.02±0.01 Vvc 0.05±0 Vmp 0.02±0.01 Vmc 0.04±0 Vvc+Vvv 0.07±0.01
SS2	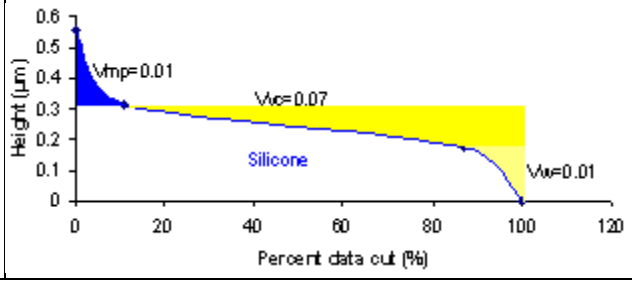	Vvv 0.01±0 Vvc 0.07±0 Vmp 0.01±0 Vmc 0.05±0 Vvc+Vvv 0.08±0

Figure 5.8 Bearing curves illustrating the core and valley fluid retention indexes of uncoated breast implants: Vvv (void volume at valley region), Vvc (void volume at a core part), Vmp (peak material volume) and Vmc (core material volume).

5.3.1.3 Wettability

The contact angle values obtained from the CAM 200 system using the DROPimage software package are given in Table 5.2, and Figure 5.5 shows profile views of a 10 μL drop of nuclease-free water on the implant sample surfaces. The baseline is shown to indicate where the droplet ends and the surface begins. The droplet shape was determined and from this the contact angles were calculated. From the measurements it was determined that the TS2 sample was the most hydrophobic surface, exhibiting a contact angle of 142 ± 2°. The SS1 sample was the least hydrophobic surface, having an average contact angle of 110.9°± 1.4°. The values indicate that the TS2 surface is less wettable than TS1.

5.3.1.4 Stiffness: Tensile test

The biologically relevant strain region is expected to be between 0 and 10% strain, and so the stretching stiffness (k), which is proportional to Young's modulus times the thickness (E x t), is approximated by the slope of the force–displacement curve. The uniaxial stress-strain relation is given by Hooke's law as

$$\sigma = E\epsilon \tag{5.1}$$

by substituting σ = F/A and ε = δ/*l* into Eq. (1)

$$F = EA\frac{\delta}{l} \tag{5.2}$$

The equation of a spring is given as $F=k\delta$

$$k = \frac{F}{\delta} \tag{5.3}$$

Substituting Eq. (2) in Eq. (3)

$$k = \frac{EA}{l} \tag{5.4}$$

Substituting $A=b\cdot t$ in Eq. (4)

$$k = E\frac{b}{l}t$$

For the experiments, *b* and *l* were fixed parameters; therefore, the stretching stiffness depends only from E and t as follows,

$$k \propto Et \tag{5.5}$$

All samples exhibited strongly non-linear force displacement behaviour. The mean force–displacement curves for each sample are shown in Figure 5.9. The stretching stiffness of the sample is the slope of the force–displacement curve. The mean stretching stiffness curves were obtained by differentiation of the polynomial fit equations and these are shown in Figure 5.10.

Poisson's ratio was considered as 0.5 (Johnston et al., 2014). The (19) bending stiffness (D) is given as

$$D \propto EI \tag{5.6}$$

The estimated stretching stiffness and bending stiffness for the samples are shown in Table 5.2. The variation in stretching stiffness can be attributed to the difference in thickness of the implant shells and in the manufacturing procedures for the different implants, whereas the variation in bending stiffness is primarily due to variation in thickness. The textured surfaces showed higher bending stiffness. Among all the surfaces, SS1 had the lowest thickness that resulted in the lowest bending stiffness. Besides the effect of surface roughness on fibroblast adhesion, the variation in thickness affects mechanical stiffness, which in turn may change the performance of breast implants.

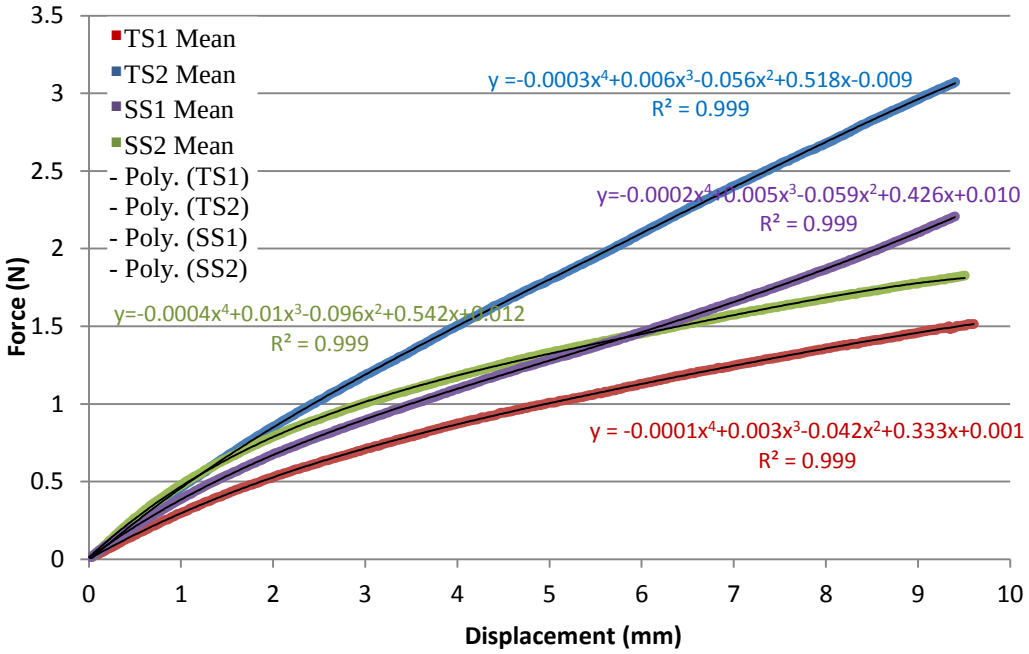

Figure 5.9 Mean force-displacement curves for all samples with fourth order polynomial fit lines and equations.

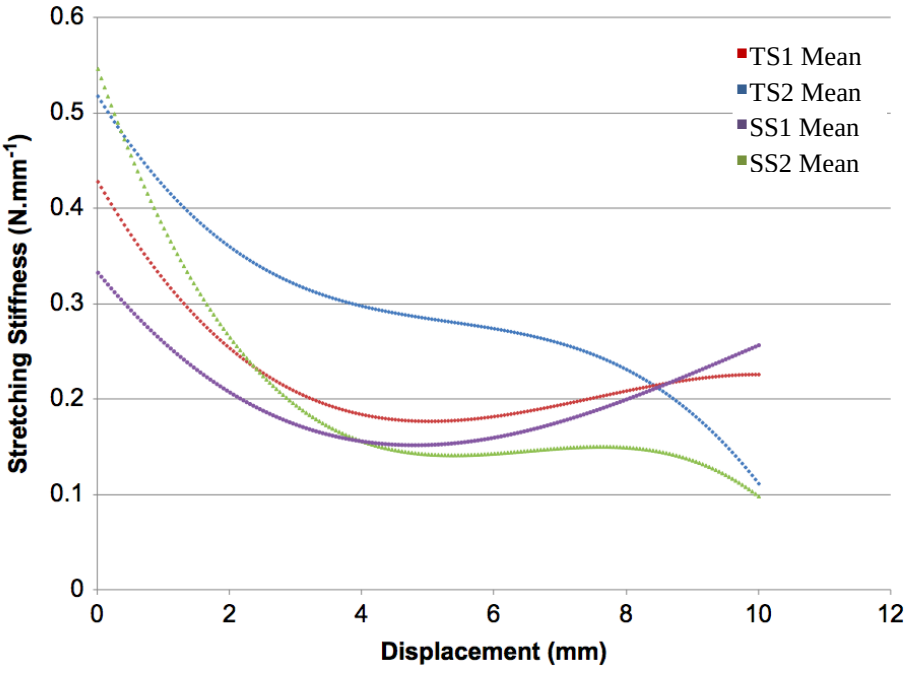

Figure 5.10 Mean stretching stiffness for all samples.

5.3.2 Kinetics of fibroblast–silicone implant surfaces detachment mediated by trypsin

This assay directly measures the number of cells that detach from the silicone surfaces following trypsinisation using the Accuri C6 flow cytometer (Accuri Cytometers, Inc., Michigan, U.S.A.). In three series of experiments at 24, 48 and 72 hrs incubation using cultures derived from healthy human skin, trypsin-induced detachment of normal cultured skin fibroblasts was scored at 2-min intervals. The resulting attachment values calculated are given in Figures 5.11-5.13 and in Table 5.2. Cell-substratum attachment at a given point in time is expressed as the percentage of attached cells relative to those attached at time zero. The results displayed are the mean percentage cell attachment derived from three experiments. Data was analyzed for significance using ANOVA. The difference between the means for all conditions was considered statistically significant at $P<0.05$ employing Prims-4 GraphPad software (San Diego, CA, USA). As expected, there was a decrease in the number of cells attached over time in all surface and a significant difference was detected in the trypsin-induced detachment rates between the smooth (SS1 and SS2) and textured (TS1 and TS2) silicone surfaces.

Upon inspection of Figure 5.11 it can be seen that after 24 hrs of incubation, there was a decrease in the number of cells attached over time as expected on all surfaces. Adhesion on the TS1, TS2 and SS2 samples did not differ significantly ($P>0.05$). Adhesion was significantly decreased on SS1 ($P<0.01$) surfaces compared with the textured surfaces.

Figures 5.12 and 5.13 indicate that after incubations times of 48 and 72 hrs, respectively, adhesion on the TS1, and TS2 textured samples did not differ significantly ($P>0.05$). In addition, there was no significant difference between the adhesion on the SS1 and SS2 samples ($P>0.05$). Adhesion on the smooth surfaces was significantly less than on the textured surfaces ($P<0.001$).

Overall, the figures indicate that the smooth surface samples (SS1 and SS2) generally exhibited lower initial adhesion than the textured surface samples (TS1 and TS2). Repeated measures two-way ANOVA on the cell attachment data with incubation time and surface texture as factors indicated that there was no significant main effect for incubation time but there was a highly significant main effect for surface texture P<0.0001).

Figure 5.14 shows that when the number of cells attached is averaged across both textured and smooth samples there is a clear difference in the rate at which cells are detached from the substrate. The linear nature of the relationship between the natural logarithm of the data and decay time indicates that cells detach in an exponential fashion. The decay constant for textured surfaces is approximately an order of magnitude smaller than for smooth surfaces (0.029 for textured compared with 0.29 for smooth).

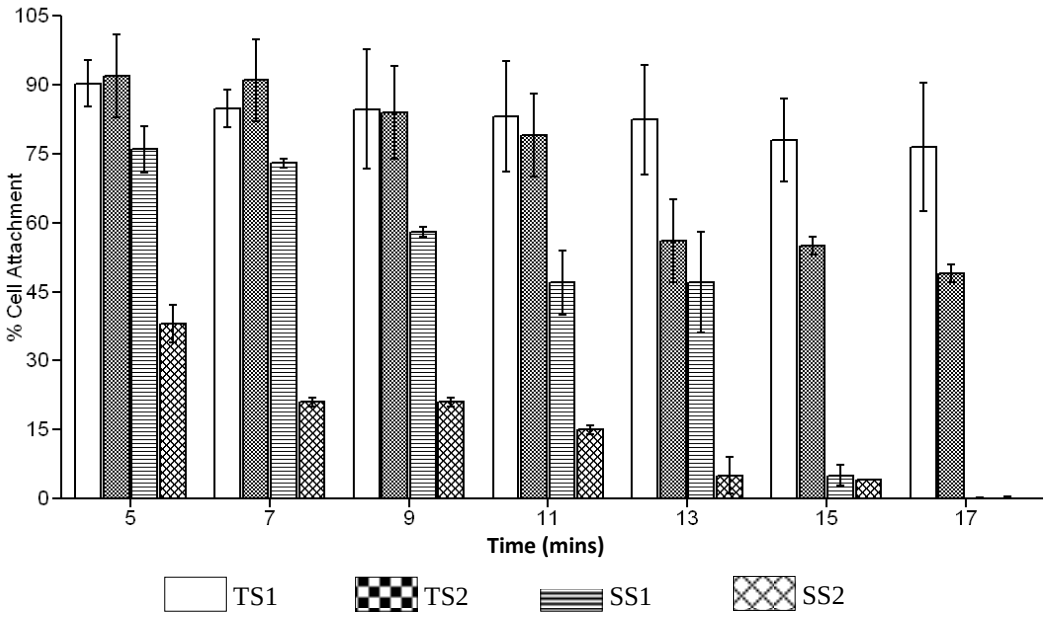

Figure 5.11 Comparison of normal skin fibroblast attachment to four implant surfaces after 24 hours of incubation.

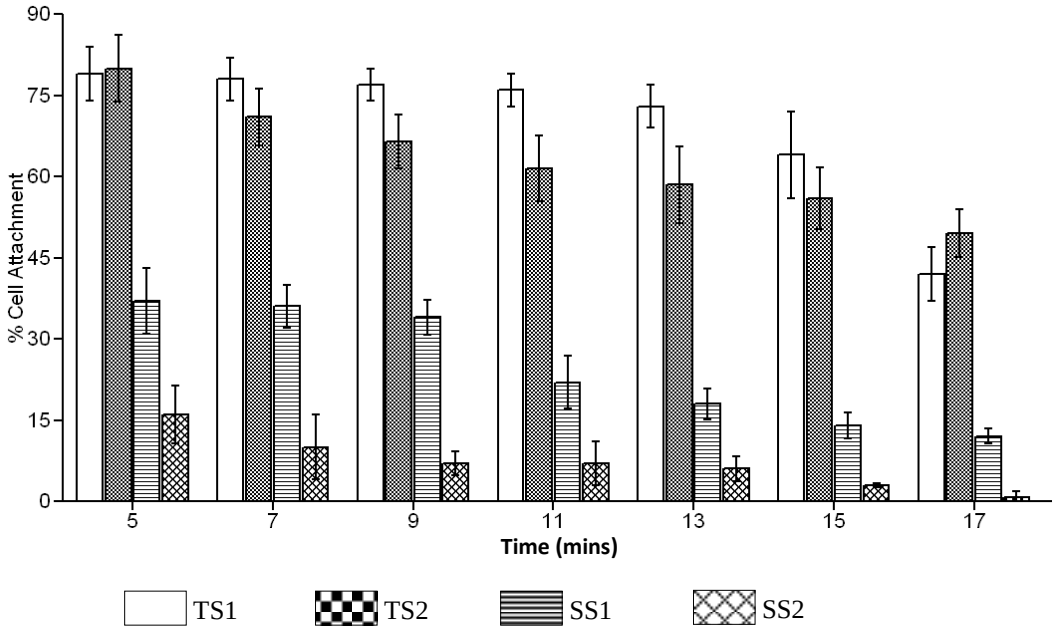

Figure 5.12 Comparison of normal skin fibroblast attachment to four implant surfaces after 48 hours of incubation.

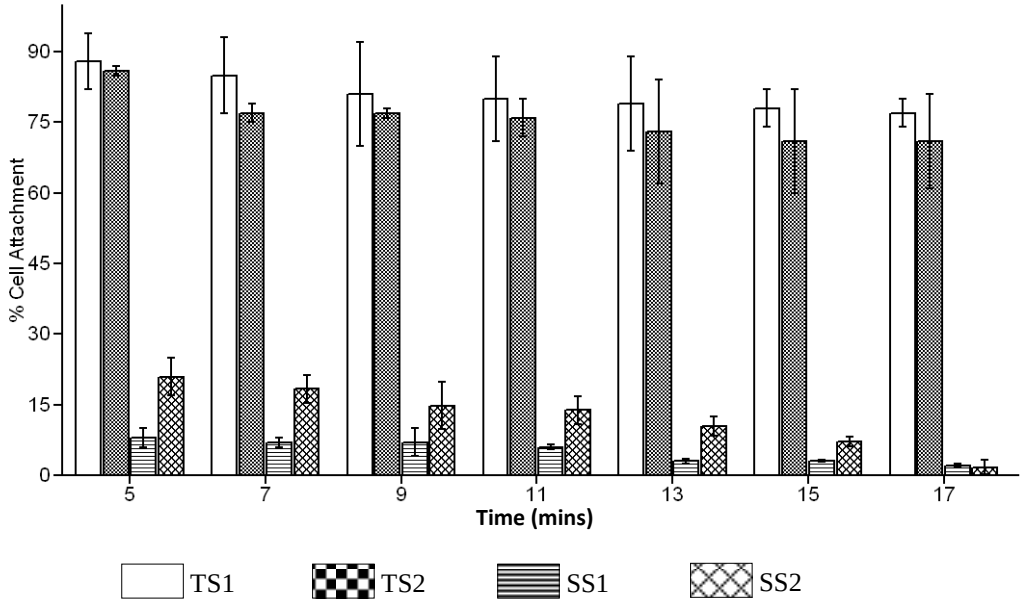

Figure 5.13 Comparison of normal skin fibroblast attachment to four implant surfaces after 72 hours of incubation.

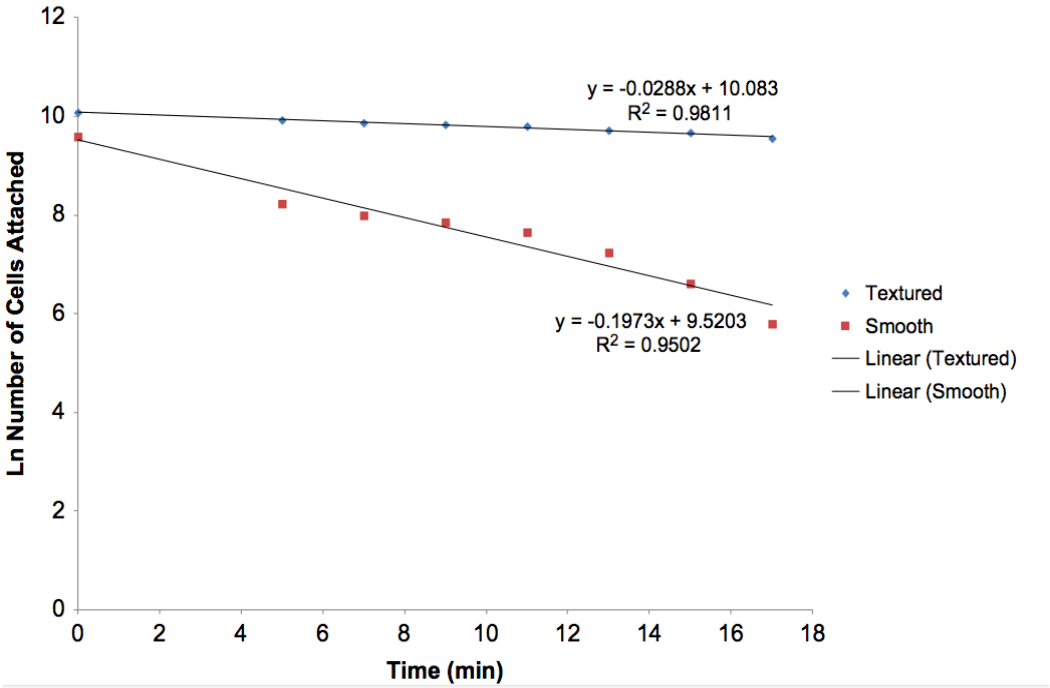

Figure 5.14 Ln of number of cells attached at each time point averaged over all textured and smooth samples.

Table 5.2 Summary of results

			TS1	TS2	SS1	SS2
LEXT OLS4000 3D Laser measuring microscope	Images Surface Features		Nodular textured surface	Granular surface, which is pitted with cuboid, shaped wells	Surface with small pits	Regular ridged topography
	Roughness S*a* (μm)		8.88±0.5	18.83±0.91	0.06±0.02	0.07±0.01
	Skewness		-0.22±0.27	0.38±0.35	14.11±3.6	12.27±1.03
	Kurtosis		8.38±1.57	10.23±0.26	333.57±108.06	281.5±48.03
	Core and Valley fluid retention ($\mu m^3/\mu m^2$)		14.93±0.84	36.92±1.07	0.07±0.01	0.08±0
Contact Angle 10μl			130 ± 2°	142 ± 2°	110.9±1.4°	111.8±1.2°
Thickness (mm)			0.71±0	0.74±0.04	0.45±0.02	0.51±0.01
Tensile Test	Stretching stiffness ($N\ mm^{-1}$)		0.37±0.03	0.47±0.03	0.29±0.02	0.46±0.05
	Bending stiffness ($N\ mm^2$)		0.19±0.02	0.26±0.02	0.06±0.01	0.12±0.01
% Cell Attachment	**24 hours incubation**	**5**	90	92	38	76
		7	85	91	21	73
		9	85	84	21	58
		11	83	79	15	47
		13	82	56	5	47
		15	78	55	4	5
		17	77	49	0	0
	48 hours incubation	**5**	79	80	16	37
		7	78	71	10	36
		9	77	66.5	7	34
		11	76	61.5	7	22
		13	73	58.5	6	18
		15	64	56	3	14
		17	42	49.5	0.66	12
	72 hours incubation	**5**	88	86	21	8
		7	85	77	18	7
		9	81	77	15	7
		11	80	76	14	6
		13	79	73	10	3
		15	78	71	7	3
		17	77	71	1.66	2

Kinetics of Attachment			
	24 hours of incubation	48 hours of incubation	72 hours of incubation
No differences were noted in fibroblast adhesion between	TS1, TS2 and SS2 (P>0.05).	TS1, and TS2 textured (P>0.05)	
		SS2 from SS1 (P>0.05).	
Fibroblasts adhesion was significantly lower on	SS1 (P<0.01) compared to the rough surfaces.	SS1 and SS2 (P<0.001) compared to the rough surfaces.	

5.4 Discussion

This study has accomplished an investigation into the characterisation of microstructure surface of commercially available breast implants. A variety of experimental techniques were employed including 3-D imaging, surface roughness and hydrophobicity measurement and micro tensile testing. In addition, experimental tests were undertaken in order to examine the kinetics of fibroblast-silicone surface detachment of the implants. The correlation between surface characteristics and fibroblast adhesion was analysed.

The 3-D imaging and surface roughness parameter measurement of the implant samples revealed the textured surfaces to be rough, nodular surfaces containing high peaks and deep crevasses. The magnitude of the skewness values obtained for the textured surfaces was relatively small indicating that the predominance of either valleys or peaks was weak in both of the samples. The SS1 and SS2 samples displayed surfaces with features that were less rough and more regular and repetitive than those of the textured surfaces. Peaks were the predominant feature on these smooth surfaces; however both the magnitudes of both peak height above and valley depth below the core roughness were relatively small compared to those of the textured surfaces.

The textured surfaces were significantly rougher than smooth surfaces exhibiting Sa measurements which were 130 - 320 times greater than the SS2and SS1 samples and a core roughness measure, Sk, that was between 69 and 160 times higher. In addition, the maximum surface heights of the textured surfaces were between 21 - 57 times greater than the smooth samples. Both maximum peak height and valley depth of the textured surfaces were significantly higher than the smooth samples, between 12 and 46 times for peak height and 56 - 98 times for valley depth.

The fluid retention indexes determined for the breast implant samples indicated that the smooth implant surfaces would require significantly less fluid than the textured samples to fill the surface voids. The contact angle measurements for water droplets placed on the sample surfaces revealed that the rougher the surface, the larger the contact angle and consequently the greater the hydophobicity (Figure 5.5). The textured surfaces exhibited higher roughness values, contact angles and hydrophobicity than the smooth sample surfaces.

The adhesiveness of human skin fibroblasts on the breast implant surfaces was analyzed in terms of the resistance to detachment with trypsin. In this study, the effect of surface roughness on normal skin cell adhesion was investigated on implant samples with Sa in the range 0.06 ± 0.02 to 18.83 ±0 .91 μm. The results show that fibroblasts adhere significantly better on the textured, rougher surfaces than on the smoother surfaces (Table 5.2). Lower levels of cell adhesion were observed on surfaces with roughness of 0.07 ± 0.01 μm and lower, while higher levels of cell adhesion were observed for the samples with Sa above 8 μm. At the end of the tests following 24 and 72 hours incubation the highest number of cells remained attached to the TS1 sample whereas following 48 hours incubation, the TS2 textured surface demonstrated the highest cell attachment. The TS1 sample exhibited higher average cell attachments than the TS2 sample over the test periods following incubations of 24, 48 and 72 hours. The skewness value obtained for the TS1 sample indicated a slight predominance of valleys in the surface topology, which is in contrast to the TS2 sample, where peaks predominate.

Comparing the kinetics of attachment after 24, 48 and 72 hours of incubation and the sample contact angle measurement measurements it was found that surfaces exhibiting contact angles of 130° and greater and Sa above 8 μm (TS1, TS2) provided greater rates of attachment compared to surfaces with contact angles less than 112° and Sa of 0.07μm and below (SS2, SS1). The rationale of this behaviour suggests that rough surfaces provide a greater area of attachment in comparison to the smooth ones because the cells are able to infiltrate the interstices of the textured

surfaces. Take into consideration that a typical fibroblast has the following dimensions 50 – 100 x 30 x 3 μm. The grooves of, for example, the TS2 textured implant surface are 52.02 - 358 μm width, so it is possible that many cells spread along these interstices. Additional studies are needed to evaluate cell attachment in the groove and ridge transitions in terms of the area of the adhesive contact and to study cell spreading in the micropatterns of these breast implants.

The results of the stiffness investigation revealed that although there was no clear hierarchy of stiffness among the implant types overall, the textured surfaces did tend to exhibit higher bending stiffness. Bending stiffness is related to change in implant shape whereas stretching stiffness is associated with change in implant volume under stress.

Chapter VI Physico-chemical characteristics of coated silicone textured versus smooth breast implants differentially influence breast-derived fibroblast morphology and behaviour

6.1 Introduction

In the previous chapter physical and mechanical characteristics of the breast implants that could influence cell-surface adhesion were studied. This is important because the breast implant surface is thought to interact directly with the breast tissue once inserted (Harvey et al., 2013). To successfully elicit specific cellular responses and direct new tissue formation, biological cues are created through the design of biomimetic scaffolds that modify biomaterials with ECM molecules (Shin et al., 2003).

The interaction of ECM proteins with cells via cell-surface integrin family receptors results in focal contacts; they provide support to cellular processes and maintain the tissue architecture. Cell spreading, adhesion, proliferation and migration are influenced by the signal transduction cascades initiated by the binding of an ECM molecule and integrin (Franz et al., 2011).

This chapter addresses the efficacy of different types of coatings on commercially available smooth and textured silicone breast implant surface topographies. To this end, the effect of four specific coatings on initial cell attachment, viability, proliferation and gene expression on these surfaces was investigated.

6.2 Materials and Methods

The study was conducted following two stages: the first stage consist of characterising the surface of silicone breast implants by measuring the arithmetic surface roughness and analysing the chemical composition, the second stage consisted of studying the *in-vitro* adhesive interactions of breast fibroblasts with implants surfaces in order to determine how implant surface textures and surface coatings affect specific functions of the cell directly involved in cell-surface adhesion. These stages are described in diagrammatic form in Figure 6.1.

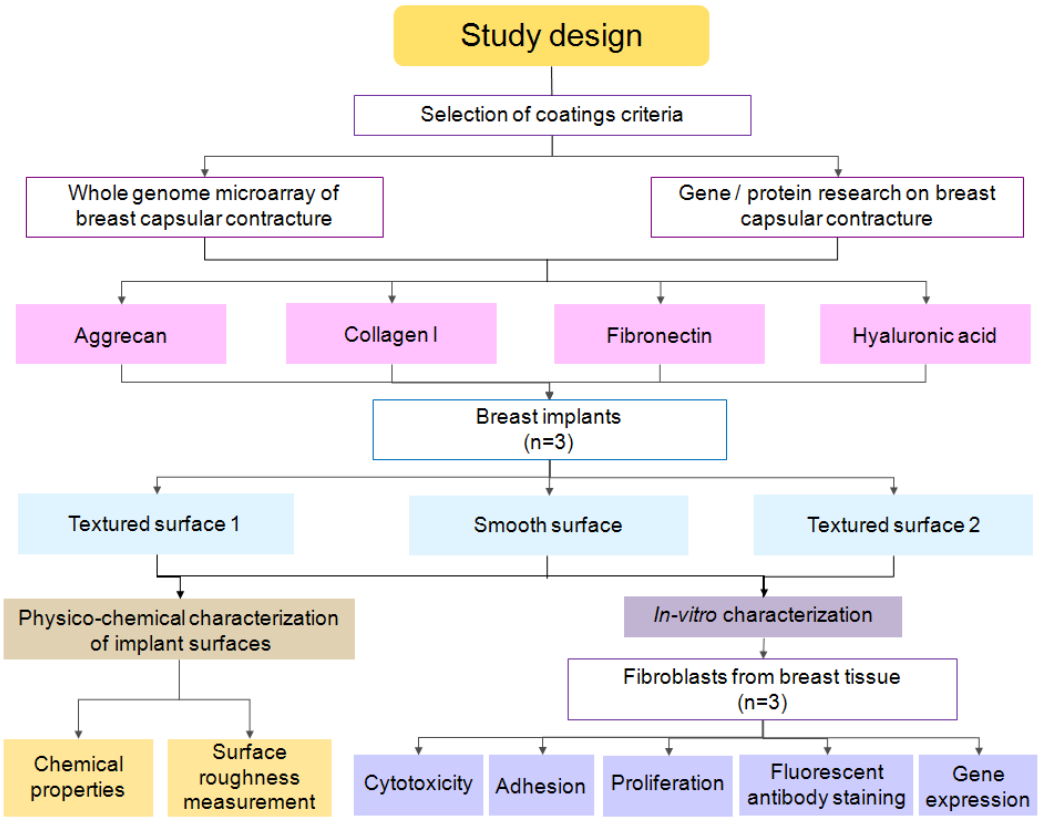

Figure 6.1 Study design to determine the implant surfaces physico-chemical characteristics and cell-surface behaviour *in-vitro*.

6.2.1 Sample preparation

The silicone breast implants studied were chosen from some of the commonly available implants (Figure 6.2) in clinical practice: (1) Textured Surface-1 (TS1) (TS1® (Mentor Worldwide LLC, Skyway Circle North Irving, Texas)); (2) Smooth

Surface (SS1) (Mentor® Smooth (Mentor Worldwide LLC, Skyway Circle North Irving, Texas)); (3) Textured Surface-2 (TS2) (Allergan Biocell® (Allergan, Inc, Santa Barbara, California)). Sample preparation was performed following the methodology of Valencia (Valencia-Lazcano *et al*., 2013). Surfaces were coated with either 5 μg/ml aggrecan (Sigma-Aldrich, USA), 5 μg/ml collagen type I (BD Biosciences, USA), 5 μg/ml fibronectin (Sigma-Aldrich, USA) or 10 μg/ml hyaluronic acid (Sigma-Aldrich, USA) solution and incubated for 1 h at 37 °C and washed twice with PBS (PAA laboratories, Austria).

6.2.2 Characterisation

Physical properties of smooth and textured breast implants were evaluated by looking at their topographical features using confocal laser microscopy following the procedure described previously by Valencia (Valencia-Lazcano *et al*., 2013). The procedure enables highly accurate 3D images of implant surfaces to be produced from which surface roughness parameter values can be obtained. Chemical characterisation was carried out recording Raman images and spectra of the implants using α300R equipped with a CCD camera, UHTS spectrometer, frequency-doubled Nd:YAG laser used for 532 nm excitation, and a Zeiss 50x air objective (N.A.=0.7) (Horiba, USA).

6.2.3 Cell culture

Cultured human breast tissue fibroblasts were established from tissue biopsies taken from healthy female patients (n=3) undergoing routine elective surgery. All patients had given full written and verbal consent for the use of discarded tissue for the experimental purposes of this ethically approved study. All cultures were passage 2 and were grown to confluence in 125 ml culture flasks in Dulbecco's Culture Medium (DMEM) (Sigma-Aldrich, UK) substituted with 10% fetal bovine serum (Sigma-Aldrich, USA), 1% L-glutamine (PAA laboratories, Austria), 1 % non-essential amino acid solution (Sigma-Aldrich, USA) and 1% penicillin/streptomycin

(PAA laboratories, Austria) at 37 ˚C in a 5 % CO_2 atmosphere. Prior to seeding the fibroblasts on the surfaces, fibroblasts were arrested to take them to the G0/G1 phase.

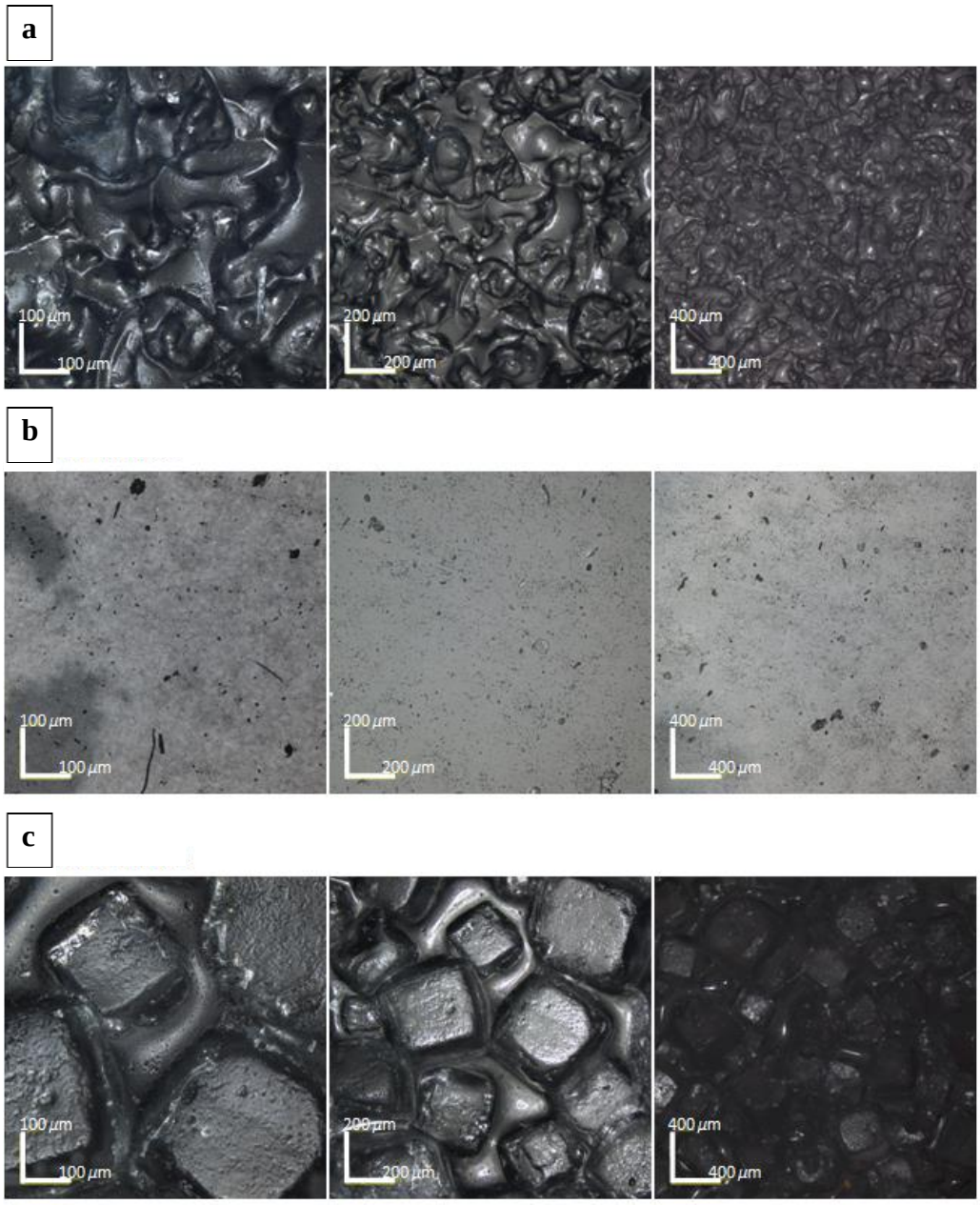

Figure 6.2 Confocal laser 3-D topography of silicone breast implants**.** (a) Textured Surface 1 (b) Smooth Surface, and (c) Textured Surface 2

6.2.4 Cytotoxicity

Cytotoxicity was tested after 24 hrs incubation; media from each well was aspired and centrifuged at 1600 rpm for 4 min. The media was transferred to a 96 well-plate at a volume of 100 μL per well by triplicate, and 100 μL of LDH (Roche, USA) was added to each well. The plate was protected from light and incubated at room temperature for 30 min. Absorbance was measured spectrophotometrically (Molecular Devices, USA) at a wavelength of 485 nm. The background absorbance of the multi-well plates was measured at 690 nm and this value was subtracted from the primary wavelength measurement. The number of replicates was 3 per surface; the control group corresponds to the uncoated surfaces.

6.2.5 Fibroblast adhesion to surfaces

Adhesion assay was tested after 2 hrs of seeding the fibroblasts onto the surfaces. Dissociated cell suspensions were washed twice with PBS (PAA laboratories, Austria) to be later re-suspended in media without serum. 5 μL of calcein AM solution (Molecular probes, USA) was added to a cell suspension of $5x10^6$ cells/ml and incubated at 37 °C for 30 min. The cells were washed twice with media and re-suspended in fresh media. The cells were seeded on breast implant surfaces in a 96 well plate in a final volume of 100 μL/well of the calcein-labelled cell suspension ($5x10^4$ cells) culture medium (Sigma-Aldrich, UK) and incubated for 2 h in a humidified atmosphere of 37 °C, 5 % CO_2. Non-adherent calcein-labelled cells were removed by washing four times with warm media (Sigma-Aldrich, UK); finally 200 μL of PBS (PAA laboratories, Austria) was added. Fluorescence was measured using a micro-plate reader (Molecular Devices, USA) at 485/538 nm. The percentage of cell adhesion was determined by dividing the corrected (background subtracted) fluorescence of adherent cells by the total of corrected fluorescence of cells added to each micro-plate well and multiplying by 100 %. The number of replicates was 3 per surface; the control group corresponds to the uncoated surfaces.

6.2.6 Fibroblast proliferation

Proliferation was tested after 24 hrs incubation in standard conditions, media from each well was aspired and 300 μL of fresh complete media (Sigma-Aldrich, UK) and 30 μL of water-soluble tetrazolium salt-1 (WST-1) cell proliferation reagent (Roche, USA) were added to each well. The well plate was wrapped in aluminium foil and placed in a shaker for 2 min at 55 rpm. After 4 h incubation in a humidified atmosphere of 37 °C, 5 % CO_2, media was removed and poured at 100 μL per well into a 96 well-plate. Absorbance was measured using a micro-plate reader (Molecular Devices, USA) at 450 - 690 nm. Cell proliferation was determined by subtracting the absorbance background control and the absorbance of 630 – 690 nm from the 450 – 500 nm measurement. Specific Absorbance = A475nm (Test) – A475nm (Blank) – A660nm (Test). The number of replicates was 3 per surface; the control group corresponds to the uncoated surfaces.

6.2.7 Immunofluorescence

Fluorescence staining of the actin (TRITC) (cytoskeleton), vinculin (FITC) (focal adhesion protein), and cell nucleus (DAPI) was performed using triple staining. Throughout the staining procedure, after 24 hrs of culture, media was removed from the well plate and the surfaces washed with PBS (PAA laboratories, Austria). Surfaces were covered with 10% formalin (Sigma-Aldrich, USA) overnight and washed with PBS (PAA laboratories, Austria). Surfaces were covered with 0.1 % Triton X-100 (Sigma-Aldrich, USA) for 10 min. Each sample was washed twice with PBS (PAA laboratories, Austria) (5min each), then covered with blocking buffer (LI-COR Biosciences, USA) for 30 min, and washed twice with PBS (PAA laboratories, Austria) (5 min each). The surfaces were labelled with 1st antibody ab2264 rabbit polyclonal to paxillin (abcam, UK) at a concentration of 1:100 overnight at 4 °C. Surfaces were washed 3 times with 0.1 % Tween 20/PBS (5 min each). Surfaces were labelled with Secondary antibody Alexa Fluor® 488 dye (abcam, UK) 1:500 dilution for 100 min at room temperature. Surfaces were washed 3 times with 0.1 % Tween 20/PBS (Fisher Scientific, USA) (5min each). The surfaces were labelled

with 4',6-diamidino-2-phenylindole (DAPI) (Molecular probes, USA) for 15 min then washed with 0.1 % Tween 20/PBS (Fisher Scientific, USA) for 5 min.

The surfaces were labelled with rhodamine-phalloidin 1:1000 (Sigma-Aldrich, USA) for 40 min at room temperature then washed once with PBS (PAA laboratories, Austria), and washed twice with 0.1% Tween 20/PBS (Fisher Scientific, USA) (5 min each), then finally being washed twice with PBS (PAA laboratories, Austria). Surfaces were mounted with ProLong® Gold antifade reagent (Invitrogen, USA), and covered with aluminium paper and stored at -4 °C. Immunofluorescence microscopy was carried out using a DeltaVision deconvolution system softWoRx v3.4.5 (Applied precision, USA) which consists of an Olympus IX-70 inverted microscope with an epi-fluorescence attachment. The images were obtained at 512 x 512 pixels with a magnification of 100x. Images were analyzed using softWoRx v3.4.5 and Image-J software (NIH, USA).

6.2.8 Quantification of gene adhesion expression

6.2.8.1 RNA extraction

After 24 hrs of culture, total RNA was extracted from each specimen by adding 500 μL of Trizol reagent (Invitrogen Ltd, UK) for 2 min. Trizol was aspired and transferred to an eppendorf tube and 350 μL of chloroform (Fisher Scientific, USA) was added; the tube was shaken and centrifuged at 14500 rpm for 15 min. Three layers were formed and the upper layer was aspired and transferred into an eppendorf tube; an equal amount of ethanol 80 % (Fisher Scientific, USA) was added and mixed by pipetting it and poured into an RNeasy mini spin column. After 15 s of centrifugation, supernatant was poured away and 600 μL of RWT buffer (Qiagen, Netherlands) was added. Centrifugation was performed for a further 15 s then the column was placed into a collection tube and 500 μL of RPE buffer (Qiagen, Netherlands) was added; this was then centrifuged for 15 s. Supernatant was poured away and the column was centrifuged for 1 min at 15000 rpm. The column was

placed into an eppendorf tube and 25 μL of RNease-free water (Qiagen, Netherlands) was added to the top layer and left for 1 min at room temperature before centrifugation at 15000 rpm for 1min. RNA concentration and purity was determined using a UV-Vis spectrophotometer (NanoDrop, USA) by absorbance measurements.

6.2.8.2 cDNA Synthesis

The quantity of nuclease free water was calculated based on RNAs (100ng) concentration to make a 20 μL solution, 4 μL of cDNA super mix (Quanta Biosciences, USA) was poured into an eppendorf tube, RNease-free water (Qiagen, Netherlands) was added and finally mRNA was added. The tube was centrifuged for 30 s and incubated at 25 °C for 5 min. Synthesis conditions comprised an initial cycle at 42 °C for 1 h and one cycle at 85 °C for 5 min to inactivate the enzyme and finally the solution was diluted in 180 μL of nuclease free water (Ambion, USA).

6.2.8.3 Quantitative real-time polymerase chain reaction

The primers used to amplify the selected genes using real time qPCR were designed using Universal ProbeLibrary (Roche, USA). Reactions were set up in a total volume of 10 μL using 4 μL of cDNA, 5 μL probes master (Roche, Germany), 0.7 μL RNease-free water (Qiagen, Netherlands) and 0.1 μL each of gene-specific primer (Table 1) and performed in a LightCycler® 480 Real-Time PCR System (Roche, Germany). The cycling conditions were: 95 °C for 10 min; 45 cycles of 95 °C for 10 s, 60 °C for 30 s and 72 °C for 1 s with a single fluorescence measurement; cooling was set at 40 °C for 30 s. Specificity of the PCR products was confirmed by analysis of the dissociation curve.

6.2.9 Statistical analysis

Statistical analysis was performed using the Prism v.5.0 software package for Windows (GraphPad Software, Inc., USA), applying the two-way ANOVA test. When the *p*-value was less than 0.05; the difference was regarded as statistically significant.

Table 1 Sequences of primers used for adhesion related genes using quantitative real-time polymerase chain reaction

Gene/Primer	Gene ID	Sequence 5' to 3'	Primer Position	Amplicon Size (bp)
(ACTN1) Alpha-actinin L	nm_001102.3	ctgttccagccatccttcat	834-853	70
(ACTN1) Alpha-actinin R	nm_001102.3	tcatgatgctgttgtaggtggt	882-903	70
(VCL) Vinculin (VCL) L	nm _014000.2	ggaggtgattaaccagccaat	2767 - 2787	88
(VCL) Vinculin (VCL) R	nm _014000.2	aatgatgtcattgcccttgc	2835 - 2854	88
(PXN) Paxillin L	nm _002859.3	cccagtgtggagagtctcttg	785 - 805	81
(PXN) Paxillin R	nm _002859.3	ctcgccctggttcacagt	848 - 865	81
(ptk2) Protein tyrosine kinase L	nm_153831.2	gtctgccttcgcttcacg	73 - 90	77
(ptk2) Protein tyrosine kinase R	nm_153831.2	gaatttgtaactggaagatgcaag	126 - 149	77

6.3. Results

6.3.1 Physico-chemical characterisation of smooth versus textured implants

Raman spectra showed all implants have the typical Raman spectrum of pure PDMS at the 490 cm^{-1} the Si-O stretch and 713 cm^{-1} the Si-C stretch modes. TS1 and SS1 possess a similar profile (Figure 6.3), while confocal laser microscopy showed different arithmetic mean surface roughness (Sa) between these two implants: TS1 is 8.88 μm rough while SS1 is 0.06 μm. TS1-SS1 and TS2 implants showed different profiles and intensity levels (Figure 6.3).

Sa was modified by coating the surfaces with specific protein, PG, and GAG coatings. In this case, the same coating procedure was performed on all surfaces, thus the changes in roughness were likely due to the interactions between implant topography and the coating structure. The surface features of the different breast implants after coating with aggrecan, collagen I, fibronectin, and hyaluronic acid were assessed using confocal laser scanning microscopy. 3D topological models were obtained using colour-height information from planar images of the implant sample surfaces (Valencia-Lazcano et al., 2013). Figures 6.4 (a) - (c) show the 3-D topography of the uncoated silicone breast implants (a) TS1, (b) SS1, and (c) TS2, were used as the control. The Sa measurements for both the coated and uncoated implant surfaces are shown in Figure 6.5 (a), where upon inspection it can be seen that significant differences ($p < 0.001$) exist among the TS1, SS1 and TS2. Coated surfaces of TS1 were found to be significantly rougher ($p < 0.001$) than the uncoated ones Figure 6.5 (b). SS coated with collagen I, fibronectin and hyaluronic acid were significantly rougher ($p < 0.01$) compared to the uncoated surfaces; however, no significant difference in Sa was observed between the aggrecan coated and uncoated SS1 (Figure 6.5 (c). TS2 coated with fibronectin and hyaluronic acid were found to be significantly rougher ($p < 0.05$) in comparison to the uncoated surfaces. No significant differences were found in the roughness values of uncoated, aggrecan and collagen I coated TS2 (Figure 6.5 (d).

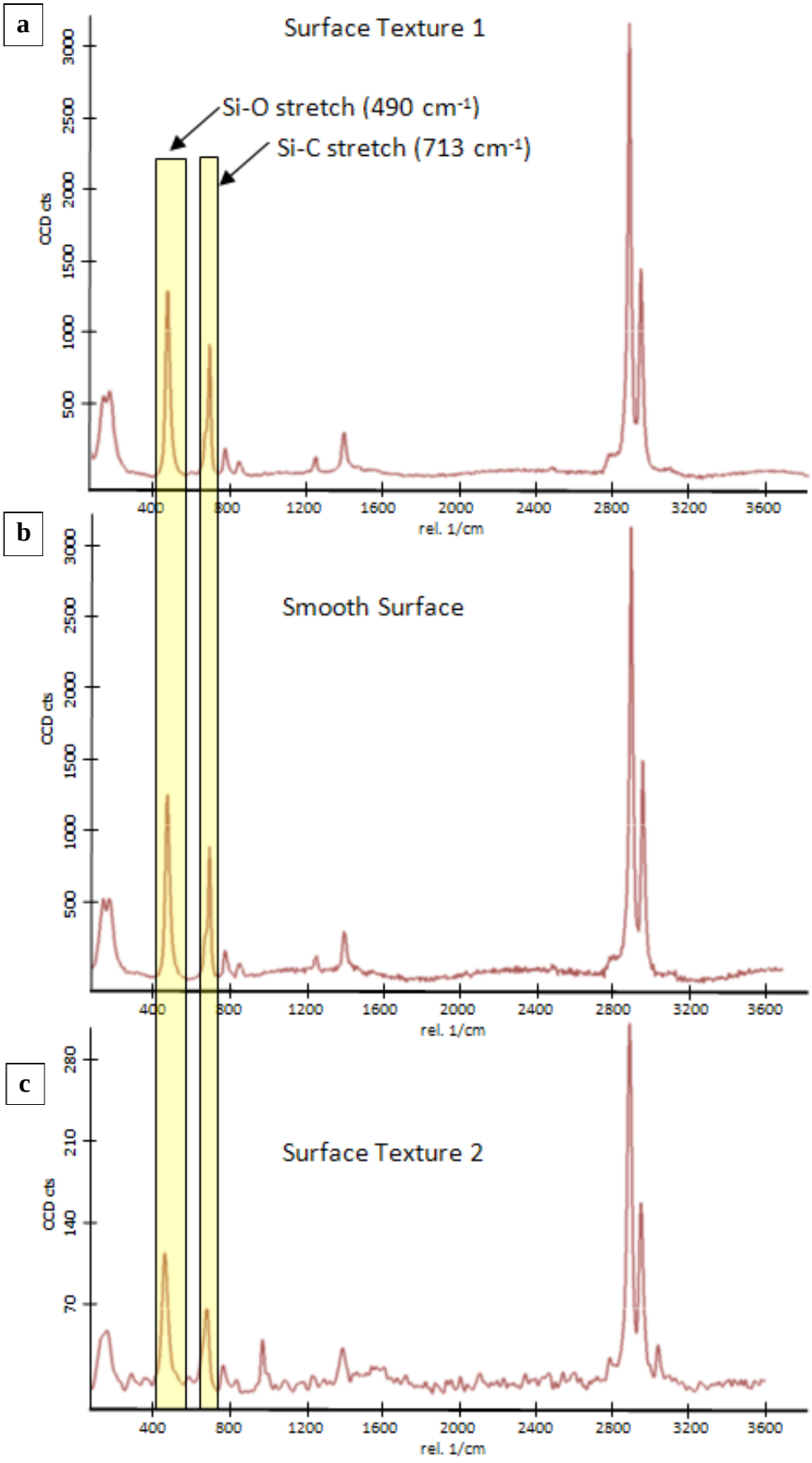

Figure 6.3 Raman spectra of silicone breast implants

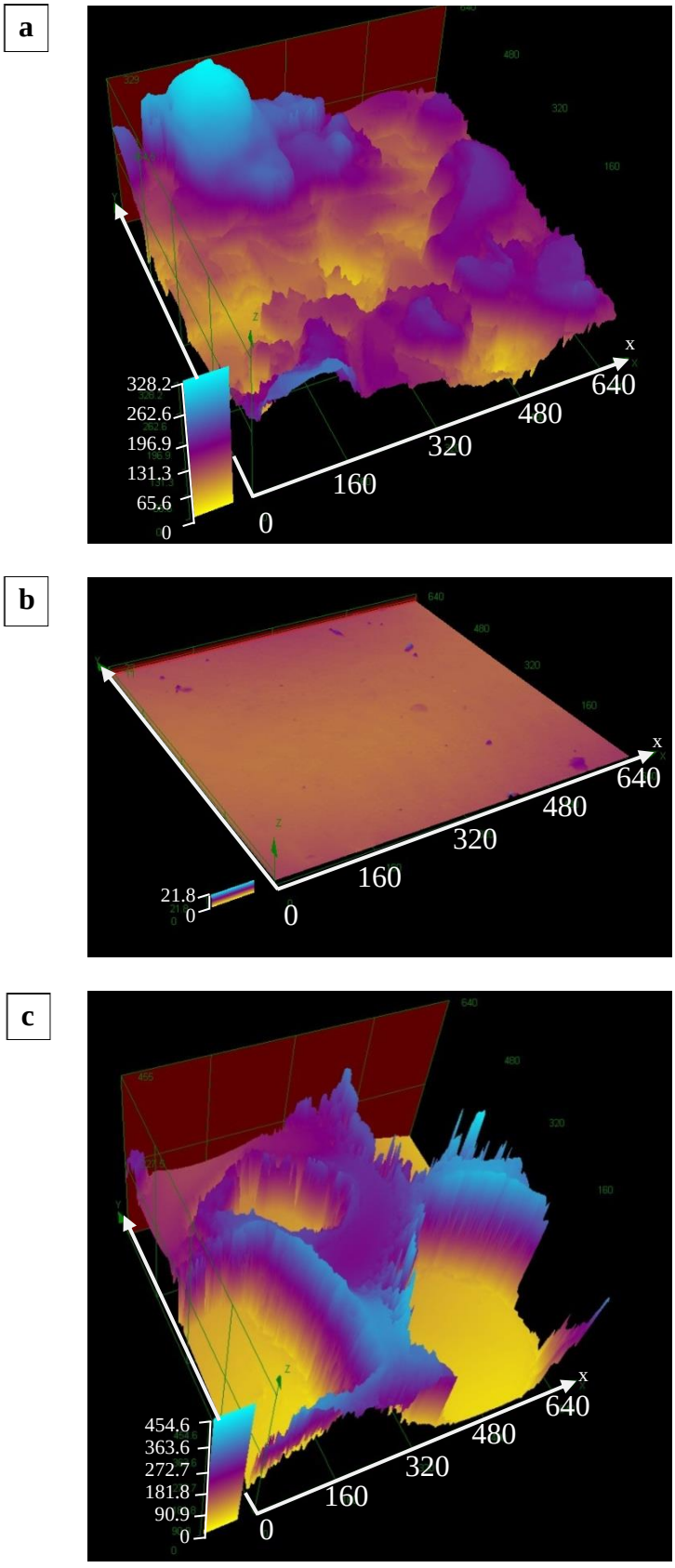

Figure 6.4 Confocal laser 3-D topography of silicone breast implants. Confocal laser 3-D topography of silicone breast implants using colour height information (644 x 642 μm). (a) Textured Surface 1, (b) Smooth Surface, and (c) Textured Surface 2.

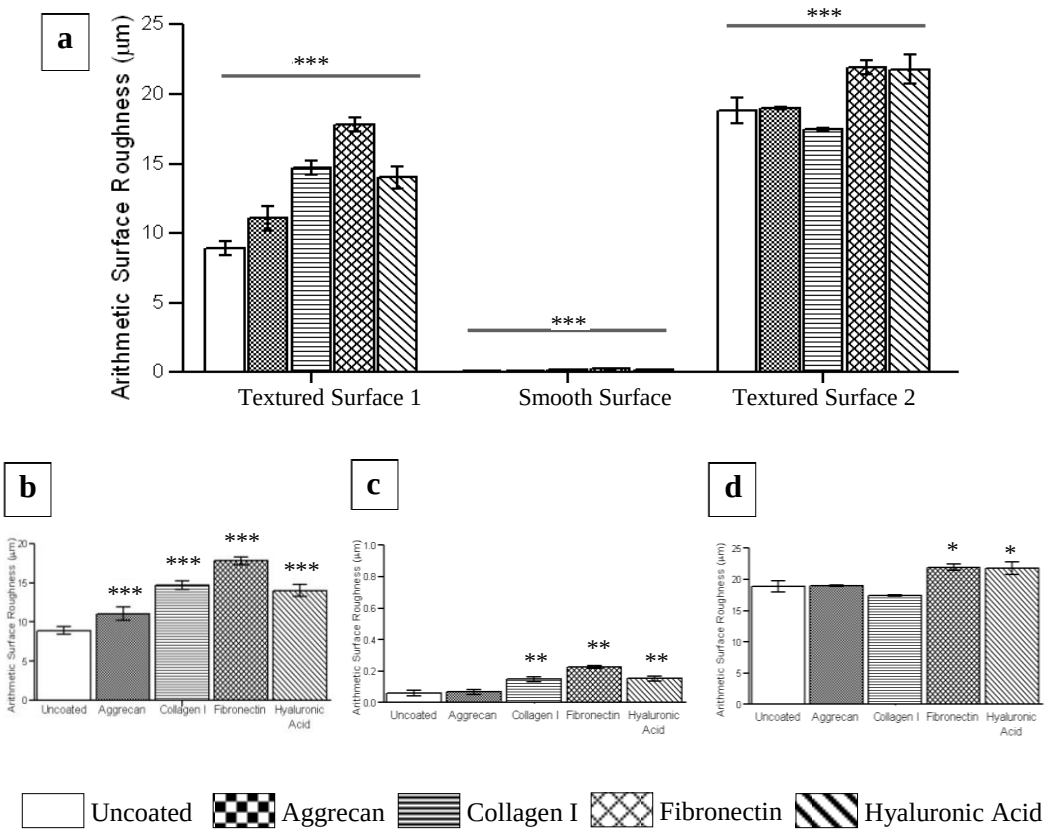

Figure 6.5 Changes in Sa of the modified coated surfaces examined by confocal laser microscopy. (a) Comparison of measured Sa among the three implants showed statistical significant differences between them ($p < 0.001$). Comparison of measured Sa among uncoated and coated (b) Textured Surface 1, (c) Smooth Surface, and (d) Textured Surface 2. Statistical analysis was performed applying the two-way ANOVA test. When the *p*-value was less than 0.05, the difference was regarded as statistically significant (*p<0.05, **p<0.01, ***p<0.001).

6.3.2 Cytotoxic effect of specific coatings on breast fibroblasts

After 24 hrs of seeding breast fibroblasts onto uncoated TS1, SS1 and TS2 and surfaces coated with aggrecan, collagen I, fibronectin, and hyaluronic acid, lactate dehydrogenase (LDH) activity in the culture media was used as an indicator of cell membrane integrity and thus a measurement of cytotoxicity (Figure 6.6). The results presented in Figure 6.6 reveal that SS1, TS1 and TS2 coated with aggrecan showed a significantly higher (p<0.001) cytotoxicity compared with the corresponding uncoated surfaces. A decrease in cytotoxicity was found on TS1 coated with collagen I (p<0.01), fibronectin (p<0.01) and hyaluronic acid (p<0.001) when compared with

uncoated TS1. No significant difference was found between the cytotoxicity values of SS1 and TS2 coated with collagen I and fibronectin compared with the uncoated SS1 and TS2, however, the cytotoxicity of the hyaluronic acid coated surfaces were significantly lower ($p<0.001$) than the uncoated surfaces.

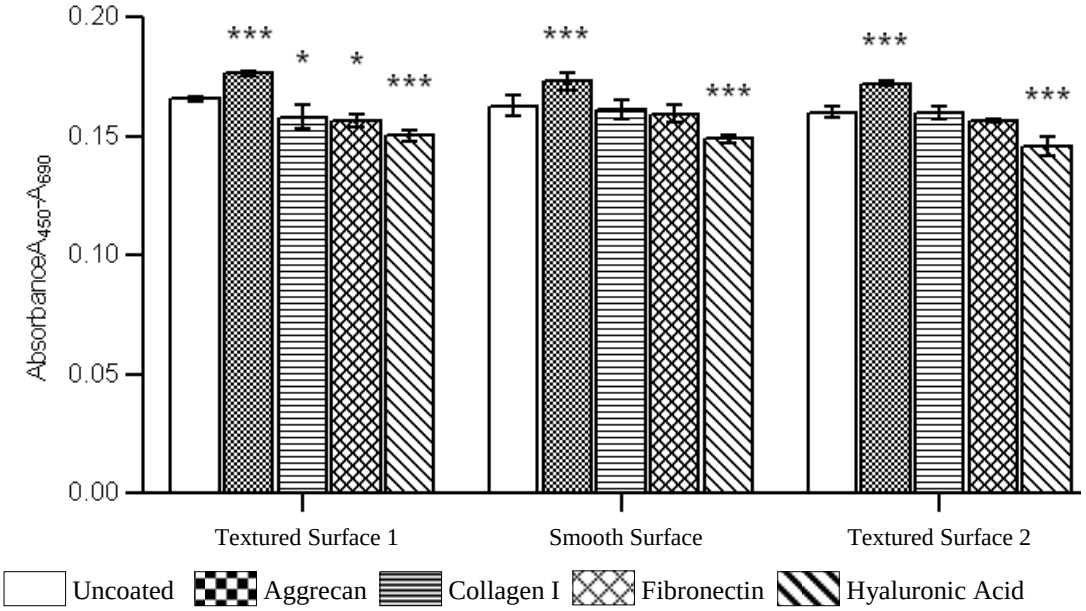

Figure 6.6 Cytotoxicity was evaluated by the quantification of plasma membrane damage by measuring the LDH activity in the 24 hrs cultured supernatant of breast-derived fibroblasts. Data shows mean ± standard deviation. Statistical analysis was performed applying the two-way ANOVA test; when the *p*-value was less than 0.05, the difference was regarded as statistically significant (*$p<0.05$, **$p<0.01$, ***$p<0.001$).

6.3.3 Effect of specific coatings on breast fibroblast attachment

A Calcein AM cell adhesion assay was used to measure the adhesion of calcein-labeled breast fibroblasts to uncoated TS1, SS1 and TS2 and surfaces coated with aggrecan, collagen I, fibronectin, and hyaluronic acid (Figure 6.7). Cell adhesion was found to be lower for fibroblasts on the smooth surfaces compared to the textured ones ($p<0.001$). Cell adhesion was significantly higher on collagen I, fibronectin and hyaluronic acid coated implants compared to the corresponding uncoated surfaces ($p<0.001$). Cell adhesion was highest (89%) for collagen I coated TS1 and TS2 and

fibronectin coated TS2 (87%). No significant difference was found between fibroblast adhesion to aggrecan coated implants compared to the corresponding uncoated surfaces (p>0.05).

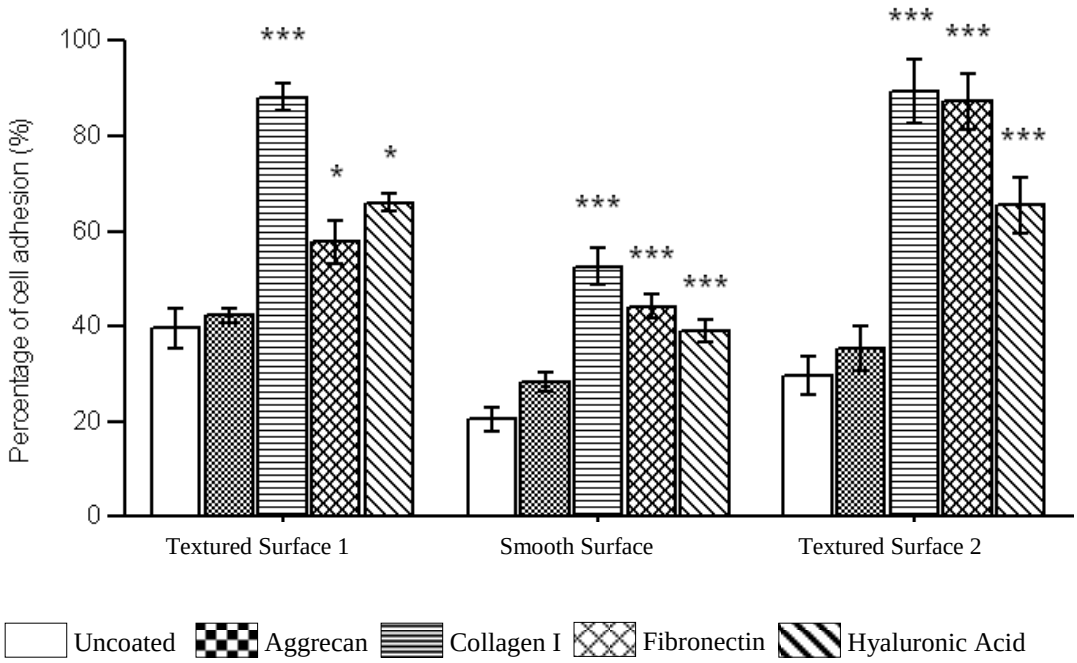

Figure 6.7 Effect of specific coatings on fibroblast attachment. Textured Surface 1, Smooth Surface, and Textured Surface 2 were coated with aggrecan, collagen I, fibronectin, and hyaluronic acid. Calcein AM cell adhesion assay was used to compare breast fibroblasts attachment after 2 hrs compared to control cultures grown onto uncoated Textured Surface 1, Smooth Surface, and Textured Surface 2. Statistical analysis was performed applying the two-way ANOVA test; when the p-value was less than 0.05, the difference was regarded as statistically significant (*p<0.05, **p<0.01, ***p<0.001).

6.3.4 Effect of specific coatings on cell proliferation

Proliferation of breast fibroblasts seeded for 24 hrs on TS1, SS1 and TS2 coated with aggrecan, collagen I, fibronectin, and hyaluronic acid was quantified using a water-soluble tetrazolium salt-1 (WST-1) cell proliferation assay and compared with control cultures grown on uncoated TS1, uncoated SS1 and uncoated TS2 (Figure 6.8). On smooth surfaces, fibroblasts proliferation rates were lower compared to the

textured surfaces for both the coated and uncoated surfaces ($p<0.001$). Cell proliferation was significantly higher for fibroblasts seeded on collagen I, fibronectin and hyaluronic acid coated implants compared to the corresponding uncoated surfaces ($p<0.001$). The highest cell proliferation rate (0.8) was found in collagen coated TS1, followed by 0.71 for fibronectin coated TS1. Lower proliferation rates were measured on uncoated and aggrecan coated surfaces ($p<0.001$).

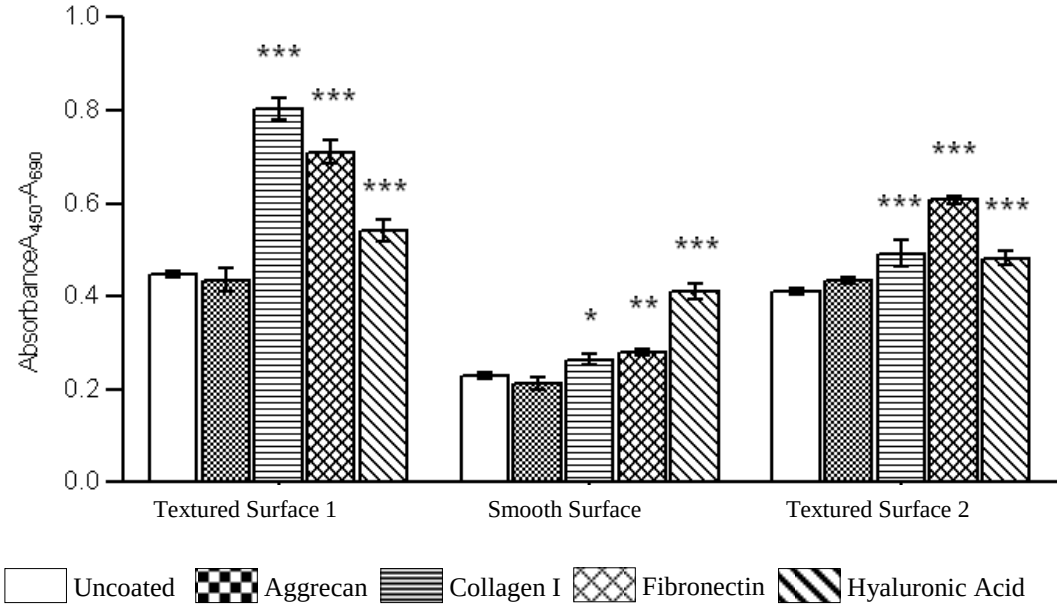

Figure 6.8 Effect of specific coatings on fibroblast proliferation after 24 hrs cell culture. Statistical analysis was performed applying the two-way ANOVA test; when the *p*-value was less than 0.05, the difference was regarded as statistically significant (*$p<0.05$, **$p<0.01$, ***$p<0.001$).

6.3.5 Effect of coatings on cytoskeleton organization

Rhodamine-phalloidin staining of breast fibroblasts cultured on uncoated and aggrecan coated TS1 and SS1, and uncoated TS2 revealed cells that exhibited fine stress fibres all around the cell periphery (Figure 6.9). Fibroblasts seeded on aggrecan coated SS1 and TS1, and uncoated TS2 were not able to form detectable cell-material adhesion complexes as well as actin cytoskeleton, and thus remained rounded, non-spread. Fibroblasts seeded on uncoated SS1 were poorly spread and showed a more random actin network than on uncoated TS1. Well spread cells in

collagen I, fibronectin and hyaluronic acid coated TS1, SS1 and TS2 exhibited thick fibres throughout the entire cell. In fibronectin coated TS2, collagen I coated SS1 and hyaluronic acid coated TS1 cells showed a well organized actin cytoskeleton. Fibroblasts seeded on fibronectin coated TS1 and on Hyaluronic Acid coated TS2 exhibited an elongated cellular phenotype. However, actin fibres were dense in all the cells in hyaluronic acid coated TS2 in comparison to fibroblasts in fibronectin coated TS1 which showed an abundance of fine fibres throughout the entire cell.

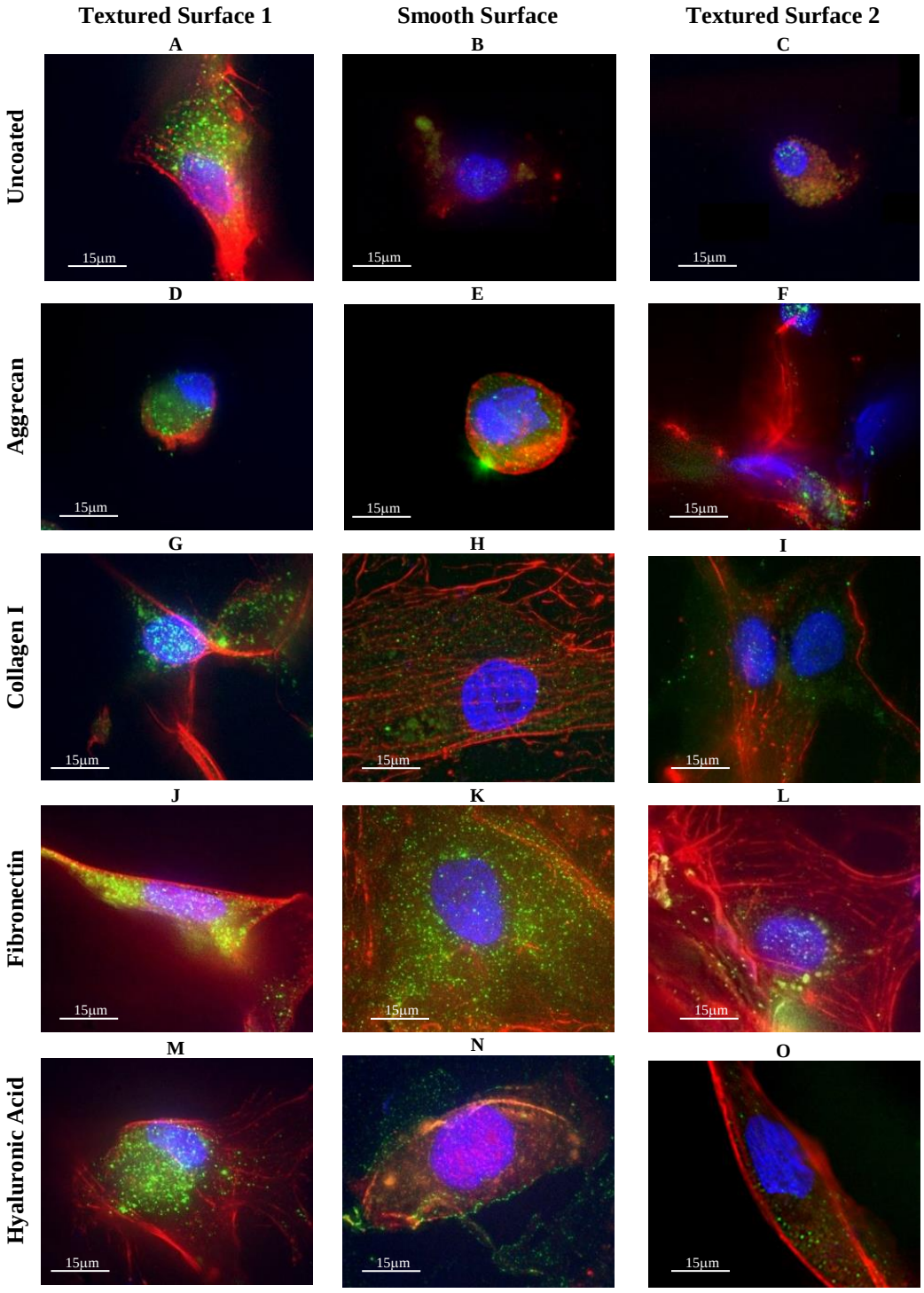

Figure 6.9 Morphology of breast fibroblasts seeded onto coated and uncoated breast implant surfaces. Immunofluorescence staining of the actin (red) (cytoskeleton), vinculin (green) (focal adhesion protein), and cell nucleus (blue) (DAPI) was performed on breast-derived fibroblasts on day 1 after seeding onto (D-F) aggrecan, (G-I) collagen I, (J-L) fibronectin, and (M-O) hyaluronic acid. Coated and uncoated (A, D, G, J, M) Surface Texture 1, (B, E, H, K, N) Smooth Surface, and (C, F, I, L, O) Surface Texture 2.

6.3.6 Effect of aggrecan, collagen I, fibronectin and hyaluronic acid coatings on adhesion expression in breast fibroblasts

After 24 hrs of incubation, total RNA was extracted from breast fibroblasts (n=3) (passage 2). The expression of alpha-actinin, FAK, paxillin, and vinculin, mRNA was determined by quantitative reverse-transcriptase polymerase chain reaction to compare the effect of the coatings with the uncoated implants in breast fibroblasts (Figure 6.10).

When the expression of the cytoskeleton components was examined, the level of α-actinin was found to be reduced in uncoated and aggrecan coated surfaces, but the α-actinin expression was higher in collagen I and fibronectin coated TS1 ($p<0.01$) and hyaluronic acid coated TS1 ($p<0.001$), and in collagen I, fibronectin and hyaluronic acid coated TS2 ($p<0.001$). The FAK level expression by breast fibroblasts was up-regulated in collagen I, fibronectin and hyaluronic acid coated surfaces ($p<0.001$) while the FAK expression was lower in both uncoated and aggrecan coated TS1, SS1 and TS2. The gene expression of paxillin was up-regulated in fibroblasts seeded on collagen I and fibronectin coated implants ($p<0.001$) and in the hyaluronic acid coated TS1 ($p<0.01$), SS1 ($p<0.05$) and TS2 ($p<0.001$). Regarding vinculin expression, a higher level was detected in the surfaces coated with collagen I and fibronectin ($p<0.001$) compared to the uncoated ones. Conclusions of the findings will be shown in the next chapter.

a

Gene expression of alpha-actinin

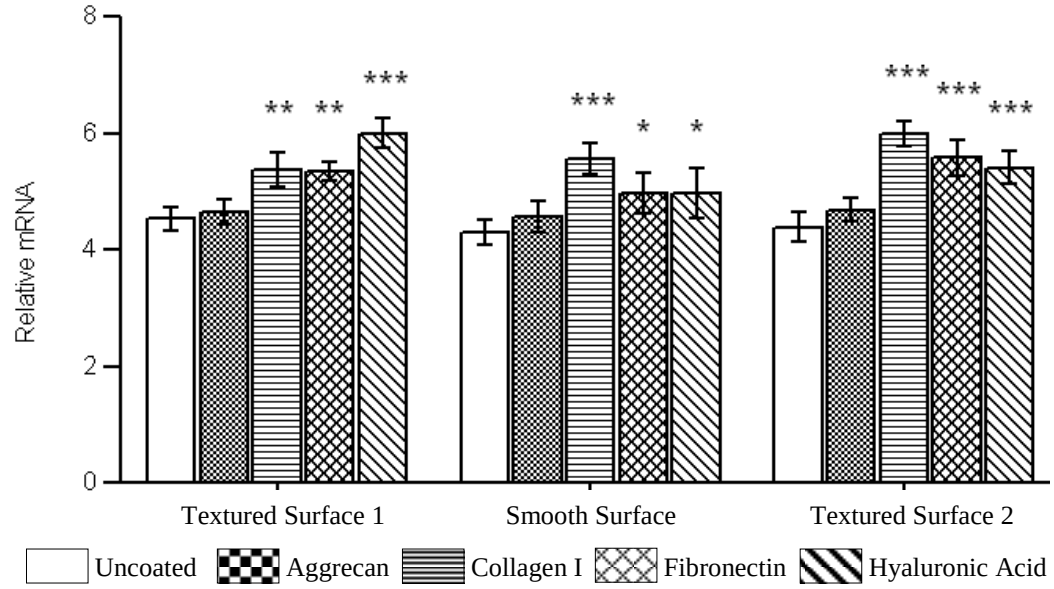

b

Gene expression of focal adhesion kinase

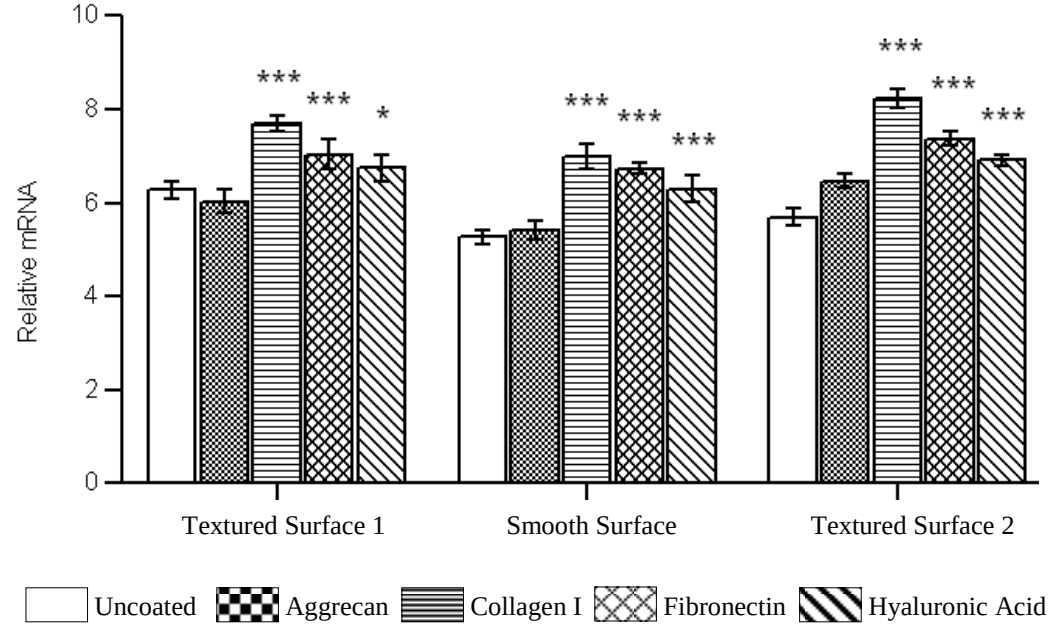

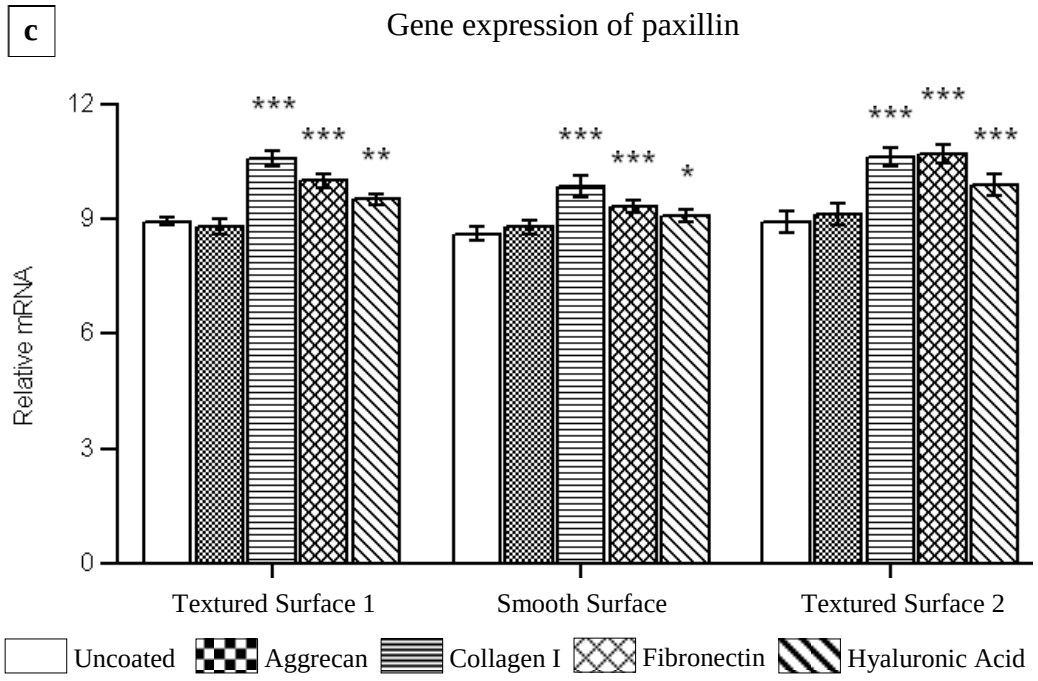

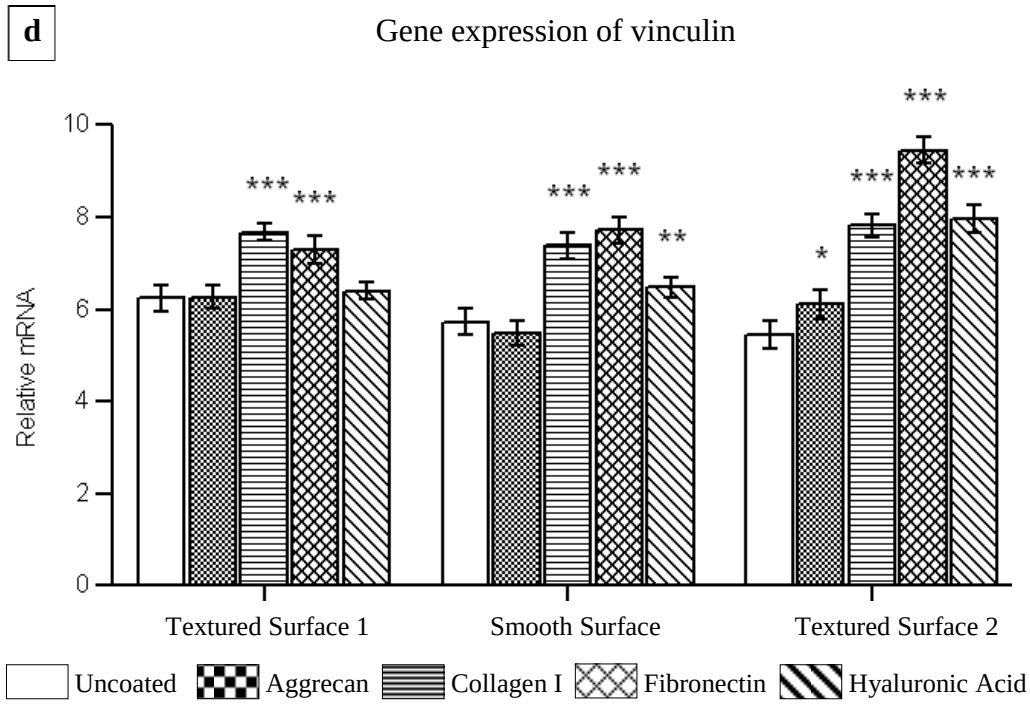

Figure 6.10 Effect of aggrecan, collagen I, fibronectin and hyaluronic acid coatings on gene adhesion expression in breast-derived fibroblasts after 24 hrs of cell culture. Results are expressed as mean ± standard deviation of triplicates. *p<0.05, **p<0.01, ***p<0.001 indicates significant difference between mRNA expression in fibroblasts seeded onto uncoated implants versus mRNA expression in fibroblasts seeded onto coated surfaces.

6.4 Discussion

In this study, for the first time, the physico-chemical characteristics of coated silicone breast implants on breast-derived fibroblast morphology and behaviour were evaluated. Chemical properties were examined by Raman spectroscopy; topographical features were studied by confocal laser microscopy, and the effect of four unique protein and glycosaminoglycan (GAG) coatings (aggrecan, collagen I, fibronectin and hyaluronic acid) on breast-derived fibroblast cytotoxicity, attachment, proliferation, morphology, and gene expression were examined.

The choice of the specific coatings evaluated in this study was based on an in-house whole genome microarray study undertaken in order to determine genes whose expression would correlate with breast capsular contracture formation and on previously published gene and protein research of relevance to breast capsular fibrosis (Kyle et al., 2013). Results showed that specific coatings can modify the physico-chemical properties of implant surfaces eliciting specific cellular reactions. Moreover, it was showed that the coated surfaces excluding aggregan, promoted cell-surface adhesion, proliferation, morphology and the up-regulation of adhesion related genes without any cytotoxic effect. These findings provide valuable information of characteristic expression of adhesion related genes; cell morphology and proliferation in breast fibroblasts following the application of specific coatings on smooth compared to textured breast implant surfaces.

Foreign body reaction is elicited by the implant placement in the body; this initiates an initial inflammatory phase where the prosthesis is encapsulated or eliminated by the host. Surface characteristics such as roughness, texture, surface free energy, surface charge and chemical composition all play key roles in cell adhesion and growth, and the nature of a biomaterial surface governs the phenotypic response of interacting cells (Prasad et al., 2010). Previous studies (Bacakova et al., 2011) have demonstrated that fibroblast activity can be modulated by specific coatings. Coating the surface of implants with these specific coatings may thus provide enhanced

support and anchorage for cells and favourably regulate cell morphology, adhesion, and proliferation (Yamamoto et al., 2006, Franz et al., 2011). In this study, specific coatings were employed on the surfaces of smooth versus textured breast implant surfaces in order to study fibroblast behaviour on these different topographies. It has been suggested that ECM proteins can be used to optimize fibroblast reaction to implants (Li et al., 2012b, Li et al., 2012a, Ungaro et al., 2006). Surface roughness and chemistry of the substrate have been shown to modulate cell-surface interaction. Furthermore, cell attachment and proliferation can be improved by utilizing coatings and altering the micro-topography of these surfaces.

The study demonstrated that cell adhesion and spreading were sensitive to both the physical and chemical properties of the substrate. Cell proliferation and cytotoxicity were also studied. It was found that surfaces coated with collagen I, fibronectin and hyaluronic acid did not elicit a cytotoxic effect on breast tissue derived fibroblasts in comparison to the uncoated surfaces. Lower proliferation rates were measured on uncoated and aggrecan coated surfaces. Fibroblast proliferation rate differed significantly among the surfaces investigated. An investigation into cell morphology showed that surface coatings promoted cell morphological modifications and the organization of actin fibres in all surfaces. Gene expression of adhesion related proteins shown to be modified by specific coatings and topography amongst the variety of surfaces tested.

Silicone breast implants investigated in this study are made with polydimethylsiloxane (PDMS); however, Raman spectra revealed a nearly matching profile for implants from the same company, however, implants from different company showed a dissimilar profile. These results are consistent with FTIR/ATR spectroscopy studies comparing breast implants from 2 different companies (Persichetti et al., 2009). Breast implants differed in chemical composition, and this could be related to the manufacturing process. In smooth implants, the silicone rubber shell is made with a shiny polished mandrel and to flatten this outer surface it is steeped in a solvent, while in textured implants, the silicone rubber shell is made

with a negative-contact imprint from a polyurethane foam or by pushing the silicone-coated mandrel into granular salt (Barr and Bayat, 2011).

Scanning electron microscopy and light microscopy have been used to analyze the topographic features (Barr et al., 2009). Changes in surface roughness after coating the surfaces were consistent with the adsorption of coatings on the valleys of the surfaces. Fibronectin coated surfaces showed the highest increment of surface roughness up to 277% in SS, 100% in TS1 and 16% in TS2 which correlates well with the highest rates of adsorption (per surface) of fibronectin on SS (0.014 mg/cm^2), TS1 (1.118 mg/cm^2) and TS2 (0.986 mg/cm^2). It was also found that cell adhesion was improved by surface roughness. Cell adhesion on rougher surfaces was higher. This means that the greater area due to texturing available for cell spreading allows increased anchoring ability by fibroblasts. In contrast, the same level of cell adhesion was not achieved on smooth surfaces, where low percentages of cell adhesion were recorded in comparison to the textured surfaces. After evaluating surface roughness, it was determined that, for the surfaces investigated in this study, fibroblast adhesion required a substrate with a surface roughness of at least 14 μm, at which point the degree of adhesion increased with surface roughness until a maximum adhesion was achieved at 21.94 μm. Furthermore, cell spreading demonstrated an incremental response to increases in surface roughness between 17.46 μm and 21.94 μm. The organization of the actin cytoskeleton was induced by the micro-topography in fibroblasts seeded on textured surfaces alone compared to smooth surfaces.

Increased cell adhesion was found on all implant surfaces coated with fibronectin and collagen I in comparison to the uncoated surfaces, which increased cell spreading. By contrast, implants coated with aggrecan demonstrated reduced cell-surface adhesion which therefore reduced cellular proliferation. These results suggest that collagen I and fibronectin act as potent regulators of cytoskeletal organization and cell spreading. This interaction is important for cell migration in wound healing (Franz et al., 2007). Cells that are forced to spread over large surface

areas, as in the case with textured surfaces, survive better and proliferate faster than cells that do not spread out (Lowery et al., 2010). The stimulatory effect of cell spreading potentially encourages tissues to regenerate after injury. If cells are lost from an epithelial layer, for example, the spreading of the remaining cells into the vacated space will stimulate them to proliferate until they fill the gap (Alberts et al., 2002). It is still uncertain, however, how a cell senses the extent of its own spreading and how it adjusts its behaviour accordingly. Cell behaviour is likely to be affected by the chemical and physical structure of the coating. Fluorescent staining images revealed that surfaces coated with collagen I and fibronectin induced organization of actin stress fibres and that collagen I affected the cytoskeletal arrangement and cell spreading, factors commonly regarded to be of significance with cell migration and wound healing.

In cell migration, a protrusion is sent in the direction of the movement, the extracellular substrate bound by integrin receptors induces integrin clustering and formation of adhesion complexes (Biname et al., 2010). This leads to the eliciting of adaptor proteins, which connect the adhesion points to the actin cytoskeleton and triggers intracellular signalling. This signal is defined by the proteins created and the type of integrin engaged in the interaction with the specific extracellular substrate. Small temporary adhesion complexes located in the leading edge of protrusions (focal complexes) mature under tension into larger structures known as focal contacts. Focal adhesions are more stable structures connected to actin stress fibres (Berrier and Yamada, 2007). Focal adhesion complexes are well established as a major adhesive and signal transducing component between the internal actin cytoskeleton and the external ECM (Petit and Thiery, 2000). Focal adhesion plays a key role in sensing surface topography in the extracellular environment. Focal adhesion kinase and the adaptor protein paxillin are focal adhesion proteins that can bind to and activate integrin B1 subunit cytoplasmic domains (Sequeira et al., 2012), along with vinculin, which connects integrins to actin filaments.

The adapter proteins that link stress fibres to integrins include alpha-actinin. An increase of alpha-actinin content was observed in the cells that had spread most with netlike actin filaments seeded on hyaluronic acid coated TS1, collagen I coated SS and fibronectin coated TS2. When SS and TS2 were coated with collagen I, TS1 and TS2 were coated with fibronectin, and TS1 and TS2 were coated with hyaluronic acid, the alpha-actinin expression was up-regulated ($p < 0.001$), which resulted in firmly attached fibroblasts to the substrate ($p < 0.001$). FAK has a role in modulation of the assembly of focal adhesions in response to tension exerted by the cytoskeleton on attachments to the extracellular substrate via integrins (Parsons, 2003). It was observed that the expression of FAK was reduced in fibroblasts seeded onto the uncoated and aggrecan coated implant surfaces. In contrast, the FAK expression was up-regulated in the surfaces coated with fibronectin and collagen I which resulted in increased cell-substrate adhesion $p < 0.001$. Paxillin, a focal adhesion-associated adaptor protein is involved in modulating cell adhesion and spreading (Wang et al., 2009). It was observed that the expression of paxillin was reduced in fibroblasts cultured on the uncoated and aggrecan coated implant surfaces. However, paxillin expression was up-regulated ($p < 0.001$), which resulted in well-spread fibroblasts, in the surfaces coated with fibronectin and collagen I. Vinculin, a membrane-cytoskeletal protein in focal adhesions that is involved in linkage of integrin adhesion molecules to the actin cytoskeleton (Maheshwari et al., 2000), was found in all surfaces. A low content of vinculin was observed in fibroblasts seeded onto uncoated and aggrecan coated surfaces ($p < 0.001$). This resulted in weakening of adhesion ($p < 0.001$), conversely a higher content of vinculin resulted in bigger focal adhesions and greater abundance of focal adhesion points in fibroblasts seeded onto collagen I and fibronectin surfaces. There is a consistent pattern in enhanced cell-surface adhesion when the surfaces were coated with collagen I. Cell proliferation highlights a significant benefit on the presence of collagen I to the surface of TS1, while hyaluronic acid did to SS, and fibronectin to TS2. TS1 represented the optimal substrate to promote spreading when coated with hyaluronic acid, while SS and TS2 did with collagen I. Surprisingly, no significant difference was identified between fibroblast adhesion and proliferation to aggrecan coated implants compared to the corresponding uncoated surfaces ($p>0.05$).

The study demonstrated that cell adhesion and spreading were sensitive to smooth and textured surfaces. Cell proliferation and cytotoxicity were also studied. It was found that surfaces coated with collagen I, fibronectin and hyaluronic acid did not elicit a cytotoxic effect on breast tissue derived fibroblasts in comparison to the uncoated surfaces. Fibroblast proliferation rate differed significantly among the surfaces investigated. An investigation into cell morphology showed that surface coatings promoted cell morphology modifications and the organization of actin fibres in all surfaces. Gene expression of adhesion related proteins shown to be modified by specific coatings and topography amongst the variety of surfaces tested.

Chapter VII Conclusions

7.1 Conclusions

In conclusion, data acquired from the 3-D images, roughness experimentations, hydrophobicity assay and tensile testing have given a unique compilation of information to enable characterisation of the smooth and textured surfaces of commercial available breast implants. Through the investigation of the physico-chemical properties of implants influencing cell adhesion behaviour, collagen I and fibronectin coated implants made the substrate less hydrophobic allowing fibroblasts to adhere and spread better. Arithmetic surface roughness increases with the use of coatings. This increases the total area of cell-substrate contact leading to an increase in fibroblast spreading. Tensile tests demonstrated that the textured surfaces tended to exhibit higher bending stiffness, a property that allows fibroblasts to increase their link between the integrins and the cytoskeleton in order to exert more force on the substrate.

This study has demonstrated the extent and strength of cell adhesion, and subsequent cell proliferation and differentiation based on the physical interactions between cells and the extracellular environment in the form of topography and on the chemical interactions mediated by specific coatings. This study has also shown that the surface coating of the silicone breast implants induced over-expression of specific adhesion related genes in breast-derived fibroblasts. It was identified that collagen I, fibronectin, and hyaluronic acid coatings did not elicit a cytotoxic effect on breast tissue derived fibroblasts in comparison to the uncoated surfaces. Fibroblast-substrate adhesion was enhanced on collagen I and fibronectin coated samples in comparison to the uncoated surfaces, which increased cell spreading. Breast-derived fibroblasts proliferate actively in response to collagen I, fibronectin and hyaluronic acid coatings. Breast-derived fibroblasts cultured on collagen I, fibronectin and hyaluronic acid coated implants exhibit morphology, in which the cells were better spread. There was a higher expression of a number of matrix genes in relation to

fibroblast attachement, which showed a greater extent on fibroblasts cultured on collagen I and fibronectin coated implants.

The research findings demonstrate that the most promising candidate in the regulation of adhesion and proliferation in the coated textured implant are fibronectin and collagen I. A good adhesion ensures that the implant holds in place, thus preventing micromotion at the host prosthesis interface, the fibroblasts will not over produce collagen in response to this host-prosthesis shearing motion. Consequently, capsules around these coated surfaces may be thinner and less contracted in comparison to the capsules surrounding the uncoated textured surface implants. The addition of appropriate coating to the surface of silicone breast implants may reduce the risk of capsular contracture formation in the near future. Further studies are required to provide a better understanding of cell-surface interaction in breast fibroblasts and silicone implants.

7.2 Limitations of the work

Breast capsular contracture aetiology remains uncertain, but it is characterised by dense fibrocollagenous connective tissue with local inflammatory response. Furthermore, breast capsule consists of myofibroblasts, which are implicated in contracting the breast implants (Hwang et al., 2010). Thus it was decided to limit the samples to breast-derived fibroblasts. However, future investigation, involving different types of cells found in breast capsules, will be of value. Another potential limitation of our study was the total number of samples used for breast tissue (n=3), a larger number of samples that includes different ethnicities would be beneficial.

7.3 Recommendations for future work

This study has aided in clarifying the relationship between surface roughness and cell adhesion. As regards the other parameters (wettability, bending and stretching

stiffness), because commercial breast implants were considered then the key parameters investigated may have had values that varied over only a relatively small range, thus making it difficult to modulate some of the key factors, which is one limitation of the study. Therefore, future work should investigate implant surfaces, not necessarily commercial ones that exhibit a wider range of surface parameters so that the cause effect relationships of some of the key surface parameters may be more clearly established.

This research represents a study focused on enhancing, by surface coating, cell-surface adhesion, spreading, and proliferation on fibroblasts seeded on breast implants. By optimising surface coating it allows the coating to be better attached to the breast implant surface. From this point, future work conducted can focus on the use of chemically grafting coatings to improve coating adhesion to the substrate resulting in a thin and more stable layer that can improve cell behaviour on breast implants.

References

Abbott, E. and Firestone, F. (1993) Specifying surface quantity - a method based on accurate measurements and comparison. *Mech. Eng,* 55**,** 569-572.

Abramo, A. C., De Oliveira, V. R., Ledo-Silva, M. C. and De Oliveira, E. L. (2010) How texture-inducing contraction vectors affect the fibrous capsule shrinkage around breasts implants? *Aesthetic Plast Surg,* 34**,** 555-560.

Abramowitz, M. (1993) Fluorescence microscopy: The essentials. *Olympus America Inc.,* 4**,** 1-4.

Adams, W. P., Jr. and Mallucci, P. (2012) Breast Augmentation. *Plast Reconstr Surg,* 130**,** 597e-611e

Adams, W. P., Robinson, J. B. and Rohrich, R. J. (1998) Lipid infiltration as a possible biologic cause of silicone gel breast implant aging. *Plast Reconstr Surg.,* 101**,** 64-68.

Ajmal, N., Riordan, C. L., Cardwell, N., Nanney, L. B. and Shack, R. B. (2003) The effectiveness of sodium 2-mercaptoethane sulfonate (mesna) in reducing capsular formation around implants in a rabbit model. *Plast Reconstr Surg,* 112**,** 1455-61.

Alberts, B., Johnson, A. and Lewis, J. (2002) Molecular biology of the cell. *Garland Science***,** 907-933.

Allergan, M. (2006) Natrelle highly cohesive silicone-filled breast implants. *Allergan,* 53**,** 1-75.

Aroca-Aguilar, J. D., Sanchez-Sanchez, F., Ghosh, S., Fernandez-Navarro, A., Coca-Prados, M. and Escribano, J. (2011) Interaction of recombinant myocilin with the matricellular protein SPARC: functional implications. *Invest Ophthalmol Vis Sci. ,* 52**,** 179-189.

Arthur, W. T. and Burridge, K. (2001) RhoA inactivation by p190RhoGAP regulates cell spreading and migration by promoting membrane protrusion and polarity. *Mol Biol Cell* 12**,** 2711-2720.

Bacakova, L., Filova, E., Parizek, M., Ruml, T. and Svorcik, V. (2011) Modulation of cell adhesion, proliferation and differentiation on materials designed for body implants. *Biotechnol Adv,* 29**,** 739-67.

Balaban, N. Q., Schwarz, U. S., Riveline, D., Goichberg, P., Tzur, G., Sabanay, I., Mahalu, D., Safran, S., Bershadsky, A., Addadi, L. and Geiger, B. (2001) Force and focal adhesion assembly: a close relationship studied using elastic micropatterned substrates. *Nat Cell Biol,* 3**,** 466-72.

Bao, X., Lu, C. and Frangos, J. A. (1999) Temporal gradient in shear but not steady shear stress induces PDGF-A and MCP-1 expression in endothelial cells: role of NO, NF kappa B, and egr-1. *Arterioscler Thromb Vasc Biol,* 19**,** 996-1003.

Barone, F. E., Perry, L., Keller, T. and Maxwell, G. P. (1992) The biomechanical and histopathologic effects of surface texturing with silicone and polyurethane in tissue implantation and expansion. *Plast Reconstr Surg,* 90**,** 77-86.

Barr, S. and Bayat, A. (2011) Breast implant surface development: perspectives on development and manufacture. *Aesthet Surg J,* 31**,** 56-67.

Barr, S., Hill, E. and Bayat, A. (2009) Current implant surface technology: an examination of their nanostructure and their influence on fibroblast alignment and biocompatibility. *Eplasty* 9**,** 198-217.

Beningo, K. A., Dembo, M., Kaverina, I., Small, J. V. and Wang, Y. L. (2001) Nascent focal adhesions are responsible for the generation of strong propulsive forces in migrating fibroblasts. *J Cell Biol,* 153**,** 881-8.

Berrier, A. L. and Yamada, K. M. (2007) Cell-matrix adhesion. *Cellular Physiology,* 213**,** 565-573.

Berry, M. G., Cucchiara, V. and Davies, D. M. (2010) Breast augmentation: Part II-Adverse capsular contracture. *J Plast Reconstr Aesthet Surg,* 63**,** 2098-107.

Berry, M. G. and Davies, D. M. (2010) Breast augmentation: Part I - a review of the silicone prosthesis. *J Plast Reconstr Aesthet Surg,* 63**,** 1761-1768.

Bershadsky, A., Chausovsky, A., Becker, E., Lyubimova, A. and Geiger, B. (1996) Involvement of microtubules in the control of adhesion-dependent signal transduction. *Curr Biol,* 6**,** 1279-89.

Bershadsky, A. D., Balaban, N. Q. and Geiger, B. (2003) Adhesion-dependent cell mechanosensitivity. *Annu Rev Cell Dev Biol,* 19**,** 677-95.

Bethesda, M. D. (2014) Breast cancer screening (PDQ): health professional version. *National Cancer Institute (US)***,** 1-30.

Biname, F., Pawlak, G., Roux, P. and Hibner, U. (2010) What makes cells move: requirements and obstacles for spontaneous cell motility. *Mol Biosyst,* 6**,** 648-661.

Bloom, L., Ingham, K. C. and Hynes, R. O. (1999) Fibronectin regulates assembly of actin filaments and focal contacts in cultured cells via the heparin-binding site in repeat III13. *Mol Biol Cell.,* 5**,** 1521-36.

Bondurant, S., Ernster, V. and Herdman, R. (1999) Safety of silicone breast implants. *NAP***,** 50-100.

Bradshaw, A. D. (2012) Diverse biological functions of the SPARC family of proteins. *Int J Biochem Cell Biol.,* 44**,** 480-488.

Braley, S. A. (1973) The use of silicones in plastic surgery: A Retrospective View. *Plast Reconstr Surg.,* 51**,** 280-288.

Brand, K. G. (1993) Infection of mammary prostheses: A survey and the question of prevention. *Ann Plast Surg,* 30**,** 289-295.

Brody, G. S. (1997) On the safety of breast implants. *Plast Reconstr Surg,* 100**,** 1314-1321.

Brohim, R. M., Foresman, P. A., Hildebrandt, P. K. and Rodeheaver, G. T. (1992) Early tissue reaction to textured breast implant surfaces. *Ann Plast Surg,* 28**,** 354-362.

Brown, S. L., Silverman, B. G. and Berg, W. A. (1997) Rupture of silicone-gel breast implants: causes, sequelae, and diagnosis. *The Lancet,* 350**,** 1531-1537.

Burkhardt, B. R., Dempsey, P. D., Schnur, P. L. and Tofield, J. J. (1986) Capsular contracture: A prospective study of the effect of local antibacterial agents. *Plast Reconstr Surg.,* 77**,** 919-930.

Caldas, I. R., Campi-Azevedo, A. C., Oliveira, L. F., Silveira, A. M., Oliveira, R. C. and Gazzinelli, G. (2008) Human schistosomiasis mansoni: immune responses during acute and chronic phases of the infection. *Acta Trop,* 108**,** 109-17.

Carlier, M. F., Le Clainche, C., Wiesner, S. and Pantaloni, D. (2003) Actin-based motility: from molecules to movement. *Bioessays,* 25**,** 336-45.

Chi, T., Ballinger, T., Olds, R. and Zecchino, M. (2005) Surface texture analysis using dektak stylus profilers. *Veeco Instruments Application Notes,* 15.

Chrzanowska-Wodnicka, M. and Burridge, K. (1996) Rho-stimulated contractility drives the formation of stress fibers and focal adhesions. *J Cell Biol,* 133**,** 1403-15.

Clark, P., Connolly, P., Curtis, A. S., Dow, J. A. and Wilkinson, C. D. (1990) Topographical control of cell behaviour: II. multiple grooved substrata. *Development,* 108**,** 635-644.

Claxton, N. S., Fellers, T. J. and Davidson, M. W. (2006) Laser scanning confocal microscopy. *Department of Optical Microscopy and Digital Imaging***,** 3-20.

Cohen, I. K. (1994) Impact of the FDA ban on silicone breast implants. *J Surg Oncol.,* 56**,** 1.

Cohen, M., Klein, E., Geiger, B. and Addadi, L. (2003) Organization and adhesive properties of the hyaluronan pericellular coat of chondrocytes and epithelial cells. *Biophys J.,* 85**,** 1996-2005.

Collins, M. N. and Birkinshaw, C. (2013) Hyaluronic acid based scaffolds for tissue engineering-A review. *Carbohydr Polym,* 92**,** 1262-1279.

Crosby, M. A. (2013) Plastic Surgery. *Plast Reconstr Surg.,* 5**,** 13-15.

Danino, A., Rocher, F., Blanchet-Bardon, C., Revol, M. and Servant, J. M. (2001) A scanning electron microscopic study of the surface of textured mammary implants and their capsules. Description of the adhesive "velcro" effect of porous-textured breast prostheses. *Ann Chir Plast Esthet,* 46**,** 23-30.

Davidson, M. W. and Abramowitz, M. (1998) Deconvolution in Optical Microscopy. *Olympus America Inc.***,** 40-47.

DeMali, K. A., Barlow, C. A. and Burridge, K. (2002) Recruitment of the Arp2/3 complex to vinculin: coupling membrane protrusion to matrix adhesion. *J Cell Biol,* 159**,** 881-91.

Demedts, M., Behr, J., Buhl, R., Costabel, U., Dekhuijzen, R., Jansen, H. M., MacNee, W., Thomeer, M., Wallaert, B., Laurent, F., Nicholson, A. G., Verbeken, E. K., Verschakelen, J., Flower, C. D., Capron, F., Petruzzelli, S., De Vuyst, P., van den Bosch, J. M., Rodriguez-Becerra, E., Corvasce, G., Lankhorst, I., Sardina, M. and Montanari, M. (2005) High-dose acetylcysteine in idiopathic pulmonary fibrosis. *N Engl J Med,* 353**,** 2229-42.

Dempsey, W. C. and Latham, W. D. (1968) Subpectoral implants in augmentation mammaplasty. Preliminary report. *Plast Reconstr Surg.,* 42**,** 515-521.

Diao, Z. Y., Fu, H. L., Nie, C. L., Hao, L. J., Yang, D. P. and Chen, W. H. (2011) Controlled release of transforming growth factor-beta receptor kinase inhibitor from thermosensitive Chitosan-based hydrogel: application for prevention of capsular contracture. *Chin Med J,* 124**,** 284-90.

Didenko, V. V. (2006) Fluorescent energy transfer nucleic acid probes: designs and protocols. *Springer***,** 3-4.

Dreieicher, E., Beck, K. F., Lazaroski, S., Boosen, M., Tsalastra-Greul, W., Beck, M., Fleming, I., Schaefer, L. and Pfeilschifter, J. (2009) Nitric oxide inhibits glomerular TGF-beta signaling via SMOC-1. *J Am Soc Nephrol,* 20**,** 1963-1974.

Drew, P., Cawthorn, S. and Michell, M. (2007) Interventional ultrasound of the breast. *CRC Press***,** 11-14.

Eftink, M. R. (2000) Use of fluorescence spectroscopy as thermodynamics tool. *Meth Enzymol,* 323**,** 459-73.

Ellis, H. and Mahadevan, V. (2013) Anatomy and physiology of the breast. *Surgery* 31**,** 11-14.

Elter, P., Weihe, T., Buhler, S., Gimsa, J. and Beck, U. (2012) Low fibronectin concentration overcompensates for reduced initial fibroblasts adhesion to a nanoscale topography: single-cell force spectroscopy. *Colloids Surf B Biointerfaces,* 95**,** 82-89.

Eming, S. A., Krieg, T. and Davidson, J. M. (2007) Inflammation in wound repair: molecular and cellular mechanisms. *J Invest Dermatol,* 127**,** 514-525.

Enoch, S. and Leaper, D. J. (2008) Basic science of wound healing. *Surgery* 26**,** 31-37.

Ersek, R. A., Beisang, A. A., Minn, R. and Iowa, D. M. (1990) Textured silicone implant prosthesis. *United States Patent***,** 1-7.

Ersek, R. A. and Navarro, J. A. (1991) Transaxillary subpectoral placement of textured breast prostheses. *Ann Plast Surg,* 27**,** 93-96.

Fallowfield, J. A., Mizuno, M., Kendall, T. J., Constandinou, C. M., Benyon, R. C., Duffield, J. S. and Iredale, J. P. (2007) Scar-associated macrophages are a major source of hepatic matrix metalloproteinase-13 and facilitate the resolution of murine hepatic fibrosis. *J Immunol,* 178**,** 5288-95.

Fenner, R. T. (1989) Mechanics of solids. *Blackwell Sci Publ***,** 98-100.

Foster, B. (1997) Optimizing light microscopy for biological and clinical laboratories. *Kendall Hunt Pub Co***,** 72-78.

Franz, M. G., Steed, D. L. and Robson, M. C. (2007) Optimizing healing of the acute wound by minimizing complications. *Curr Probl Surg,* 44**,** 691-763.

Franz, S., Rammelt, S., Scharnweber, D. and Simon, J. C. (2011) Immune responses to implants - A review of the implications for the design of immunomodulatory biomaterials. *Biomaterials,* 32**,** 6692-6709.

Gabriel, S. E., Woods, J. E., O'Fallon, W. M., Beard, C. M., Kurland, L. T. and Melton, L. J. (1997) Complications leading to surgery after breast implantation. *N Engl J Med,* 336**,** 677-682.

Geiger, B. and Bershadsky, A. (2001) Assembly and mechanosensory function of focal contacts. *Curr Opin Cell Biol,* 13**,** 584-92.

Geiger, B., Bershadsky, A., Pankov, R. and Yamada, K. M. (2001) Transmembrane crosstalk between the extracellular matrix-cytoskeleton crosstalk. *Nat Rev Mol Cell Biol,* 2**,** 793-805.

Gillespie, P. G. and Walker, R. G. (2001) Molecular basis of mechanosensory transduction. *Nature,* 413**,** 194-202.

Ginsberg, M. (1981) Role of platelets in inflammation and rheumatic disease. *Adv Inflam* 2**,** 53-71.

Goldstein, D. J. (1999) Understanding the light microscope: a computer-aided introduction. *Academic Press***,** 90-97.

Goldwyn, R. M. (1978) Vincenz Czerny and beginnings of breast reconstruction. *Plast Reconstr Surg.,* 61**,** 673-681.

Grigg, M., Bondurant, S., Ernster, V. L. and Herdman, R. (2000) Information for women about the safety of silicone breast implant. *National Academies Press***,** 1-30.

Gruber, R., Pforte, A., Beer, B. and Riethmuller, G. (1996) Determination of gamma/delta and other T-lymphocyte subsets in bronchoalveolar lavage fluid and

peripheral blood from patients with sarcoidosis and idiopathic fibrosis of the lung. *APMIS,* 104**,** 199-205.

Gurunluoglu, R., Kubek, E. and Arton, J. (2013) Dual pedicle mastopexy technique for reorientation of volume and shape after subglandular and submuscular breast implant removal. *Eplasty,* 13**,** 397-412.

Hakelius, L. and Ohlsen, L. (1997) Tendency to capsular contracture around smooth and textured gel-filled silicone mammary implants: a five-year follow-up. *Plast Reconstr Surg,* 100**,** 1566-9.

Hamill, O. P. and Martinac, B. (2001) Molecular basis of mechanotransduction in living cells. *Physiol Rev,* 81**,** 685-740.

Handel, N., Jensen, J. A., Black, Q., Waisman, J. R. and Silverstein, M. J. (1995) The fate of breast implants: a critical analysis of complications and outcomes. *Plast Reconstr Surg,* 96**,** 1521-33.

Harvey, A. G., Hill, E. W. and Bayat, A. (2013) Designing implant surface topography for improved biocompatibility. *Expert Rev Med Devices,* 10**,** 257-67.

Haugland, R. P., Gregory, J., Spence, M. T. Z., Johnson, I. and Miller, E. (2002) *Introduction to fluorescence techniques*, Molecular Probes, Inc.

Hauser, J., Zietlow, J., Koller, M., Esenwein, S. A., Halfmann, H., Awakowicz, P. and Steinau, H. U. (2009) Enhanced cell adhesion to silicone implant material through plasma surface modification. *J Mater Sci Mater Med,* 20**,** 2541-2548.

Heath, J. P. and Dunn, G. A. (1978) Cell to substratum contacts of chick fibroblasts and their relation to the microfilament system. A correlated interference-reflexion and high-voltage electron-microscope study. *J Cell Sci,* 29**,** 197-212.

Helfman, D. M., Levy, E. T., Berthier, C., Shtutman, M., Riveline, D., Grosheva, I., Lachish-Zalait, A., Elbaum, M. and Bershadsky, A. D. (1999) Caldesmon inhibits nonmuscle cell contractility and interferes with the formation of focal adhesions. *Mol Biol Cell,* 10**,** 3097-112.

Henriksen, T. F., Fryzek, J. P., Holmich, L. R., McLaughlin, J. K., Kjoller, K., Hoyer, A. P., Olsen, J. H. and Friis, S. (2005) Surgical intervention and capsular contracture after breast augmentation: a prospective study of risk factors. *Ann Plast Surg,* 54**,** 343-51.

Herman, B. (1998) Fundamentals of fluorescence. *Bios Scient* 40**,** 1-14.

Hester, T. R., Nahai, F., Bostwick, J. and Cukic, J. (1988) A 5-year experience with polyurethane-covered mammary prostheses for treatment of capsular contracture, primary augmentation mammoplasty, and breast reconstruction. *Clin Plast Surg,* 15**,** 569-585.

Hibbs, A. R. (2000) Confocal microscopy for biologists: an intensive introductory course. *BIOCON***,** 81-88.

Hidalgo, D. A. (2000) Breast augmentation: choosing the optimal incision, implant, and pocket plane. *Plast Reconstr Surg.,* 105**,** 2202-2216.

Hilborn, J. and Bjursten, L. M. (2007) A new and evolving paradigm for biocompatibility. *J Tissue Eng Regen Med,* 1**,** 110-9.

Hunt, T. K. (1980) Disorders of wound healing. *World J Surg,* 4**,** 271-7.

Hurst, N. M. (1996) Lactation after augmentation mammoplasty - Reply. *Obstet Gynecol.,* 87**,** 1063-1063.

Hwang, K., Sim, H. B., Huan, F. and Kim, D. J. (2010) Myofibroblasts and capsular tissue tension in breast capsular contracture. *Aesthetic Plast Surg,* 34**,** 716-21.

Jenkins, M. E., Friedman, H. I. and Von Recum, A. F. (1996) Breast implants: facts, controversy, and speculations for future research. *J Invest Surg.,* 9**,** 1 - 12.

Jiang, Y., Wang, M., Celiker, M. Y., Liu, Y. E., Sang, Q. X., Goldberg, I. D. and Shi, Y. E. (2001) Stimulation of mammary tumorigenesis by systemic tissue inhibitor of matrix metalloproteinase 4 gene delivery. *Cancer Res.* , 61**,** 2365-2370.

Johnston, I. D., McCluskey, D. K., Tan, C. K. L. and Tracey, M. C. (2014) Mechanical characterization of bulk Sylgard 184 for microfluidics and microengineering. *J Micromech Microeng,* 24**,** 1-7.

Jopp, J., Grüll, H. and Yerushalmi-Rozen, R. (2004) Wetting behavior of water droplets on hydrophobic microtextures of comparable size. *Langmuir,* 20**,** 10015-10019.

Katoh, K., Kano, Y., Amano, M., Onishi, H., Kaibuchi, K. and Fujiwara, K. (2001) Rho-kinase-mediated contraction of isolated stress fibers. *J Cell Biol,* 153**,** 569-84.

Katzin, W. E., Centeno, J. A., Feng, L. J., Kiley, M. and Mullick, F. G. (2005) Pathology of lymph nodes from patients with breast implants: A histologic and spectroscopic evaluation. *Am J Surg Pathol,* 29**,** 506-511.

Khorasani, M. T. and Mirzadeh, H. (2004) BHK cells behaviour on laser treated polydimethylsiloxane surface. *Colloids Surf B Biointerfaces,* 35**,** 67-71.

Kiani, C., Chen, L., Wu, Y. J., Yee, A. J. and Yang, B. B. (2002) Structure and function of aggrecan. *Cell Res,* 12**,** 19-32.

Kim, Y. J., Kim, Y. W. and Cheon, Y. W. (2014) Prevention of implant malposition in inframammary augmentation mammaplasty. *Arch Plast Surg,* 41**,** 407-13.

Kjoller, K., Holmich, L. R., Jacobsen, P. H., Friis, S., Fryzek, J., McLaughlin, J. K., Lipworth, L., Henriksen, T. F., Jorgensen, S., Bittmann, S. and Olsen, J. H. (2001) Capsular contracture after cosmetic breast implant surgery in Denmark. *Ann Plast Surg.,* 47**,** 359-366.

Koike, N., Kassai, Y., Kouta, Y., Miwa, H., Konishi, M. and Itoh, N. (2007) Brorin, a novel secreted bone morphogenetic protein antagonist, promotes neurogenesis in mouse neural precursor cells. *J Biol Chem.* , 282**,** 15843-15850.

Korurer, E., Kenar, H., Doger, E. and Karaoz, E. (2014) Production of a composite hyaluronic acid/gelatin blood plasma gel for hydrogel-based adipose tissue engineering applications. *J Biomed Mater Res Part A,* 102A**,** 2220-2229.

Kostas, M. (2007) The effects of breast augmentation surgery on future ability to lactate. *Breast J.*, 13**,** 62-67.

Kubitscheck, U. (2013) Fluorescence microscopy: from principles to biological applications. *Wiley***,** 24-25.

Kuhn, A., Singh, S., Smith, P. D., Ko, F., Falcone, R., Lyle, W. G., Maggi, S. P., Wells, K. E. and Robson, M. C. (2000) Periprosthetic breast capsules contain the fibrogenic cytokines TGF-beta1 and TGF-beta2, suggesting possible new treatment approaches. *Ann Plast Surg,* 44**,** 387-91.

Kulmala, I., McLaughlin, J. K., Pakkanen, M., Lassila, K., Holmich, L. R., Lipworth, L., Boice, J. D., Jr., Raitanen, J. and Luoto, R. (2004) Local complications after cosmetic breast implant surgery in Finland. *Ann Plast Surg,* 53**,** 413-9.

Kyle, D. J., Harvey, A. G., Shih, B., Tan, K. T., Chaudhry, I. H. and Bayat, A. (2013) Identification of molecular phenotypic descriptors of breast capsular contracture formation using informatics analysis of the whole genome transcriptome. *Wound Repair Regen,* 21**,** 762-9.

Lafuma, A. and Quere, D. (2003) Superhydrophobic states. *Nat Mater,* 2**,** 457-60.

Lakowicz, J. R. (2007) Principles of fluorescence spectroscopy. *Springer***,** 1-5.

Lampin, M., Warocquier-Clérout, R., Legris, C., Degrange, M. and Sigot-Luizard, M. F. (1997) Correlation between substratum roughness and wettability, cell adhesion, and cell migration. *J Biomed Mater Res,* 36**,** 99-108.

Lee, H. K., Jin, U. S. and Lee, Y. H. (2011) Subpectoral and precapsular implant repositioning technique: correction of capsular contracture and implant malposition. *Aesthetic Plast Surg,* 35**,** 1126-32.

Leibovich, S. J. and Ross, R. (1975) The role of the macrophage in wound repair. A study with hydrocortisone and antimacrophage serum. *Am J Pathol,* 78**,** 71-100.

Lewis, J. R. (1965) The augmentation mammaplasty. *Plast Reconstr Surg.*, 35**,** 51-59.

Li, Y., Zhang, S., Guo, L., Dong, M., Liu, B. and Mamdouh, W. (2012a) Collagen coated tantalum substrate for cell proliferation. *Colloids Surf B Biointerfaces,* 95**,** 10-15.

Li, Y. C., Lin, Y. C. and Young, T. H. (2012b) Combination of media, biomaterials and extracellular matrix proteins to enhance the differentiation of neural stem/precursor cells into neurons. *Acta Biomater,* 8**,** 3035-3048.

Liu, S., Calderwood, D. A. and Ginsberg, M. H. (2000) Integrin cytoplasmic domain-binding proteins. *J Cell Sci,* 113**,** 3563-71.

Lo, C. M., Wang, H. B., Dembo, M. and Wang, Y. L. (2000) Cell movement is guided by the rigidity of the substrate. *Biophys J,* 79**,** 144-52.

Lowery, J. L., Datta, N. and Rutledge, G. C. (2010) Effect of fiber diameter, pore size and seeding method on growth of human dermal fibroblasts in electrospun poly(epsilon-caprolactone) fibrous mats. *Biomaterials,* 31**,** 491-504.

Lydon, M. J., Minett, T. W. and Tighe, B. J. (1985) Cellular interactions with synthetic polymer surfaces in culture. *Biomaterials,* 6**,** 396-402.

Maheshwari, G., Brown, G., Lauffenburger, D. A., Wells, A. and Griffith, L. G. (2000) Cell adhesion and motility depend on nanoscale RGD clustering. *Cell Science,* 113**,** 1677-1686.

Marianne, N., Sandra, D., Joy, S., David, Y., Marilyn, L. and Miriam, O. (1990) The influence of breast surgery, breast appearance, and pregnancy-induced breast changes on lactation sufficiency as measured by infant weight gain. *Birth,* 17**,** 31-38.

Marshall, W. R., Godfrey, M., Hollister, D. W., Balkovich, M. E. and Lindgren, V. V. (1989) Types of collagen in breast capsules. *Ann Plast Surg,* 23**,** 401-5.

Matsumura, F., Ono, S., Yamakita, Y., Totsukawa, G. and Yamashiro, S. (1998) Specific localization of serine 19 phosphorylated myosin II during cell locomotion and mitosis of cultured cells. *J Cell Biol,* 140**,** 119-29.

Maxwell, G. P. and Gabriel, A. (2009) The evolution of breast implants. *Plast Reconstr Surg,* 36**,** 1-13.

McNally, J., Karpova, T., Cooper, J. and Conchello, J. (1999) Three-dimensional imaging by deconvolution microscopy. *Methods,* 19**,** 373-385

Mendonca, R. J. and Coutinho-Netto, J. (2009) Cellular aspects of wound healing. *An Bras Dermatol,* 84**,** 257-62.

Middleton, M. S. (1998) Magnetic resonance evaluation of breast implants and soft-tissue silicone. *Top Magn Reson Imaging,* 9**,** 92-137.

Middleton, M. S. and McNamara, M. P. (2000) Breast implant classification with MR imaging correlation. *Radiographics,* 20**,** 1-72.

Miwa, H., Miyake, A., Kouta, Y., Shimada, A., Yamashita, Y., Nakayama, Y., Yamauchi, H., Konishi, M. and Itoh, N. (2009) A novel neural-specific BMP antagonist, Brorin-like, of the Chordin family. *FEBS Letters,* 583**,** 3643-3648.

Muschler, J. and Streuli, C. H. (2010) Cell-matrix interactions in mammary gland development and breast cancer. *Cold Spring Harb Perspect Biol,* 2**,** 1-17.

Mwenifumbo, S. and Stevens, M. M. (2007) Biomedical Nanostructures. ECM interactions with cells from the macro to nanoscale. *John Wiley & Sons, Inc.***,** 223-260.

Nassau, K. (2001) Color produced by vibrations and rotations. *Wiley-Interscience***,** 69-80.

Nichter, L. S. and Hamas, R. S. (2012) Two-year outcomes with a novel, double-lumen, saline-filled breast implant. *Aesthet Surg J,* 32**,** 861-867.

Notas, G., Kisseleva, T. and Brenner, D. (2009) NK and NKT cells in liver injury and fibrosis. *Clin Immunol,* 130**,** 16-26.

Oppenheimer, B. S., Oppenheimer, E. T., Danishefsky, I., Stout, A. P. and Eirich, F. R. (1955) Further studies of polymers as carcinogenic agents in animals. *Cancer research,* 15**,** 333-340.

Pandya, S. and Moore, R. G. (2011) Breast development and anatomy. *Clin Obstet Gynecol,* 54**,** 91-95

Parker, J. A., Walboomers, X. F., Von den Hoff, J., Maltha, J. C. and Jansen, J. A. (2002) Soft tissue response to microtextured silicone and polylactic acid implants: fibronectin pre-coating vs. radio-frequency glow discharge treatment. *Biomaterials,* 23**,** 3545-3553.

Parsons, J. T. (2003) Focal adhesion kinase: the first ten years. *Cell Science* 116**,** 1409-1416.

Pawley, J. B., Dailey, M., Manders, E., Soll, D. and Terasaki, M. (2006) Handbook of biological confocal microscopy. Confocal microscopy of living cells. *Springer US***,** 381-403.

Pawley, J. B. and Inoué, S. (2006) Handbook of biological confocal microscopy. Foundations of confocal scanned imaging in light microscopy. 1-19.

Pelham, R. J. and Wang, Y. (1997) Cell locomotion and focal adhesions are regulated by substrate flexibility. *Proc. Natl. Acad. Sci. USA,* 94**,** 13661-5.

Pereira, L. and Sterodimas, A. (2009) Transaxillary breast augmentation: a prospective comparison of subglandular, subfascial, and submuscular implant insertion. *Aesthetic Plast Surg,* 33**,** 752-759.

Persichetti, P., Tenna, S., Delfino, S., Abbruzzese, F., Trombetta, M. and Scuderi, N. (2009) Textured and Smooth Breast Implants: Is There a Difference in the Chemical Structure of Silicone?: An Analysis With Fourier Transformation Infrared and Attenuated Total Reflectance Spectroscopy. *Annals of Plastic Surgery,* 63**,** 373-377.

Petit, V. and Thiery, J. P. (2000) Focal adhesions: structure and dynamics. *Biol Cell,* 92**,** 477-494.

Pittet, B., Montandon, D. and Pittet, D. (2005) Infection in breast implants. *Lancet Infect Dis,* 5**,** 94-106.

Polo, M., Smith, P. D., Kim, Y. J., Wang, X., Ko, F. and Robson, M. C. (1999) Effect of TGF-B_2 on proliferative scar fibroblast cell kinetics. *Ann Plast Surg,* 43**,** 185-90.

Prakobwong, S., Pinlaor, S., Yongvanit, P., Sithithaworn, P., Pairojkul, C. and Hiraku, Y. (2009) Time profiles of the expression of metalloproteinases, tissue inhibitors of metalloproteases, cytokines and collagens in hamsters infected with Opisthorchis viverrini with special reference to peribiliary fibrosis and liver injury. *Int J Parasitol,* 39**,** 825-35.

Prantl, L., Schreml, S., Fichtner-Feigl, S., Poppl, N., Eisenmann-Klein, M., Schwarze, H. and Fuchtmeier, B. (2007) Clinical and morphological conditions in capsular contracture formed around silicone breast implants. *Plast Reconstr Surg,* 120**,** 275-84.

Prasad, B. R., Brook, M. A., Smith, T., Zhao, S., Chen, Y., Sheardown, H., D'Souza, R. and Rochev, Y. (2010) Controlling cellular activity by manipulating silicone surface roughness. *Colloids Surf B Biointerfaces,* 78**,** 237-242.

Raso, D. S. and Greene, W. B. (1997) Silicone breast implants: pathology. *Ultrastruct Pathol,* 21**,** 263-271.

Rietdorf, J. and Sibarita, J. B. (2005) Microscopy techniques. Deconvolution microscopy. *Springer,* 95**,** 201-243.

Riveline, D., Zamir, E., Balaban, N. Q., Schwarz, U. S., Ishizaki, T., Narumiya, S., Kam, Z., Geiger, B. and Bershadsky, A. D. (2001) Focal contacts as mechanosensors: externally applied local mechanical force induces growth of focal contacts by an mDia1-dependent and ROCK-independent mechanism. *J Cell Biol,* 153**,** 1175-86.

Rivero, M. A., Schwartz, D. S. and Mies, C. (1994) Silicone lymphadenopathy involving intramammary lymph nodes: a new complication of silicone mammaplasty. *AJR Am J Roentgenol,* 162**,** 1089-1090.

Roberts, A. B. (1995) Transforming growth factor-beta: activity and efficacy in animal models of wound healing. *Wound Repair Regen,* 3**,** 408-18.

Roberts, M. J., Bhatt, N., Voge, C. M., Meshot, E. R., Stegemann, J. P. and Hart, A. J. (2013) Self-assembly of suspended collagen films and their viability as cell culture substrates. *J. Mater. Chem. B,* 1**,** 4711-4718.

Rottner, K., Hall, A. and Small, J. V. (1999) Interplay between Rac and Rho in the control of substrate contact dynamics. *Curr Biol,* 9**,** 640-8.

Roughley, P., Martens, D., Rantakokko, J., Alini, M., Mwale, F. and Antoniou, J. (2006) The involvement of aggrecan polymorphism in degeneration of human intervertebral disc and articular cartilage. *Eur Cell Mater,* 11**,** 1-7.

San-Martin, A., Dotor, J., Martinez, F. and Hontanilla, B. (2010) Effect of the inhibitor peptide of the transforming growth factor beta (p144) in a new silicone pericapsular fibrotic model in pigs. *Aesthetic Plast Surg,* 34**,** 430-437.

Sequeira, S. J., Soscia, D. A., Oztan, B., Mosier, A. P., Jean-Gilles, R., Gadre, A., Cady, N. C., Yener, B., Castracane, J. and Larsen, M. (2012) The regulation of focal adhesion complex formation and salivary gland epithelial cell organization by nanofibrous PLGA scaffolds. *Biomaterials,* 33**,** 3175-3186.

Shackleton, M., Vaillant, F., Simpson, K. J., Stingl, J., Smyth, G. K., Asselin-Labat, M. L., Wu, L., Lindeman, G. J. and Visvader, J. E. (2006) Generation of a functional mammary gland from a single stem cell. *Nature,* 439**,** 84-88.

Shaw, P. (1998) Cell biology: a laboratory handbook. Computational deblurring of fluorescence microscope images. *Academic Press,* 2**,** 206-217

Shin, H., Jo, S. and Mikos, A. G. (2003) Biomimetic materials for tissue engineering. *Biomaterials,* 24**,** 4353-4364.

Slayter, E. (1970) Optical methods in biology. Interactions of light and matter. *Wiley-Interscience***,** 119-152

Snoeijer, J. H. and Andreotti, B. (2008) A microscopic view on contact angle selection. *Phys Fluids,* 20**,** 57101-11.

Spear, S. L., Baker Jr, J. L. and Caffee, H. H. (1995) Classification of capsular contracture after prosthetic breast reconstruction. *Plast Reconstr Surg,* 96**,** 1119-1124.

Spear, S. L., Bulan, E. J. and Venturi, M. L. (2004) Breast augmentation. *Plast Reconstr Surg,* 114**,** 73E-81E.

Spector, D., Goldman, R. and Leinwand, L. (1988) Cells: a laboratory manual, light microscopy and cell structure. Confocal microscopy and deconvolution techniques. *Cold Spring Harbor Laboratory Press,* 2**,** 96.1-96.23

Srinivasan, V. (1998) Discrete morphological filters for metrology. *6th. Symp. on Quality Control in Production***,** 623-628.

Steiert, A. E., Boyce, M. and Sorg, H. (2013) Capsular contracture by silicone breast implants: Possible causes, biocompatibility, and prophylactic strategies. *Medical Devices: Evidence and Research,* 6**,** 211-218.

Steward, R. L., Jr., Cheng, C. M., Ye, J. D., Bellin, R. M. and LeDuc, P. R. (2011) Mechanical stretch and shear flow induced reorganization and recruitment of fibronectin in fibroblasts. *Sci Rep,* 1**,** 1-12.

Stout, K. J. (1993) Development of methods for the characterisation of roughness in three dimensions. *Penton Press***,** 200-241.

Tan, K. T., Baildam, A. D., Juma, A., Milner, C. M., Day, A. J. and Bayat, A. (2011) Hyaluronan, TSG-6, and inter-alpha-inhibitor in periprosthetic breast capsules:

reduced levels of free hyaluronan and TSG-6 expression in contracted capsules. *Aesthet Surg J,* 31**,** 47-55.

Tebbetts, J. B. and Teitelbaum, S. (2010) High- and extra-high-projection breast implants: potential consequences for patients. *Plast Reconstr Surg,* 126**,** 2150-9.

Tebbetts, J. B. M. D. (2006) Dual plane breast augmentation: optimizing implant-soft-tissue relationships in a wide range of breast types. *Plast Reconstr Surg.,* 118**,** 81S-98S.

Thomsen, J. L., Christensen, L., Nielsen, M., Brandt, B., Breiting, V. B., Felby, S. and Nielsen, E. (1990) Histologic changes and silicone concentrations in human breast tissue surrounding silicone breast prostheses. *Plast Reconstr Surg,* 85**,** 38-41.

Tran, P. L., Houdjati, H., Barau, G. and Boukerrou, M. (2014) Breastfeeding after breast surgery: information for patients. *Gynecol Obstet Fertil,* 42**,** 205-209.

Tredget, E. E., Shankowsky, H. A., Pannu, R., Nedelec, B., Iwashina, T., Ghahary, A., Taerum, T. V. and Scott, P. G. (1998) Transforming growth factor-beta in thermally injured patients with hypertrophic scars: effects of interferon alpha-2b. *Plast Reconstr Surg,* 102**,** 1317-28.

Trelleborg, S. S. (2008) Aerospace engineering guide. *Alphaomega***,** 21-22.

Tu, Y., Wu, S., Shi, X., Chen, K. and Wu, C. (2003) Migfilin and Mig-2 link focal adhesions to filamin and the actin cytoskeleton and function in cell shape modulation. *Cell,* 113**,** 37-47.

Tulinska, J., Jahnova, E., Dusinska, M., Kuricova, M., Liskova, A., Ilavska, S., Horvathova, M., Wsolova, L., Kyrtopoulos, S. A., Collins, A., Harrington, V. and Fuortes, L. (2004) Immunomodulatory effects of mineral fibres in occupationally exposed workers. *Mutat Res,* 553**,** 111-24.

Udalova, I. A., Ruhmann, M., Thomson, S. J. and Midwood, K. S. (2011) Expression and immune function of tenascin-C. *Crit Rev Immunol,* 31**,** 115-45.

Ulrich, D., Ulrich, F., Pallua, N. and Eisenmann-Klein, M. (2009) Effect of tissue inhibitors of metalloproteinases and matrix metalloproteinases on capsular formation around smooth and textured silicone gel implants. *Aesthetic Plast Surg.,* 33**,** 555-562.

Ungaro, F., Biondi, M., Indolfi, L., De Rosa, G., La Rotonda, M. I., Quaglia, F. and Netti, P. (2006) Bioactivated polymer scaffolds for tissue engineering. In Topics in Tissue Engineering *N. Ashammakhi & R.L. Reis,* 2**,** 1-38.

Valencia-Lazcano, A. A., Alonso-Rasgado, T. and Bayat, A. (2013) Characterisation of breast implant surfaces and correlation with fibroblast adhesion. *J Mech Behav Biomed Mater,* 21**,** 133-148.

Van Diest, P. J., Beekman, W. H. and Hage, J. J. (1998) Pathology of silicone leakage from breast implants. *J Clin Pathol***,** 493-7.

Wang, Y. H., Yan, Z. Q., Shen, B. R., Zhang, L., Zhang, P. and Jiang, Z. L. (2009) Vascular smooth muscle cells promote endothelial cell adhesion via microtubule dynamics and activation of paxillin and the extracellular signal-regulated kinase (ERK) pathway in a co-culture system. *Eur J Cell Biol,* 88**,** 701-709.

Wangoo, A., Sparer, T., Brown, I. N., Snewin, V. A., Janssen, R., Thole, J., Cook, H. T., Shaw, R. J. and Young, D. B. (2001) Contribution of Th1 and Th2 cells to protection and pathology in experimental models of granulomatous lung disease. *J Immunol,* 166**,** 3432-9.

Westreich, M. (2009) Breast Augmentation. Anthropomorphic measurement of the breast. *Springer,* 3**,** 27-44.

Whalen, R. L. (1988) Improved textured surfaces for implantable prostheses. *ASAIO Trans,* 34**,** 887-892.

Whitehouse, D. (2002) Profile and areal (3D) parameter characterisation. In: Surfaces and their measurement 2002. *Kogan Page Science***,** 5-6.

Williams, T. J. and Jose, P. J. (1981) Mediation of increased vascular permeability after complement activation. Histamine-independent action of rabbit C5a. *J Exp Med,* 153**,** 136-53.

Wilson, N. J., Boniface, K., Chan, J. R., McKenzie, B. S., Blumenschein, W. M., Mattson, J. D., Basham, B., Smith, K., Chen, T., Morel, F., Lecron, J. C., Kastelein, R. A., Cua, D. J., McClanahan, T. K., Bowman, E. P. and de Waal Malefyt, R. (2007) Development, cytokine profile and function of human interleukin 17-producing helper T cells. *Nat Immunol,* 8**,** 950-7.

Winter, G. D. (1962) Formation of the scab and the rate of epithelization of superficial wounds in the skin of the young domestic pig. *Nature,* 193**,** 293-4.

Wynn, T. A. (2008) Cellular and molecular mechanisms of fibrosis. *J Pathol,* 214**,** 199-210.

Wynn, T. A., Barron, L., Thompson, R. W., Madala, S. K., Wilson, M. S., Cheever, A. W. and Ramalingam, T. (2011) Quantitative assessment of macrophage functions in repair and fibrosis. *Curr Protoc Immunol***,** 1-15.

Yamamoto, S., Tanaka, M., Sunami, H., Arai, K., Takayama, A., Yamashita, S., Morita, Y. and Shimomura, M. (2006) Relationship between adsorbed fibronectin and cell adhesion on a honeycomb-patterned film. *Surface Science,* 600**,** 3785-3791.

Yang, N. and Muradali, D. (2011) The augmented breast: a pictorial review of the abnormal and unusual. *ARRS,* 196**,** W451-W460.

Young, T. (1805) An essay on the cohesion of fluids. *Phil Trans R Soc Lond,* 95**,** 65-87.

Young, V. L. and Watson, M. E. (2000) Treatment of subglandular capsular contracture. *Phil Trans R Soc Lond,* 7**,** 137-143.

Young, V. L., Watson, M. E., Boswell, C. B. and Centeno, R. F. (2004) Initial results from an online breast augmentation survey. *Aesthetic Surgery Journal,* 24**,** 117-135.

Zaccone, P., Fehervari, Z., Jones, F. M., Sidobre, S., Kronenberg, M., Dunne, D. W. and Cooke, A. (2003) Schistosoma mansoni antigens modulate the activity of the innate immune response and prevent onset of type 1 diabetes. *Eur J Immunol,* 33**,** 1439-49.

Zahavi, A., Sklair, M. L. and Ad-El, D. (2006) Capsular contracture of the breast: working towards a better classification using clinical and radiologic assessment. *Ann Plast Surg,* 57**,** 248-251.

Zamir, E. and Geiger, B. (2001) Molecular complexity and dynamics of cell-matrix adhesions. *J Cell Sci,* 114**,** 3583-90.

Zhibo, X. and Miaobo, Z. (2009) Effect of sustained-release lidocaine on reduction of pain after subpectoral breast augmentation. *Aesthetic Surgery Journal,* 29**,** 32-34.

Zygo, C. (2005) Surface Texture Parameters. *Metrol Meas Syst***,** 1-20.

Appendix

JOURNAL OF THE MECHANICAL BEHAVIOR OF BIOMEDICAL MATERIALS 21 (2013) 133–148

Available online at www.sciencedirect.com

SciVerse ScienceDirect

www.elsevier.com/locate/jmbbm

Research Paper

Characterisation of breast implant surfaces and correlation with fibroblast adhesion

Anai A. Valencia-Lazcano[a], *Teresa Alonso-Rasgado*[d,*], *Ardeshir Bayat*[b,c]

[a]Bioengineering Group, School of Mechanical, Aerospace and Civil Engineering, The University of Manchester, Manchester M13 9PL, UK
[b]Plastic & Reconstructive Surgery Research, Manchester Institute of Biotechnology, The University of Manchester, Manchester, UK
[c]Department of Plastic & Reconstructive Surgery, University Hospital of South Manchester NHS Foundation Trust, Wythenshawe Hospital, Manchester, UK
[d]School of Materials, The University of Manchester, Manchester Manchester, M13 9PL, UK

ARTICLE INFO

Article history:
Received 16 September 2012
Received in revised form
28 January 2013
Accepted 4 February 2013
Available online 27 February 2013

Keywords:
Breast implants
Cell attachment
Roughness
Wettability
Topography of silicone surfaces
Stiffness

ABSTRACT

Introduction: Capsular contracture formation is a common complication following breast augmentation surgery. Breast implant shells have either a smooth or a textured surface. Smooth surfaces demonstrate a higher incidence of contracture formation. The 3-dimensional surface of textured implants is thought to disrupt contractile forces and reduce capsular contracture rates.

Aim: To investigate the interaction of fibroblasts with silicone breast implant surfaces through characterization of their unique features.

Method: Surfaces of smooth and textured breast implants were characterized using a confocal laser scanning microscope, a microtest 5 kN tensile testing device, and a contact angle goniometer. The kinetics of fibroblast interaction with these surfaces was further analysed.

Results: The textured surfaces were rough, and nodular containing high peaks and deep crevasses with roughness (Sa) values in the range 8.88–18.83 μm and contact angles between 130° and 142°. The smooth implant surfaces were less rough, more regular and repetitive with 0.06–0.07 μm surface roughness, and contact angles between 110.9° and 111.8°. The textured surfaces displayed higher bending stiffness than the smooth surfaces (0.19 and 0.26 N mm). Significant ($p<0.05$) numbers of fibroblasts were attached to the textured surfaces compared to the smooth surfaces which had higher levels of cell adhesion with surface roughness above 8 μm and contact angles above 130°.

Conclusions: In summary, surfaces with arithmetical mean deviation of greater roughness and reduced hydrophilicity with high water contact angles enhanced cell adhesion. These features aid design of improved surfaces, which may help, in prevention of breast capsular formation.

*Corresponding author. Tel.: +44 161 306 3857; fax: +44 161 306 4608.
E-mail address: teresa.rasgado@manchester.ac.uk (A.A. Valencia-Lazcano).

1751-6161/$ - see front matter © 2013 Elsevier Ltd. All rights reserved.
http://dx.doi.org/10.1016/j.jmbbm.2013.02.005

1. Introduction

Capsular contracture is an abnormal hardening and tightening of the capsule around a breast implant, which is a common complication of augmentation mammoplasty (Kjoller et al., 2001). Symptoms, including pain and/or firmness, may be so severe that further surgery is required (Marshall et al., 1989, Spear et al., 2003). A variety of aetiologies have been proposed (see for example, Lavine, 1993, Handel et al., 1995, Burkhardt et al., 1986, Adams et al., 2006) that may predispose to capsular contracture formation including the implant surface topography (Hakelius and Ohlsen, 1997, Ersek, 1991).

Texturing silicone in a pre-determined pattern can alter the host's response to wound healing, so that tissue ingrowth may produce a host prosthesis interface that is more stable, compatible and thinner, that remains softer for longer and promotes decreased capsular contracture (Ersek et al., 1990, Barr and Bayat, 2011). The irregular surface characteristics of textured surfaces promote the growth of fibroblasts into and around the interstices of the surface resulting in an environment where contractile forces tend to cancel each other out. This contact inhibition may result in a thinner capsule formation (Margaret and Ulrich, 2010).

Conversely, smooth surfaces tend to elicit a fibrous reaction wherein all of the collagen fibrils are aligned cumulatively in a connective-tissue capsule adjacent to the implant (Batra et al., 1995). Contractile forces are then parallel to the surface of the prosthesis (Wyatt et al., 1998), which may prevent any attachment of the scar capsule to the prosthesis. Therefore, any movement of the host creates a shearing effect on any microscopic surface irregularity, resulting in a chronic inflammatory, thickly scarred pseudo-bursa around the smooth implant (Emery et al., 1994).

Investigations into the topography, chemical structure and mechanical properties of breast implants have been previously undertaken in order to characterize these implant surfaces in greater detail. Light microscopy, scanning electron microscopy (SEM) and fluorescence optical microscopy have been used to analyze the topography of a range of commercially available breast implants (Barr et al., 2010, Danino et al., 2001, Abramo et al., 2010). These studies have involved both smooth and textured implant surfaces and have revealed the distinct micro- and nano-scale topographies of the sample surfaces considered.

The surface roughness of silicone breast implants has been studied qualitatively using SEM (Schmidt and Von Recum, 1991, Prasad et al., 2010, Mirzadeh et al., 2003) and quantitatively using a variety of techniques including atomic force microscopy (AFM), optical profilometry and scanning mechanical microscopes (Prasad et al., 2010, Lampin et al., 1997). Prasad et al. (2010) measured the surface roughness of polydimethylsiloxane (PDMS) samples using AFM and an optical profilometer. Lampin et al. (1997) obtained surface roughness values when characterizing poly(methyl methacrylate) (PMMA) surfaces using a scanning mechanical microscope. In addition, water contact angles were also obtained for the surfaces.

Mechanical, electromechanical and dynamic testing devices have also been employed in order to provide information regarding implant properties for surface characterization. Necchi et al. (2011) obtained the shell mechanical properties of silicone gel-filled breast implants by means of tensile, dynamic mechanical and tear tests. Prager-Khoutorsky et al. (2011) measured the rigidity of PDMS substrates with an Instron (Instron Ltd, UK) universal testing machine. De Bruijn et al. (2009) undertook tensile strength and pliability testing on a polyester mesh implant used for mastopexy.

Fibroblast growth on breast implant material surfaces has been investigated in an attempt to elucidate the relationship between wound healing and surface topography and consequently the conditions under which capsular contracture could be averted. Prasad et al. (2010) investigated the growth of 3T3 fibroblasts on silicone elastomer samples of varying roughness. Fibroblast growth was found to decrease with increasing surface roughness. A variety of additional techniques have also been applied to provide insightful information, including infrared thermography (Park and Ha, 2009), Fourier transform infrared/attenuated total reflectance (FTIR/ATR) spectroscopy (Persichetti et al., 2009) and differential scanning calorimetry (Mirzadeh et al., 2003) amongst others.

Kolind et al. (2010) studied human fibroblast proliferation and mechanical response of 169 distinct topographies. Fibroblasts proliferated the least and elongated strongly disrupting the actin cytoskeleton anchored to focal adhesions between the pillars on 4–6 μm inter-pillar gap surfaces. Grinnell and Ho (2013) studied the human fibroblast morphological response to substrate stiffness ranging from 0.5 to 40 kPa. They found that high substrate stiffness resulted in strong substrate interactions. Hu et al. (2011) studied the interaction of C2C12 myoblasts and human bone marrow stem cells (hMSCs) with silk-tropoelastin biomaterials. A combination of low surface roughness (Ra=22.8–41.4 nm) and high elastic modulus (20–28 MPa) was favourable for proliferation and differentiation of C2C12 cells. In contrast, hMSCs showed enhanced proliferation at higher surface roughness (Ra=90 nm).

Brown et al. (2010) explored the effect of tissue stiffness on platelet-derived growth factor (PDGF) signalling in vascular smooth muscle cells (VSMCs) using engineered substrates with different mechanical properties. Cell area increased significantly with increased substrate stiffness. Cell area on the 84 kPa substrates was 180% larger than on the 31 kPa substrates ($p<0.01$). Ranella et al. (2010) investigated NIH/3T3 fibroblast cell adhesion on silicon surfaces of gradient roughness ratios and wettabilities. The number of attached cells per unit area decreased as the roughness ratio and wetting angle increased. Huang et al. (2004) investigated the effect of surface roughness of ground Ti on the initial adhesion of osteoblast-like U-2 OS cells. Ti specimens (Ra=0.05 and 0.07 μm) had a surface roughness less optimal for initial cell adhesion (30 min to 24 h), while Ti specimens with Ra of 0.15 μm had the optimal cell adhesion behaviour. Tamada and Ikada (1993) studied the effect of surface wettability on mice fibroblasts adhesion. The optimal water contact angle for cell adhesion was found to be approximately 70°.

It is clear from these studies that the topographical features of the interfaces (surface morphology and surface roughness), and the mechanical properties of the extracellular materials (elastic modulus and rigidity) can have an

important effect on cell adhesion. And although the topography and mechanical properties of breast implants have been investigated, little research has been undertaken to try to elucidate the impact of topography and mechanical properties on implant surface—fibroblast cell interaction, information which may aid in the design of new implants less prone to contracture.

The aim of this study is to investigate the interaction of fibroblasts with silicone breast implant surfaces through characterization of the microstructure of the implant surfaces.

Precise characterisation of the silicone implant surfaces will play a vital role in the development of new, better performing breast implant surfaces with improved qualities. Characterisation of the silicone surfaces will provide properties and features of the surfaces under examination that will enable a deeper understanding of silicone surface—fibroblast cell interaction, allowing the development of surfaces that are less prone to capsular contracture (Barr and Bayat, 2011, Anselme, 2010; Mirzadeh et al., 2003).

2. Methods

Circular samples of 14 mm diameter were removed from each silicone implant shell. These samples were then sterilised by initial sonication in detergent for 10 min, before being rinsed in distilled water. This was followed by sonication in acetone for 10 min. Subsequently the samples were air dried and kept in petri dishes (Barr et al., 2010). The samples were sterilised in order to eliminate any possible contamination from particles on their surfaces.

Three samples of each of the following implant types were used in each of the experimental tests

1. Mentor Siltex surface (Mentor Corporation, Santa Barbara, California).
2. Mentor smooth surface (Mentor Corporation, Santa Barbara, California).
3. Allergan Biocell textured surface (Allergan Medical Corporation, Santa Barbara, California)
4. Allergan smooth surface (Allergan Medical Corporation, Santa Barbara, California)

The characterisation of the breast implant surface shells was investigated using three approaches

1) 3D imaging—surface roughness texture parameter measurement.
2) Optical tensiometry (goniometry) —contact angle measurement.
3) Micro tensile testing—measurement of bending and stretching stiffness.

In addition, the kinetics of fibroblast–silicone implant surface detachment mediated by trypsin was undertaken in order to investigate the adhesive interaction between the fibroblasts and the breast implant surfaces. All experiments were conducted in triplicate. The characterisation and kinetics of detachment tests were performed on the surfaces that come into contact with the tissue of the patient. All tests were performed on these surfaces.

2.1. *Characterisation of the silicone surfaces*

2.1.1. *3-D images*

Silicone surfaces were observed at 20× magnification in three different areas (dimension of each area 644× 642 μm) of each implant after being scanned using a LEXT OLS4000 3D confocal laser scanning microscope. The LEXT OLS4000 uses a 408 nm laser diode and has a resolution on the Z-axis of 10 nm with finely controlled movement of the nosepiece. The microscope creates optical slices from in-focus pixels and combines a stack of slices (z-stack) into one image forming a 2D representation as shown in Figs. 1—4a. These optical slices were then arranged into a highly accurate 3D image (Figs. 1–4b) from which the surface roughness parameter values were obtained. The 20× objective has a depth of field of 6 μm and the number of z slices to construct the 3D image was selected automatically by the software from the objective and magnification settings. Detailed information about the internal settings of the microscope, including pin hole size, cannot be reproduced here as it is proprietary to the manufacturer.

The tests were undertaken five times in order to ensure repeatability of the tests.

2.1.2. *Surface roughness parameters*

Surface texture measurements were carried out using the Olympus LEXT laser microscope (Olympus Corporation, Japan). The tests were carried out on three sample areas using a 100 μm scale.

Roughness, skewness and kurtosis were measured in order to characterise the surface of the implants. Maximum values of peak height, valley depth and surface height of the surface were also obtained.

Skewness represents the degree of symmetry of the surface heights about the mean plane. A negative value of skewness indicates the predominance of valleys; a positive value indicates the predominance of peaks. Kurtosis indicates the randomness of heights and sharpness of the structures comprising the surface. A perfectly random surface has a kurtosis value of 3; the farther the result is from 3, the less random and more repetitive the surface is.

In addition, measurements of the core roughness of the surface, reduced peak height, reduced valley depth, load area ratio of reduced peak part to core part and load area ratio of reduced valley part to core part, were undertaken.

Core roughness (peak-to-valley) of the surface is the roughness of the surface calculated with the predominant peaks and valleys removed. Reduced peak height is a measure of the peak height above the core roughness; reduced valley depth is a measure of the valley depth below the core roughness. The load area ratio of reduced peak part to core part indicates the percentage of material that comprises t he peak structures associated with the reduced peak height. The load area ratio of reduced valley part to core part relates to the percentage of the measurement area that comprises

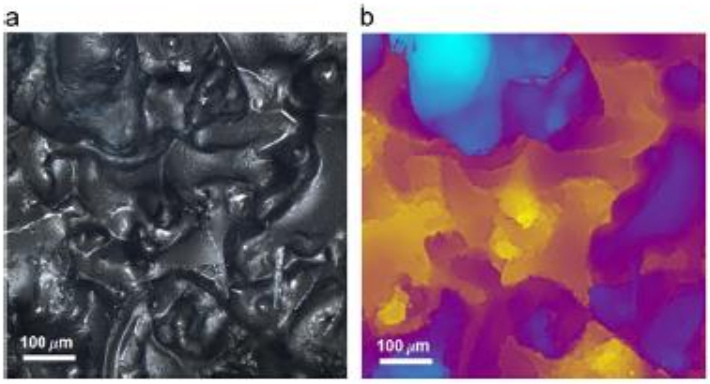

Fig. 1 – Mentor Siltex textured surface. (a) Shows 100 μm scale planar image visualised on a LEXT OLS4000 3D laser measuring microscope. The topography reveals a rough surface composed of textured nodules with high peaks and deep plunging crevasses. The nodular outcrops are separated from one another by apparently smooth-surface crevasses. The surface is almost geographical with peaks that are frequently covered in silicone debris. (b) Shows the confocal laser scanning microscope image obtained using colour height information (taken on the Olympus LEXT with 20 × magnification, image scale bar 100 μm). The yellow coloured areas indicate the valleys which are from 0 to 66 μm deep, while the purple areas correspond to the core of the profile which is between 132 and 197 μm in height. The peaks of the surface can be discerned by the blue coloured areas which are 263 to 328 μm high. The image was captured as a 3D data set and the measurement of plane roughness on the entire surface (644 × 642 μm) was taken. The average surface roughness measurement of three different areas was evaluated and an arithmetic mean roughness value of 8.88 ± 0.5 μm was obtained. (For interpretation of the references to colour in this figure legend, the reader is referred to the web version of this article.)

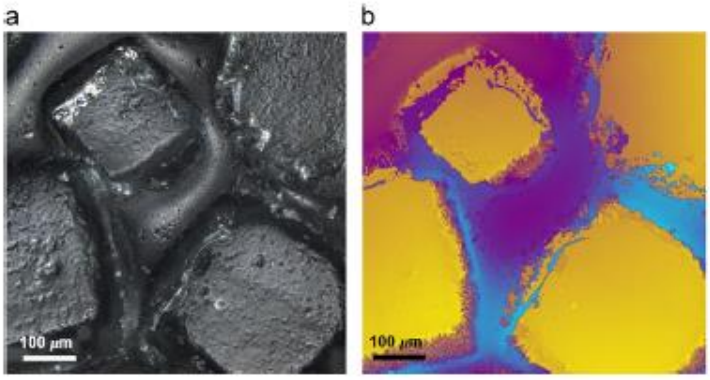

Fig. 2 – Allergan Biocell surface. (a) Shows 100 μm scale planar image visualised on a LEXT OLS4000 3D laser measuring microscope. The image shows a granular surface which is pitted with cuboid shaped wells. The bases of these pits are irregular with ridges. (b) Shows the confocal laser scanning microscope image obtained using colour height information (taken on the Olympus LEXT with 20 × magnification, image scale bar 100 μm). The valleys of the surface, shown in yellow, are from 0 to 91 μm deep. The purple coloured regions, which correspond to the core of the profile, are between 182 and 273 μm high. The peaks of the surface can be distinguished in blue, and range from 364 to 455 μm in height. The image was captured as a 3D data set and the measurement of plane roughness on the entire surface (644 × 642 μm) was taken. The average surface roughness measurement of three areas was evaluated and an arithmetic mean roughness value of 18.83 ± 0.91 μm was obtained. (For interpretation of the references to colour in this figure legend, the reader is referred to the web version of this article.)

the deeper valley structures associated with the reduced valley depth.

The criterion employed to determine the core roughness is based on the linear material ratio curve. This curve represents the material ratio of the profile and it is defined as a three-layer surface model, evaluating the peaks, the core and the valleys separately (ISO 13565-2). The evaluation process for determining parameters from the linear representation of the material ratio curve describes the increase of the material portion of the surface with increasing depth of the roughness

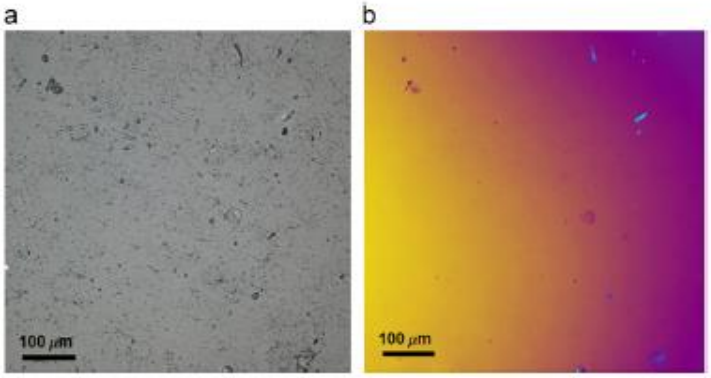

Fig. 3 – Mentor smooth surface. (a) Shows 100 μm scale planar image visualised on a LEXT OLS4000 3D laser measuring microscope. The image reveals an inherently regular, ridged topography. The surface depicts a geographical surface with rocky formations and small pits. (b) Shows the confocal laser scanning microscope image obtained using colour height information (taken on the Olympus LEXT with 20x magnification, image scale bar 100 μm). The deepest areas of the sample are shown in yellow and range from 0 to 4.4 μm in depth, while the purple areas correspond to the core of the profile which are from 8.7 to 13 μm high. The surface peaks are coloured blue and range from 17.4 to 22 μm in height. The average surface roughness measurement of three areas was evaluated and an arithmetic mean roughness value of 0.06 ± 0.02 μm was obtained. (For interpretation of the references to colour in this figure legend, the reader is referred to the web version of this article.)

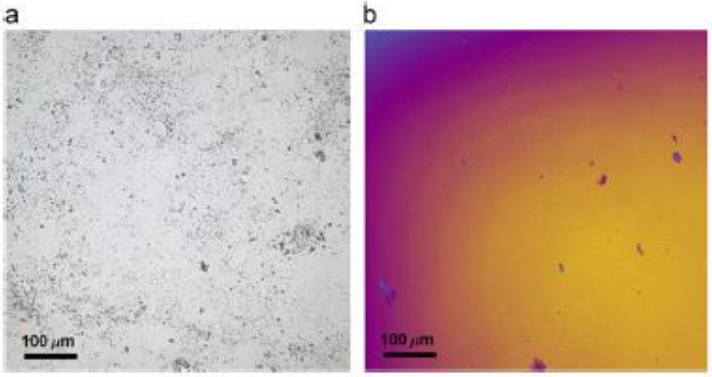

Fig. 4 – Allergan smooth surface. (a) Shows 100 μm scale planar image visualised on a LEXT OLS4000 3D laser measuring microscope. The image reveals an inherently regular, ridged topography. The surface is geographical with rocky formations and small pits. (b) Shows the confocal laser scanning microscope image obtained using colour height information (taken on the Olympus LEXT with 20 × magnification, image scale bar 100 μm). The yellow coloured areas indicate the valleys which are from 0 to 2.2 μm deep, while the purple areas correspond to the core of the profile which is between 4.5 to 6.7 μm high. The surface peaks can be distinguished in blue and range from 9 to 11 μm in height. The average surface roughness measurement of three areas was evaluated and an arithmetic mean roughness value of 0.07 ± 0.01 μm was obtained. (For interpretation of the references to colour in this figure legend, the reader is referred to the web version of this article.)

profile. The kernel is established by using 40% of the measured profile points to find the most horizontal region (Rk line). This is determined by moving the secant line for $\Delta Mr = 40\%$ along the material ratio curve, starting at the $Mr = 0\%$ position. The secant line for $\Delta Mr = 40\%$ which has the smallest gradient establishes the central region of the material ratio curve. The peak and valley transitions were found based on the Rk line. The parameters reduced peak height and the reduced valley depth are each calculated as the height of the right-angle triangle which is constructed to have the same area as the peak area or valley area respectively.

Void volume parameters were ascertained for each sample of the implant surfaces, namely, the void volume at a valley region, void volume at a core part, actual volume at a peak region and actual volume at a core part.

The void volume at the valley region and the void volume at a core part together yield a measure of the void volume provided by the surface between various heights as established by the chosen material ratio values. Thus these two void volume parameters indicate how much fluid would fill the surface. The actual volume at a peak region provides a measure of the material forming the surface at the various heights down from the highest peak of the surface or between various heights as defined for the region. It indicates how much material may be worn away for a given depth of the bearing curve. The actual volume at a core part, indicates how much material is available for load support once the top levels of a surface are worn away.

The values of the surface roughness texture parameters were obtained by applying the Olympus LEXT laser microscope software to the scanned images. The cut-off length was chosen to be 80 μm as the dimensions of the scanned area were 644 × 642 μm.

2.1.3. *Optical tensiometry—contact angle measurement*

Contact angle, θ, is the angle formed by a liquid at the three-phase boundary where a liquid, gas and solid intersect. It is a quantitative measure of the wettability of a solid by a liquid. The contact angle of a drop of water on the textured and smooth implant surfaces was measured enabling a comparison to be made. Measurements were taken using a contact angle meter CAM 200 system [ramé-hart instrument co, USA]. The CAM 200 is a video camera based computer with a controlled contact angle meter that provides video capture of images for analysis. The DROPimage image analysis software package [ramé-hart instrument co, USA] was employed to calculate contact angle values from the images obtained from the CAM 200 system (Jopp et al., 2004). Fig. 5 shows how the contact angle was calculated for a drop of water on the breast implant samples from images captured using the CAM 200 system using the DROPimage image analysis software package.

2.1.4. *MicroTensile testing—measurement of bending and stretching stiffness.*

In order to determine the mechanical properties of the breast implant surfaces a tensile test was carried out using a Microtest 5 kN tensile testing device (Deben, UK). Fig. 6a depicts the Deben UK instrument used for this test. Three samples from each of Allergan (smooth and textured) and Mentor (smooth and textured) implants were tested. These samples had dimensions of 30 mm × 10 mm and their thicknesses varied from 0.45 to 0.75 mm. In order to carry out the test, a sample was mounted horizontally onto the machine. The sample was clamped by a pair of jaws leaving 10 mm length in the middle as gauge length. During the tensile test a dual screw pulled the jaws symmetrically in opposite directions (Fig. 6b). The samples were stretched at a constant speed of 1.5 mm per minute up to 100% strain and force–elongation data was recorded every 200 ms. The tensile testing stage was computer controlled and the resulting force/displacement curves were displayed in real time.

The force–displacement data were used to estimate the dynamic elasticity of the samples at biologically relevant strains.

For the purpose of characterisation of the breast implant surfaces, stiffness is a more suitable parameter than the Young's modulus (E), as stiffness includes the effect of implant thickness (t). Hence two stiffness parameters—stretching stiffness (Et) and bending stiffness (D) (Fenner, 1989, Fellers, 2009) —were estimated for the samples.

2.1.5. *Kinetics of fibroblast–silicone surface detachment mediated by trypsin*

Cultured human skin fibroblasts were established from skin biopsies taken from a healthy subject. All cultures were passage three and were grown to confluence in 125 ml culture flasks in Dulbecco's Culture Medium (DMEM) substituted with 10% fetal bovine serum, 1% L-glutamine (PAA), 1% non-essential amino acid solution (Sigma) and 1% penicillin/streptomycin (PAA) at 37 °C in a 5% CO_2 atmosphere.

The cells were arrested to take them to the G0/G1 phase, 16 h later dissociated cell suspensions were seeded in triplicate on silicone surfaces placed in the tissue culture in 24 well-plates to a concentration of 5.1×10^4 cells in 1 ml of complete media per well and incubated for 24, 48 and 72 h at 37 °C. After setting times the incubation media was discarded and the surfaces were washed once with PBS. 400 μl of 0.25%

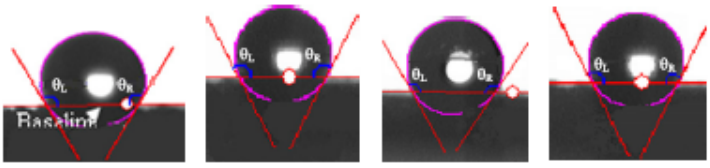

Fig. 5 – Contact angle values of the silicone sample surfaces measured using a contact angle meter. Profile views of a 10 μl drop of nuclease-free water on the implant sample surfaces. The baseline is shown to indicate where the droplet ends and the surface begins. The droplet shape was determined and from this the contact angles were calculated. The contact angle is the average of the right (θ_R) and left (θ_L) contact angles for the drop. Values are the average of nine measurements. From the measurements it was determined that the Allergan Biocell textured sample is the most hydrophobic surface, exhibiting a contact angle of 142 ± 2°. The Mentor smooth sample was the least hydrophobic surface, having an average contact angle of 110.9° ± 1.4°.

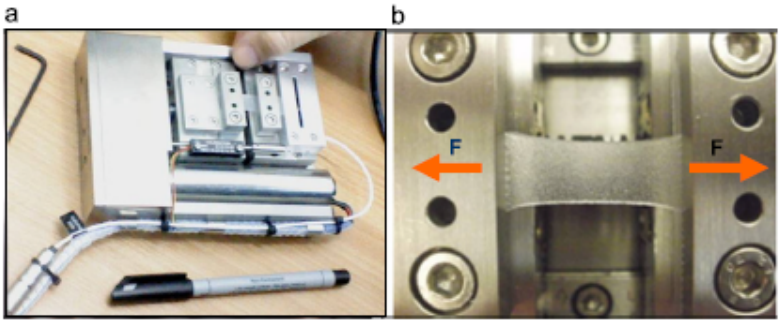

Fig. 6 – Microtest 5 kN tensile, compression and horizontal bending stage module (Deben, UK) depicted during a tensile test of the Mentor textured implant sample. (a) Shows the sample prior to testing. (b) Shows the sample during tensile testing with the Mentor textured implant sample elongated by 10 mm.

trypsin was added to each well. At 2-min intervals (from 5 to 17 min) a sample of 100 μl of trypsin was then removed from each well and replaced with 100 μl of fresh trypsin. The well plate was moved gently before taking the sample to homogenize it. The sample of trypsin was poured into an eppendorf tube and 200 μl of complete media was added to stop the trypsin reaction. The detached cells were then centrifuged and resuspended in 200 μl complete media and their number counted with a C6 flow cytometer (Accuri Cytometers, Inc., Michigan, U.S.A.). Wells of cells prepared for the zero-time point of trypsinisation were incubated in trypsin until they were completely detached. Cell-substratum detachment at a given time point was expressed as the percentage of detached cells relative to those detached at time zero. Each experiment was conducted in triplicate.

3. Results

3.1. Surface characterization

3.1.1. 3-D images

The 3-D images of the samples surfaces obtained using the LEXT OLS4000 3D laser measuring microscope are shown in Figs. 1–4. The planar images obtained are depicted in Figs. 1–4a; the corresponding topological models obtained using colour-height information are shown in Figs. 1–4b. The images reveal the textured surfaces to be relatively rough and nodular, consisting of high peaks and deep crevasses, having roughness (*Sa*) values in the range 8.88–18.83 μm. The smooth implant surfaces are more regular and repetitive and less rough, exhibiting roughness (*Sa*) values in the range 0.06–0.07 μm.

3.1.1.1. *Mentor Siltex surface*. The Mentor textured surface shows high peaks and deep plunging crevasses (Fig. 1). The topography reveals a rough surface composed of textured nodules. The texture is an outcome of the manufacturing process in which a negative-contact imprint of polyurethane foam is formed on the surface (Barr and Bayat 2011). The nodular outcrops are separated from one another by apparently smooth-surface crevasses. The surface is almost geographical and the arithmetic mean roughness was 8.88 ± 0.5 μm.

3.1.1.2. *Allergan Biocell textured surface*. The Allergan Biocell textured surface depicts a granular surface which is pitted with cuboid shaped wells (Fig. 2). These wells are formed by granular salt during the manufacturing phase, which are subsequently washed away (Barr and Bayat, 2011). The bases of these pits are irregular with ridges. The polyhedra are approximately 235–522 μm in width and the distance between them varies from 37 to 358 μm. The arithmetic mean roughness was 18.83 ± 0.91 μm.

3.1.1.3. *Allergan and Mentor smooth surfaces*. The Allergan and Mentor smooth surfaces were characterised by an inherently regular, ridged topography; both surfaces depicted a geographical surface with rocky formations and small pits (Figs. 3 and 4). The topography observed results from silicone creeping down the implant template during the curing process (Barr and Bayat, 2011). The arithmetic mean roughness was 0.07 ± 0.01 μm for the Allergan smooth surface and 0.06 ± 0.02 μm for the Mentor smooth surface.

3.1.2. Surface roughness parameters

The roughness parameters of the textured and smooth samples were obtained using the LEXT OLS4000 3D laser measuring microscope. The maximum average surface roughness was obtained for Allergan Biocell textured sample, which had a value of 18.83 μm and the lowest, 0.06 μm, was obtained for the Mentor smooth surface. The values obtained for the additional roughness parameters are given in Tables 1–4.

The negative skewness value measured for the Mentor Siltex sample (*Ssk* = −0.22) indicates the predominance of valleys on this surface; the positive skewness values exhibited by the Allergan Biocell (*Ssk* = 0.38), Allergan smooth (*Ssk* = 12.27) and the Mentor smooth (*Ssk* = 14.11) samples reveal that peaks are the prevailing characteristic on the surfaces of these samples.

The Mentor smooth samples exhibited a relatively high kurtosis value (*Sku* = 333.57) indicating a repetitive surface with spikes. The lower kurtosis values obtained for the

Table 1 – 3D surface parameters—amplitude parameters skewness and kurtosis measured with LEXT OLS4000 3D laser measuring microscope. Skewness (Ssk) represents the degree of symmetry of the surface heights about the mean plane. Kurtosis (Sku) indicates the randomness of heights and sharpness of the structures comprising the surface.

Breast implant	Skewness		Kurtosis	
Mentor Siltex textured	−0.22 ± 0.27	Predominance of valleys	8.38 ± 1.57	Random and bumpy surfaces
Allergan Biocell textured	0.38 ± 0.35	Predominance of peaks	10.23 ± 0.26	
Mentor smooth	14.11 ± 3.6		333.57 ± 108	More repetitive surface with spikes
Allergan smooth	12.27 ± 1.03		281.53 ± 48	

Mentor Siltex (*Sku*=8.38), and Allergan Biocell (*Sku*=10.23) implants indicate that these surfaces are more random and bumpy.

The relatively large reduced peak height value obtained for the Allergan Biocell sample (*Spk*=62.75 μm), implies a surface composed of high peaks providing small initial contact area and thus high areas of contact stress (force/area) when the surface is contacted. Thus reduced peak height may represent the nominal height of the material that may be removed during a 'running-in' operation. Consistent with reduced peak height, the load area ratio of reduced peak part to core part (*SMr1*) represents the percentage of the surface that may be removed during 'running-in'. The Allergan Biocell sample has the highest *SMr1* value indicating that for this sample, a larger percentage of area would be removed once the implant was in place in the body. The core roughness measure indicates the roughness of the surface over which a load may be distributed after the surface has been 'run-in'. The Mentor textured sample has the highest core roughness value, *Sk*=17.52 μm, which is relatively high in comparison with the value obtained for the Mentor smooth surface, *Sk*=0.11 μm.

The reduced valley depth is a measure of the valley depth below the core roughness and may be related to fluid retention and debris entrapment. The implant surface which would potentially retain the greatest amount of fluid and debris is the Allergan Biocell sample, with *Svk*=58.67 μm and load area ratio of reduced valley part to core part, *SMr2*=74.19%. The implant that is likely to retain the least fluid is the Allergan smooth surface, with *Svk*=0.17 μm and *SMr2*=86.94%.

The void volume parameters ascertained for the samples indicate that the Allergan Biocell surface can contain the largest volume of fluid, with *Vvc*+*Vvv*=36.92 μm while the Mentor smooth implant can only contain *Vvc*+*Vvv*=0.07 μm, the lowest value of all the samples considered. Of the four implant surfaces tested, the Allergan Biocell sample exhibited the highest value for the volume that may be worn away in the run-in period, having a *Vmp* value of 3.32 μm. The Allergan biocell textured sample has the greatest volume of material available to support load, with *Vmc*=14.04 μm.

3.1.3. *Hydrophobicity: Contact angle measurement*

The resulting contact angle values obtained from the CAM 200 system using the DROPimage image analysis software package are given in Fig. 7 and Table 4. The largest contact angle (142 ± 2°) belongs to the Allegan Biocell textured surface while the lowest was obtained for the Mentor smooth surface (110.9 ± 1.4°). The values indicate that the Allergan Biocell textured surface is less wettable than the Mentor smooth surface.

3.1.4. *Stiffness: Microtest tensile testing*

All samples exhibited strongly non-linear force displacement behaviour. The mean force–displacement curves for each sample are shown in Fig. 8.

The stretching stiffness of the sample is the slope of the force–displacement curve, and this is also strongly non-linear. The mean dynamic stretching stiffness curves were obtained by differentiation of the polynomial fit equations and these are shown in Fig. 9.

The biologically relevant strain region is expected to be between 0 and 10% strain, and so the stretching stiffness (*k*), which is given by Young's modulus times the thickness ($E \times t$), is approximated by the slope of the force–displacement curve. The bending modulus (*D*) is proportional to $k \times t^2$ provided Poisson's ratio is constant in the region of interest. The estimated stretching stiffness and bending modulus for the samples are shown in Table 4. The variation in stretching stiffness can be attributed to the difference in manufacturing procedures for different implants, whereas the variation in bending stiffness is primarily due to variation in thickness. The textured surfaces showed higher bending stiffness. Among all the surfaces, Mentor smooth implants had the lowest thickness that resulted in the lowest bending stiffness. Besides the effect of surface roughness on fibroblast adhesion, the variation in thickness affects mechanical stiffness, which in turn may change the performance of breast implants.

3.1.5. *Kinetics of fibroblast–silicone implant surfaces detachment mediated by trypsin*

This assay directly measures the number of cells that detach from the silicone surfaces following trypsinisation using the Accuri C6 flow cytometer (Accuri Cytometers, Inc., Michigan, U.S.A.). In three series of experiments at 24, 48 and 72 h incubation using cultures derived from healthy human skin, trypsin-induced detachment of normal cultured skin fibroblasts was scored at 2-min intervals. The resulting attachment values calculated are given in Figs. 10–12 and in Table 4. Cell-substratum attachment at a given point in time is expressed as the percentage of attached cells relative to those attached at time zero. The results displayed are the mean percentage cell attachment derived from three experiments. Data was analyzed for significance using ANOVA. The difference between the means for all conditions was

Table 2 – Areal material parameters measured with LEXT OLS4000 3D laser measuring microscope. *Spk* (reduced peak height), *Sk* (level difference for a core part, a measure of core roughness), *Svk* (reduced valley depth), *SMr1* (load area ratio to separate between a reduced peak part and a core part) and *SMr2* (load area ratio to separate between a reduced valley part and a core part).

Breast implant	Profile	Areal material parameters	
Mentor Siltex textured	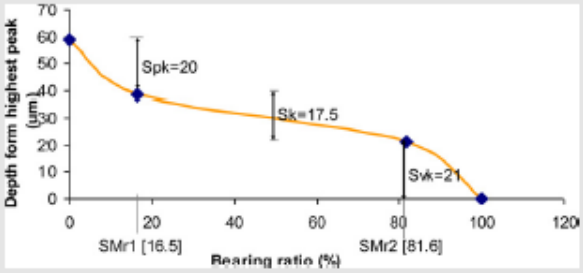	Sk[μm] Spk[μm] Svk[μm] SMr1[%] SMr2[%]	17.52±1.4 20.05±2.1 21.09±1.6 16.58±0.3 81.68±1.1
Allergan Biocell textured	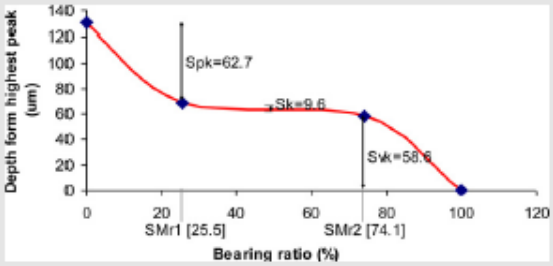	Sk[μm] Spk[μm] Svk[μm] SMr1[%] SMr2[%]	9.63±2.8 62.75±3.9 58.67±2.1 25.50±0.7 74.19±1.3
Mentor smooth	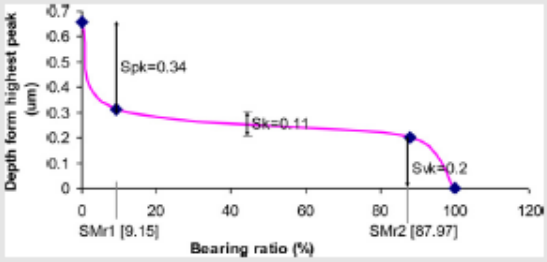	Sk[μm] Spk[μm] Svk[μm] SMr1[%] SMr2[%]	0.11±0.01 0.34±0.2 0.20±0.1 9.15±0.1 87.97±1
Allergan smooth	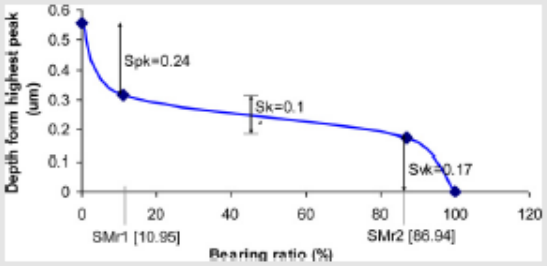	Sk[μm] Spk[μm] Svk[μm] SMr1[%] SMr2[%]	0.14±0.006 0.24±0.04 0.17±0.01 10.95±0.6 86.94±0.1

considered statistically significant at $P<0.05$ employing Prims-4 GraphPad software (San Diego, CA, USA). As expected, there was a decrease in the number of cells attached over time in all surface and a significant difference was detected in the trypsin-induced detachment rates between the smooth and textured silicone surfaces.

Upon inspection of Fig. 10 it can be seen that after 24 h of incubation, there was a decrease in the number of cells attached over time as expected on all surfaces. Adhesion on the Mentor Siltex, Allergan Biocell and Allergan smooth samples did not differ significantly ($P>0.05$). Adhesion was significantly decreased on Mentor smooth ($P<0.01$) surfaces compared with the textured surfaces.

Figs. 11 and 12 indicate that after incubations times of 48 and 72 h, respectively, adhesion on the Mentor siltex, and Allergan Biocell textured samples did not differ significantly ($P>0.05$). In addition, there was no significant difference between the adhesion on the Mentor smooth and Allergan

Table 3 – Bearing curves illustrating the core and valley fluid retention indexes measured with LEXT OLS4000 3D laser measuring microscope. *Vvv* (void volume at valley region), *Vvc* (void volume at a core part), *Vmp* (actual volume at a peak region), *Vmc* (actual volume at a core part).

Breast implant	Profile	Material volume parameters (μm³/μm²)	
Mentor Siltex textured	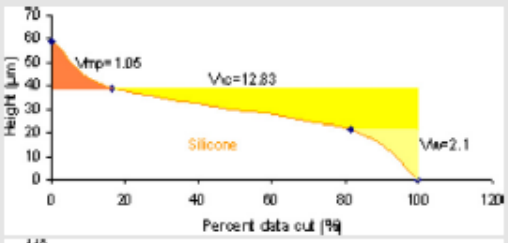	Vvv Vvc Vmp Vmc Vvc+Vvv	2.1±0.16 12.83±0.75 1.05±0.13 8.56±0.31 14.93±0.84
Allergan Biocell textured	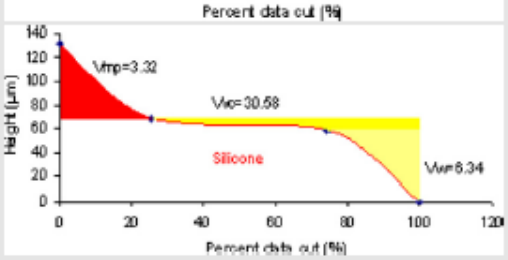	Vvv Vvc Vmp Vmc Vvc+Vvv	6.34±0.39 30.58±0.87 3.32±0.36 14.04±0.43 36.92±1.07
Allergan smooth	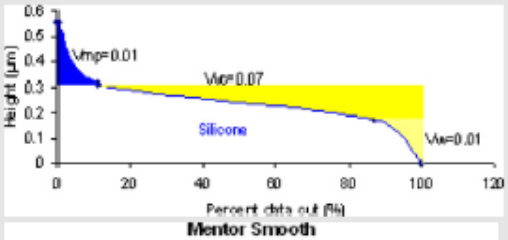	Vvv Vvc Vmp Vmc Vvc+Vvv	0.01±0 0.07±0 0.01±0 0.05±0 0.08±0
Mentor smooth	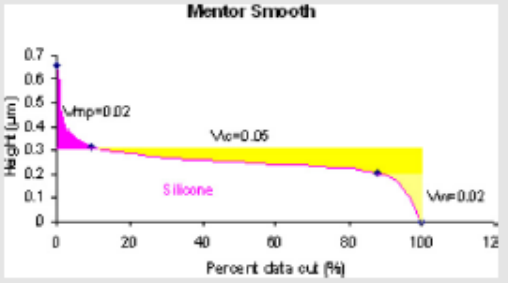	Vvv Vvc Vmp Vmc Vvc+Vvv	0.02±0.01 0.05±0 0.02±0.01 0.04±0 0.07±0.01

smooth samples ($P>0.05$). Adhesion on the smooth surfaces was significantly less than on the textured surfaces ($P<0.001$).

Overall, the figures indicate that the smooth surface samples (Mentor and Allergan smooth) generally exhibited lower initial adhesion than the textured surface samples (Mentor Siltex textured, and Allergan Biocell textured). Repeated measures two-way ANOVA on the cell attachment data with incubation time and surface texture as factors indicated that there was no significant main effect for incubation time but there was a highly significant main effect for surface texture $P<0.0001$).

Fig. 13 shows that when the number of cells attached is averaged across both textured and smooth samples there is a clear difference in the rate at which cells are detached from the substrate. The linear nature of the relationship between the natural logarithm of the data and decay time indicates that cells detach in an exponential fashion. The decay constant for textured surfaces is approximately an order of magnitude smaller than for smooth surfaces (0.029 for textured compared with 0.29 for smooth).

4. Discussion

This paper has described an investigation into the characterization of microstructure surfaces of commercially available breast implants. A variety of experimental techniques were

Table 4 – Summary of results.

			Mentor Siltex textured	Allergan Biocell textured	Mentor smooth	Allergan smooth
LEXT OLS4000 3D laser measuring microscope	Images surface features		Nodular textured surface.	Granular surface which is pitted with cuboid shaped wells.	Surface with small pits.	Regular ridged topography.
	Roughness Sa (μm)		8.88 ± 0.5	18.83 ± 0.91	0.06 ± 0.02	0.07 ± 0.01
	Skewness		−0.22 ± 0.27	0.38 ± 0.35	14.11 ± 3.6	12.27 ± 1.03
	Kurtosis		8.38 ± 1.57	10.23 ± 0.26	333.57 ± 108.06	281.53 ± 48.03
	Core and valley fluid retention ($\mu m^3/\mu m^2$)		14.93 ± 0.84	36.92 ± 1.07	0.07 ± 0.01	0.08 ± 0
Contact angle 10 μl			130 ± 2°	142 ± 2°	110.9 ± 1.4°	111.8 ± 1.2°
Mean thickness (mm)			0.71 ± 0	0.74 ± 0.04	0.45 ± 0.02	0.51 ± 0.01
Stretching stiffness ($N\,mm^{-1}$)			0.37 ± 0.03	0.47 ± 0.03	0.29 ± 0.02	0.46 ± 0.05
Bending modulus (N mm)			0.19 ± 0.02	0.26 ± 0.02	0.06 ± 0.01	0.12 ± 0.01
% Cell attachment	**24 h Incubation**	5	90	92	38	76
		7	85	91	21	73
		9	85	84	21	58
		11	83	79	15	47
		13	82	56	5	47
		15	78	55	4	5
		17	77	49	0	0
	48 h Incubation	5	79	80	16	37
		7	78	71	10	36
		9	77	66.5	7	34
		11	76	61.5	7	22
		13	73	58.5	6	18
		15	64	56	3	14
		17	42	49.5	0.66	12
	72 h Incubation	5	88	86	21	8
		7	85	77	18	7
		9	81	77	15	7
		11	80	76	14	6
		13	79	73	10	3
		15	78	71	7	3
		17	77	71	1.66	2
Kinetics of attachment						
	24 h of incubation		48 h of incubation		72 h of incubation	
No differences were noted in fibroblast adhesion between	Mentor Siltex, Allergan Biocell and Allergan smooth ($P > 0.05$)		Mentor Siltex, and Allergan Biocell textured ($P > 0.05$) Allergan smooth from Mentor smooth ($P > 0.05$)			
Fibroblasts adhesion was significantly lower on	Mentor smooth ($P < 0.01$) compared to the rough surfaces		Mentor and Allergan smooth ($P < 0.001$) compared to the rough surfaces			

employed including 3-D imaging, surface roughness and hydrophobicity measurement and micro tensile testing. In addition, experimental tests were undertaken in order to examine the kinetics of fibroblast–silicone surface detachment of the implants. The correlation between surface characteristics and fibroblast adhesion was analysed.

The 3-D imaging and surface roughness parameter measurement of the implant samples revealed the textured surfaces to be rough, nodular surfaces containing high peaks and deep crevasses. The magnitude of the skewness values obtained for the textured surfaces was relatively small indicating that the predominance of either valleys or peaks was weak in both of the samples. The Mentor and Allergan smooth samples displayed surfaces with features that were less rough and more regular and repetitive than those of the textured surfaces. Peaks were the predominant feature on these smooth surfaces, however both the magnitudes of both peak height above and valley depth below the core roughness were relatively small compared to those of the textured surfaces.

The textured surfaces were significantly rougher than smooth surfaces exhibiting average surface roughness measurements which were 130–320 times greater than the Allergan and Mentor smooth samples and a core roughness measure, Sk, that was between 69 and 160 times higher. In addition, the maximum surface heights of the textured surfaces were between 21–57 times greater than the smooth samples. Both maximum peak height and valley depth of the textured surfaces were significantly higher than the smooth samples, between 12 and 46 times for peak height and 56–98 times for valley depth.

The fluid retention indices determined for the breast implant samples indicated that the smooth implant surfaces

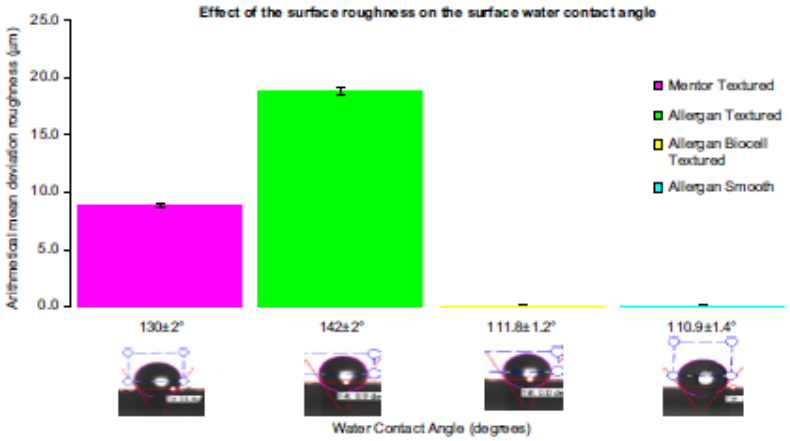

Fig. 7 – Effect of silicone implant surface roughness (Sa) on the surface water contact angle. The Allergan Biocell textured implant was the most hydrophobic surface as well as the roughest surface, while the Mentor smooth implant was the smoothest and least hydrophobic surface among all the breast implants studied.

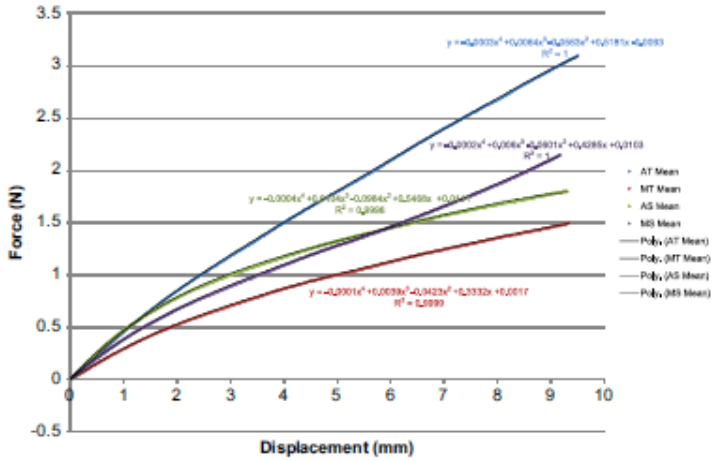

Fig. 8 – Mean force–displacement curves for all samples with fourth order polynomial fit lines and equations.

would require significantly less fluid than the textured samples to fill the surface voids. The contact angle measurements for water droplets placed on the sample surfaces revealed that the rougher the surface, the larger the contact angle and consequently the greater the hydophobicity (Fig. 7). The textured surfaces exhibited higher roughness values, contact angles and hydrophobicity than the smooth sample surfaces.

The adhesiveness of human skin fibroblasts on the breast implant surfaces was analyzed in terms of the resistance to detachment with trypsin. In this study, the effect of surface roughness on normal skin cell adhesion was investigated on implant samples with surface roughnesses in the range 0.06 ± 0.02 to $18.83 \pm 0.91\,\mu m$. The results show that fibroblasts adhere significantly better on the textured, rougher surfaces than on the smoother surfaces (Table 4). Lower levels of cell adhesion were observed on surfaces with roughnesses of $0.07 \pm 0.01\,\mu m$ and lower, while higher levels of cell adhesion were observed for the samples with surface roughness above $8\,\mu m$. At the end of the tests following 24 and 72 h incubation the highest number of cells remained attached to the Mentor Siltex textured sample whereas following 48 h incubation, the Allergan Biocell textured surface demonstrated the highest cell attachment. The Mentor Siltex sample exhibited higher average cell attachments than the Allergan Biocell sample over the test periods following incubations of 24, 48 and 72 h. The skewness value obtained for the Mentor Siltex sample indicated a slight predominance of valleys in the surface topology, which is in contrast to the Allergan Biocell sample, where peaks predominate.

Comparing the kinetics of attachment after 24, 48 and 72 h of incubation and the sample contact angle measurement, it

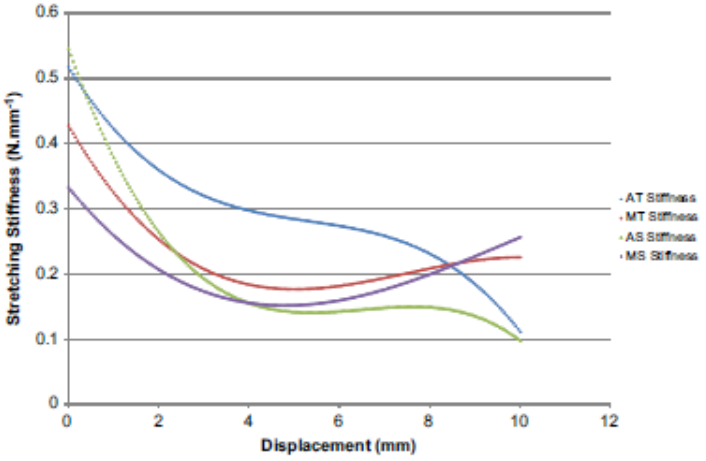

Fig. 9 – Mean dynamic stretching stiffness for all samples.

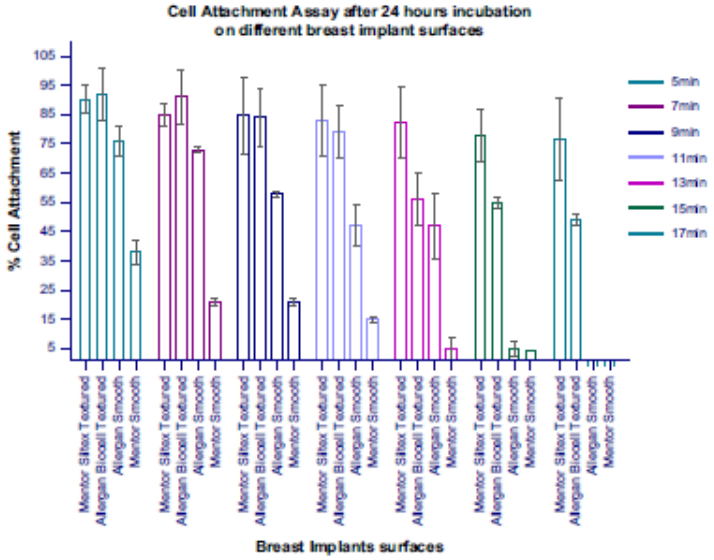

Fig. 10 – Comparison of normal skin fibroblast attachment to four implant surfaces after 24 h of incubation.

was found that surfaces exhibiting contact angles of 130° and greater and surface roughnesses above 8 μm (Mentor Siltex, Allergan Biocell) provided greater rates of attachment compared to surfaces with contact angles less than 112° and roughnesses of 0.07 μm and below (Allergan smooth, Mentor smooth). The rationale of this behaviour suggests that rough surfaces provide a greater area of attachment in comparison to the smooth ones because the cells are able to infiltrate the interstices of the textured surfaces. Take into consideration that a typical fibroblast has the following dimensions 50–100 × 30 × 3 μm. The grooves of, for example, the Allergan Biocell textured implant surface are 52.02–358 μm width, so it is possible that many cells spread along these interstices. Additional studies are needed to evaluate cell attachment in the groove and ridge transitions in terms of the area of the adhesive contact and to study cell spreading in the micropatterns of these breast implants.

The results of the stiffness investigation revealed that although there was no clear hierarchy of stiffness among the implant types overall, the textured surfaces did tend to exhibit higher bending stiffness. Bending stiffness is related to change in implant shape whereas stretching stiffness is associated with change in implant volume under stress.

The analysis described in this paper has aided in clarifying the relationship between surface roughness and cell adhesion.

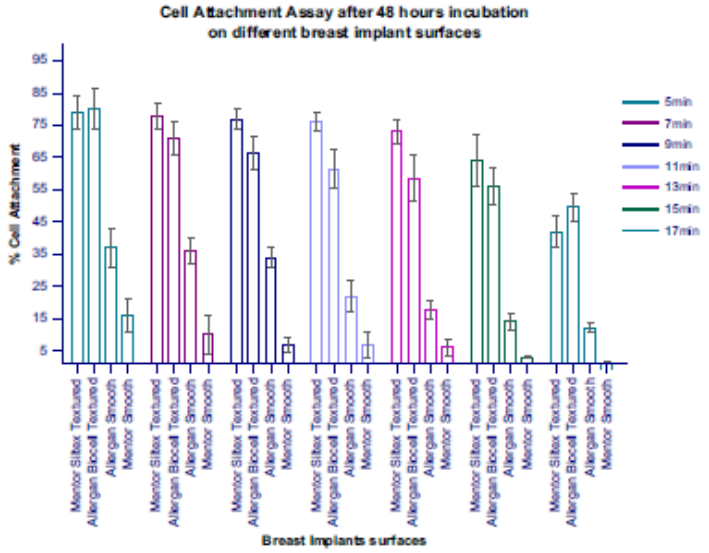

Fig. 11 – Comparison of normal skin fibroblast attachment to four implant surfaces after 48 h of incubation.

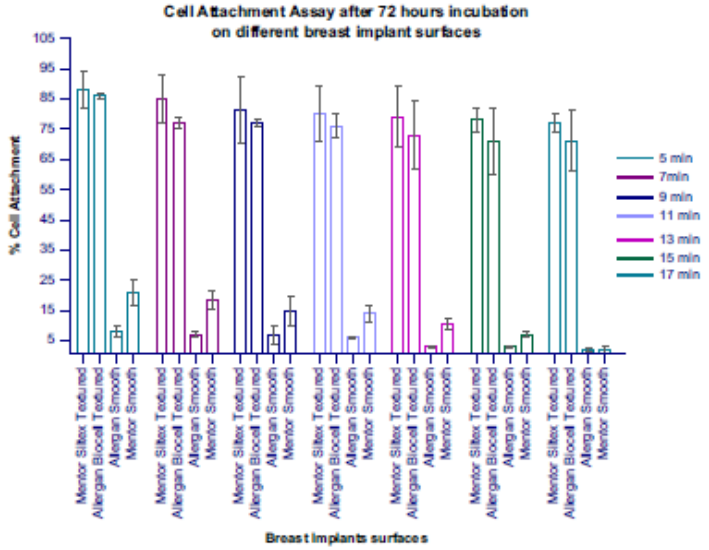

Fig. 12 – Comparison of normal skin fibroblast attachment to four implant surfaces after 72 h of incubation.

As regards the other parameters (wettability, bending and stretching stiffness etc), because commercial breast implants were considered then the key parameters investigated may have had values that varied over only a relatively small range, thus making it difficult to modulate some of the key factors, which is one limitation of the study. We suggest therefore that future work should investigate implant surfaces, not necessarily commercial ones, that exhibit a wider range of surface parameters so that the cause effect relationships of some of the key surface parameters may be more clearly established. It is hoped that the information provided by the investigation and described in this paper will be of use to researchers investigating contracture.

5. Conclusion

The data acquired from the 3-D images, roughness experimentations, hydrophobicity assay, tensile testing and kinetics of detachment tests have given a unique compilation

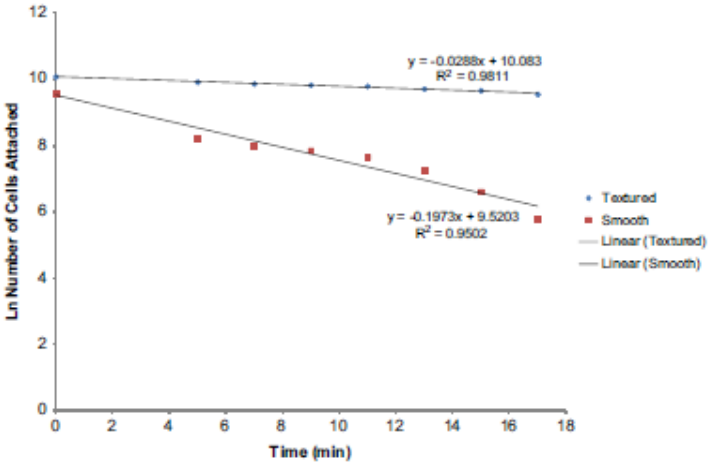

Fig. 13 – Ln of number of cells attached at each time point averaged over all textured and smooth samples.

of information to enable characterization of the smooth and textured surfaces of commercially available breast implants.

The textured implant surface samples were found to be more nodular than the smooth samples and exhibited higher values of surface roughness, contact angle, stiffness, fluid retention and cell adhesion but lower values of skewness (absolute values) and kurtosis. Whilst it was possible to broadly distinguish cell adhesion behaviour between the textured and smooth samples, it was found that the precise nature of the relationship between adhesion and surface parameters was complex, with adhesion being influenced by a range of surface characteristics. The analysis did reveal a significant main effect for surface texture and clearly demonstrated that cells adhere more strongly to textured implant surfaces.

In light of current thinking, it is apparent that surfaces that demonstrate high cell attachment would promote tissue ingrowth and this would be beneficial in producing an enhanced host–prosthesis interface. However, it can only be concluded that implant surfaces which are highly rough and irregular exhibit large water contact angles and fluid retention but lower values of skewness and kurtosis. In order to more clearly elucidate the relationship between implant characteristics and cell adhesion additional work should be undertaken that includes investigating surfaces that exhibit a wider range of surface parameters.

Acknowledgements

The authors would like to thank the Consejo Nacional de Ciencia y Tecnología (Mexico) for supporting the postgraduate student involved in this work.

REFERENCES

Abramo, A.C., De Oliveira, V.R., Ledo-Silva, M.C., De Oliveira, E.L., 2010. How texture-inducing contraction vectors affect the fibrous capsule shrinkage around breasts implants?. Aesthetic Plastic Surgery 34, 555–560.

Adams Jr., W.P., Rios, J.L., Smith, S.J., 2006. Enhancing patient outcomes in aesthetic and reconstructive breast surgery using triple antibiotic breast irrigation: six-year prospective clinical study. Plastic and Reconstructive Surgery 117 (30–36) 10.1097/01.prs.0000185671.51993.7e.

Anselme, 2010. Relative influence of surface topography and surface chemistry on cell response to bone implant materials. Part 2: Biological aspects. Proceedings of the Institution of Mechanical Engineers, Part H: Journal of Engineering in Medicine, 224.

Barr, S., Bayat, A., 2011. Breast implant surface development: perspectives on development and manufacture. Aesthetic Surgery Journal 31 (1), 56–67.

Barr, S., Hill, E., Bayat, A., 2010. Patterning of novel breast implant surfaces by enhancing silicone biocompatibility, using biomimetic topographies. ePlasty, 10.

Batra, M.M.D., Bernard, S.M.D., Picha, G.M.D.P.D., 1995. Histologic comparison of breast implant shells with smooth, foam, and pillar microstructuring in a rat model from 1 day to 6 months. Plastic and Reconstructive Surgery 95 (354-363).

Brown, X.Q., Bartolak-Suki, E., Williams, C., Walker, M.L., Weaver, V.M., Wong, J.Y., 2010. Effect of substrate stiffness and PDGF on the behavior of vascular smooth muscle cells: implications for atherosclerosis. Journal of Cellular Physiology 225, 115–122.

Burkhardt, B.R., Dempsey, P.D., Schnur, P.L., Tofield, J.J., 1986. Capsular contracture: a prospective study of the effect of local antibacterial agents. Plastic and Reconstructive Surgery 77, 919–930.

Danino, A., Rocher, F., Blanchet-Bardon, C., Revol, M., Servant, J.M., 2001. A scanning electron microscopic study of the surface of textured mammary implants and their capsules. Description of the adhesive "velcro" effect of porous-textured breast prostheses. Annales de Chirurgie Plastique Esthetique 46, 23–30.

De Bruijn, H.P., Ten Thije, R.H.W., Johannes, S., 2009. Mastopexy with mesh reinforcement: the mechanical characteristics of polyester mesh in the female breast. Plastic and Reconstructive Surgery 124, 364–371.

Emery, J.A., Spanier, S.S., Kasnic Jr, G., Hardt, N.S., 1994. The synovial structure of breast-implant-associated bursae. Modern Pathology: An Official Journal of the United States and Canadian Academy of Pathology, Inc 7, 728–733.

Ersek, R., 1991. Rate and incidence of capsular contracture: a comparison of smooth and textured silicone double-lumen breast prostheses. Plastic and Reconstructive Surgery 77, 919–932.
Ersek, R.A., Beisang, A.A., Beisang III, A.A., 1990. Textured Silicone Implant Prosthesis. United States, Bioplasty, Inc, St. Paul, MN.
Fellers, C., 2009. Paper physics. In: Ek, M., Gellerstedt, G., Henriksson, G. (Eds.), Pulp and Paper Chemistry and Technology. Volume 4: Products Physics and Technology. de Gruyter, Berlin, pp. 25–58.
Fenner, R.T., 1989. Mechanics of Solids. Blackwell Scientific Publications, Oxford.
Grinnell, F., Ho, C.-H., 2013. The effect of growth factor environment on fibroblast morphological response to substrate stiffness. Biomaterials 34, 965–974.
Hakelius, L.M.D., Ohlsen, L.M.D., 1997. Tendency to capsular contracture around smooth and textured gel-filled silicone mammary implants: a 5-Year Follow-Up. Plastic and Reconstructive Surgery 100, 1566–1569.
Handel, N.M.D., Jensen, J.A.M.D., Black, Q.B.S., Waisman, J.R.M.D., Silverstein, M.J.M.D., 1995. The fate of breast implants: a critical analysis of complications and outcomes. Plastic and Reconstructive Surgery 96, 1521–1533.
Hu, X., Park, S.H., Gil, E.S., Xia, X.X., Weiss, A.S., Kaplan, D.L., 2011. The influence of elasticity and surface roughness on myogenic and osteogenic-differentiation of cells on silk–elastin biomaterials. Biomaterials 32, 8979–8989.
Huang, H.-H., Ho, C.-T., Lee, T.-H., Lee, T.-L., Liao, K.-K., Chen, F.-L., 2004. Effect of surface roughness of ground titanium on initial cell adhesion. Biomolecular Engineering 21, 93–97.
Jopp, J., Grüll, H., Yerushalmi-Rozen, R., 2004. Wetting behavior of water droplets on hydrophobic microtextures of comparable size. Langmuir, 20.
Kjoller, K.M.D., Holmich, L.R.M.D., Jacobsen, P.H.M.D., Friis, S.M.D., Fryzek, J.P., McLaughlin, J.K.P., Lipworth, L.S., Henriksen, T.F.M.D., Jorgensen, S.M.D., Bittmann, S.M.D., Olsen, J.H.M.D., 2001. Capsular contracture after cosmetic breast implant surgery in Denmark. Annals of Plastic Surgery 47, 359–366.
Kolind, K., Dolatshahi-Pirouz, A., Lovmand, J., Pedersen, F.S., Foss, M., Besenbacher, F., 2010. A combinatorial screening of human fibroblast responses on micro-structured surfaces. Biomaterials 31, 9182–9191.
Lampin, M., Warocquier-Clérout, R., Legris, C., Degrange, M., Sigot-Luizard, M.F., 1997. Correlation between substratum roughness and wettability, cell adhesion, and cell migration. Journal of Biomedical Materials Research 36, 99–108.
Lavine, D.M., 1993. Saline inflatable prostheses: 14 years' experience. Aesthetic Plastic Surgery 17, 325–330.
Margaret, G., Ulrich, S., 2010. Cell-substrate interactions. Journal of Physics: Condensed Matter 22, 190301.
Marshall, W.R., Godfrey, M., Hollister, D.W., Balkovich, M.E., Lindgren, V.V., 1989. Types of collagen in breast capsules. Annals of Plastic Surgery 23, 401–405.
Mirzadeh, H., Shokrolahi, F., Daliri, M., 2003. Effect of silicon rubber crosslink density on fibroblast cell behavior in vitro. Journal of Biomedical Materials Research Part A 67A, 727–732.
Necchi, S., Molina, D., Turri, S., Rossetto, F., Rietjens, M., Pennati, G., 2011. Failure of silicone gel breast implants: Is the mechanical weakening due to shell swelling a significant cause of prostheses rupture?. Journal of the Mechanical Behavior of Biomedical Materials 4, 2002–2008.
Park, I.S., Ha, J.S., 2009. Thickness measurement of silicon thin film coated on metal mold by analyzing infrared thermal image. International Communications in Heat and Mass Transfer 36, 462–466.
Persichetti, P.M.D.P., Tenna, S.M.D.P., Delfino, S.M.D.P., Abbruzzese, F.P., Trombetta, M.P., Scuderi, N.M.D., 2009. Textured and smooth breast implants: is there a difference in the chemical structure of silicone? An analysis with Fourier transformation infrared and attenuated total reflectance spectroscopy. Annals of Plastic Surgery 63, 373–377.
Prager-Khoutorsky, M., Lichtenstein, A., Krishnan, R., Rajendran, K., Mayo, A., Kam, Z., Geiger, B., Bershadsky, A.D., 2011. Fibroblast polarization is a matrix-rigidity-dependent process controlled by focal adhesion mechanosensing. Nature Cell Biology 13, 1457–1465.
Prasad, B.R., Brook, M.A., Smith, T., Zhao, S., Chen, Y., Sheardown, H., D'Souza, R., Rochev, Y., 2010. Controlling cellular activity by manipulating silicone surface roughness. Colloids and Surfaces B: Biointerfaces 78, 237–242.
Ranella, A., Barberoglou, M., Bakogianni, S., Fotakis, C., Stratakis, E., 2010. Tuning cell adhesion by controlling the roughness and wettability of 3D micro/nano silicon structures. Acta Biomaterialia 6, 2711–2720.
Schmidt, J.A., Von Recum, A.F., 1991. Texturing of polymer surfaces at the cellular level. Biomaterials 12, 385–389.
Spear, S.L., Carter, M.E., Ganz, J.C., 2003. The correction of capsular contracture by conversion to "dual-plane" positioning: technique and outcomes. Plastic and Reconstructive Surgery 112, 456–466.
Tamada, Y., Ikada, Y., 1993. Cell adhesion to plasma-treated polymer surfaces. Polymer 34, 2208–2212.
Wyatt, L.E.M.D., Sinow, J.D.M.D., Wollman, J.S.M.D., Sami, D.A.B.S., Müller, T.A.M.D., 1998. The influence of time on human breast capsule histology: smooth and textured silicone-surfaced implants. Plastic and Reconstructive Surgery 102, 1922–1931.

JOURNAL OF THE MECHANICAL BEHAVIOR OF BIOMEDICAL MATERIALS 40 (2014) 140–155

Available online at www.sciencedirect.com

ScienceDirect

www.elsevier.com/locate/jmbbm

Research Paper

Physico-chemical characteristics of coated silicone textured versus smooth breast implants differentially influence breast-derived fibroblast morphology and behaviour

Anai A. Valencia-Lazcano[a], *Teresa Alonso-Rasgado*[b], *Ardeshir Bayat*[c,d,*]

[a]Bioengineering Group, School of Mechanical, Aerospace and Civil Engineering, The University of Manchester, Manchester, UK

[b]School of Materials, The University of Manchester, Manchester, UK

[c]Plastic & Reconstructive Surgery Research, Manchester Institute of Biotechnology, The University of Manchester, Manchester, UK

[d]Faculty of Medical and Human Sciences, Institute of Inflammation and Repair, University of Manchester, Manchester Academic Health Science Centre, Manchester, UK.

ARTICLE INFO

Article history:
Received 28 June 2014
Received in revised form
20 August 2014
Accepted 21 August 2014
Available online 3 September 2014

Keywords:
Specific coatings
Breast tissue fibroblasts
Silicone breast implants
Adhesion
Gene expression

ABSTRACT

Capsule formation is an inevitable consequence of silicone breast implantation. Clinically challenging dense fibrocollagenous capsular contractures occur at different rates between smooth compared to textured surfaces. Host response is influenced by several factors including implant surface texture, chemistry and interactions between cells and the extracellular matrix (ECM). Specific coatings can modify the physico-chemical properties of implant surfaces eliciting specific cellular reactions. Therefore, we evaluated the physico-chemical characteristics of coated smooth versus textured silicone breast implants on breast-derived fibroblast morphology and behaviour using (a) confocal laser microscopy, (b) Raman spectroscopy and (c) the effect of four unique protein and glycosaminoglycan (GAG) coatings (aggrecan, collagen I, fibronectin and hyaluronic acid) on breast-derived fibroblast attachment, proliferation, morphology, spreading, cytotoxicity and gene expression. Collagen I, fibronectin and hyaluronic acid coatings exhibited satisfactory fibroblast adhesion ($p<0.001$) in comparison to uncoated surfaces. Cell adhesion was less on smooth surfaces compared to textured surfaces ($p<0.001$). Fibroblasts cultured on collagen I, fibronectin and hyaluronic acid coated implants demonstrated improved cell proliferation than uncoated surfaces ($p<0.001$). LDH assay showed that coating surfaces with collagen I, fibronectin and hyaluronic acid did not induce cytotoxicity. Alpha-actinin expression and fibroblast adhesion to the substrate were upregulated ($p<0.001$), in textured versus smooth surfaces. FAK, vinculin and paxillin expression were upregulated ($p<0.001$), in all surfaces coated with fibronectin and collagen I. In conclusion, we present original data for expression of adhesion-related genes, cell

*Corresponding author at: Principal Investigator, Plastic & Reconstructive Surgery Research, Institute of Inflammation and Repair, Manchester Institute of Biotechnology, University of Manchester, 131 Princess Street, Manchester M1 7DN. Tel: +44 (0)161 306 5177.
E-mail address: Ardeshir.Bayat@manchester.ac.uk (A. Bayat).

http://dx.doi.org/10.1016/j.jmbbm.2014.08.018

morphology and proliferation in breast fibroblasts following the application of specific coatings on breast implant surfaces.

1. Introduction

Capsule formation is an inevitable consequence of implant insertion into a body cavity. Breast capsules are thus typically formed after silicone breast implant insertion into the breast cavity; however, some capsules can undergo contracture formation. A fibrous capsule usually forms around silicone breast implants. This is a relatively hypocellular membrane of rather uniform thickness which is rich in collagen. There may be a thin discontinuous layer of activated epithelioid myofibroblasts next to where the implant was situated and a thin acellular protein film between the implant and capsule. Both within and directly below this membrane, there are usually foam cells and lymphocytes, often in large numbers (Van Diest et al., 1998). However, whilst aetiology remains unknown, a variety of associations have been proposed that may predispose implants to capsular contracture formation including the filler material, implant placement technique, surface texture, presence of foreign bodies (such as glove talcum powder), subclinical infections near the area of implantation, hematoma and seroma (Berry et al., 2010). Breast capsular contracture is a clinical challenge for both the patient and the clinician in view of the degree of physical severity and availability of limited options for management. There are two types of surfaces for the most commonly used silicone breast implants today (Fig. 1). Silicone breast implant surface texture is considered to influence the rate of breast capsular contracture formation (Barr and Bayat, 2011). An implant surface is thought to interact directly with the breast tissue once inserted. A number of prospective studies have shown evidence of the benefit of textured compared to smooth implants in the first year post-implantation, although this benefit is maintained at 5 and 10 years (Poeppl et al., 2007, Barnsley et al., 2006, Hakelius and Ohlsen, 1997, Malata et al., 1997, Coleman et al., 1991, Ersek, 1991, Ma and Gao, 2008). Meta-analyses calculated the occurrence of breast capsular contracture on textured surfaces to be about fivefold less in comparison to smooth surfaces, which was maintained for 3 years (Wong et al., 2006, Barnsley et al., 2006). However, one previous study showed no statistically significant difference between saline-filled smooth and textured breast implants (Fagrell et al., 2001). Moreover, studies carried out in animal models are conflicting, as two studies found an increase in the rate of capsular contracture in smooth surface implants (Brohim et al., 1993, Clugston et al., 1994), while other studies found thicker and tighter capsules around textured surfaces (Barone et al., 1992, Bucky et al., 1994, Bern et al., 1992). Rationale behind the efficacy of reducing capsular contracture with textured breast implants is based on the fact that cells grow into and around the interstices of the surface resulting in an environment where contractile forces tend to cancel each other out, resulting in thinner capsule formation by contact inhibition (Harvey et al., 2013). Smooth surfaces elicit a fibrous reaction where collagen fibrils align cumulatively in a connective-tissue capsule adjacent to the implant.

Third-generation biomaterials are designed to stimulate cell behaviour in a specific manner at molecular level (Hench and Polak, 2002). Molecular modifications on the surface of the implants induce specific interactions with cell receptors such as integrins directing cell proliferation, differentiation and ECM production and organisation. Coating surfaces is an alternative route to influence the implant surface topography by creating cues for cellular adhesion and the subsequent induction of tissue integration (Harvey et al., 2013, Hauser et al., 2009). Different techniques of coating have been performed on breast implants with the aim of reducing the rate of capsular contracture. Polyurethane covered breast implants consists of silicone shell covered with fine-cell urethane and filled with silicone gel. The polyurethane coating is 1 mm thick and the septum is built into the prosthesis featuring a Y-shape thin-walled that allows the implant fixes within the chest wall (Ashley, 1970). This capsule surrounding the polyurethane consisted of five layers: a single layer of macrophages, foreign body giant cells, and epithelioid cells, a layer of subacute inflammatory tissue, a plasmacytic infiltrate, a thick layer of connective tissue and a layer of lax connective tissue along the breast parenchyma (Vazquez, 1999). The polyurethane coating induces a vascular foreign body reaction that prevents fibroblasts from producing collagen in a continuous plane so the contracture of the capsule is minimum and only 10% of patients have shown capsular contracture at 4 years; however, 25% of the patients showed capsular contracture at 10 years, and this may be due to the disintegration of the polyurethane coating (Berry and Davies, 2010). In the 1990s, polyurethane-covered Même breast implants were withdrawn from the market due to the risk of chemical breakdown of the polyurethane foam to carcinogen 2-toluene diamine (Collis et al., 2000). Currently, polyurethane is joined at the base to the implant, instead of being glued to the implant which was the case before it was withdrawn. Therefore, polyurethane does not become detached and a capsule is formed only around the polyurethane and not between the foam and the implant as it was previously (Vazquez, 1999, Vazquez and Pellon, 2007). Roca studied autologous fat grafting with textured silicone gel implants in porcine models showing softer capsules around the implants (Roca et al., 2014). Park covalently coated silicone implants with a biomembrane-mimicking polymer (PMPC) and showed a significant decrease in capsular thickness compared to non-coated implants in rat models (Park et al., 2014). Zeplin coated silicone implants with recombinant spider silk proteins and showed reduced post-operative inflammation and fibrosis in rat models only (Zeplin et al.,

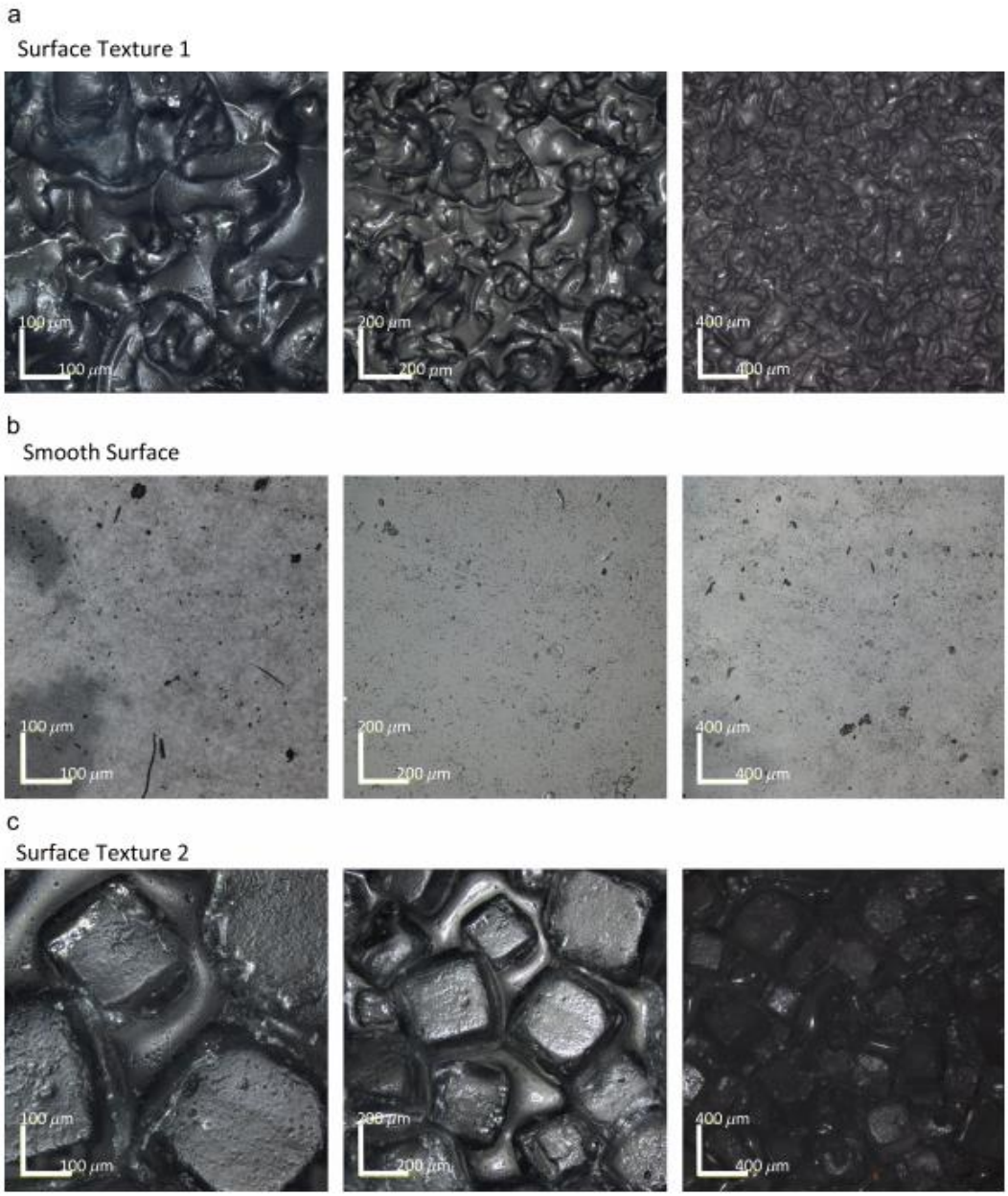

Fig. 1 – Confocal laser 3-D topography of silicone breast implants. Confocal laser 3-D topography of silicone breast implants (image scale bars 100 μm, 200 μm and 400 μm). (a) Textured Surface 1 reveals a texture composed of nodules with high peaks and deep crevasses, (b) Smooth Surface shows a geographical surface with rocky formations and small pits, and (c) Textured Surface 2 depicts a granular surface pitted with cuboid shaped wells.

2014). The extracellular matrix (ECM) in the breast tissue is comprised of specific proteins and proteoglycans (Muschler and Streuli, 2010). Fibroblasts use surface receptors to interact physically with their immediate environment (Bershadsky et al., 2003). ECM receptors, mainly integrins, provide attachment to the surrounding stroma. The associations of the heterodimeric receptors formed by integrins define the influence to different ECM components. To successfully elicit

specific cellular responses and direct new tissue formation, biological cues are created through the design of biomimetic scaffolds that modify biomaterials with ECM molecules (Shin et al., 2003). The interaction of ECM proteins with cells via cell-surface integrin family receptors results on focal contacts; they provide support to cellular processes and maintain the tissue architecture. Cell spreading, adhesion, proliferation and migration are influenced by the signal transduction cascades initiated by the binding of an ECM molecule and integrin.

Protein, proteoglycan (PG) and glycosaminoglycan (GAG)-based coatings have been used to promote fibroblast activity modification (Steward et al., 2011, Li et al., 2012a, Hauser et al., 2009). Aggrecan is a proteoglycan found in the ECM of cartilage, which has a molecular mass of >2,500 kDa (Roughley et al., 2006). Another constituent element of ECM is collagen, which enhances cell attachment and proliferation and can be found in the form of filaments, sheets and fibrils (Li et al., 2012b), providing tensile strength to the tissue scaffolding. Collagen type I was chosen to coat the surfaces because it is a major constituent of breast tissue and supporting structures. In addition, collagen type I fibres are recognised by integrin cell surface receptors and thus appropriate as an ideal interface for the cell-surface interaction (Mwenifumbo and Stevens, 2007). An essential component of ECM related to cell adhesion is fibronectin, a 450 kDa dimeric glycoprotein that can bind specifically to two widely expressed cell surface receptors, integrins $\alpha 5\beta 3$ and $\alpha v\beta 3$ (Elter et al., 2012). Fibronectin plays an important role in the adhesion of cells to material surfaces; it can even strengthen the cell-surface adhesion (Elter et al., 2012). Hyaluronic acid transports the metabolites and nutrients, provides tissue resistance to compressive forces and controls cell migration and cell proliferation (Cohen et al., 2003). Hyaluronic acid provides the perfect scaffold for cells to proliferate and migrate (Collins and Birkinshaw, 2013, Korurer et al., 2014).

The above four candidates were chosen from a whole genome microarray study (Kyle et al., 2013) performed in cDNA of 23 breast capsules: 12 capsules of Baker grades I and II and 11 capsules of Baker grades III and IV; 122 genes were found to be upregulated and 22 downregulated (Baker grades I and II refer to normal capsules compared to grades III and IV which refer to severely contracted capsules) (Baker, 1975). The candidate genes were selected from the microarray data by grouping genes according to three categories. The first category consisted of all the downregulated genes, the second category comprised of the genes related to cell adhesion and ECM and the third category was formed based on the smallest statistical p-value. Genes that matched the three categories were selected, and a literature review into gene and protein expression of fibrosis and breast capsules was also conducted in order to corroborate the microarray data.

Therefore, the aim of the study was to compare the efficacy of different types of ECM coatings and known smooth versus textured silicone breast implant surface topographies. To this end, the effect of four specific coatings on initial cell attachment, viability, proliferation and gene expression on these surfaces was investigated. We examined the hypothesis that micrometre-sized surface textures affect adhesion-related breast tissue fibroblast function to a different degree depending on the scale of micro-topography and the properties of the coatings by assessing cytotoxicity, cell morphology, adhesion, proliferation and the expression of α-actinin, vinculin, paxillin and FAK. By focusing on integrin-mediated focal adhesion structure and intracellular signalling molecules, we examined the effect of topography and coating on cell function, morphology and behaviour.

2. Materials and methods

The study was conducted following two stages: the first stage consists of characterising the surface of silicone breast implants by measuring the arithmetic surface roughness and analysing the chemical composition and the second stage consisted of studying the in vitro adhesive interactions of breast fibroblasts with implants surfaces in order to determine how implant surface textures and surface coatings affect specific functions of the cell directly involved in cell-surface adhesion. These stages are described in Fig. 2.

2.1. *Sample preparation*

The silicone breast implants studied were chosen from some of the commonly available implants in clinical practice: (1) Textured Surface-1 (TS1) (Mentor Siltex® (Mentor Worldwide LLC, Skyway Circle North Irving, Texas)); (2) Smooth Surface (SS) (Mentor® Smooth (Mentor Worldwide LLC, Skyway Circle North Irving, Texas)); (3) Textured Surface-2 (TS2) (Allergan Biocell® (Allergan, Inc, Santa Barbara, California)). Sample preparation was performed following the methodology of Valencia (Valencia-Lazcano et al., 2013). Surfaces were coated with either 5 μg/ml aggrecan (Sigma-Aldrich, USA), 5 μg/ml collagen type I (BD Biosciences, USA), 5 μg/ml fibronectin (Sigma-Aldrich, USA) or 10 μg/ml hyaluronic acid (Sigma-Aldrich, USA) solution and incubated for 1 h at 37 °C and washed twice with PBS (PAA laboratories, Austria).

2.2. *Characterisation*

Physical properties of smooth and textured breast implants were evaluated by looking at their topographical features using confocal laser microscopy following the procedure described previously by Valencia (Valencia-Lazcano et al., 2013). The procedure enables highly accurate 3D images of implant surfaces to be produced from which surface roughness parameter values can be obtained. Chemical characterisation was carried out recording Raman images and spectra of the implants using confocal Raman spectrometer equipped at an excitation of 532 nm and a magnification of 50x air objective (N.A.=0.7) (Horiba, USA).

2.2.1. *Adsorption*

The adsorption of aggrecan, collagen, fibronectin and hyaluronic acid onto the breast implant surfaces was determined by first measuring the thickness of the coating with the confocal laser microscope following the procedure described previously by Valencia (Valencia-Lazcano et al., 2013). From the measured thickness (d), the surface mass density of the

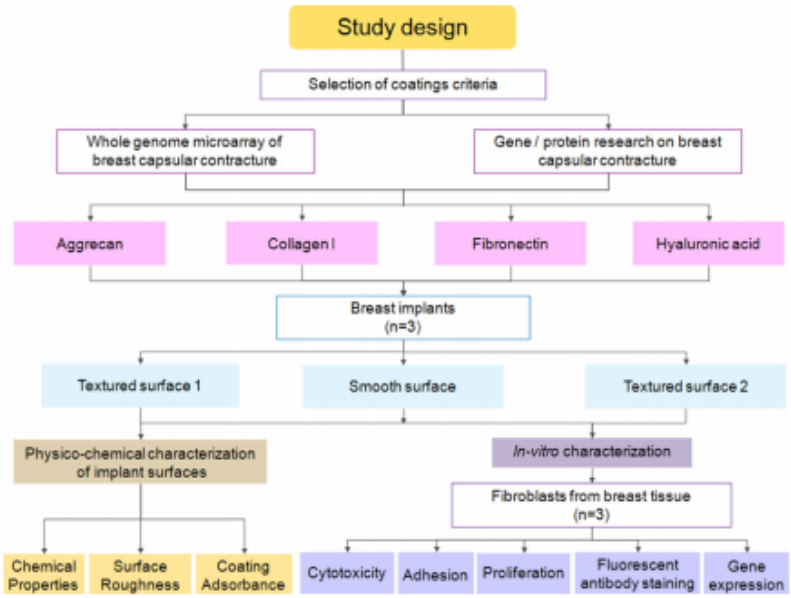

Fig. 2 – Study design. The study was conducted following two stages: the first stage consisted of characterising the surface of the breast implants by measuring the arithmetic surface roughness and analysing the chemical composition; the second stage consisted of studying the in vitro adhesive interactions of breast-derived fibroblasts with implant surfaces in order to determine how implant surface textures and surface coatings affect specific functions of the cell directly involved in cell-surface adhesion, behaviour and morphology.

coating was determined by the Feijters formula:

$$\text{Adsorbance} = d\frac{n_{protein} - n_{buffer}}{dn/dc}$$

where $n_{protein}$ and n_{buffer} are the refractive index of the protein and buffer, respectively, and dn/dc is the refractive index increment for a given concentration.

2.3. Cell culture

Cultured human breast tissue fibroblasts were established from tissue biopsies taken from healthy female patients ($n=3$) undergoing routine elective surgery. All patients had given full written and verbal consent for the use of discarded tissue for the experimental purposes of this ethically approved study. All cultures were passage 2 and were grown to confluence in 125 ml culture flasks in Dulbecco's Culture Medium (DMEM) (Sigma-Aldrich, UK) substituted with 10% foetal bovine serum (Sigma-Aldrich, USA), 1% L-glutamine (PAA laboratories, Austria), 1% non-essential amino acid solution (Sigma-Aldrich, USA) and 1% penicillin/streptomycin (PAA laboratories, Austria) at 37 °C in a 5% CO_2 atmosphere. Prior to seeding the fibroblasts on the surfaces, fibroblasts were arrested to take them to the G0/G1 phase.

2.4. Cytotoxicity

Cytotoxicity was tested after 24 h incubation; media from each well was aspired and centrifuged at 1600 rpm for 4 min. The media was transferred to a 96-well plate at a volume of 100 μL per well by triplicate, and 100 μL of LDH (Roche, USA) was added to each well. The plate was protected from light and incubated at room temperature for 30 min. Absorbance was measured spectrophotometrically (Molecular Devices, USA) at a wavelength of 485 nm. The background absorbance of the multi-well plates was measured at 690 nm and this value was subtracted from the primary wavelength measurement. The number of replicates was 3 per surface; the control group corresponds to the uncoated surfaces.

2.5. Fibroblast adhesion to surfaces

Adhesion assay was tested after 2 h of seeding the fibroblasts onto the surfaces. Dissociated cell suspensions were washed twice with PBS (PAA laboratories, Austria) to be later re-suspended in media without serum. Five microlitre of calcein AM solution (Molecular probes, USA) was added to a cell suspension of 5×10^6 cells/ml and incubated at 37 °C for 30 min. The cells were washed twice with media and re-suspended in fresh media. The cells were seeded on breast implant surfaces in a 96-well plate in a final volume of 100 μL/well of the calcein-labelled cell suspension (5×10^4 cells) culture medium (Sigma-Aldrich, UK) and incubated for 2 h in a humidified atmosphere of 37 °C, 5% CO_2. Non-adherent calcein-labelled cells were removed by washing four times with warm media (Sigma-Aldrich, UK); finally 200 μL of PBS (PAA laboratories, Austria) was added. Fluorescence was measured using a micro-plate reader (Molecular

Table 1 – Adsorption of aggrecan, collagen I, fibronectin and hyaluronic acid onto the smooth and textured breast implant surfaces.

	Adsorption at the peaks (mg/cm²)	Adsorption at the valleys (mg/cm²)
TS1		
Aggrecan	0.106736	0.222958
Collagen I	0.815139	0.583375
Fibronectin	0.754097	1.118097
Hyaluronic acid	0.463333	0.516182
SS		
Aggrecan	0.004392	0.003883
Collagen I	0.022865	0.012413
Fibronectin	0.026128	0.013628
Hyaluronic acid	0.017784	0.010052
TS2		
Aggrecan	0.071719	0.108
Collagen I	0.747899	0.556514
Fibronectin	0.932552	0.985569
Hyaluronic acid	1.970208	0.735697

Devices, USA) at 485/538 nm. The percentage of cell adhesion was determined by dividing the corrected (background subtracted) fluorescence of adherent cells by the total of corrected fluorescence of cells added to each micro-plate well and multiplying by 100%. The number of replicates was 3 per surface; the control group corresponds to the uncoated surfaces.

2.6. *Fibroblast proliferation*

Proliferation was tested after 24 h incubation in standard conditions; media from each well was aspired and 300 μL of fresh complete media (Sigma-Aldrich, UK) and 30 μL of water-soluble tetrazolium salt-1 (WST-1) cell proliferation reagent (Roche, USA) were added to each well. The well plate was wrapped in aluminium foil and placed in a shaker for 2 min at 55 rpm. After 4 h incubation in a humidified atmosphere of 37 °C, 5% CO_2, media was removed and poured at 100 μL per well into a 96-well plate. Absorbance was measured using a micro-plate reader (Molecular Devices, USA) at 450–690 nm. Cell proliferation was determined by subtracting the absorbance background control and the absorbance of 630–690 nm from the 450–500 nm measurement. Specific absorbance = A475 nm (test) – A475 nm (blank) – A660 nm (test). The number of replicates was 3 per surface; the control group corresponds to the uncoated surfaces.

2.7. *Immunofluorescence*

Fluorescence staining of the actin (TRITC) (cytoskeleton), vinculin (FITC) (focal adhesion protein) and cell nucleus (DAPI) was performed using triple staining. Throughout the staining procedure, after 24 h of culture, media was removed from the well plate and the surfaces washed with PBS (PAA laboratories, Austria). Surfaces were covered with 10% formalin (Sigma-Aldrich, USA) overnight and washed with PBS (PAA laboratories, Austria). Surfaces were covered with 0.1% Triton X-100 (Sigma-Aldrich, USA) for 10 min. Each sample was washed twice with PBS (PAA laboratories, Austria) (5 min each), then covered with blocking buffer (LI-COR Biosciences, USA) for 30 min and washed twice with PBS (PAA laboratories, Austria) (5 min each). The surfaces were labelled with first antibody ab2264 rabbit polyclonal to paxillin (abcam, UK) at a concentration of 1:100 overnight at 4 °C. Surfaces were washed three times with 0.1% Tween 20/PBS (5 min each). Surfaces were labelled with secondary antibody Alexa Fluor® 488 dye (abcam, UK) 1:500 dilution for 100 min at room temperature. Surfaces were washed three times with 0.1% Tween 20/PBS (Fisher Scientific, USA) (5 min each). The surfaces were labelled with 4′,6-diamidino-2-phenylindole (DAPI) (Molecular probes, USA) for 15 min and then washed with 0.1% Tween 20/PBS (Fisher Scientific, USA) for 5 min.

The surfaces were labelled with rhodamine-phalloidin 1:1000 (Sigma-Aldrich, USA) for 40 min at room temperature and then washed once with PBS (PAA laboratories, Austria), twice with 0.1% Tween 20/PBS (Fisher Scientific, USA) (5 min each) and finally twice with PBS (PAA laboratories, Austria). Surfaces were mounted with ProLong® Gold antifade reagent (Invitrogen, USA) and covered with aluminium paper and stored at −4 °C. Immunofluorescence microscopy was carried out using a DeltaVision deconvolution system softWoRx v3.4.5 (Applied precision, USA) which consists of an Olympus IX-70 inverted microscope with an epi-fluorescence attachment. The images were obtained at 512 × 512 pixels with a magnification of 100x. Images were analysed using softWoRx v3.4.5 and Image-J software (NIH, USA).

2.8. *Quantification of gene adhesion expression*

2.8.1. *RNA extraction*

After 24 h of culture, total RNA was extracted from each specimen by adding 500 μL of Trizol reagent (Invitrogen Ltd, UK) for 2 min. Trizol was aspired and transferred to an eppendorf tube and 350 μL of chloroform (Fisher Scientific, USA) was added; the tube was shaken and centrifuged at 14500 rpm for 15 min. Three layers were formed and the upper layer was aspired and transferred into an eppendorf tube; an equal amount of ethanol 80% (Fisher Scientific, USA) was added and mixed by pipetting it and poured into an RNeasy mini spin column. After 15 s of centrifugation, supernatant was poured away and 600 μL of RWT buffer (Qiagen, Netherlands) was added. Centrifugation was performed for a

Table 2 – Sequences of primers used for adhesion-related genes using quantitative real-time polymerase chain reaction.

Gene/Primer	Gene ID	Sequence 5′ to 3′	Primer Position	Amplicon Size (bp)
(ACTN1) Alpha-actinin L	nm_001102.3	ctgttccagccatccttcat	834–853	70
(ACTN1) Alpha-actinin R	nm_001102.3	tcatgatgctgttgtaggtggt	882–903	70
(VCL) Vinculin (VCL) L	nm _014000.2	ggaggtgattaaccagccaat	2767–2787	88
(VCL) Vinculin (VCL) R	nm _014000.2	aatgatgtcattgcccttgc	2835–2854	88
(PXN) Paxillin L	nm _002859.3	cccagtgtggagagtctcttg	785–805	81
(PXN) Paxillin R	nm _002859.3	ctcgccctggttcacagt	848–865	81
(ptk2) Protein tyrosine kinase L	nm_153831.2	gtctgccttcgcttcacg	73–90	77
(ptk2) Protein tyrosine kinase R	nm_153831.2	gaatttgtaactggaagatgcaag	126–149	77

further 15 s and then the column was placed into a collection tube and 500 μL of RPE buffer (Qiagen, Netherlands) was added; this was then centrifuged for 15 s. Supernatant was poured away and the column was centrifuged for 1 min at 15000 rpm. The column was placed into an eppendorf tube and 25 μL of RNease-free water (Qiagen, Netherlands) was added to the top layer and left for 1 min at room temperature before centrifugation at 15000 rpm for 1 min. RNA concentration and purity were determined using a UV–vis spectrophotometer (NanoDrop, USA) by absorbance measurements.

2.8.2. *cDNA synthesis*

The quantity of nuclease-free water was calculated based on RNAs (100 ng) concentration; to make a 20 μL solution, 4 μL of cDNA super mix (Quanta Biosciences, USA) was poured into an eppendorf tube, RNease-free water (Qiagen, Netherlands) was added and finally mRNA was added. The tube was centrifuged for 30 s and incubated at 25 °C for 5 min. Synthesis conditions comprised an initial cycle at 42 °C for 1 h and one cycle at 85 °C for 5 min to inactivate the enzyme, and finally the solution was diluted in 180 μL of nuclease-free water (Ambion, USA).

2.8.3. *Quantitative real-time polymerase chain reaction*

The primers used to amplify the selected genes using real time qPCR were designed using Universal ProbeLibrary (Roche, USA). Reactions were set up in a total volume of 10 μL using 4 μL of cDNA, 5 μL probes master (Roche, Germany), 0.7 μL RNease-free water (Qiagen, Netherlands) and 0.1 μL each of gene-specific primer (Table 2) and performed in a LightCycler® 480 Real-Time PCR System (Roche, Germany). The cycling conditions were 95 °C for 10 min; 45 cycles of 95 °C for 10 s, 60 °C for 30 s and 72 °C for 1 s with a single fluorescence measurement; cooling was set at 40 °C for 30 s. Specificity of the PCR products was confirmed by analysis of the dissociation curve.

2.9. *Statistical analysis*

Statistical analysis was performed using the Prism v.5.0 software package for Windows (GraphPad Software, Inc., USA), applying the two-way ANOVA test; when the *p*-value was less than 0.05, the difference was regarded as statistically significant.

3. Results

3.1. *Physico-chemical characterisation of smooth versus textured implants*

Raman spectra showed TS1, TS2 and SS implants have the typical Raman spectrum of pure PDMS at the 490 cm^{-1} the Si-O stretch and 713 cm^{-1} the Si-C stretch modes. Implants from the same manufacturer, TS1 and SS possess a similar profile (Fig. 3) in spite of their surface roughness. Confocal laser microscopy showed different surface roughness between these two implants: TS1 is 8.88 μm rough while SS is 0.06 μm. TS2, whose surface roughness was 18.83 μm, showed a different profile and lower intensity levels in comparison to TS1 and SS (Fig. 3).

Surface roughness was modified by coating the surfaces with specific protein, PG and GAG coatings. In this case, the same coating procedure was performed on all surfaces; thus the changes in roughness were likely due to the interactions between implant topography and the coating structure. The surface features of the different breast implants after coating with aggrecan, collagen I, fibronectin and hyaluronic acid were assessed using confocal laser scanning microscopy. 3D topological models were obtained using colour-height information from planar images of the implant sample surfaces (Valencia-Lazcano et al., 2013). Fig. 4 (a)–(c) show the 3-D topography of the uncoated silicone breast implants (a) TS1, (b) SS, and (c) TS2, were used as the control. The arithmetic surface roughness measurements for both the coated and uncoated implant surfaces are shown in (Fig. 5a), where upon inspection it can be seen that surface roughness was significantly different ($p<0.001$) among the TS1, SS and TS2. Coated surfaces of TS1 were found to be significantly rougher ($p<0.001$) than the uncoated ones (Fig. 5b). SS surfaces coated with collagen I, fibronectin and hyaluronic acid were significantly rougher ($p<0.01$) compared to the uncoated surfaces; however, no significant difference in surface roughness was observed between the aggrecan-coated and uncoated SS (Fig. 5c). TS2 coated with fibronectin and hyaluronic acid were found to be significantly rougher ($p<0.05$) compared to the uncoated surfaces. No significant differences were found in the roughness values of uncoated, aggrecan and collagen I coated TS2 (Fig. 5d).

3.1.1. *Adsorption*

The adsorption values of aggrecan, collagen I, fibronectin and hyaluronic acid onto TS1, SS and TS2 are presented in

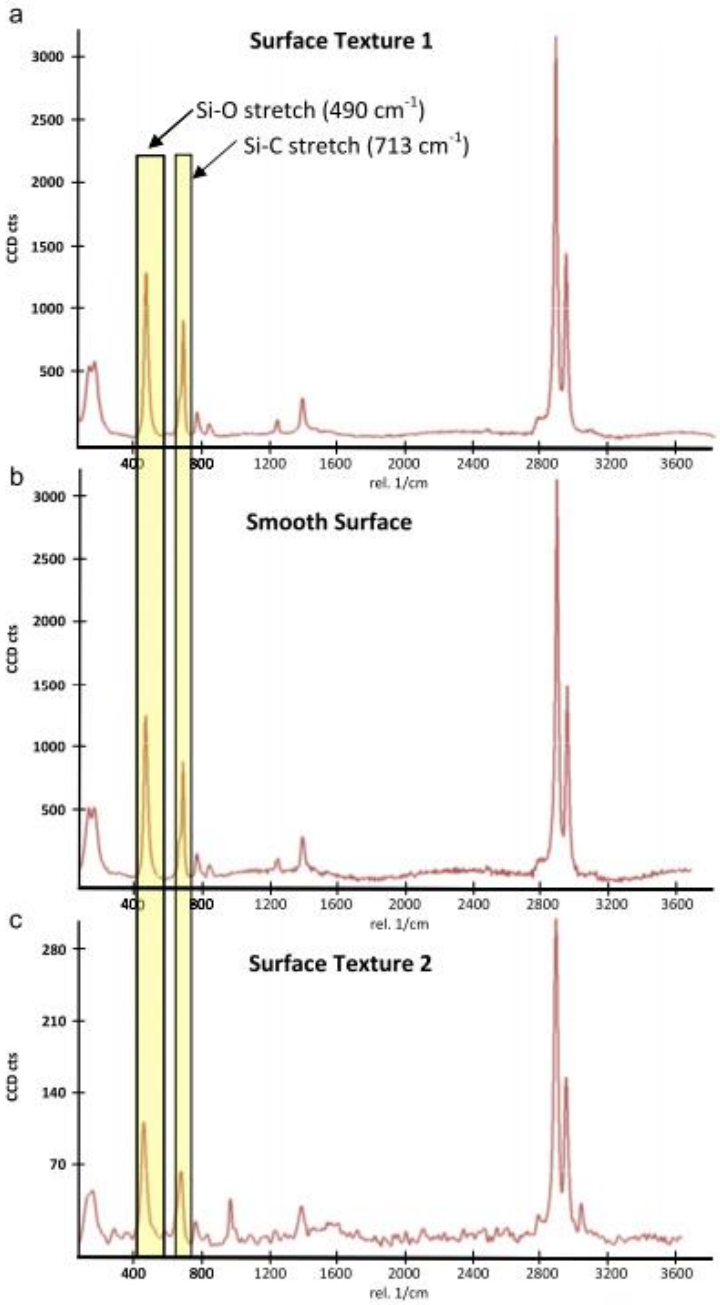

Fig. 3 – Raman spectra of silicone breast implants. Spectra of the textured and smooth silicone breast implants showed the key Raman features of PDMS in all implants: Si-O stretch (490 cm^{-1}) and the Si-C stretch (713 cm^{-1}).

Table 1. The highest adsorption at the peaks occurred on TS2 coated with hyaluronic acid (1.97 mg/cm^2) and fibronectin (0.93 mg/cm^2), while SS coated with aggrecan showed the lowest adsorption (0.004 mg/cm^2) among all surfaces.

The highest adsorption at the valleys occurred on TS1 (1.11 mg/cm^2) and TS2 (0.98 mg/cm^2) coated with fibronectin, while SS coated with aggrecan showed the lowest adsorption (0.004 mg/cm^2) among all surfaces.

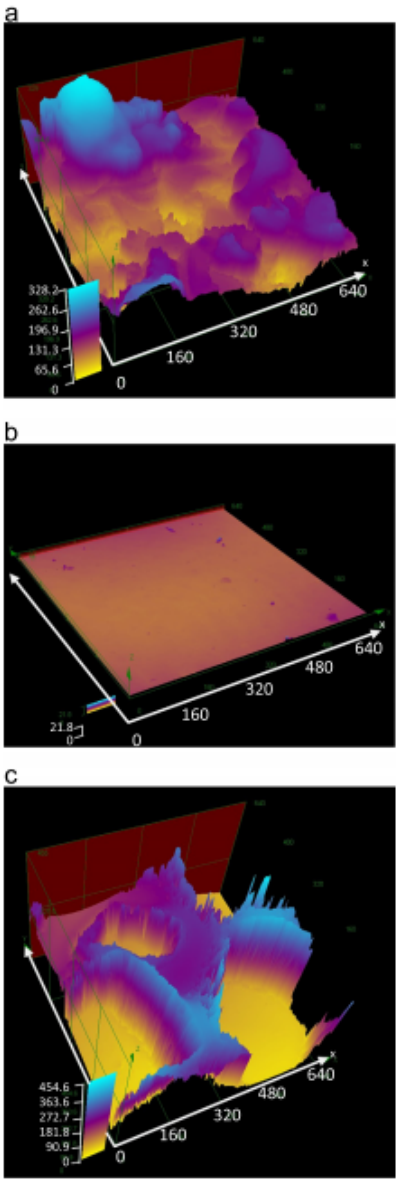

Fig. 4 – Confocal laser 3-D topography of silicone breast implants. Confocal laser 3-D topography of silicone breast implants using colour height information (644 × 642 μm). (a) Textured Surface 1, (b) Smooth Surface, and (c) Textured Surface 2.

3.2. *Cytotoxic effect of specific coatings on breast fibroblasts*

After 24 h of seeding breast fibroblasts onto uncoated TS1, SS and TS2 and surfaces coated with aggrecan, collagen I, fibronectin and hyaluronic acid, lactate dehydrogenase (LDH) activity in the culture media was used as an indicator of cell membrane integrity and thus a measurement of cytotoxicity (Fig. 6). The results presented in Fig. 6 reveal that SS, TS1 and TS2 coated with aggrecan showed a significantly higher ($p<0.001$) cytotoxicity compared with the corresponding uncoated surfaces. A decrease in cytotoxicity was found on TS1 coated with collagen I ($p<0.01$), fibronectin ($p<0.01$) and hyaluronic acid ($p<0.001$) when compared with uncoated TS1. No significant difference was found between the cytotoxicity values of SS and TS2 coated with collagen I and fibronectin compared with the uncoated SS and TS2; however, the cytotoxicity of the hyaluronic acid coated surfaces was significantly lower ($p<0.001$) than the uncoated surfaces.

3.3. *Effect of specific coatings on breast fibroblast attachment*

A calcein AM cell adhesion assay was used to measure the adhesion of calcein-labelled breast fibroblasts to uncoated TS1, SS and TS2 and surfaces coated with aggrecan, collagen I, fibronectin and hyaluronic acid (Fig. 7). Cell adhesion was found to be lower for fibroblasts on the smooth surfaces compared to the textured ones ($p<0.001$). Cell adhesion was significantly higher on collagen I, fibronectin and hyaluronic acid coated implants compared to the corresponding uncoated surfaces ($p<0.001$). Cell adhesion was highest (89%) for collagen I coated TS1 and TS2 and fibronectin coated TS2 (87%). No significant difference was found between fibroblast adhesion to aggrecan coated implants compared to the corresponding uncoated surfaces ($p>0.05$).

3.4. *Specific coatings induce a variable proliferation rate in breast fibroblasts*

Proliferation of breast fibroblasts seeded for 24 h on TS1, SS and TS2 coated with aggrecan, collagen I, fibronectin and hyaluronic acid was quantified using a water-soluble tetrazolium salt-1 (WST-1) cell proliferation assay and compared with control cultures grown on uncoated TS1, uncoated SS and uncoated TS2 (Fig. 8). On smooth surfaces, fibroblasts proliferation rates were lower compared to the textured surfaces for both the coated and uncoated surfaces ($p<0.001$). Cell proliferation was significantly higher for fibroblasts seeded on collagen I, fibronectin and hyaluronic acid coated implants compared to the corresponding uncoated surfaces ($p<0.001$). The highest cell proliferation rate (0.8) was found in collagen coated TS1, followed by 0.71 for fibronectin coated TS1. Lower proliferation rates were measured on uncoated and aggrecan coated surfaces ($p<0.001$).

3.5. *Effect of coatings on cytoskeleton organisation*

Rhodamine-phalloidin staining of breast fibroblasts cultured on uncoated and aggrecan coated TS1 and SS, and uncoated TS2 revealed cells that exhibited fine stress fibres all around the cell periphery (Fig. 9). Fibroblasts seeded on aggrecan coated SS and TS1, and uncoated TS2 were not able to form detectable cell-material adhesion complexes as well as actin cytoskeleton, and thus remained rounded, non-spread. Fibroblasts seeded on uncoated SS were poorly spread and showed

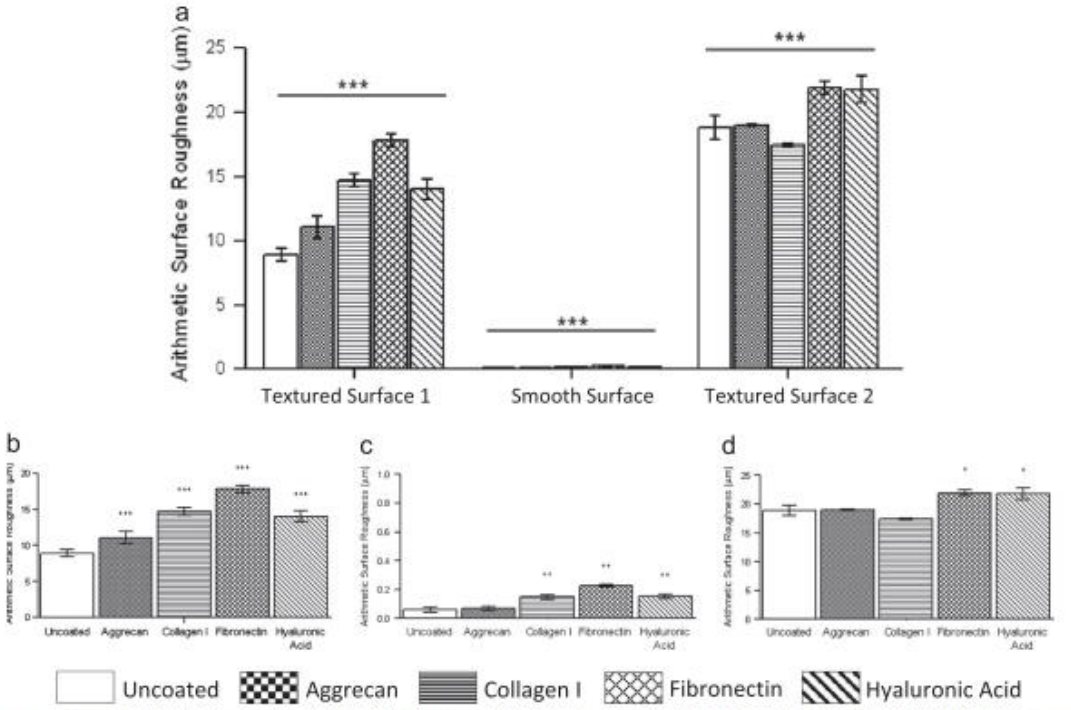

Fig. 5 – Changes in surface roughness of the modified coated surfaces examined by confocal laser microscopy. (a) Comparison of measured arithmetic surface roughness among the three implants showed statistical significant differences between them ($p<0.001$). Comparison of measured arithmetic surface roughness among uncoated and coated (b) Textured Surface 1, (c) Smooth Surface and (d) Textured Surface 2. Statistical analysis was performed applying the two-way ANOVA test; when the p-value was less than 0.05, the difference was regarded as statistically significant ($^{*}p<0.05$, $^{**}p<0.01$, $^{***}p<0.001$).

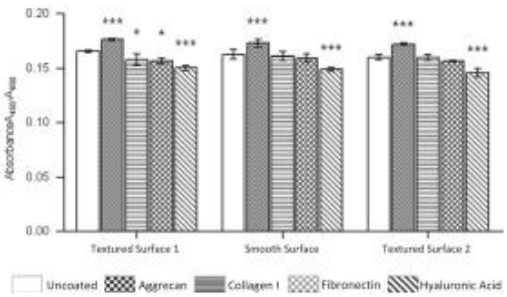

Fig. 6 – Cytotoxicity was evaluated by the quantification of plasma membrane damage by measuring the LDH activity in the cultured supernatant of breast-derived fibroblasts. Bar graphs show the toxicity effects of the coating proteins on breast-derived fibroblasts after 24 h of seeding them onto Textured Surface 1, Smooth Surface and Textured Surface 2 coated with aggrecan, collagen I, fibronectin and hyaluronic acid. Data shows mean ± standard deviation. Statistical analysis was performed applying the two-way ANOVA test; when the p-value was less than 0.05, the difference was regarded as statistically significant ($^{*}p<0.05$, $^{**}p<0.01$, $^{***}p<0.001$).

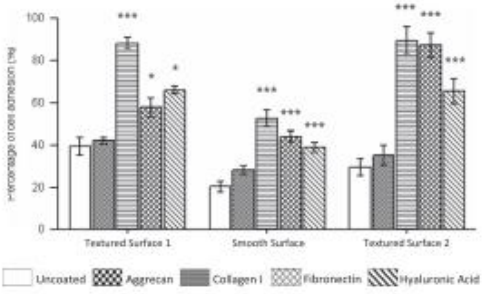

Fig. 7 – Effect of specific coatings on fibroblast attachment. Textured Surface 1, Smooth Surface and Textured Surface 2 were coated with aggrecan, collagen I, fibronectin and hyaluronic acid. Calcein AM cell adhesion assay was used to compare breast fibroblasts attachment after 2 h compared to control cultures grown onto uncoated Textured Surface 1, Smooth Surface and Textured Surface 2. Data shows mean ± standard deviation and the attachment is represented as a percentage of the total number of cells seeded. Statistical analysis was performed applying the two-way ANOVA test; when the p-value was less than 0.05, the difference was regarded as statistically significant ($^{*}p<0.05$, $^{**}p<0.01$, $^{***}p<0.001$).

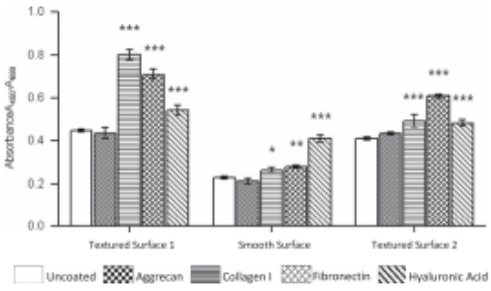

Fig. 8 – Effect of specific coatings on fibroblast proliferation. Textured Surface 1, Smooth Surface and Textured Surface 2 were coated with aggrecan, collagen I, fibronectin and hyaluronic acid. Proliferation of breast-derived fibroblasts was quantified using water-soluble tetrazolium salt-1 (WST-1) cell proliferation assay and compared with control cultures grown onto uncoated Textured Surface 1, Smooth Surface and Textured Surface 2. Measurements were recorded over a 24 h period and data plotted as mean ± standard deviation. Fibroblast seeded onto collagen I and fibronectin significantly increased absorbance (*$p<0.05$, **$p<0.01$, ***$p<0.001$) in comparison to the uncoated surfaces.

a more random actin network than on uncoated TS1. Well spread cells in collagen I, fibronectin and hyaluronic acid coated TS1, SS and TS2 exhibited thick fibres throughout the entire cell. In fibronectin coated TS2, collagen I coated SS and hyaluronic acid coated TS1 cells showed a well-organised actin cytoskeleton. Fibroblasts seeded on fibronectin coated TS1 and on hyaluronic acid coated TS2 exhibited an elongated cellular phenotype. However, actin fibres were dense in all the cells in hyaluronic acid coated TS2 in comparison to fibroblasts in fibronectin coated TS1 which showed an abundance of fine fibres throughout the entire cell.

3.6. *Effect of aggrecan, collagen I, fibronectin and hyaluronic acid coatings on adhesion expression in breast fibroblasts*

After 24 h of incubation, total RNA was extracted from breast fibroblasts ($n=3$) (passage 2). The expression of alpha-actinin, FAK, paxillin, vinculin mRNA was determined by quantitative reverse-transcriptase polymerase chain reaction to compare the effect of the molecular coatings with the uncoated implants in breast fibroblasts (Fig. 10).

When the expression of the cytoskeleton components was examined, the level of α-actinin was found to be reduced in uncoated and aggrecan coated surfaces, but the α-actinin expression was higher in collagen I and fibronectin coated TS1 ($p<0.01$) and hyaluronic acid coated TS1 ($p<0.001$), and in collagen I, fibronectin and hyaluronic acid coated TS2 ($p<0.001$). The FAK level expression by breast fibroblasts was upregulated in collagen I, fibronectin and hyaluronic acid coated surfaces ($p<0.001$), while the FAK expression was lower in both uncoated and aggrecan coated TS1, SS and TS2. The gene expression of paxillin was upregulated in fibroblasts seeded on collagen I and fibronectin coated implants ($p<0.001$) and in the hyaluronic acid coated TS1 ($p<0.01$), SS ($p<0.05$) and TS2 ($p<0.001$). Regarding vinculin expression, a higher level was detected in the surfaces coated with collagen I and fibronectin ($p<0.001$) compared to the uncoated ones.

4. Discussion

In this study, for the first time, we evaluated the physicochemical characteristics of coated silicone breast implants on breast-derived fibroblast morphology and behaviour. Chemical properties were examined by Raman spectroscopy; topographical features were studied by confocal laser microscopy, and the effect of four unique protein and glycosaminoglycan (GAG) coatings (aggrecan, collagen I, fibronectin and hyaluronic acid) on breast-derived fibroblast cytotoxicity, attachment, proliferation, morphology and gene expression were examined.

The choice of the specific coatings evaluated in this study was based on an in-house whole genome microarray study undertaken in order to determine genes whose expression would correlate with breast capsular contracture formation and on previously published gene and protein research of relevance to breast capsular fibrosis (Kyle et al., 2013). Our results showed that specific coatings can modify the physicochemical properties of implant surfaces eliciting specific cellular reactions. Moreover, we showed that the coated surfaces excluding aggregan, promoted cell-surface adhesion, proliferation, morphology and the upregulation of adhesion-related genes without any cytotoxic effect. These findings provide valuable information of characteristic expression of adhesion-related genes, cell morphology and proliferation in breast fibroblasts following the application of specific coatings on smooth compared to textured breast implant surfaces.

Foreign body reaction is elicited by the implant placement in the body; this initiates an initial inflammatory phase where the prosthesis is encapsulated or eliminated by the host. Surface characteristics such as roughness, texture, surface free energy, surface charge and chemical composition all play key roles in cell adhesion and growth, and the nature of a biomaterial surface governs the phenotypic response of interacting cells (Prasad et al., 2010). Previous studies (Bacakova et al., 2011) have demonstrated that fibroblast activity can be modulated by specific coatings. Coating the surface of implants with these specific coatings may thus provide enhanced support and anchorage for cells and favourably regulate cell morphology, adhesion and proliferation (Yamamoto et al., 2006, Franz et al., 2011). In this study, specific coatings were employed on the surfaces of smooth versus textured breast implant surfaces in order to study fibroblast behaviour on these different topographies. It has been suggested that ECM proteins can be used to optimise fibroblast reaction to implants (Li et al., 2012a, Li et al., 2012b, Ungaro et al., 2006). Surface roughness and chemistry of the substrate have been shown to modulate cell-surface interaction. Furthermore, cell attachment and proliferation can be improved by utilising coatings and altering the microtopography of these surfaces.

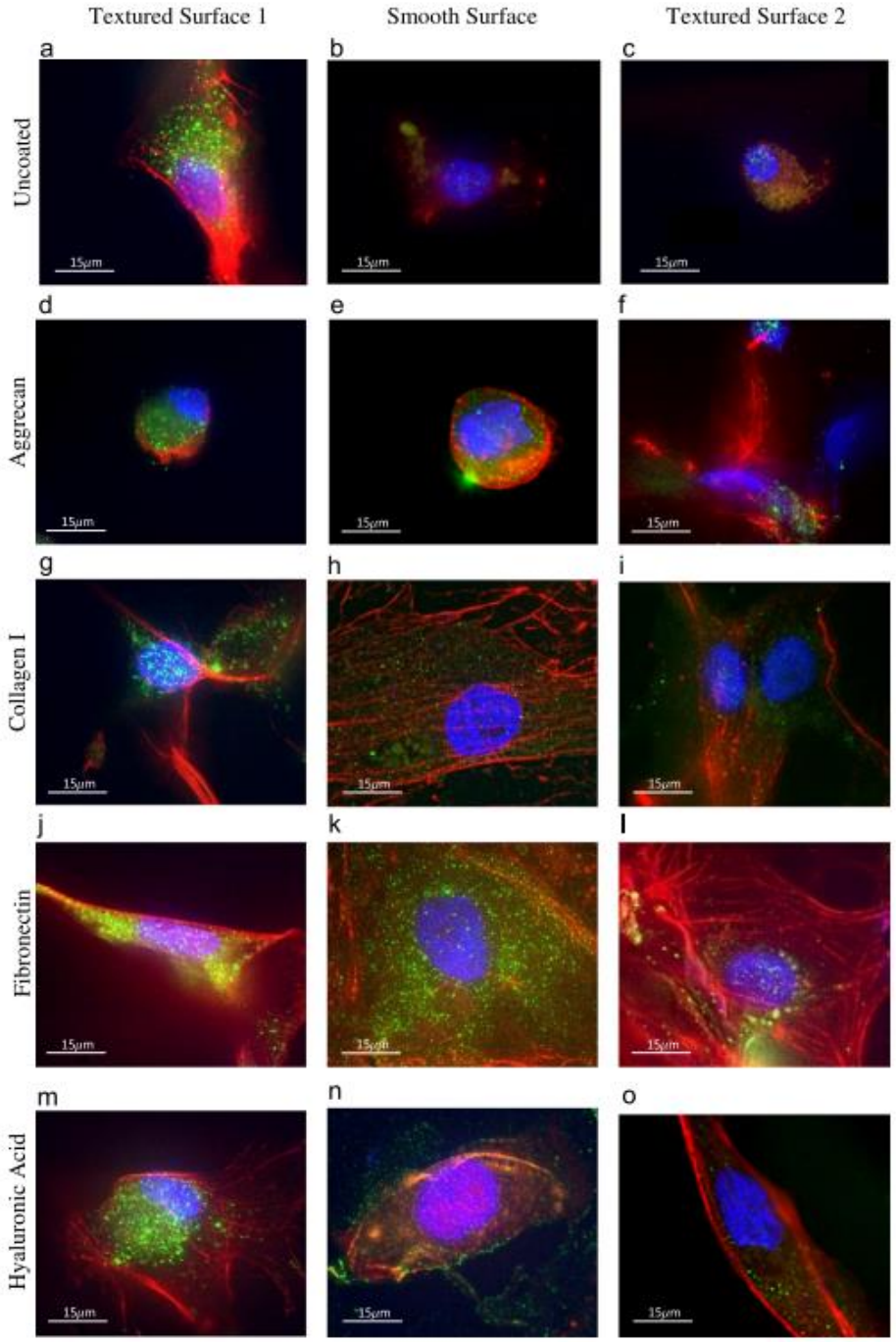

Fig. 9 – Morphology of breast fibroblasts seeded onto coated and uncoated breast implant surfaces. Immunofluorescence staining of the actin (red) (cytoskeleton), vinculin (green) (focal adhesion protein) and cell nucleus (blue) (DAPI) was performed on breast-derived fibroblasts on day 1 after seeding onto (D–F) aggrecan, (G–I) collagen I, (J–L) fibronectin and (M-O) hyaluronic acid. Coated and uncoated (A, D, G, J, M) Surface Texture 1, (B, E, H, K, N) Smooth Surface and (C, F, I, L, O) Surface Texture 2. Pictures were taken using DeltaVision deconvolution system at 100x magnification.

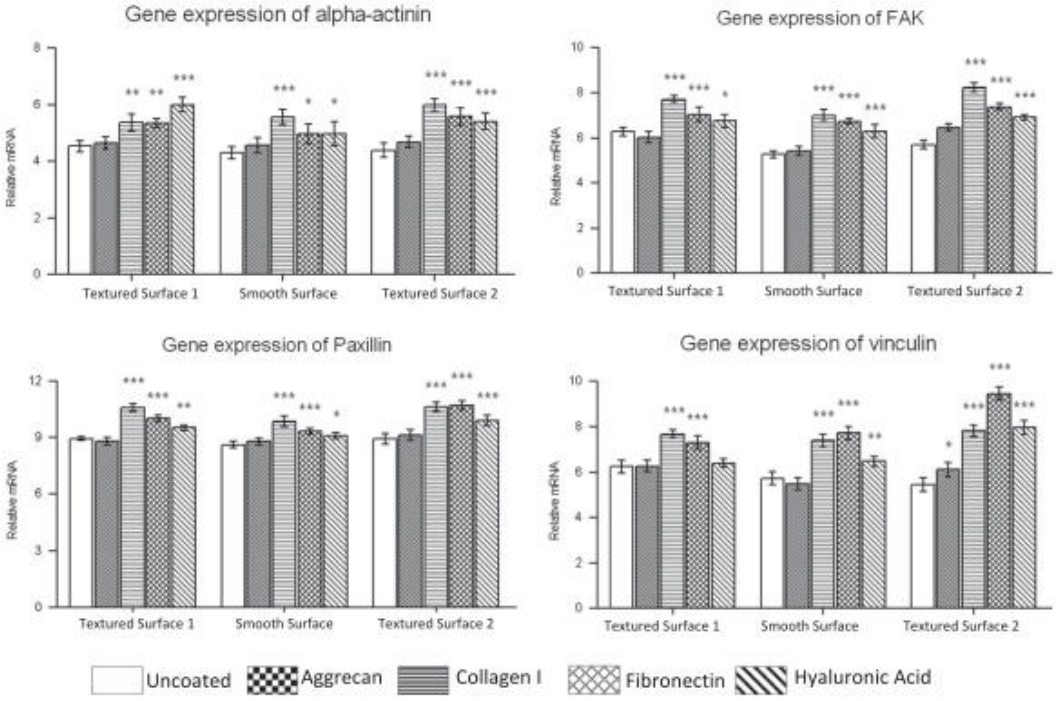

Fig. 10 – Effect of aggrecan, collagen I, fibronectin and hyaluronic acid coatings on adhesion expression in breast-derived fibroblasts. After 24 h of incubation, total RNA was extracted from breast-derived fibroblasts ($n=3$) (passage 2). The expression of α-actinin, FAK, paxillin and vinculin mRNA was determined by quantitative reverse-transcriptase polymerase chain reaction. The expression of the above markers was normalised to RPL32. Results are expressed as mean ± standard deviation of triplicates. *$p<0.05$, **$p<0.01$, ***$p<0.001$ indicate significant difference between mRNA expression in fibroblasts seeded onto uncoated implants versus mRNA expression in fibroblasts seeded onto coated surfaces.

The study demonstrated that cell adhesion and spreading were sensitive to both the physical and chemical properties of the substrate. Cell proliferation and cytotoxicity were also studied. It was found that surfaces coated with collagen I, fibronectin and hyaluronic acid did not elicit a cytotoxic effect on breast tissue–derived fibroblasts in comparison to the uncoated surfaces. Lower proliferation rates were measured on uncoated and aggrecan coated surfaces. Fibroblast proliferation rate differed significantly among the surfaces investigated. An investigation into cell morphology showed that surface coatings promoted cell morphological modifications and the organisation of actin fibres in all surfaces. Gene expression of adhesion-related proteins was shown to be modified by specific coatings and topography amongst the variety of surfaces tested.

Silicone breast implants investigated in this study are made with polydimethylsiloxane (PDMS); Raman spectra revealed a nearly matching profile for implants from the same company; however, implants from different company showed a dissimilar profile. These results are consistent with FTIR/ATR spectroscopy studies comparing breast implants from two different companies (Persichetti et al., 2009). Breast implants differed in chemical composition, and this could be related to the manufacturing process. In smooth implants, the silicone rubber shell is made with a shiny polished mandrel, and to flatten this outer surface, it is steeped in a solvent, while in textured implants, the silicone rubber shell is made with a negative-contact imprint from a polyurethane foam or by pushing the silicone-coated mandrel into granular salt (Barr and Bayat, 2011) (Fig. 1).

Scanning electron microscopy and light microscopy have been used to analyse the topographic features (Barr et al., 2009). Changes in surface roughness after coating the surfaces were consistent with the adsorption of coatings on the valleys of the surfaces. Fibronectin coated surfaces showed the highest increment of surface roughness up to 277% in SS, 100% in TS1 and 16% in TS2 which correlates well with the highest rates of adsorption (per surface) of fibronectin on SS (0.014 mg/cm^2), TS1 (1.118 mg/cm^2) and TS2 (0.986 mg/cm^2). It was also found that cell adhesion was improved by surface roughness. Cell adhesion on rougher surfaces was higher. This means that the greater area due to texturing available for cell spreading allows increased anchoring ability by fibroblasts. In contrast, the same level of cell adhesion was not achieved on smooth surfaces, where low percentages of cell adhesion were recorded in comparison to the textured surfaces. After evaluating surface roughness, it was determined that, for the surfaces investigated in this study,

fibroblast adhesion required a substrate with a surface roughness of at least 14 μm, at which point the degree of adhesion increased with surface roughness until a maximum adhesion was achieved at 21.94 μm. Furthermore, cell spreading demonstrated an incremental response to increases in surface roughness between 17.46 μm and 21.94 μm. The organisation of the actin cytoskeleton was induced by the microtopography in fibroblasts seeded on textured surfaces alone compared to smooth surfaces.

Increased cell adhesion was found on all implant surfaces coated with fibronectin and collagen I in comparison to the uncoated surfaces, which increased cell spreading. By contrast, implants coated with aggrecan demonstrated reduced cell-surface adhesion which therefore reduced cellular proliferation. These results suggest that collagen I and fibronectin act as potent regulators of cytoskeletal organisation and cell spreading. This interaction is important for cell migration in wound healing (Franz et al., 2007). Cells that are forced to spread over large surface areas, as in the case with textured surfaces, survive better and proliferate faster than cells that do not spread out (Lowery et al., 2010). The stimulatory effect of cell spreading potentially encourages tissues to regenerate after injury. If cells are lost from an epithelial layer, for example, the spreading of the remaining cells into the vacated space will stimulate them to proliferate until they fill the gap (Alberts et al., 2002). It is still uncertain, however, how a cell senses the extent of its own spreading and how it adjusts its behaviour accordingly. Cell behaviour is likely to be affected by the chemical and physical structure of the coating. Fluorescent staining images revealed that surfaces coated with collagen I and fibronectin induced organisation of actin stress fibres and that collagen I affected the cytoskeletal arrangement and cell spreading, factors commonly regarded to be of significance with cell migration and wound healing.

In cell migration, a protrusion is sent in the direction of the movement; the extracellular substrate bound by integrin receptors induces integrin clustering and formation of adhesion complexes (Biname et al., 2010). This leads to the eliciting of adaptor proteins, which connect the adhesion points to the actin cytoskeleton and triggers intracellular signalling. This signal is defined by the proteins created and the type of integrin engaged in the interaction with the specific extracellular substrate. Small temporary adhesion complexes located in the leading edge of protrusions (focal complexes) mature under tension into larger structures known as focal contacts. Focal adhesions are more stable structures connected to actin stress fibres (Berrier and Yamada, 2007). Focal adhesion complexes are well established as a major adhesive and signal transducing component between the internal actin cytoskeleton and the external ECM (Petit and Thiery, 2000). Focal adhesion plays a key role in sensing surface topography in the extracellular environment. Focal adhesion kinase and the adaptor protein paxillin are focal adhesion proteins that can bind to and activate integrin B1 subunit cytoplasmic domains (Sequeira et al., 2012), along with vinculin, which connects integrins to actin filaments

The adapter proteins that link stress fibres to integrins include alpha-actinin. An increase in alpha-actinin content was observed in the cells that had spread most with netlike actin filaments seeded on hyaluronic acid coated TS1, collagen I coated SS and fibronectin coated TS2. When SS and TS2 were coated with collagen I, and TS1 and TS2 were coated with fibronectin and hyaluronic acid, the alpha-actinin expression was upregulated ($p<0.001$), which resulted in firmly attached fibroblasts to the substrate ($p<0.001$). FAK has a role in modulation of the assembly of focal adhesions in response to tension exerted by the cytoskeleton on attachments to the extracellular substrate via integrins (Parsons, 2003). We observed that the expression of FAK was reduced in fibroblasts seeded onto the uncoated and aggrecan coated implant surfaces. In contrast, the FAK expression was upregulated in the surfaces coated with fibronectin and collagen I which resulted in increased cell-substrate adhesion; $p<0.001$. Paxillin, a focal adhesion-associated adaptor protein is involved in modulating cell adhesion and spreading (Wang et al., 2009). We observed that the expression of paxillin was reduced in fibroblasts cultured on the uncoated and aggrecan coated implant surfaces. However, paxillin expression was upregulated ($p<0.001$), which resulted in well-spread fibroblasts, in the surfaces coated with fibronectin and collagen I. Vinculin, a membrane-cytoskeletal protein in focal adhesions that is involved in linkage of integrin adhesion molecules to the actin cytoskeleton (Maheshwari et al., 2000), was found in all surfaces. A low content of vinculin was observed in fibroblasts seeded onto uncoated and aggrecan coated surfaces ($p<0.001$). This resulted in weakening of adhesion ($p<0.001$), conversely a higher content of vinculin resulted in bigger focal adhesions and greater abundance of focal adhesion points in fibroblasts seeded onto collagen I and fibronectin surfaces. There is a consistent pattern in enhanced cell-surface adhesion when the surfaces were coated with collagen I. Cell proliferation highlights a significant benefit on the presence of collagen I to the surface of TS1, while hyaluronic acid did to SS, and fibronectin to TS2. TS1 represented the optimal substrate to promote spreading when coated with hyaluronic acid, while SS and TS2 did with collagen I. Surprisingly, no significant difference was identified between fibroblast adhesion and proliferation to aggrecan coated implants compared to the corresponding uncoated surfaces ($p>0.05$).

Breast capsular contracture aetiology remains uncertain, but it is characterised by dense fibrocollagenous connective tissue with local inflammatory response. Furthermore, breast capsule consists of myofibroblasts, which are implicated in contracting the breast implants (Hwang et al., 2010). Thus we decided to limit our samples to breast-derived fibroblasts. However, future investigation, involving different types of cells found in breast capsules, will be of value. Another potential limitation of our study was the total number of samples used for breast tissue ($n=3$); a larger number of samples that includes different ethnicities would be beneficial. Our research represents a study focused on enhancing cell-surface adhesion, spreading and proliferation on fibroblasts seeded on breast implants. Coating deposition has been used successfully to improve cell behaviour of medical devices (Filova et al., 2014), but often results in coatings that are too thick, non-uniform and unstable. However, based on previous reports, we can speculate that coating deposition

can be improved by functionalising the substrate in order to covalently attach the coatings. Chemically grafting coatings to substrates can improve coating adhesion (Kandel et al., 2014) to the substrate resulting in a thin and more stable layer as described previously for other biomedical research techniques.

The study demonstrated that cell adhesion and spreading were sensitive to smooth and textured surfaces. Cell proliferation and cytotoxicity were also studied. It was found that surfaces coated with collagen I, fibronectin and hyaluronic acid did not elicit a cytotoxic effect on breast tissue derived fibroblasts in comparison to the uncoated surfaces. Fibroblast proliferation rate differed significantly among the surfaces investigated. An investigation into cell morphology showed that surface coatings promoted cell morphology modifications and the organisation of actin fibres in all surfaces. Gene expression of adhesion-related proteins was shown to be modified by specific coatings and topography amongst the variety of surfaces tested.

5. Conclusion

In summary, this study has demonstrated the extent and strength of cell adhesion, and subsequent cell proliferation and differentiation based on the physical interactions between cells and the extracellular environment in the form of topography and on the chemical interactions mediated by specific coatings. We have shown that the surface coating of the silicone breast implants induced over-expression of specific adhesion-related genes in breast-derived fibroblasts. Our findings demonstrate that the most promising candidates in the regulation of adhesion and proliferation in the coated textured implant are fibronectin and collagen I. A good adhesion ensures that the implant holds in place; thus preventing micromotion at the host prosthesis interface, the fibroblasts will not over-produce collagen in response to this host-prosthesis shearing motion. Consequently, capsules around these coated surfaces may be thinner and less contracted in comparison to the capsules surrounding the uncoated textured surface implants. The addition of appropriate coating to the surface of silicone breast implants may reduce the risk of capsular contracture formation in the near future. Further studies are required to provide a better understanding of cell-surface interaction in breast fibroblasts and silicone implants.

REFERENCES

Alberts, B., Johnson, A., Lewis, J., 2002. Molecular Biology of the Cell. Garland Science, New York.

Ashley, F.L., 1970. A new type of breast prosthesis. Preliminary report. Plast. Reconstr. Surg. 45, 421–424.

Bacakova, L., Filova, E., Parizek, M., Ruml, T., Svorcik, V., 2011. Modulation of cell adhesion, proliferation and differentiation on materials designed for body implants. Biotechnol. Adv. 29, 739–767.

Baker, J., 1975. Classification of spherical contractures. Aesthetic breast symposium. Scottsdale, Arizona.

Barr, S., Bayat, A., 2011. Breast implant surface development: perspectives on development and manufacture. Aesthet. Surg. J. 31, 56–67.

Barr, S., Hill, E., Bayat, A., 2009. Current implant surface technology: an examination of their nanostructure and their influence on fibroblast alignment and biocompatibility. Eplasty 9, 22.

Berrier, A.L., Yamada, K.M., 2007. Cell-matrix adhesion. Cell. Physiol 213, 565–573.

Berry, M.G., Davies, D.M., 2010. Breast augmentation: Part I - a review of the silicone prosthesis. J. Plast. Reconstr. Aesthet. Surg. 63, 1761–1768.

Bershadsky, A.D., Balaban, N.Q., Geiger, B., 2003. Adhesion-dependent cell mechanosensitivity. Annu. Rev. Cell Dev. Biol. 19, 677–695.

Biname, F., Pawlak, G., Roux, P., Hibner, U., 2010. What makes cells move: requirements and obstacles for spontaneous cell motility. Mol. BioSyst 6, 648–661.

Cohen, M., Klein, E., Geiger, B., Addadi, L., 2003. Organization and adhesive properties of the hyaluronan pericellular coat of chondrocytes and epithelial cells. Biophys. J. 85, 1996–2005.

Collins, M.N., Birkinshaw, C., 2013. Hyaluronic acid based scaffolds for tissue engineering-A review. Carbohydr. Polym. 92, 1262–1279.

Elter, P., Weihe, T., Buhler, S., Gimsa, J., Beck, U., 2012. Low fibronectin concentration overcompensates for reduced initial fibroblasts adhesion to a nanoscale topography: single-cell force spectroscopy. Colloid Surface B 95, 82–89.

Filova, E., Brynda, E., Riedel, T., Chlupac, J., Vandrovcova, M., Svindrych, Z., Lisa, V., Houska, M., Pirk, J., Bacakova, L., 2014. Improved adhesion and differentiation of endothelial cells on surface-attached fibrin structures containing extracellular matrix proteins. J. Biomed. Mater. Res. A 102, 698–712.

Franz, M.G., Steed, D.L., Robson, M.C., 2007. Optimizing healing of the acute wound by minimizing complications. Curr. Probl. Surg. 44, 691–763.

Franz, S., Rammelt, S., Scharnweber, D., Simon, J.C., 2011. Immune responses to implants - A review of the implications for the design of immunomodulatory biomaterials. Biomaterials 32, 6692–6709.

Harvey, A.G., Hill, E.W., Bayat, A., 2013. Designing implant surface topography for improved biocompatibility. Expert Rev. Med. Devices 10, 257–267.

Hauser, J., Zietlow, J., Koller, M., Esenwein, S.A., Halfmann, H., Awakowicz, P., Steinau, H.U., 2009. Enhanced cell adhesion to silicone implant material through plasma surface modification. J. Mater. Sci. Mater. Med. 20, 2541–2548.

Hench, L.L., Polak, J.M., 2002. Third-generation biomedical materials. Science 295, 1014–1017.

Hwang, K., Sim, H.B., Huan, F., Kim, D.J., 2010. Myofibroblasts and capsular tissue tension in breast capsular contracture. Aesthetic. Plast. Surg. 34, 716–721.

Kandel, J., Lee, H.S., Sobolewski, P., Tomczyk, N., Composto, R.J., Eckmann, D.M., 2014. Chemically grafted fibronectin for use in QCM-D cell studies. Biosens. Bioelectron. 58, 249–257.

Korurer, E., Kenar, H., Doger, E., Karaoz, E., 2014. Production of a composite hyaluronic acid/gelatin blood plasma gel for hydrogel-based adipose tissue engineering applications. J. Biomed. Mater. Res. A 102A, 2220–2229.

Kyle, D.J., Harvey, A.G., Shih, B., Tan, K.T., Chaudhry, I.H., Bayat, A., 2013. Identification of molecular phenotypic descriptors of breast capsular contracture formation using informatics analysis of the whole genome transcriptome. Wound Repair Regen. 21, 762–769.

Li, Y.-C., Lin, Y.-C., Young, T.-H., 2012a. Combination of media, biomaterials and extracellular matrix proteins to enhance the differentiation of neural stem/precursor cells into neurons. Acta Biomater. 8, 3035–3048.

Li, Y., Zhang, S., Guo, L., Dong, M., Liu, B., Mamdouh, W., 2012b. Collagen coated tantalum substrate for cell proliferation. Colloid Surface B 95, 10–15.
Lowery, J.L., Datta, N., Rutledge, G.C., 2010. Effect of fiber diameter, pore size and seeding method on growth of human dermal fibroblasts in electrospun poly(É›-caprolactone) fibrous mats. Biomaterials 31, 491–504.
Maheshwari, G., Brown, G., Lauffenburger, D.A., Wells, A., Griffith, L.G., 2000. Cell adhesion and motility depend on nanoscale RGD clustering. Cell Sci 113, 1677–1686.
Muschler, J., Streuli, C.H., 2010. Cell-matrix interactions in mammary gland development and breast cancer. Cold Spring Harb. Perspect. Biol. 2, 1–17.
Mwenifumbo, S., Stevens, M.M., 2007. ECM interactions with cells from the macro- to nanoscale. Biomed. Nanostruct, 223–260.
Park, J.U., Ham, J., Kim, S., Seo, J.-H., Kim, S.-H., Lee, S., Min, H.J., Choi, S., Choi, R.M., Kim, H., Oh, S., Hur, J.A., Choi, T.H., Lee, Y., 2014. Alleviation of capsular formations on silicone implants in rats using biomembrane-mimicking coatings. Acta Biomater..
Parsons, J.T., 2003. Focal adhesion kinase: the first ten years. Cell Sci. 116, 1409–1416.
Persichetti, P., Tenna, S., Delfino, S., Abbruzzese, F., Trombetta, M., Scuderi, N., 2009. Textured and smooth breast implants: is there a difference in the chemical structure of silicone?: an analysis with fourier transformation infrared and attenuated total reflectance spectroscopy. Ann. Plas. Surg 63, 373–377.
Petit, V., Thiery, J.-P., 2000. Focal adhesions: structure and dynamics. Biol. Cell 92, 477–494.
Prasad, B.R., Brook, M.A., Smith, T., Zhao, S., Chen, Y., Sheardown, H., D'Souza, R., Rochev, Y., 2010. Controlling cellular activity by manipulating silicone surface roughness. Colloid Surface B 78, 237–242.
Roca, G.B., Graf, R., da Silva Freitas, R., Salles Jr., G., Francisco, J.C., Noronha, L., Maluf Jr., I., 2014. Autologous fat grafting for treatment of breast implant capsular contracture: a study in pigs. Aesthet. Surg. J. 34, 769–775.
Roughley, P., Martens, D., Rantakokko, J., Alini, M., Mwale, F., Antoniou, J., 2006. The involvement of aggrecan polymorphism in degeneration of human intervertebral disc and articular cartilage. Eur. Cell. Mater. 11, 1–7.
Sequeira, S.J., Soscia, D.A., Oztan, B., Mosier, A.P., Jean-Gilles, R., Gadre, A., Cady, N.C., Yener, B., Castracane, J., Larsen, M., 2012. The regulation of focal adhesion complex formation and salivary gland epithelial cell organization by nanofibrous PLGA scaffolds. Biomaterials 33, 3175–3186.
Shin, H., Jo, S., Mikos, A.G., 2003. Biomimetic materials for tissue engineering. Biomaterials 24, 4353–4364.
Steward Jr., R.L., Cheng, C.M., Ye, J.D., Bellin, R.M., LeDuc, P.R., 2011. Mechanical stretch and shear flow induced reorganization and recruitment of fibronectin in fibroblasts. Sci. Rep. 1, 147.
Ungaro, F., Biondi, M., Indolfi, L., De Rosa, G., La Rotonda, M.I., Quaglia, F., Netti, P., 2006. Bioactivated polymer scaffolds for tissue engineering. in topics in tissue engineering. N. Ashammakhi & R.L. Reis 2, 1–38.
Valencia-Lazcano, A.A., Alonso-Rasgado, T., Bayat, A., 2013. Characterisation of breast implant surfaces and correlation with fibroblast adhesion. J. Mech. Behav. Biomed. Mater. 21, 133–148.
Vazquez, G., 1999. A ten-year experience using polyurethane-covered breast implants. Aesthetic. Plast. Surg. 23, 189–196.
Vazquez, G., Pellon, A., 2007. Polyurethane-coated silicone gel breast implants used for 18 years. Aesthetic. Plast. Surg. 31, 330–336.
Wang, Y.-H., Yan, Z.-Q., Shen, B.-R., Zhang, L., Zhang, P., Jiang, Z.-L., 2009. Vascular smooth muscle cells promote endothelial cell adhesion via microtubule dynamics and activation of paxillin and the extracellular signal-regulated kinase (ERK) pathway in a co-culture system. Eur. J. Cell. Biol. 88, 701–709.
Yamamoto, S., Tanaka, M., Sunami, H., Arai, K., Takayama, A., Yamashita, S., Morita, Y., Shimomura, M., 2006. Relationship between adsorbed fibronectin and cell adhesion on a honeycomb-patterned film. Surf. Sci 600, 3785–3791.
Zeplin, P.H., Maksimovikj, N.C., Jordan, M.C., Nickel, J., Lang, G., Leimer, A.H., Römer, L., Scheibel, T., 2014. Spider silk coatings as a bioshield to reduce periprosthetic fibrous capsule formation. Adv. Funct. Mater. 24, 2658–2666.